

Secteur des Sciences de la Santé  
Ecole doctorale des Sciences Pharmaceutiques et Biomédicales  
Louvain Drug Research Institute  
Unité de Résonance Magnétique Biomédicale

**Radiolabelled antibody-targeted gold nanoparticles for cancer imaging:  
effects of nanoparticle conjugation on the biological properties of the  
antibody and tumour targeting**

Linda KARMANI

Thèse présentée en vue de l'obtention du grade de  
Docteur en Sciences Biomédicales et Pharmaceutiques

Promoteur: Professeur B. Gallez  
Co-promoteur: Professeur T. Vander Borgh

Bruxelles, janvier 2014

## **Jury de thèse**

**Promoteur:** Professeur Bernard Gallez, Université Catholique de Louvain

**Co-promoteur:** Professeur Thierry Vander Borgh, Université Catholique de Louvain

**Président du jury:** Professeur Olivier Feron, Université Catholique de Louvain

### **Membres du jury:**

Professeur Vincent Grégoire, Université Catholique de Louvain

Professeur Stéphane Lucas, Université de Namur

Professeur Françoise Kraeber-Bodéré, Université de Nantes

Professeur Tony Lahoutte, Vrije Universiteit Brussel



## Remerciements

Ce travail issu de quatre années de recherches réalisées au sein du laboratoire de résonance magnétique biomédicale n'aurait pu être mené à bien sans la participation de nombreuses personnes que je tiens à remercier.

Je souhaiterais tout d'abord remercier mon promoteur, le Professeur Bernard Gallez pour m'avoir permis de réaliser une thèse au sein de son laboratoire et pour le respect qu'il accorde au travail réalisé, ses précieux conseils, sa disponibilité et surtout pour ses encouragements tout au long de ce travail de thèse.

Je remercie également mon co-promoteur, le professeur Thierry Vander Borght sans qui je n'aurais sans doute pas eu l'opportunité de réaliser une thèse. Je le remercie de m'avoir accordé sa confiance et pour l'intérêt qu'il a continuellement manifesté à l'égard de mes travaux.

Je remercie les membres de mon jury, les Professeurs Olivier Feron, Vincent Grégoire et Stéphane Lucas pour leurs conseils avisés et le suivi constructif au cours de l'ensemble de mes comités, ainsi que les membres extérieurs, les Professeurs Françoise Kraeber-Bodéré et Tony Lahoutte pour avoir accepté de réviser ce travail et d'y apporter un regard critique.

Je tiens à remercier les personnes des différentes unités, avec qui j'ai apprécié de collaborer et qui ont participé à l'édifice de cette thèse:

- L'unité FATH-IREC-UCL du Professeur Olivier Feron et particulièrement, Caroline Bouzin que je remercie pour sa grande disponibilité et pour toute l'aide et conseils prodigués.
- L'unité PMR-LARN-Université de Namur du Professeur Stéphane Lucas que je remercie pour m'avoir impliquée dans le projet TARGAN duquel découle mon projet de thèse, et qui m'a énormément enrichi de par son aspect pluridisciplinaire. Je remercie aussi Virginie Bouchat, Vanessa Valembois et Nicolas Moreau pour leur grande disponibilité et patience à produire les précieuses nanoparticules d'or.
- L'unité MIRO-IREC-UCL du Professeur Vincent Grégoire que je remercie pour m'avoir donné l'opportunité de réaliser les expériences d'imagerie au sein de son unité. Je remercie également Daniel Labar pour sa persévérance à multiplier les tirs cyclotron en vue de produire du  $^{89}\text{Zr}$  (à l'origine de mes premières lueurs d'espoir quant à l'avancement de mes travaux), je le remercie aussi pour sa grande disponibilité, son dévouement pour le travail accompli et sa sympathie. Merci aussi à Jacques Gillart pour son aide, ainsi qu'à Anne Bol pour m'avoir initiée à l'utilisation du PET-scan et du SPECT/CT et pour sa disponibilité et sa patience dans la résolution des problèmes liés aux traitements d'images.

- L'unité URBC-Université de Namur du Professeur Carine Michiels que je remercie pour sa disponibilité, son aide précieuse dans la mise en place des tests de reconnaissance ELISA, pour le partage de son expérience et pour son regard éclairé lors des réunions TARGAN. Je remercie également Marc Dieu pour le temps consacré au séquençage de l'anticorps anti-endogline par spectrométrie de masse.
- L'unité NARC-Université de Namur du Professeur Davide Bonifazi et en particulier Praveen Ganesh Nagaswaran et Riccardo Marega pour la mise au point des essais de couplage ainsi que pour les analyses par thermogravimétrie.
- L'unité LTAP-UCL du Professeur Vincent Haufroid et en particulier Gladys Deumer pour son aide lors de la mise au point des analyses ICP-MS.

Enfin, je souhaiterais remercier toutes les personnes qui m'ont accordé de leur temps afin de mener à bien ce travail en commençant par Jacques Adline pour m'avoir initiée aux marquages radioactifs. Je remercie également Stéphan Walrand du service de médecine nucléaire de l'UCL pour m'avoir initiée au logiciel PMOD d'analyse d'images, merci aussi à Laurence Alexandre pour l'iode radioactif fourni lors de la mise au point des radiomarquages.

J'aimerais terminer par mes collègues du laboratoire REMA avec qui j'ai parcouru ces quatre dernières années et à qui j'adresse toute ma reconnaissance pour leur soutien. Je commencerais par mon collègue de bureau Philippe Levêque, sans qui les manipulations auraient été plus difficiles à apprivoiser. Merci Philippe pour ton regard critique, tes connaissances diverses que tu savais partager, pour ton écoute et tes conseils judicieux. Merci aussi pour ton aide considérable dans la résolution des problèmes rencontrés. Je remercie aussi Bénédicte et Julie M. pour leur soutien et leurs encouragements, Anne-Catherine pour sa grande écoute, son précieux soutien et sa gentillesse ; Oussama pour ses conseils, sa disponibilité et son humour ; Valérie pour son dévouement et son écoute, Pierre pour ses conseils et son esprit critique, Quentin pour sa bonne humeur, Lionel et An les forces tranquilles du labo, Géraldine et Julie K. pour leur gentillesse et leur sympathie, Florence pour son dynamisme, ainsi qu'aux derniers arrivés Venkatesan, Marie-Aline et Céline à qui je souhaite beaucoup de succès.

Enfin, je remercie ma famille pour son soutien constant et pour ses encouragements qui m'ont portée tout au long de ces quatre dernières années, et j'adresse une pensée émue à ma grand-mère qui nous a récemment quittés et qui m'a tant apportée.

## Table of contents

ABBREVIATION LIST .....	1
FOREWORD .....	2
CHAPTER 1 : INTRODUCTION .....	4
I. Radioimmunotargeting of cancer cells .....	6
1. Radioimmunotargeting approach .....	6
2. Radioimmunotargeting issues .....	7
2.1. Antibody formats for improving radioimmunotargeting.....	7
2.2. Radioimmunodetection aspects .....	11
a. Radionuclides for cancer imaging .....	11
b. Rational for the selection of the radionuclide.....	12
c. Clinical applications of radioimmunodetection.....	13
2.3. Radioimmunotherapy aspects .....	13
a. Radionuclides for cancer therapy .....	13
b. Clinical applications of radioimmunotherapy .....	14
3. Radioimmunotargeting limitations.....	15
4. Radiochemistry issues .....	17
4.1. Radiolabelling with radioiodine.....	17
4.2. Radiolabelling with zirconium-89.....	19
5. <i>In vivo</i> explorations in mice .....	21
5.1. Invasive <i>ex-vivo</i> studies.....	21
5.2. Noninvasive <i>in vivo</i> studies.....	21
a. Single-photon emission computed tomography (SPECT).....	21
b. Positron emission tomography (PET) .....	22
c. Computed tomography and dual mode imaging.....	23

---

II. Cancer targets addressed in the thesis .....	25
1. Epidermal growth factor receptor (EGFR).....	25
2. Endoglin (CD105).....	27
III. Nanoparticle drug delivery systems .....	32
1. Overview of nanoparticle properties .....	32
2. Gold nanoparticles (AuNPs) .....	32
2.1. Production .....	33
a. Wet chemical method.....	33
b. Physical vapour deposition method (PVD).....	33
2.2. Physical properties and biomedical applications .....	34
a. Photophysical properties of gold nanoparticles.....	35
b. Gold nanoparticles as contrast agents.....	35
c. Gold nanoparticles as therapeutic agents.....	36
2.3. Strategies of tumour targeting.....	41
a. Enhanced permeation and retention effect (EPR) .....	41
b. Active targeting .....	43
2.4. Pharmacokinetic behaviour of gold nanoparticles .....	44
2.5. Toxicity .....	46
IV. Radiolabelled antibody-targeted gold nanoparticles.....	49
1. Synthesis of radiolabelled antibody-conjugated gold nanoparticles .....	49
2. Influence of targeting ligands on tumour uptake of conjugated gold nanoparticles .....	50
3. Potential biomedical applications.....	52
CHAPTER 2 : AIMS OF THE THESIS .....	55

CHAPTER 3 : RESULTS .....	58
I. Targeting cancer cells using $^{125}\text{I}$ -labelled anti-EGFR antibody-conjugated gold nanoparticles .....	59
II. <i>In vivo</i> deiodination impact of $^{125}\text{I}$ -labelled anti-CD105 antibody on tumour targeting in mice .....	69
III. Targeting cancer cells using $^{89}\text{Zr}$ -labelled anti-EGFR antibody-conjugated gold nanoparticles .....	93
IV. Targeting cancer cells using $^{89}\text{Zr}$ -labelled anti-endoglin antibody-conjugated gold nanoparticles .....	103
CHAPTER 4 : DISCUSSION AND PROSPECTS .....	138
REFERENCES.....	162
APPENDIX .....	188



## Abbreviation list

%ID g <sup>-1</sup>	percentage of the injected dose per gram of tissue	NIR	near infrared
%ID ml <sup>-1</sup>	percentage of the injected dose per milliliter	NP	nanoparticle
ADCC	antibody-dependent cell-mediated cytotoxicity	PDT	photodynamic therapy
ALK	activin receptor-like kinase	PEG	polyethylene glycol
AuNPs	gold nanoparticles	PET	positron emission tomography
CD	cluster of differentiation	PK	pharmacokinetics
CD105	endoglin	PPAA	plasma-polymerized allylamine
CDC	complement-dependent cytotoxicity	PTT	photothermal therapy
CT	computed tomography	PVD	physical vapour deposition
d	day	RES	reticuloendothelial system
DC	direct current	RF	radiofrequency
Df	desferrioxamine B	RID	radioimmunodetection
DNA	deoxyribonucleic acid	RIT	radioimmunotherapy
EC	endothelial cell	ROS	reactive oxygen species
ECM	extracellular matrix	RTK	tyrosine kinase receptor
EGF	epidermal growth factor	s	second
EGFR	epidermal growth factor receptor	scFv	single-chain variable fragment
EPR	enhanced permeation and retention	siRNA	small interfering ribonucleic acid
Fab	fragment antigen binding	SPECT	single-photon emission computed tomography
Fc	crystallisable fragment	SPR	surface plasmon resonance
FcRn	neonatal Fc receptor	T/B	tumour-to-blood ratio
FcγR	Fc gamma receptor	T/Bg	tumour-to-background ratio
Fv	single variable domain fragment	t <sub>1/2</sub>	half-life
h	hour	TEM	transmission electron microscopy
HAMA	human anti-mouse antibodies	TGF-α	transforming growth factor α
ICP-MS	inductively coupled plasma mass spectrometry	TGF-β	transforming growth factor β
IgG	immunoglobulin G	TKI	tyrosine kinase inhibitors
kDa	kilodalton	TLT	transplantable liver tumours
keV	kiloelectron volt	TβR	transforming growth factor-β receptor
LET	linear energy transfer	UV	ultraviolet
m/z	mass-to-charge ratio	VEGF	vascular endothelial growth factor
mAb	monoclonal antibody	y	year
MeV	megaelectron volt	Z	atomic number
min	minute	β <sup>+</sup>	positron
MRI	magnetic resonance imaging	ρ	density
MS	mass spectrometer		
MW	molecular weight		
NHL	non-Hodgkin's lymphoma		



## Foreword

The last fifty years have seen remarkable progress in the prevention, detection and treatment of cancer. However, the current methods for cancer management including radiation, surgery and chemotherapy suffer from many disappointments, such as non-specific suppression of proliferating cancer cells, non-specific systemic distribution, inadequate drug concentration at the target site, development of resistance, and a limited ability to monitor the response to therapy. The concept of the “magic bullet”, proposed by Paul Ehrlich more than 100 years ago, postulated that the ideal drug should selectively target and destroy the cause of disease. Therefore, due to their high specificity, the monoclonal antibodies have shown a great promise in the treatment of cancer. However, the effectiveness of antibodies against cancer, and specifically against solid tumours, which are harder to treat, might be improved. In this context, antibodies are being administered in combination with other therapeutic strategies, such as chemotherapy or radiation, or developed as targeted vehicles by attaching toxins or radionuclides. An extension of these approaches is the study of antibody-modified nanomaterials, and particularly antibody-functionalized gold nanoparticles, which use gold nanoparticles as therapeutic agents and antibodies as targeting ligands, offering a promise of selectively conducting the nanoparticles to tumour cells, and thus a focused targeting thanks to the antibody selectivity. These gold nanoparticles may be used for photothermal therapy, as sensitizers in radiation therapy, and offer more flexibility of design in providing platforms for binding of several therapeutic agents in a single structure for effective improvement of cancer therapy.

The general goal of this thesis was to explore the efficiency of targeting cancer cells by using antibodies directed against EGFR, or anti-CD105 antibodies directed against endoglin after their conjugation to gold nanoparticles. It is a proof of concept, where these immunonanoconjugates were evaluated as an imaging tool with the hope of operating them in future therapies and even in theranostic purposes. The approach of conjugating bioactive anticancer molecules, such as antibodies, to nanoparticles has some limitations, notably the risk of losing the antibody specificity for the target after the conjugation reaction. Thus, the assessment of target recognition properties and comparative biodistribution studies of antibodies before and after conjugation to gold nanoparticles were performed. In order to trace these immunonanoconjugates *in vivo*, the antibodies were firstly radiolabelled before

nanoparticle conjugation. For conjugation reaction to gold nanoparticles, we chose two types of monoclonal antibodies directed against EGFR or endoglin (CD105).

In this work, our efforts focused on the development of a tool that could be used as an imaging probe in a first step. The first specific aim consisted in the assessment of the effect of nanoparticle conjugation on the antibody biodistribution and on the antibody specificity for its target. Regarding antibody recognition properties, we studied the binding properties of these immunonanoconjugates *in vitro* and *in vivo* through blocking experiments, and we tried to explain the reasons of the possible loss of antibody immunoreactivity through structural characterization of these conjugates.

Another aspect that was treated in this work consisted in justifying the choice of the radiolabel for tracking these immunoconjugates *in vivo*. We initially directly radiolabelled the antibodies with radioiodine, a common and easy procedure used in laboratory. The unexpected tumour uptake profile of iodinated anti-CD105 antibodies, compared with the known kinetics of most intact antibodies, led us to reconsider the choice of the radiolabel. We studied the biological distribution of anti-CD105 antibodies in mice bearing tumours (two tumour models), and we compared the pharmacokinetic profile of iodinated anti-CD105 antibodies and that of  $^{89}\text{Zr}$ -labelled anti-CD105 antibodies, as validated tracers, in order to highlight the limitations of the direct anti-CD105 antibody radioiodination on stable antibody tracking.

Besides the validation of these immunonanoconjugates as tracers suitable for cancer imaging, we have high expectations of investigating their therapeutic potential. As highly potent and selective drugs are still lacking, we hope that these assemblies, as novel agents for cancer management, will provide an effective strategy to improve cancer therapy through combining the targeting properties of antibodies and the additional therapeutic properties of gold nanoparticles.

# **Chapter 1: INTRODUCTION**

## Outlines

The introduction has been divided into four chapters.

The first chapter deals with the concept of immunotargeting of cancer cells, and particularly the radioimmunotargeting approach for diagnostic and therapeutic purposes. The promises and limitations of radioimmunotargeting are presented. The experimental aspects, including radiolabelling processes of antibodies and *in vivo* explorations of their biodistribution through *ex-vivo* experiments and *in vivo* imaging studies are detailed. With regard to radioimmunotargeting limitations, especially in therapy, the first chapter highlights that there exists a need in the art to improve the efficacy of antibody-based therapies.

The second chapter describes EGFR and endoglin as tumour markers of particular interest in cancer treatment. Their implications as interesting tumour targets for the immunotargeting are addressed.

The third chapter browses the general properties of nanoparticle systems, with a particular focus on gold nanoparticles. The production of gold nanoparticles, their toxicity, the passive and active targeting strategies and resulting pharmacokinetic profile are described. The gold-based diagnostic and therapeutic systems, based on the photophysical properties of gold nanoparticles, are also discussed in this chapter.

The fourth chapter describes the nanoparticle vectorization process using monoclonal antibodies, as targeting ligands. The question of the influence of targeting ligands on tumour uptake of conjugated gold nanoparticles is addressed. An overview of potential biomedical applications of these immunonanoconjugates is presented.

## I. Radioimmunotargeting of cancer cells

### 1. Radioimmunotargeting approach

The immunotargeting approach was conceived through increased understanding of the biological pathways involved in the pathogenesis of cancer, and subsequently based on the identification of the most appropriate antigens to target. The immunotargeting of cancer cells involves the use of antibodies or antibody fragments against a tumour antigen overexpressed by cancer cells. The selective immunotargeting appears to be possible thanks to the high specificity of the antigen-antibody recognition for selectively targeting noxious cells, without harming healthy host cells.

Monoclonal antibodies (mAbs) have emerged as an important and a rapidly expanding drug class for treating a wide variety of human diseases, including cancer. The anticancer properties of mAbs can be achieved by several biological mechanisms and may have direct or indirect cytotoxic effects. The direct mechanisms of antibody-mediated cell killing include apoptosis induction (Scott 2012), blocking of growth factor receptors and subsequent inhibition of cancer cell proliferation (Baselga 1994), inhibition of tumour angiogenesis invasiveness and malignant spread of cancerous cells, and production of anti-idiotypic antibodies (Schmolling 1995, Fagerberg 1994). The indirect effects include antibody-dependent cell-mediated cytotoxicity (ADCC) and complement-dependent cytotoxicity (CDC) (Scott 2012). However, the direct and indirect actions of mAbs may be insufficient to provide a significant cytotoxicity.

Over the last forty years, there has been an increase of activities in the field of radioimmunotargeting. The radioimmunotargeting approach is based on combining radioactive isotopes with specific mAbs. This approach makes feasible *in vivo* tracing and/or treating of tumour cells using radiolabelled mAbs. The radiolabelling of mAbs enables to demonstrate the specificity of the immunotargeting, and remains attractive for diagnostic as well as therapeutic purposes, depending on the delivered dose and the physical properties of the bound radionuclide. Further, the radioimmunotargeting applications can be performed for diagnosis using the gamma-camera, when the radioisotope is a gamma-emitter, or using the positron emission tomography (PET), when the radioisotope is a positron-emitter. On the other hand, the radioimmunotargeting for therapeutic purposes, termed radioimmunotherapy,

uses mAbs radiolabelled with high energy beta particles, alpha-emitters, and Auger electron- or conversion electron-emitting radionuclides.

Although mAbs can be relatively effective alone and in “naked” or unconjugated form in the treatment of solid tumours and hematological malignancies (O’Mahony 2006), their combination with conventional cytotoxic chemo-drugs, radiation or surgery have improved clinical treatment outcomes (Reichert 2002, Goldenberg 2002, Carter 2001, Reichert 2001). Moreover, many innovative approaches have been developed to improve the efficacy of antibody-based therapies (Carter 2001). Indeed, mAbs can be conjugated to cytotoxic compounds (drugs, toxins or cytokines) or to cytotoxic radioactive isotopes. Such conjugates represent broadly applicable approaches to enhance the antitumour activity of antibodies in delivering the therapeutic agent directly to antigen-bearing tumour cells, and for improving the tumour-to-normal tissue ratios of conjugated moieties (Green 2000). Further, mAbs can also be used as targeting agents, which are grafted to nanomaterials, such as gold nanoparticles, in order to improve their specific delivery to treat cancer cells through combining the targeting properties of antibodies with the additional therapeutic properties of gold nanoparticles.

## **2. Radioimmunotargeting issues : imaging strategy to guide molecular therapy**

### **2.1. Antibody formats for improving radioimmunotargeting (Olafsen 2010)**

The nuclear imaging approach requires the accumulation of the signal delivered by a probe at the target site. MAbs are high affinity molecules that can be used for a specific high delivery to cell surface antigens. However, their long circulation time in blood may make them less suitable as imaging probes. Indeed, a more rapid clearance from the blood is warranted for imaging purposes in order to increase the imaging contrast. The efforts to improve the antibody pharmacokinetics without compromising the antibody affinity and specificity have been made through protein engineering. Different antibody formats that differ in antigen binding sites and in size have been produced and evaluated as imaging probes to target the tissues of interest (Olafsen 2010).

The majority of mAbs studied to date have been whole antibodies or fragmented. A major disadvantage of using intact mAbs as imaging probes is that they circulate in the blood for several days. For this reason, the Fab fragments produced by proteolytic reaction digesting

mAbs were developed as imaging agents (Figure 1). Early studies of antibody-based imaging agents showed that the blood clearance was inversely related to the size of the protein. The clearance rate of: Fab or Fab' (MW ~50 kDa) > F(ab')<sub>2</sub> (MW ~110 kDa) > IgG (MW ~150 kDa) (Wu 2000). However, the disadvantage of Fab and Fab' fragments is their only one antigen binding site, which reduces the avidity of the antibody and induces subsequent difficulties in localizing and accumulating the activity in target tissue.

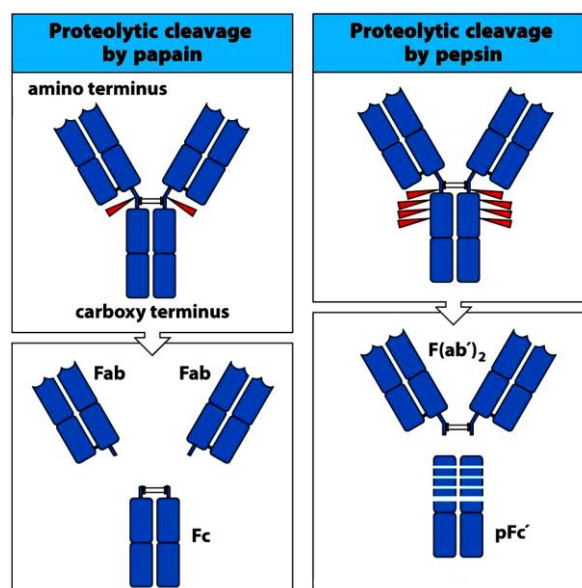


Figure 1: Schematic presentation of an intact antibody molecule (IgG), which can be dissected by partial digestion with proteases. Left panel: the papain cleaves IgG into three pieces, two Fab fragments and one Fc fragment. The Fab fragment contains the binding antigen region. Right panel: the pepsin cleaves IgG to yield one F(ab')<sub>2</sub> fragment and many small pieces of Fc fragment, the largest of which is called pFc' fragment. Fab' is written with a prime because it contains a few more amino acids than Fab, including the cysteines that form the disulphide bonds (Janeway's Immunobiology 8<sup>th</sup> ed., Garland Science 2012).

The production of genetically engineered antibody fragments of different sizes and with multiple valences started with the introduction of fast clearing fragments, such as single-chain variable fragments (scFv, MW ~25 kDa). Because of their monovalent binding, these fragments demonstrate a modest retention time in tumours, due to a rapid dissociation from the target antigen, and a low exposure time to the target (Olafsen 2010, Bird 1988). Consequently, these fragments may provide potentially a poor image quality. Using scFv as building block, larger antibody fragments such as diabodies (dimers of scFv, MW ~50 kDa), minibodies (dimers of scFv-CH3, MW ~80 kDa) and scFv-Fc dimers (MW ~105 kDa) have been generated (Wu 2005). These fragments have exhibited a better tumour penetration due to

a balance between their longer residence time in blood (compared with scFv fragment) and a faster clearance kinetics (compared with intact antibody). These properties result in an excellent tumour-to-blood ratio, which is desirable for imaging probes. The rapid elimination has been attributed to their size and the lack of interaction with the neonatal Fc receptor (FcRn). The imaging studies using these fragments after their radiolabelling have demonstrated an excellent high imaging contrast with  $\gamma$ -camera and PET scanner (Figure 2).

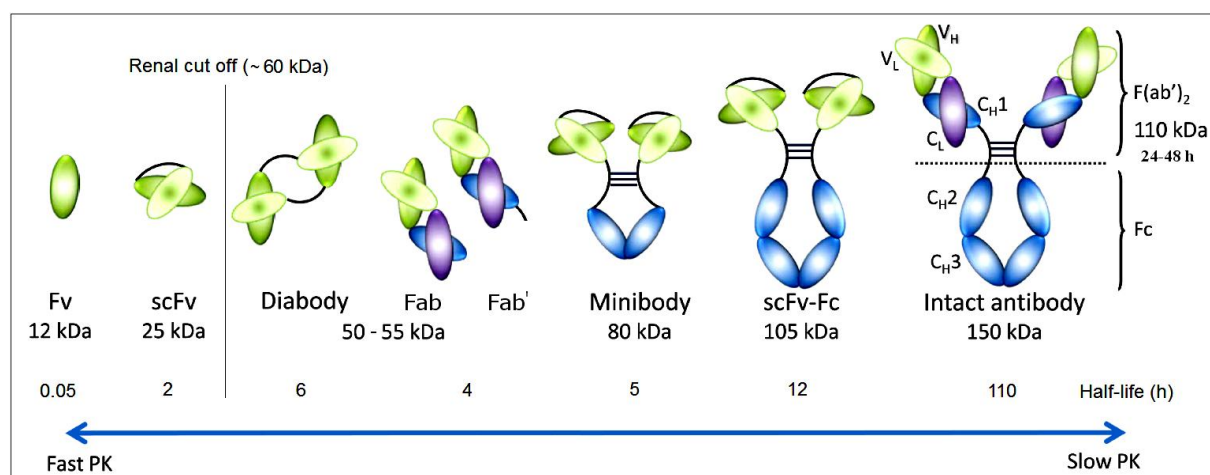


Figure 2: Schematic presentation of an intact antibody and antibody fragments derived from it, including the single variable domain fragment (Fv), single chain Fv (scFv), diabody, Fab/Fab', minibody and scFv-Fc dimer. The approximate values of molecular weights and the blood half-lives are indicated below each fragment.  $V_L$ : variable light chain (light green),  $V_H$ : variable heavy chain (dark green),  $C_L$ : constant light chain (pink),  $C_H$ : constant heavy chain (blue) (Adapted from Olfasen 2010).

Many other attractive features of antibody variants have been produced through the engineering field. These fragments are even smaller scaffolds, encompassing a range of protein domain-based frameworks that are neither conventional antibodies nor peptides (Gebauer 2009, Nuttall 2008). Among these new directions, there are non-immunoglobulin based scaffolds, such as affibodies (MW ~7 kDa) and immunoglobulin based scaffolds, such as nanobodies (Nanobody<sup>®</sup>)<sup>‡</sup>. The affibodies are derived from staphylococcal surface protein A and seem to be favourable as an alternative imaging agent (Friedman 2009). Nanobodies are derived from naturally occurring antibodies that lack the light chain, and are found in camelids (Figure 3). Nanobodies are novel antibody vectors, which are characterized by a single antigen binding domain ( $V_{HH}$  domain, MW ~15 kDa). Because of their small size, the

<sup>‡</sup> Nanobody is a registered trademark of Ablynx N.V.

$V_{HH}$  domains rapidly pass the renal filter (cut off  $\sim 60$  kDa), resulting in their rapid blood clearance and a fast tissue penetration (Cortez-Retamozo 2008, Huang 2008).

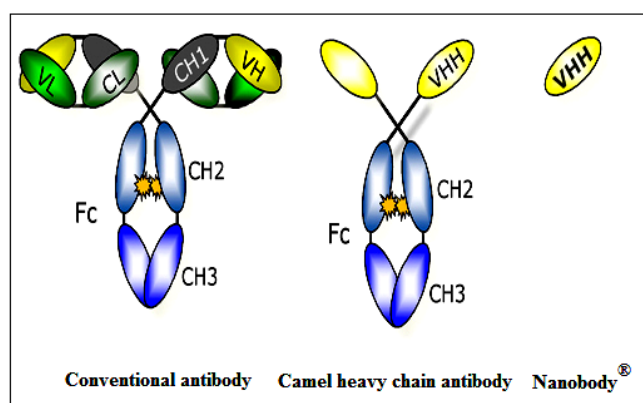


Figure 3: Schematic presentation of a conventional antibody: heavy and light chains, both required for antigen binding and stability; a camel antibody: only heavy chains with full antigen binding capacity and high stability; VHH domain, called Nanobody<sup>®</sup> and derived from camel antibody: the smallest functional fragment of a single chain antibody (Adapted from Prof. Serge Muyldermans, Vrije Universiteit Brussel).

There are several factors that influence the successful targeting and imaging of tumours using different antibody formats. These factors include the antibody design and the choice of the radiolabel according to the pharmacokinetic behaviour of the antibody format. The antibody modifications, such as MW, preserved Fc domain, valency and specificity have an impact on the antibody pharmacokinetics (Olafsen 2010). Indeed, the larger antibody fragments (MW > 60 kDa) clear through the liver, whereas those below this size clear through the kidneys. The presence of Fc domain increases the serum residence time and the exposure time to the target. The specificity and the avidity are important for localizing and accumulating antibody in the target tissue.

Overall, the antibody-based molecular imaging will play an important role in diagnosis and in the management of cancer and other diseases, by enabling relatively early imaging of malignant lesions that will accelerate the evaluation of patient care and treatment. Indeed, several intact antibodies and to a lesser extent antibody fragments have been evaluated in patients and have shown encouraging results (Wu 2009, van Dongen 2007) (Appendix 1A).

## 2.2. Radioimmunodetection aspects (Fass 2008)

Molecular imaging is a rapidly growing field and a powerful tool in the clinical diagnosis of diseases (Jaffer 2005). Among the molecular imaging approaches, the nuclear medicine imaging provides functional informations at the molecular and cellular level and has the advantages of a high intrinsic sensitivity, an unlimited depth penetration, and a broad range of clinically tested molecular imaging agents. The radioimmunodetection (RID) uses radiolabelled mAbs, which have the ability to interact with specific molecular targets involved in many diseases, including cancer.

### *a. Radionuclides for cancer imaging*

The radioimmunoimaging involves the use of gamma ( $\gamma$ ) or positron ( $\beta^+$ )-emitting radionuclides, as labels of mAbs or antibody fragments. The label is a radioisotope with a decay scheme that facilitates the detection and the imaging with a  $\gamma$ -camera system or with a PET scanner. An ideal radionuclide for imaging applications requires some particular characteristics. The most widely used  $\gamma$ -emitting radioisotope is  $^{99m}\text{Tc}$ , which has ideal characteristics for imaging.  $^{99m}\text{Tc}$  has a reasonable physical half-life ( $t_{1/2}$  6.02 h), long enough to obtain images or to examine biological processes, and short enough to limit the radiation exposure to the patient.  $^{99m}\text{Tc}$  emits  $\gamma$ -rays with convenient energy of 140 keV, high enough to be detected by the radiation detectors of the  $\gamma$ -camera, which is positioned outside the body, but low enough to avoid a high absorbed radiation dose to the patient. Most tracers used in nuclear medicine are radiolabelled with  $^{99m}\text{Tc}$ .  $^{99m}\text{Tc}$  chemistry enables to label antibodies for imaging applications, such as  $^{99m}\text{Tc}$ -arcitumomab (CEA-Scan<sup>®</sup>), which is a murine IgG<sub>1</sub> Fab' directed against carcinoembryonic antigen for detection of recurrent and/or metastatic colorectal carcinoma. Finally,  $^{99m}\text{Tc}$  is easily and locally produced at a low cost using the technetium generator. The most routinely used  $\beta^+$ -emitter for PET imaging is  $^{18}\text{F}$ . Because of its short physical half-life ( $t_{1/2}$  109.8 min),  $^{18}\text{F}$  is widely used for radiolabelling of biomolecules and in molecular imaging of biological and biochemical processes. However,  $^{18}\text{F}$  is produced in a cyclotron and is thus expensive, and less easily available.  $^{18}\text{F}$  may be used for radiolabelling of low molecular weight antibody fragments, such as affibodies (Kramer-Marek 2012, Kiesewetter 2008). Many other radioisotopes are commonly used in nuclear medicine imaging for radioimmunodetection goals (Appendix 2).

### b. Rationale for the selection of the radionuclide

The nature of the radiolabel may affect the targeting. It must be mentioned that all  $\gamma$ - or  $\beta^+$ -emitting radioisotopes, having adequate properties for imaging, are not all suitable for antibody radiolabelling. The choice of the radioisotope for antibody radiolabelling depends on some considerations. In fact, the physical half-life of the radionuclide should be matched with the pharmacokinetic properties of the selected antibody. The radionuclides with longer physical half-lives, such as  $^{111}\text{In}$  ( $t_{1/2}$  2.83 d),  $^{124}\text{I}$  ( $t_{1/2}$  4.2 d) and  $^{89}\text{Zr}$  ( $t_{1/2}$  3.3 d) are suitable for labelling intact antibodies, which have a slow *in vivo* kinetics and which require several days (2-4 d) to reach a maximum tumour uptake and a favourable tumour-to-background ratio (T/Bg). On the other hand, the antibody fragments are more rapidly cleared from the blood than whole antibodies. The radiolabelling of antibody fragments may use  $\gamma$ -emitting radionuclides with shorter half-lives, such as  $^{99\text{m}}\text{Tc}$  ( $t_{1/2}$  6.02 h) and  $^{123}\text{I}$  ( $t_{1/2}$  13.0 h) or  $\beta^+$ -emitters, such as  $^{18}\text{F}$  ( $t_{1/2}$  109.8 min) and  $^{68}\text{Ga}$  ( $t_{1/2}$  68.1 min) for labelling fragments with very rapid uptake and clearance, while radiolabelling with ultra-short half-life radionuclides, such as  $^{15}\text{O}$  ( $t_{1/2}$  2.07 min),  $^{13}\text{N}$  ( $t_{1/2}$  9.96 min) and  $^{11}\text{C}$  ( $t_{1/2}$  20.38 min) is not appropriate. For instance, several  $\beta^+$ -emitters for immuno-PET are currently under investigation, and can be grouped according to their physical half-lives that ideally should be paired with the biological half-life of the antibody format. Thus, the short-lived  $\beta^+$ -emitters, such as  $^{68}\text{Ga}$  ( $t_{1/2}$  68.1 min) and  $^{18}\text{F}$  ( $t_{1/2}$  109.8 min) are suitable for rapid clearing fragments, such as scFv and diabodies. The intermediate-lived  $\beta^+$ -emitters, such as  $^{64}\text{Cu}$  ( $t_{1/2}$  12.7 h),  $^{86}\text{Y}$  ( $t_{1/2}$  14.7 h) and  $^{76}\text{Br}$  ( $t_{1/2}$  16.1 h) are suitable for antibody fragments with intermediate clearance properties, such as minibodies and modified scFv-Fc fragments. The long-lived  $\beta^+$ -emitters, such as  $^{89}\text{Zr}$  ( $t_{1/2}$  3.3 d) and  $^{124}\text{I}$  ( $t_{1/2}$  4.2 d) are suitable to image intact antibodies and scFv-Fc (Olafsen 2009, Sundaresan 2003). There is a great interest regarding clinical translation of antibody fragments and variable affinity scaffolds for tumour targeting.

On the other hand, the internalization process of the antibody after binding to its target into tumour cells should also be considered for the choice of the radiolabel. For example, the direct iodinated mAbs are unstable *in vivo* due to the intracellular catabolization, which leads to the deiodination and the rapid release of the radioactivity from cells after antibody internalization. In contrast, radioactive metals, such as  $^{111}\text{In}$  and  $^{89}\text{Zr}$  are residualizing isotopes, which are trapped inside the cell after antibody internalization (Vugts 2011). Thus,

the labelling with intracellularly retained isotopes has an advantage over released ones both in diagnosis and therapy.

*c. Clinical applications of radioimmunodetection*

The cancer patient management is an important application of nuclear medicine imaging in terms of staging of new patients, restaging for treatment planning and prediction of therapy response. Moreover, *in vivo* imaging using radionuclide-based detection can be repeated to monitor the treatment response and the disease recurrence, because the technique is noninvasive and generates a relatively low radiation absorbed dose. Several clinical studies have explored a wide variety of cancers using RID, including but not limited to the cancer of colon, ovary, prostate, breast and lung. Only a handful of mAbs or antibody fragments have been approved (Appendix 1A), such as  $^{111}\text{In}$ -labelled capromab pendetide (ProstaScint<sup>®</sup>) for prostate cancer imaging. In addition to straight diagnostic applications, the radioimmunoimaging can provide targeting and dosimetry informations that can guide therapy. Thus, the radioimmunoimaging has been traditionally developed in parallel with radioimmunotherapy. For example,  $^{111}\text{In}$  ( $t_{1/2}$  2.83 d) is a  $\gamma$ -emitting radioisotope that can be imaged and which mimics the dosimetry of  $^{90}\text{Y}$  ( $t_{1/2}$  2.67 d). The  $^{90}\text{Y}$  is a  $\beta^-$ -emitter that cannot be detected through scintigraphy, SPECT or PET imaging. Another example concerns mAbs radiolabelled with  $^{124}\text{I}$  ( $t_{1/2}$  4.2 d), a  $\beta^+$ -emitter that enables the accurate quantification of tumour uptake and healthy organs using PET imaging. The  $^{124}\text{I}$ -labelled mAbs have the same kinetic as when labelled with the therapeutic nuclide  $^{131}\text{I}$  ( $t_{1/2}$  8.04 d).

2.1. Radioimmunotherapy aspects (Boswell 2007, Goldenberg 2002)

In addition to the RID which uses radiolabelled mAbs as radiotracers, the mAbs radiolabelled with therapeutic radionuclides, termed radioimmunotherapy (RIT), has also shown promise in cancer management. The challenge of RIT is to improve the delivered radiation dose and to achieve a more uniform distribution of ionizing radiation, with the ultimate goal to specifically irradiate tumours while sparing normal tissues.

*a. Radionuclides for cancer therapy*

The relevant radionuclides for cancer therapy are selected for their non-penetrating and damaging particulate emissions. The suitability of a radionuclide for RIT depends on its physical and chemical properties, its *in vivo* fate after antibody metabolism, and the nature of

emitted radiation (i.e. high linear energy transfer (LET)). Such high LET radiation induces profound effects on DNA, causing strand breaks. Moreover, the efficacy of the radiation is influenced by the target location, the size, the morphology, the physiology and the radiosensitivity of the tumour, and also by the kinetic profile of the antibody. The most widely used high energy  $\beta^-$ -particle emitters are  $^{131}\text{I}$  ( $t_{1/2}$  8.04 d) and  $^{90}\text{Y}$  ( $t_{1/2}$  2.67 d). However, these emitters have a  $\beta$ -range in tissue of several millimetres, which creates a “crossfire” effect and may affect the antigen negative cells. Thus,  $\beta$ -particle therapy is preferred for large tumours. The  $\alpha$ -particle therapy uses  $\alpha$ -particle emitters, such as  $^{213}\text{Bi}$  ( $t_{1/2}$  0.77 h),  $^{212}\text{Bi}$  ( $t_{1/2}$  1 h) and  $^{211}\text{At}$  ( $t_{1/2}$  7.2 h). These emitters have a short  $\alpha$ -range in tissue of several micrometres, high energies of several MeV and high LET. Hence, the  $\alpha$ -particle emitters should be better suited for the treatment of micrometastases or for targeting circulating tumour cells. Since these  $\alpha$ -emitters have short half-lives, their conjugation to mAbs must be rapid and are less compatible with the slow *in vivo* kinetics of intact antibodies, which require several days to reach an optimal tumour uptake. The physical properties of all mentioned radioisotopes are listed in Appendix 3.

#### *b. Clinical applications of radioimmunotherapy*

The RIT have been used in the management of hematopoietic tumours, especially non-Hodgkin’s lymphoma (NHL), as well as for treating solid tumours, which express targeted antigen (Appendix 1B). The antitumour activity is primarily due to the radionuclide attached to the antibody, which emits continuous irradiation with heterogeneous dose deposition. In some cases, the antibody itself contributes to the tumour destruction through an immune response *via* the antibody-mediated cell destruction. Many considerations should be taken to improve the efficacy of RIT, including the nature of the antibody (specificity, affinity, avidity, dose, immunoreactivity and mechanism of action), the attached radiolabel (emission properties, half-life and stability of radioimmunoconjugate), the antigen targeted (location, modulation, stability, density and expression), the nature of the tumour (radiosensitivity, location, size, vascularization, immunogenicity and proliferative rate), and other factors, such as the heterogeneity of dose deposition and the dose-rate effects (Goldenberg 2002). Two radiolabelled mAbs directed against the CD20 antigen, expressed on the surface of normal and malignant B-lymphocytes, are approved for the treatment of NHL, the  $^{90}\text{Y}$ -labelled ibritumomab tiuxetan (Zevalin<sup>®</sup>) and the  $^{131}\text{I}$ -labelled tositumomab (Bexxar<sup>®</sup>). It must be

mentioned that the solid tumours are less responsive compared with hematopoietic tumours. This may be explained among others by the inhomogeneous targeting, which may be more significant for often poorly vascularized solid tumours (Blumenthal 1995). Thus, multiple administrations or combinations with other treatment modalities may be required. Indeed, the RIT may be used as a consolidation treatment in patients with residual solid tumour after for example, surgical management.

### 3. Radioimmunotargeting limitations

The radiolabeled mAbs have not yet achieved the status of a routine clinical use. In fact, several limitations in radioimmunotargeting field have been observed. For nuclear medicine imaging, the characteristics required for an ideal radiopharmaceutical include: efficient accumulation and retention of the tracer in the target tissue, no accumulation in non-target tissues, high specificity for effective antigen discrimination, no side effects, rapid clearance from background<sup>§</sup>, *in vivo* stability, and easy preparation at low cost (Müller 2013). With regard to RIT, the limitations are depending on the physical properties of the bound radionuclide, which should be suitable to induce damages on targeted cells, but also depend on the tumour accumulation of radiolabelled mAbs, which remains the major limitation for delivering effective radiation doses, notably for solid tumour. In fact, the challenge of RIT is to achieve a high local concentration of radiolabelled mAbs and thus to deliver effective levels of therapeutic radiations. Many other critical factors influence the tumour dosimetry and the therapeutic ratio<sup>\*\*</sup>, such as the residence time of radiolabelled mAbs at the target tissue, which is depending on their affinity for tumour cells, the rate of clearance of radiolabelled mAbs from normal tissues, and the heterogeneity of the tumour mass, which may decrease the antibody effectiveness, especially because of the antigen expression disparity on tumour cells (Green 2000).

Some of observed radioimmunotargeting limitations are inherent to the immunotargeting concept and especially to the intrinsic antibody properties. Firstly, because the mAbs target cells overexpressing a particular antigen, there is a possibility of cross-reactivity with normal tissues expressing the same antigen. For this reason, considerable researches have gone towards finding tumour-specific antigens. Further, although these specific antigens are found

---

<sup>§</sup> Background : non-specific tissues and blood

<sup>\*\*</sup> Therapeutic ratio: the dose delivered to the tumour compared with the dose delivered to normal tissues

almost exclusively on tumours or are expressed at a greater level in tumour cells than in the corresponding normal cells, the disparity of antigen expression on cancer cells contributes to the tumour heterogeneity, which results in a variable recognition of cells by the given antibody (Aerts 2009). On the other hand, it should be noted that the murine or other non-human antibodies, such as chimeric human-mouse mAbs are immunogenic, and may lead to extensive formation of immune complexes, which can cause renal failure in severe cases. The murine mAbs have many disadvantages that prevent them from having optimal efficacy. As they are non-human, these antibodies themselves are capable of eliciting an immune response by producing human anti-mouse mAbs (HAMA), which can be formed against the given therapeutic antibody. The HAMA response reduces the plasma concentration of administered antibody under the necessary level to achieve therapeutic effect and decreases the ability to administer multiple times the same therapy to the patient. Indeed, the HAMA development occurs usually after repeated exposure to the administered antibody. Once an immune response occurs, the administered antibodies can be rapidly cleared from the circulation. To decrease the immunogenicity of the murine and chimeric antibodies, humanized mAbs and antibody fragments may be a partial solution (Oriuchi 2005). Finally, one of the major problems of radioimmunotargeting is non-specific localization of the tracer. It is known that one of the limitations of antibody-based imaging and therapy is the high background signal in the reticuloendothelial system, particularly in the liver, where antibodies are mainly metabolized (Sands 1987). Overall, these limitations might lead to an insufficient tumour uptake and/or a too high tracer level in blood and non-specific tissues, and thus a hampered tumour visualisation. When used for immunotherapy, such unfavourable *in vivo* behaviour aspects of mAbs would give an inconvenient radioactivity dose in the tumour, and a detrimental dose to normal tissues.

Other critical parameters for radioimmunotargeting are related to the radiolabelling process. The radiolabelling reaction, as well as any other conjugation reactions, may influence the pharmacokinetic profile, the immunological properties and the pharmacological effect of the antibody. It is important to control the integrity and the immunoreactivity of mAbs after radiolabelling reaction. The radiolabelling process should not greatly affect the antigen recognition, the antibody internalization by tumour cells, and the antibody efficacy. It is also necessary to characterize the stability of the linker between the antibody and the radioisotope. Other important considerations include the choice of radiolabelling methods and the related

operating conditions, which may affect the radionuclide-to-antibody ratio and subsequently, the antibody recognition properties. Finally, *in vivo* applications require also the purification of mAbs before and after the radiolabelling process. The goal is to produce radiolabelled mAbs pure and stable enough, without significantly altering their properties. For all these reasons, the best set of conditions for any particular protein radiolabelling has to be optimized.

#### 4. Radiochemistry issues

The advances of radioimmunotargeting in the cancer field have occurred thanks to two parallel paths: the radiochemistry developments and the new imaging methods.

##### 4.1. Radiolabelling with radioiodine (Slater 1990)

The radiohalogenation is the process of chemically modifying a molecule to contain one or more atoms of radiohalogen. The radiohalogens, such as radioiodine ( $^{123}\text{I}$ ,  $^{125}\text{I}$ ,  $^{124}\text{I}$  and  $^{131}\text{I}$ ) may be used to radiolabel mAbs. There are direct and indirect methods of radiohalogenation. The indirect method involves the use of bifunctional reagent, which is an intermediate linker, attached to the radioisotope prior to the antibody conjugation. The direct method involves the direct incorporation of the radiohalogen into proteins, and it is generally rapid and convenient, giving high yields and specific activities. Several different methods are available for the direct radioiodination of proteins, such as mAbs. Essentially, they differ in the nature of the oxidizing agent, which is used to convert the commercially available radioactive iodine  $[\text{I}]$  into the reactive species  $[\text{I}^+]$  (iodonium). The iodonium reacts most readily with tyrosine residues (phenol group) of the antibody (Figure 4), but the electrophilic substitution into other residues, particularly histidine (imidazole group) can occur. It is generally agreed that the incorporation of one iodine atom per antibody molecule provides an optimum specific activity and stability of labelled molecules. It has to be kept in mind that radioiodination should result in the minimum possible change in the protein. The iodine atom has approximately the same size as a benzene nucleus. Thus, the addition of even one iodine atom may have a profound effect on the structure and the physicochemical properties of the labelled protein, especially if the latter is an antibody with an active recognition site. Therefore, the control of the antibody integrity after radiolabelling is essential. The target recognition capacity of the radiolabelled

antibody has also to be controlled. The choice of the oxidizing agent and the incubation time can be optimized in order to control the substitution rate and the antibody integrity.

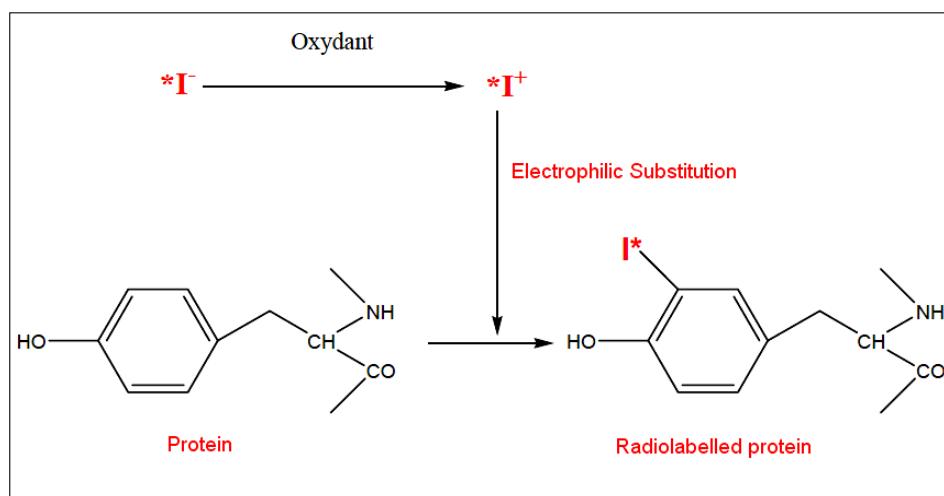


Figure 4: General scheme illustrating the radioiodination reaction of proteins. The oxidizing agent converts the radioactive iodide [ $^*I^-$ ] into reactive species [ $^*I^+$ ], which reacts with tyrosine residues by means of electrophilic aromatic substitution reaction (Adapted from Prof. Bernard Gallez, UCL).

MAbs can be directly labelled with radioiodine by means of several well-established radioiodination methods, which include the use of chloramine T<sup>††</sup> or Iodogen<sup>®‡‡</sup> as oxidants. The procedure that uses chloramine T was introduced by Hunter and Greenwood (Hunter 1962). It is probably the most widely used method thanks to its reproducibility, economy and efficiency. Chloramine T breaks down in aqueous solution, producing hypochlorous acid, which oxidizes the radioactive iodide at a neutral pH that is optimum to protect antibodies against denaturation. The reaction is stopped after a certain incubation time by adding a reducing agent. Iodogen<sup>®</sup> procedure was first described by Fraker and Speck (Fraker 1978), as a reaction that involves the use of a solid phase oxidation reagent for iodination of proteins and cell membranes. Iodogen<sup>®</sup> is a softer oxidant that is very slightly soluble in aqueous media. Thus, any damage to the protein during the labelling process, brought about by the oxidant agent, is likely to be very small. Iodogen<sup>®</sup> is dissolved in a suitable organic solvent and is deposited as a thin solid coat on the walls of tubes. The iodination reaction in coated tubes is terminated simply by removal of the incubation mixture. After radioiodination reaction, the radiolabelled mAbs are purified using gel filtration chromatography for

<sup>††</sup> Chloramine T : sodium salt of the N-monochloro derivative of *p*-toluene sulphonamide

<sup>‡‡</sup> Iodogen<sup>®</sup> : 1,3,4,6-tetrachloro-3 $\alpha$ , 6 $\alpha$ -diphenyl glycoluril

removing free iodine. The efficiency of iodine incorporation depends on the pH value, the incubation time and the introduced amount of proteins, iodine and oxidizing agent (Paus 1982, Hunter 1962).

One of the problems associated with the direct radioiodination is the unwanted oxidation of susceptible groups, such as methionine and tryptophan residues. The methionine residues can be oxidized to sulfoxides and sulfones, which can often render the protein biologically inactive. The procedures that use strong oxidizing agents, such as chloramine T are more likely to lead to these oxidation problems, whereas the milder oxidants, such as Iodogen<sup>®</sup> are less likely to oxidize the proteins (Slater 2002). Moreover, the direct iodinated mAbs are unstable *in vivo* due to the proteolysis, the deiodination and the release of the radioactivity from cells after antibody internalization (Vugts 2011).

#### 4.1. Radiolabelling with zirconium-89

Within the commonly used  $\beta^+$ -emitters for PET imaging, only a few of them are suitable for antibody labelling, since immuno-PET requires that the radioisotope should be attached to the antibody with a good *in vivo* stability, and that the decay half-life of the radionuclide should match with the biological half-life of antibodies. For instance, <sup>89</sup>Zr ( $t_{1/2}$  78.4 h), <sup>64</sup>Cu ( $t_{1/2}$  12.7 h) and <sup>86</sup>Y ( $t_{1/2}$  14.7 h) are radiometals used for imaging purposes and suitable for antibody radiolabelling.

<sup>89</sup>Zr is an appropriate candidate for immuno-PET because of its long physical half-life ( $t_{1/2}$  78.4 h), which is compatible with the time needed for most intact antibodies to reach optimal biodistribution and target-to-non target ratio. Moreover, <sup>89</sup>Zr unlike iodine is a residualizing isotope, which is trapped inside the cell after antibody internalization (Vugts 2011). The antibody radiolabelling with <sup>89</sup>Zr can be achieved through various types of bifunctional chelating agents, such as a bifunctional derivative of desferrioxamine B (Df-Bz-NCS)<sup>§§</sup>. These chelate agents have two functionalities: one functional portion that chelates the metallic radionuclide and the other one is a reactive functional group that covalently binds the antibody. Generally, the antibody is first, functionalized with the chelate agent, and the radiometal is then added to form the final conjugate. Different procedures have been developed for antibody labelling with <sup>89</sup>Zr. The simplified two-step procedure (Vosjan 2010) produces a

---

<sup>§§</sup> Df-Bz-NCS : *p*-isothiocyanatobenzyl-desferrioxamine B

quantitative  $^{89}\text{Zr}$ -complexation of cetuximab<sup>\*\*\*</sup> and provides a reproducible chelate:mAb ratio of 1.5:1 using only a three molar excess of Df-Bz-NCS (Perk 2010). Such a low chelate:mAb ratio should avoid the alteration of the antibody pharmacokinetics and the antibody immunoreactivity. Briefly,  $^{89}\text{Zr}$  is produced through the irradiation of natural yttrium *via*  $^{89}\text{Y}(p,n)^{89}\text{Zr}$  reaction, followed by purification using affinity chromatography on an hydroxamate functionalized column (Meijs 1994). The antibodies are first conjugated with Df-Bz-NCS, followed by purification using gel filtration chromatography. The isothiocyanate group of the chelate agent forms a thiourea bond with a primary amine of the antibody lysine groups at pH 9. Next, the functionalized antibody is labelled by adding  $^{89}\text{Zr}$  at neutral pH ( $^{89}\text{Zr}$ -Df-Bz-NCS-mAbs), followed by purification using gel filtration chromatography (Figure 5). The chelate agent chosen is the desferrioxamine B (Df). It is the only chelate agent identified up to now that forms stable complexes with  $^{89}\text{Zr}$ . The Df chelate consists of three hydroxamate groups that chelate  $^{89}\text{Zr}^{4+}$  and result in 6-coordinated zirconium complex, which is stable *in vivo* (Holland 2010, Meijs 1992). Moreover, no adverse reactions, such as immunogenic responses were observed after the injection of Df-containing conjugates (Borjesson 2006). Finally,  $^{89}\text{Zr}$ -Df-Bz-NCS-mAb can be best stored at 4 °C in sodium acetate buffer in the presence of the antioxidant gentisic acid (Perk 2010).

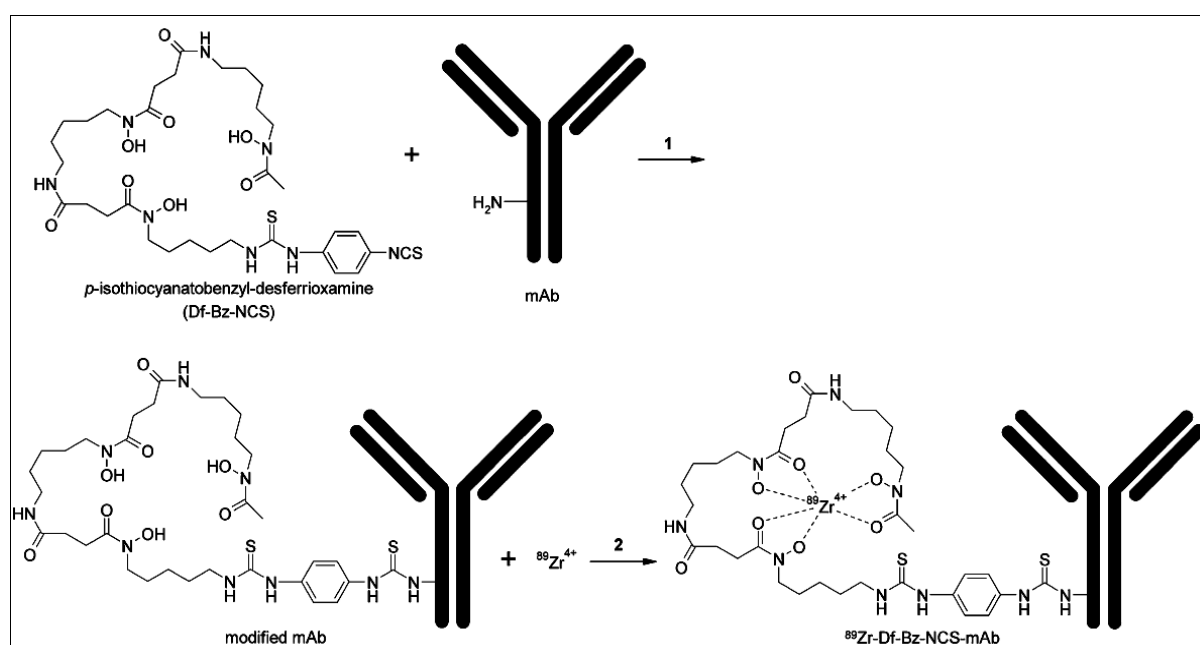


Figure 5: General scheme illustrating the monoclonal antibody modification with Df-Bz-NCS [step 1] and subsequent labelling with  $^{89}\text{Zr}$  [step 2] (Vosjan 2010).

\*\*\* Cetuximab : anti-EGFR mAb (Erbix<sup>®</sup>)

## 5. *In vivo* explorations in mice

Different methods are dedicated to *in vivo* explorations of the distribution profile of tracers in mice and for the quantitative determining of the tracer uptake by the tissues.

### 5.1. Invasive *ex-vivo* studies

The tracer, such as radiolabelled mAbs, is injected intravenously into mice, which are killed and dissected at different times after injection. The organs and tissues are collected, weighed and counted using a radioactivity counter. The radioactivity uptake can be expressed as a percentage of the injected dose per gram of tissue (%ID g<sup>-1</sup>), and as a tumor-to-blood ratio (T/B). This conventional *ex-vivo* study requires more experimental animals, longer time for tissue isolation, and results in longer time for data analysis compared with imaging modalities, which allow repeated and rapid acquisitions of data from the same animal over time.

### 5.2. Noninvasive *in vivo* studies: anatomic and functional imaging

Since over three decades, the RID is performed by using planar gamma cameras, single photon emission computed tomography (SPECT) or positron emission tomography (PET). These imaging modalities enable to explore *in vivo* physiological functions based on radiation originating from radionuclides, which are injected to patients in tracer amounts. The radioimmunoscintigraphy, the SPECT and the immuno-PET techniques are based on radiolabelled monoclonal antibody imaging, through antigen identification on a cellular level and thanks to the high specific antigen-antibody recognition. Thus, these imaging techniques have the potential to impact significantly on patient care because they detect antigens on a cellular level and differ fundamentally from anatomic imaging modalities, such as computed tomography (CT), ultrasound and magnetic resonance imaging (MRI), which identify the gross morphological changes. Moreover, the RID has shown a good potential to identify primary tumours and metastases that have not been found with anatomic imaging techniques.

#### *a. Single-photon emission computed tomography (SPECT)*

The  $\gamma$ -ray photons emitted from *in vivo* administered radiotracer penetrate through the subject's body and are detected by a collimated radiation detectors that is often NaI(Tl) scintillation detectors. The projection data are acquired from different views around the subject. The SPECT imaging provides a three-dimensional visualization of the radiotracer

distribution within the body. It involves the detection of a single  $\gamma$ -ray emitted from radionuclides as opposed to PET imaging, which detects two coincident 511 keV annihilation photons. SPECT imaging requires the collimation of  $\gamma$ -rays emitted from the object. The collimator is placed in front of the NaI(Tl) scintillation crystal and serves as a lens in an optical system. It contains hundreds of small holes (parallel, diverging or converging; high sensitivity; low resolution) or a limited number of pinholes (low sensitivity; high resolution), which allow photons to travel to the crystal (Figure 6).

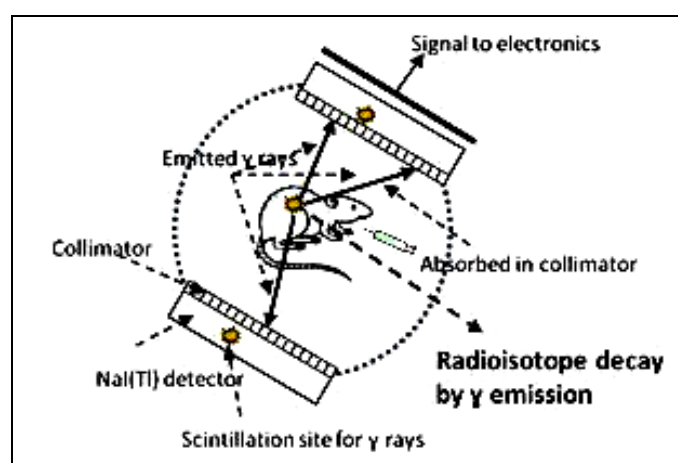


Figure 6: Schematic principle of SPECT

(Adapted from [http://www.med.lu.se/bioimaging\\_center/modalities/pet\\_spect\\_ct/basic\\_principles](http://www.med.lu.se/bioimaging_center/modalities/pet_spect_ct/basic_principles)).

Although PET imaging is more sensitive than SPECT modality, the latter offers advantages, such as broad availability, and lower costs of radioisotopes and  $\gamma$ -scanning instruments. In addition, since SPECT radionuclides emit photons with different energies, several biomarkers can potentially be distinguished at the same time, as opposed to PET radionuclides which all emit the same energy photons of 511 keV.

#### *b. Positron emission tomography (PET)*

The administered radionuclide decays by emission of a positron ( $\beta^+$ ). After travelling at most a few millimeters in tissue, the  $\beta^+$  collides with an electron, and their mutual annihilation results in two  $\gamma$ -photons. The PET scanner is based on the detection of these high energy two collinear  $\gamma$ -rays (511 keV), which are simultaneously localized within a very short time by opposing detectors that correspond to multiple rings of scintillation crystals. By collecting a statistically significant number of radioactive events, mathematical algorithms reconstruct a

three-dimensional image, revealing the distribution of the  $\beta^+$ -emitting tracer in the tissues (Figure 7).

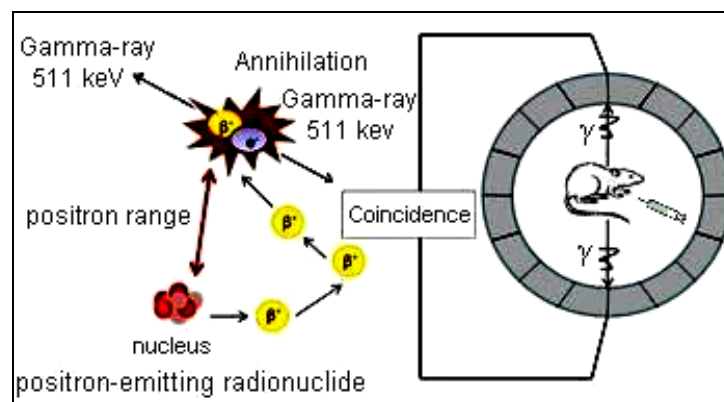


Figure 7: Schematic principle of PET: a positron-emitter emits a positron ( $\beta^+$ ) in the decay process. The  $\beta^+$  travels a short distance and collides with one of the surrounding electrons. Then, the  $\beta^+$  and the electron rapidly annihilate: its mass is converted into two  $\gamma$ -photons of 511 keV, which are emitted simultaneously at approximately  $180^\circ$  to each other. If these two photons hit the detectors on opposite sides almost at the same time and are detected as a coincidence event, the line along which the annihilation occurred is known. By surrounding the subject with many detectors, the annihilation photons, emitted in a large volume and in many angles, can be detected (Adapted from [http://www.med.lu.se/bioimaging\\_center/modalities/pet\\_spect\\_ct/basic\\_principles](http://www.med.lu.se/bioimaging_center/modalities/pet_spect_ct/basic_principles)).

The PET imaging has the additional advantages of being fully quantitative and providing higher spatial resolution than SPECT technique. However, the limitation of PET imaging is the requirement for a cyclotron to generate PET radionuclides and the high cost.

### *c. Computed tomography and dual mode imaging*

X-ray computed tomography (CT) is a radiological method of observing internal organs in a noninvasive manner in order to obtain high quality volumetric images. CT enables to visualize the tissue density differences that provide image contrast owing to X-ray attenuation between soft tissues and dense bones. When passing through the body, the energy of X-ray beams is absorbed. This attenuation depends on the type of tissue. For instance, the bone attenuation is high and the bones appear in white, while the air in lungs appears in black. The other tissues are represented by various shades of gray (Figure 8).

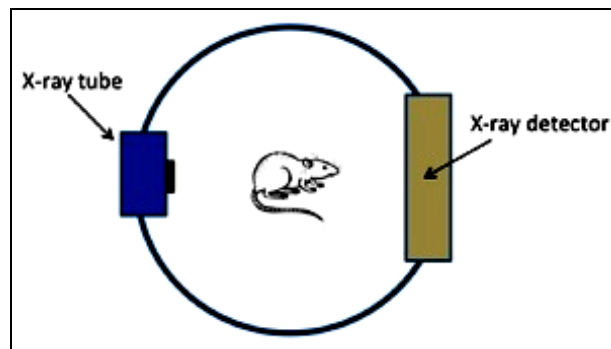


Figure 8: The principle of CT with an X-ray source and a detector rotating synchronously around the subject. The tomographic imaging consists of directing X-rays towards an object from multiple orientations and to measure the decrease in X-ray intensity along a series of linear paths. This decrease is characterized by Beer's Law, which describes the intensity reduction as a function of X-ray energy, path length and material linear attenuation coefficient. A specialized algorithm is then used to reconstruct the distribution of X-ray attenuation in the volume being imaged (Accessed at [http://www.med.lu.se/bioimaging\\_center/modalities/pet\\_spect\\_ct/basic\\_principles](http://www.med.lu.se/bioimaging_center/modalities/pet_spect_ct/basic_principles)).

The limitation of nuclear imaging is the lower resolution compared to other molecular imaging systems, such as MRI. However, this constraint is being addressed by introducing CT fusion systems (PET/CT or SPECT/CT). These hybrid imaging systems integrate the lower-resolution molecular information from PET or SPECT with the higher-resolution anatomical detail from CT to obtain complimentary functional and anatomical informations into a single image (Figure 9).

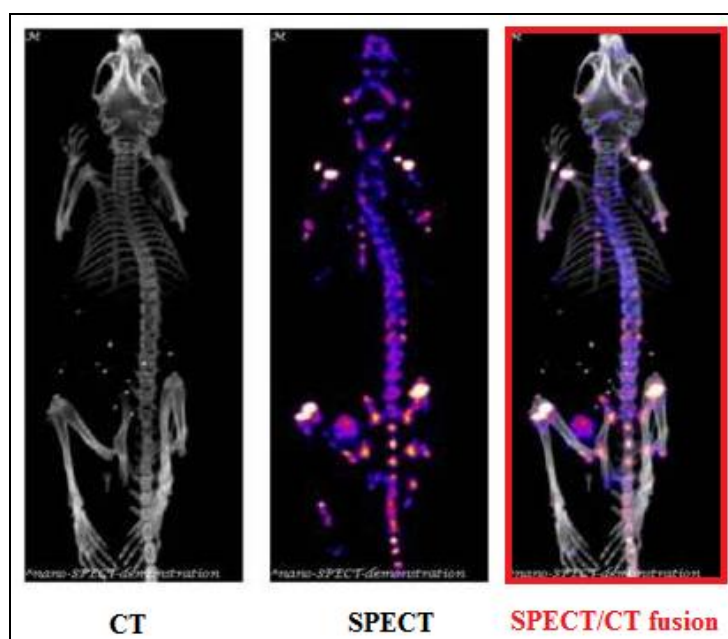


Figure 9: SPECT/CT coregistration of  $^{99m}\text{Tc}$ -MDP Bone Scan (Accessed at <http://www.umassmed.edu/saicf/petctimages.aspx>).



## II. Cancer targets addressed in the thesis

### 1. Epidermal growth factor receptor (EGFR)

Epidermal growth factor receptor (EGFR) is a member of the ErbB family of tyrosine kinase receptors (RTKs). EGFR is a transmembrane glycoprotein, which is present at the cell surface and which has an extracellular ligand-binding domain and an intracellular tyrosine kinase domain. EGFR is activated by several receptor-specific ligands, such as epidermal growth factor (EGF) and transforming growth factor- $\alpha$  (TGF- $\alpha$ ). After ligand binding, the receptor forms homo- or heterodimeric complex, activating the tyrosine kinase domain and the autophosphorylation (Yarden 2001, Olayioye 2000). Subsequently, the intracellular proteins involved in the signalling pathways are phosphorylated and activated, resulting in the modulation of gene transcription (Schlessinger 2000). EGFR plays an essential role in regulating a number of cellular processes, including cellular proliferation, differentiation, survival and migration (Hynes 2001). The dysregulation of the EGFR activity is therefore associated with tumorigenesis and makes EGFR as one of the most frequent implicated cell-surface marker of human cancer (Kuan 2001). Indeed, the overexpression of EGFR may occur in a wide range of epithelial tumours, including but not limited to those of breast, colon, head and neck, kidney, lung and prostate cancer (O'Dwyer 2002, Herbst 2002). EGFR is thus involved in malignant transformation and tumour growth through cell proliferation, in inhibition of apoptosis, in promotion of angiogenesis and metastasis (Zandi 2007). Therefore, EGFR is a rational target for antitumour strategies (El-Rayes 2004).

There are two classes of agents targeting EGFR: mAbs and low MW tyrosine kinase inhibitors (TKIs). MAb directed against EGFR are the most common approach to inhibit the EGFR signalling in the anticancer therapeutic context and can be combined with cytotoxic chemotherapy in several tumour types. The anti-EGFR mAbs bind to the extracellular domain of EGFR and inhibit the ligand binding to the receptor (Sato 1983). After EGFR binding, the antibodies induce the receptor dimerization and inhibit the receptor phosphorylation and subsequent downstream signalling pathways (Li 2005). Therefore, the anti-EGFR mAbs have an antiproliferative effect on cancer cells expressing EGFR through cell cycle arrest in G1 (Harari 2004, Narita 2001, Goldstein 1995), apoptosis enhancement (Janmaat 2003) and angiogenesis inhibition (Luwor 2005, Petit 1997) (Figure 10).

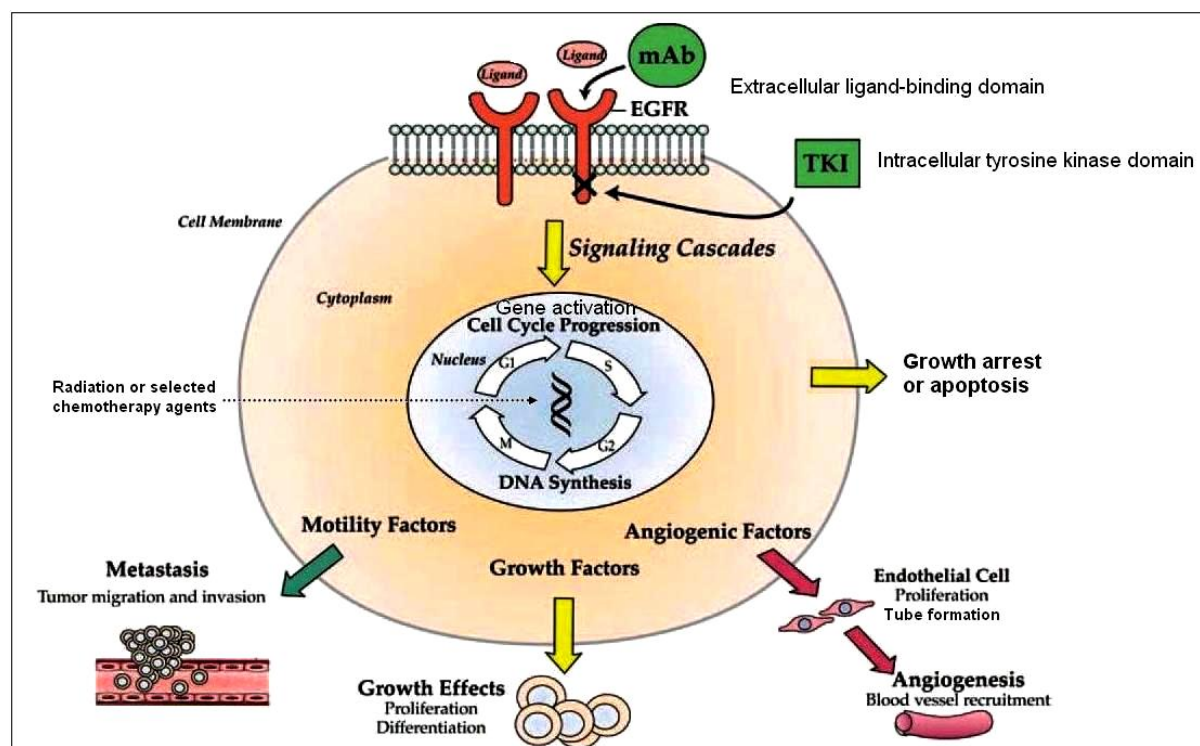


Figure 10: Simplified illustration of the EGFR pathways, highlighting the potential downstream cellular and tissue effects of inhibited EGFR by mAbs (Adapted from Harari 2004 and 2000).

Currently, two mAbs targeting EGFR (cetuximab (Erbix<sup>®</sup>) and panitumumab (Vectibix<sup>®</sup>)) are approved for the treatment of metastatic colorectal cancer; and additional mAbs are in clinical development for various indications (Rivera 2008). It has been reported that cetuximab, a chimeric human-mouse mAb, increases the survival in patients with advanced colorectal cancer, when administered in combination with irinotecan and fluorouracil (Van Cutsem 2009). Cetuximab has also an indirect antitumour effect through antibody-mediated engagement of immunologic effector cells *via* FcγR binding, resulting in ADCC response (Kurai 2007). Moreover, cetuximab has been implicated in the acceleration of the EGFR internalization and mimics the ligand-induced endocytosis and the degradation of active EGFRs (Prewett 1996). Normally, the natural ligand binding to EGFR induces a rapid internalization, which is followed by recycling of the receptor to the cell surface or its degradation in lysosomes, depending on the signal intensity and the cellular context (Huang 2006 [a], Barbieri 2000, Sorkin 1991). The susceptibility of EGFR to undergo the internalization and the degradation after antibody binding differed among cancer cell lines. The lack of a sufficient internalization and degradation of EGFR may explain the partial resistance to anti-EGFR mAbs therapy. Moreover, the endogenous ligands continue to

compete with anti-EGFR mAbs for binding to EGFR at the cancer cell surface, resulting in treatment desensitization or resistance (Pedersen 2010). Furthermore, the limited penetration of antibodies through tumour tissue is also an important cause of therapy resistance. The mAb distribution from blood vessels within the tumour depends on the antibody diffusion and/or its convection, and is inhibited by the consumption in proximal cells (Lee 2010, Thurber 2008). Therefore, the blood vessel targeting, and particularly the tumour angiogenesis may constitute a good alternative to overcome the poor distribution of some anticancer drugs in solid tumors.

## **2. Endoglin (CD105)**

Endoglin, also known as CD105, is an auxiliary receptor for transforming growth factor- $\beta$  (TGF- $\beta$ ). It is a homodimeric transmembrane glycoprotein with a short intracellular domain, which presents several potential phosphorylation sites that are phosphorylated by TGF- $\beta$  receptor kinase, and a large extracellular region (Bernabeu 2007, Gougos 1990, Haruta 1986). There are two isoforms of CD105 characterized in human and murine tissues, termed long (L)- and short (S)-endoglin, which differ in their cytoplasmic domain and in their pattern of tissue distribution. The L-endoglin is the most abundantly expressed form in mouse tissues and is also the predominant form in endothelial cells (ECs), while the S-form is expressed in liver and lungs at significant levels (Pérez-Gómez 2005). Endoglin is a cell surface protein that interacts with T $\beta$ R type I or T $\beta$ R type II to form TGF- $\beta$  receptor complex, which is activated by several receptor-specific ligands belonging to the TGF- $\beta$  superfamily, such as TGF- $\beta$ 1 and TGF- $\beta$ 3 (Guerrero-Esteo 2002). The level of CD105 expression on ECs can affect the response of ECs to TGF- $\beta$ , modulating their proliferation. It has been proposed that within this complex, CD105 regulates its own phosphorylation status, and subsequently modulates the TGF- $\beta$  signalling pathways. Endoglin is expressed on vascular ECs, and is overexpressed in proliferating ECs of tissues undergoing angiogenesis, such as regenerated and inflamed tissues or tumours (Wikstrom 2002, Fonsatti 2000, Miller 1999, Burrows 1995). A number of studies have reported the involvement of CD105 in the physiologic generation of blood vessels and in the development of tumour-associated angiogenesis (Bernabeu 2009, Bernabeu 2007). In ECs, two pathways with opposite effects have been identified and activated by TGF- $\beta$  after CD105-T $\beta$ R type II association. The TGF- $\beta$ /ALK5 pathway induces

Smad\* 2/3 phosphorylation, while the TGF- $\beta$ /ALK1 pathway promotes Smad 1/5 phosphorylation. The latter pathway promotes the EC proliferation, the migration and the tube formation, while the first pathway inhibits these cellular responses to TGF- $\beta$  and induces the EC quiescence. Upon activation, the phosphorylated Smad 2/3 and Smad 1/5 assemble with Smad 4 to form a complex that accumulates in the nucleus, binds to DNA together with other DNA binding transcription factors, and regulates the transcription of target genes (Goumans 2009, Lebrin 2004, Goumans 2002) (Figure 11).

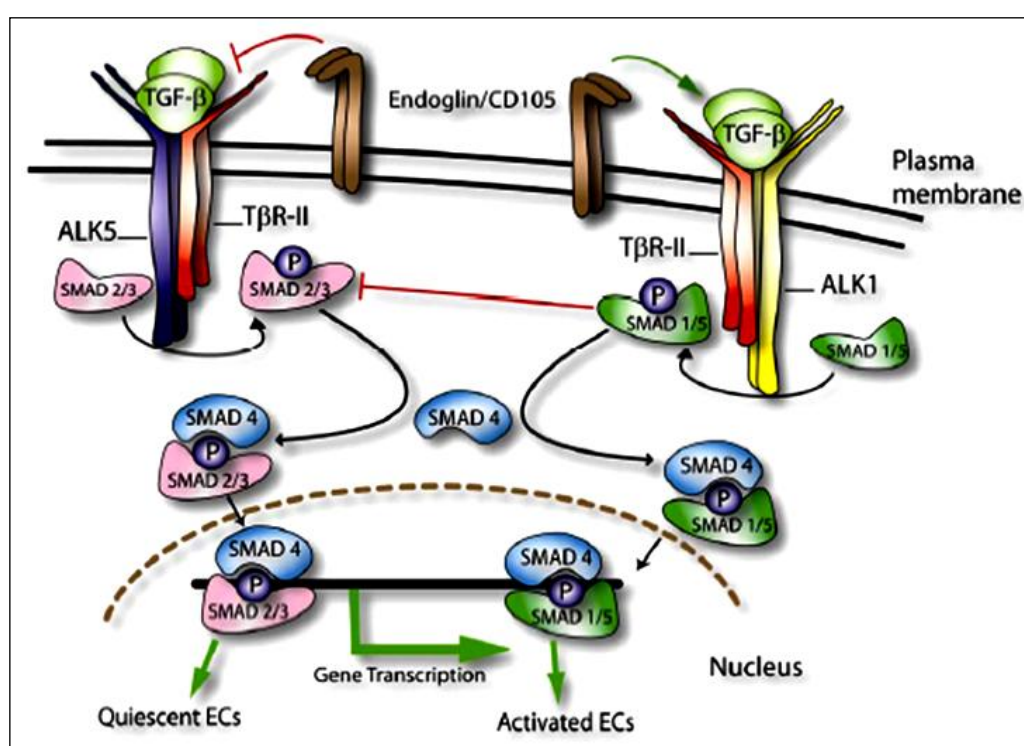


Figure 11: A schematic hypothetical role of endoglin (CD105) in TGF- $\beta$ /ALK1 and TGF- $\beta$ /ALK5 signalling pathways in endothelial cells (ECs) (Fonsatti 2010).

Endoglin is highly expressed in tumour-associated endothelium in many solid cancers, including breast, prostate and cervical cancer (El-Gohary 2007, Beresford 2006, Wikström 2002, Brewer 2000). It must be mentioned that endoglin may also be abundantly expressed in some cancer cells, such as melanoma (Sun 2008, Hussein 2005) and choriocarcinoma cells (Letamendía 1998). Furthermore, the vascular density, determined using the anti-CD105 mAbs, is correlated with the prognosis of breast cancer patients (Kumar 1999), the risk of developing metastatic disease in colorectal cancer (Romani 2006) and the recurrence of

\* Smad: intracellular proteins, which act as effectors of TGF- $\beta$  signalling pathways by transducing signals from TGF- $\beta$  superfamily ligands upon the activation of receptor serine/threonine kinases.

malignancy of head and neck squamous cell carcinoma (Marioni 2010). Recently, several studies have indicated that CD105 represents a more specific and sensitive marker for tumour angiogenesis and tumour progression than the commonly used pan-endothelial markers, such as CD34 and CD31 in various types of human malignancies, such as breast carcinoma, colorectal carcinoma and non-small cell lung cancer (Charpin 2004, Li 2003, Tanaka 2001, Kumar 1999). Moreover, the CD105 targeting by using anti-CD105 mAbs is an antiangiogenic therapy based on attacking blood vessels, each of them supporting thousands of cancer cells in the tumour mass, in addition to directly attacking cancer cells that overexpress CD105 (Carmeliet 2011). Indeed, the direct targeting of angiogenic ECs is emerging as an attractive approach to cut down the blood supply of oxygen and nutrients to neoplastic cells in the tumour mass. By attacking blood vessels, these antiangiogenic agents inhibit the recruitment of the new blood vessels by tumours, and regulate the metastatic capabilities of tumours (Figure 12).

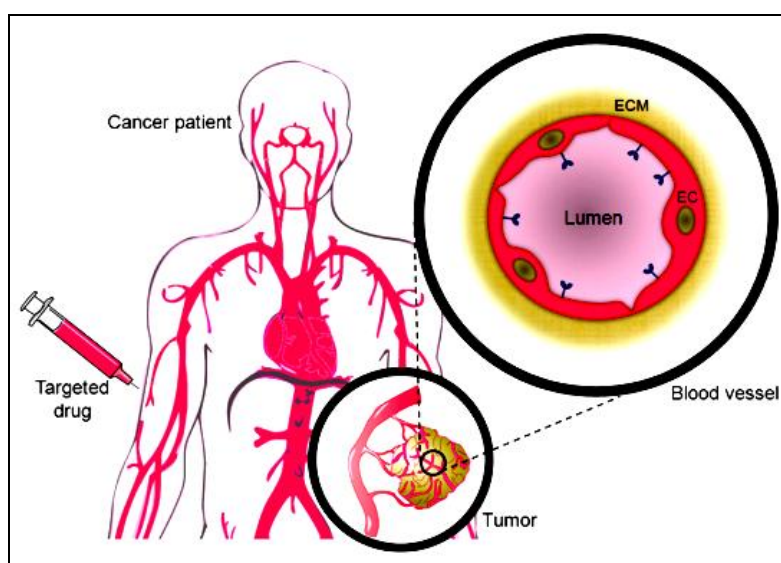


Figure 12: The concept of antibody-based tumour vascular targeting. The targeted compound is injected intravenously and homes to the tumour-specific vascular antigen, resulting in drug localization at the tumour site. The vascular antigen, such as endoglin, is expressed on the luminal surface of endothelial cells (ECs). ECM: extracellular matrix (ECM) (Schliemann 2007).

The expression of CD105 on cells directly exposed to the bloodstream (ECs) enables to overcome difficulties observed with large-sized mAbs to reach neoplastic target cells, which are in most cases away from the bloodstream. The mechanisms of action of anti-CD105 mAbs combine among others, the inhibition of TGF- $\beta$  signalling pathways and subsequently EC

proliferation, the direct killing of target cells through the activation of immunologic mechanisms, such as ADCC response, and the delivery of therapeutic agents at tumour sites, such as antibodies labelled with cytotoxic radionuclides (Figure 13).

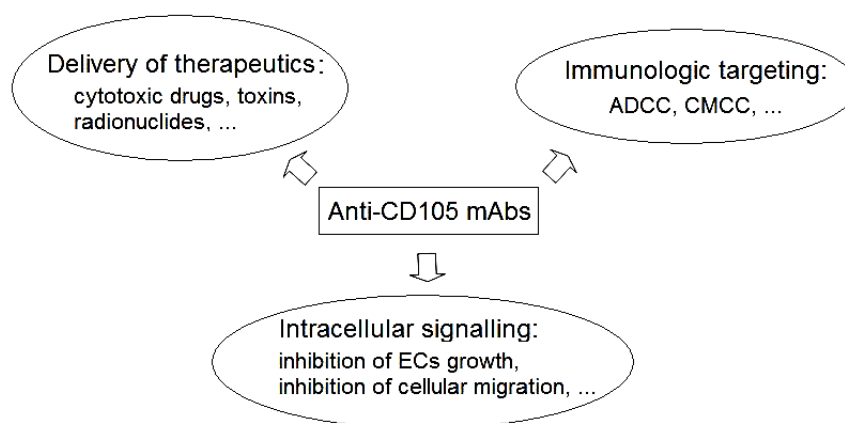


Figure 13: An overview of possible mechanisms of action of therapeutic anti-CD105 mAbs (Adapted from Maio 2006).

In the last few years, significant advances have been made regarding the biology of CD105 in cancer, enabling to identify the potential advantages and limitations of CD105 targeting in diagnosis as well as in therapy (Table 1).

Strengths	Limitation
Optimal accessibility of targeted site from the bloodstream: <ul style="list-style-type: none"> <li>- without need of extravasation</li> <li>- with direct binding to the receptors after intravenous injection</li> </ul>	Presence of soluble form of CD105
Selective toxicity independent from the antigen expression on neoplastic cells and thanks to the CD105 overexpression on tumour endothelia as compared to normal endothelium	
Decrease of the risk of emerging resistance thanks to the genetically stability of endothelial cells as compared to tumour cells	
No tumour-histotype specificity: most of endothelial cell markers are expressed whatever the tumour type	
Amplified effect: since targeting a single blood vessel leads to the death of several tumour cells, which are all dependent to this targeted blood vessel	

Table 1: Potential advantages and limitations of CD105 targeting (Adapted from Fonsatti 2010).

Several *in vitro* and *in vivo* preclinical studies have strongly supported the use of mAbs directed against CD105 overexpressed on tumour-associated endothelia, both for imaging and therapy (Appendix 4). Moreover, multicenter clinical trials are in progress and their results may validate CD105 as a novel target for cancer treatment (Rosen 2012) (Table 2).

Phase (Sponsor)	Treatment	Cancer indication	Main purposes
I/II (NCI)	Anti-CD105 mAbs (TRC105) + bevacizumab (Avastin <sup>®</sup> )	Recurrent glioblastoma multiforme	- MTD establishment (phase I) - Assessment of safety and adverse events (phase II) - Efficacy assessment as measured by progression-free survival of the combination compared to bevacizumab alone (phase II)
II (NCI)	Anti-CD105 mAbs (TRC105) + bevacizumab (Avastin <sup>®</sup> )	Metastatic kidney cancer	- Comparison of the progression-free survival at 12 and 24 weeks under bevacizumab alone or in combination with TRC105 - Toxicity and RECIST response rate for the combination compared to bevacizumab alone
I (Tracon Pharmaceuticals Inc.)	Anti-CD105 mAbs (TRC105) + bevacizumab (Avastin <sup>®</sup> )	Advanced or metastatic solid cancer	Safety/tolerability assessment and MTD establishment
I/II (Tracon Pharmaceuticals Inc.)	Anti-CD105 mAbs (TRC105) + capecitabine (Xeloda <sup>®</sup> )	Progressive or recurrent metastatic breast cancer	Safety/tolerability assessment and MTD establishment

Table 2: Illustrative examples of some human studies undergoing clinical trials for the efficacy assessment of anti-CD105 mAbs in cancer management. NCI: National Cancer Institute, MTD: maximum tolerated dose, bevacizumab: anti-VEGF humanized mAbs, RECIST: Response Evaluation Criteria in Solid Tumors (Accessed at [www.clinicaltrials.gov](http://www.clinicaltrials.gov)).

Despite the promising antitumour effect of anti-CD105 mAbs, the tumours may still become resistant to antiangiogenic therapies (Mitchell 2010). Therefore, the combination of antiangiogenic agents with conventional cytotoxic agents or radiation therapy, may results in additive or synergistic antitumour effects (Gasparini 2005). Moreover, other approaches using anti-CD105 mAbs conjugated to cytotoxic compounds, such as immunotoxins or radioantibodies are effective for suppression of tumour growth (Tsuji 2008, Tsuji 2006, Takahashi 2001, Tabata 1999, Matsuno 1999, Seon 1997) and metastasis (Uneda 2009). Finally, although anti-CD105 mAbs are used successfully as intrinsic therapeutic agents, they can also be exploited as targeting agents. Within this context, the antibody-targeted nanomaterials, and particularly antibody-functionalized gold nanoparticles, may represent an interesting combined approach for improving the efficacy of the standard inhibitors of angiogenesis thanks to the additional therapeutic properties of gold nanoparticles.



### III. Nanoparticle drug delivery systems

#### 1. Overview of nanoparticle properties

The field of nanotechnology is currently undergoing important development on many fronts. A wide variety of nanoparticles (NPs) have been investigated in the last few years in order to explore their potential as nanoparticle-based cancer therapeutics, and as molecular imaging agents (Nune 2009). NPs show a potential in noninvasive tumour imaging, in early detection and in drug delivery, while exhibiting optical, magnetic and structural properties that are not common for conventional molecules. NPs are defined as nanometer size scale complex systems ranging from 1 to 100 nm (The Royal Society and the Royal Academy of Engineering, 2004). NPs over other systems show many advantages because of their unique pharmacokinetics, vast surface area, diverse surface chemistry, which enables surface modifications for further conjugation, and the possibility of encapsulation of large amounts of therapeutic agents. Moreover, they can combine several functionalities and target specifically the tumours (Sajja 2009). Finally, NPs can be classified into two groups, organic NPs, such as lipid-based NPs, and inorganic systems, such as gold nanoparticles.

#### 2. Gold nanoparticles (AuNPs)

Gold nanoparticles (AuNPs) are emerging as interesting tools in many biomedical applications thanks to their unique chemical, physical and optical properties. The gold represents an attractive metal for nanoparticle development due to its biocompatibility, inertia, extreme resistance to oxidation, convenient surface functionalization, high absorption coefficient and high physical density ( $Z = 79$ ,  $\rho = 19.32 \text{ g cm}^{-3}$ ). Moreover the colloidal AuNPs are available in a variety of different sizes and shapes, and are widely used for biomedical applications. This section addresses exclusively spherical AuNPs but it must be mentioned that there is a variant of metallic AuNPs, called nanoshells. The nanoshells are nano-sized NPs consisting of a nonconducting silica core coated with a thin gold shell (Loo 2005). By fine-tuning the thickness of the core and the shell, these metal-dielectric composite structures absorb and scatter specific wavelengths of light across the visible and NIR spectrum, and are used for cancer imaging (Sajja 2009). However, their primary use continues to be in thermal ablation therapy (O'Neal 2004).

## 2.1. Production

There are robust and facile synthetic methods for producing AuNPs with a precise control of the particle size and shape (Murphy 2008, Sperling 2008). A large quantity of AuNPs in solution is often prepared by wet chemistry techniques. Alternative approaches implying physical methods were also developed. One can cite UV (Mallick 2001) or  $\gamma$ -irradiation (Choi 2005), sonochemistry (Jin 2007, Park 2006), spark discharge method (Tseng 2008), low-pressure techniques, such as physical vapour deposition (PVD) (Moreau 2009). Moreover, the AuNPs can be synthesized using relatively safe reagents, which is important, considering the emerging concerns about nanomaterial safety and toxicity for biomedical applications (Murphy 2008, Lewinski 2008).

### *a. Wet chemical method*

The wet chemistry provides well-known tools enabling both synthesis and surface modifications of AuNPs. Spherical AuNPs with precise size can be synthesized in aqueous or organic solvents (Daniel 2004). In general, the reduction of gold salts, such as  $\text{AuCl}_4^-$ , leads to the nucleation of gold atoms (Kimling 2006, Frens 1973, Turkevich 1951). The synthesis of AuNPs in aqueous medium typically uses reducing agents, either trisodium citrate that produces monodisperse particles with controlled diameter from 10 to 60 nm, or sodium borohydride that produces smaller particles with a diameter lower than 5 nm (Brust 1995, Brust 1994). The precisely control of the reducing agent concentration leads to the formation of small and uniform AuNPs. As AuNPs are not stable, a stabilizing agent is required through physically adsorption or chemically binding to gold surface.

### *b. Physical vapour deposition method (PVD)*

Among other physical methods, AuNPs may be produced through PVD method (Limage 2011, Dreesen 2009). This process enables to synthesize AuNPs with a mean diameter of 5 nm (Moreau 2009). In this case, the synthesis of NPs is based on the aggregation of free gold atoms in ionized gas phase (plasma). Gold atoms are generated by magnetron sputtering of a gold target in argon atmosphere (Figure 14). This method produces NPs with a narrow size distribution on a flat surface (Bouchat 2011). AuNPs are deposited onto a salt layer (NaCl) in order to allow their subsequent transfer into a liquid solution and avoiding as much as possible their aggregation. Moreover, large quantities of AuNPs could be obtained by

repeating the deposition cycle. In addition, the unique features of plasma process make possible the nanoparticle surface functionalization. Indeed, the nanoparticle coating may be achieved by plasma polymerization of a monomer, such as plasma-polymerized allylamine (PPAA) (Moreau 2011, Lucas 2008). The amine functionalization of AuNPs provides many advantages, such as allowing the synthesis of antibody-conjugated gold nanoparticles. Moreover, when uncoated AuNPs aggregate immediately after being suspended in the liquid phase, coated AuNPs suspension shows a good stability, which could be explained by the strong hydrophilic character of the coating layer (Hamerli 2003).

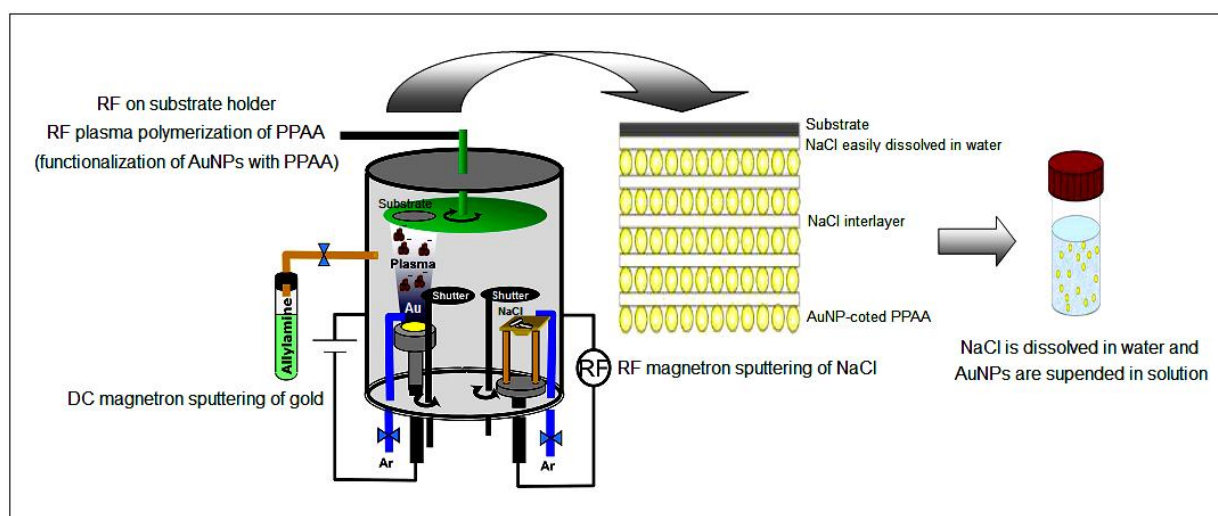


Figure 14: Schematic principle of physical vapour deposition technique (PVD), illustrating the synthesis of gold nanoparticles (AuNPs). RF: radiofrequency; DC: direct current; PPAA: plasma-polymerized allylamine; Ar: argon; Au: gold (Adapted from Bouchat 2011).

## 2.2. Physical properties and biomedical applications

The biomedical applications of AuNPs, especially in the area of cancer, are resulting from their photophysical properties that are used for the photodiagnostic and phototherapy. Further, the gold nanostructures provide a versatile platform to integrate diagnostic or therapeutic agents or both options for a theranostic approach. Thus, a multifunctional tool based on conjugating AuNPs with targeting ligands, therapeutic molecules and imaging contrast agents, holds an array of encouraging directions for cancer research.

### *a. Photophysical properties of gold nanoparticles*

When a metal nanoparticle is exposed to light, the oscillating electromagnetic field of the light induces a collective coherent oscillation of the free electrons of the metal (Huang 2010). The collective excitations of conductive electrons in metals are called “plasmons” (Kreibig 1995). The coherent oscillation of the free electrons in resonance with the electromagnetic field is called the surface plasmon resonance (SPR). The energy loss of electromagnetic wave after passing through a matter results from absorption and scattering processes. Due to the SPR oscillation, the light absorption and scattering are strongly enhanced for AuNPs, compared with those of the most strongly absorbing organic dye molecules and the most strongly fluorescent molecules. The radiative properties of AuNPs (absorption and scattering properties) are largely dependent on the size, shape and structure of nanoparticles (Huang 2010, Link 2003, El-Sayed 2001, Link 2000, Link 1999).

The optical properties of spherical AuNPs are determined by their SPR light-scattering, which is localized in the visible spectral region at approximately 520-530 nm. This is the origin of the brilliant red colour of AuNPs in solution (Dykman 2012). In addition to the enhanced and tunable radiative properties, AuNPs can convert the absorbed light into heat *via* nonradiative processes (Huang 2010). Indeed, AuNPs are very photostable and represent a new generation of contrast agents for photothermal therapy (PTT). The PTT of cancer using AuNPs is based on the high efficient and localized light-to-heat conversion, which should be sufficient to induce cellular damage *via* thermal effects (Huang 2010). The exact physical basis of heat generation by AuNPs is not entirely clear and is under active investigation (Raouf 2011).

### *b. Gold nanoparticles as contrast agents*

The strongly enhanced SPR light-scattering of AuNPs may be used for imaging applications. Because the light scattered from AuNPs is in the visible region of the electromagnetic spectrum in accordance with their plasmon band, it is possible to optically track the position of individual NPs, paving the way for cellular imaging in sensing strategies (Murphy 2008, El-Sayed 2005, Raub 2004, Sokolov 2003 [a]). The radiative properties of AuNPs make them detectable in a visible light microscope. Moreover, AuNPs have emerged as colorimetric biosensors in diagnostic through the agglomeration-based sensing. The assay is based on a change in colour resulting from a change in the plasmon resonance frequency,

which depends on the average distance between AuNPs (Zhao 2008) (Figure 15). Indeed, during the formation of nanoparticle agglomerates, the colour changes from red to purple or blue. During dispersion of agglomerates, the reverse colour change is observed. Further, the AuNPs biosensing is also based on changes in local refractive index due to chemical binding, such as the interaction between NPs containing receptors when an anti-receptor is added (Elghanian 1997). Finally, metallic NPs, and particularly AuNPs, possess a potential as X-ray contrast imaging agents owing to their potent X-ray absorption (Kim 2007, Hainfeld 2006). Thus, the rich surface chemistry and the absorption capacity of AuNPs have triggered interest for their use in X-ray CT imaging applications.

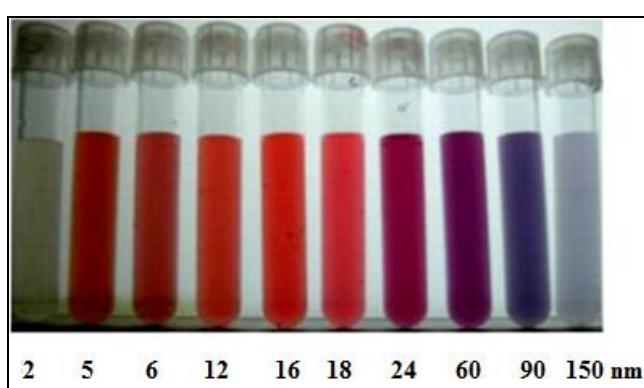


Figure 15: Colloidal gold suspensions of various nanoparticle sizes  
(From Dr. Irawati Kandela, University of Wisconsin, BBPIC laboratory).

### *c. Gold nanoparticles as therapeutic agents*

AuNPs could potentially play a role in cancer therapeutics. They can be used as drug delivery vectors to improve the delivery of anticancer drugs, such as water-insoluble photosensitizers for photodynamic therapy (PDT). They can also produce heat on exposure to UV, NIR radiations or RF energy, and hence provide the possibility to kill cancer cells through PTT. Finally, gold-based therapies may combine more than one treatment for creating a more aggressive and effective strategy against cancer through the enhancement of damages induced by associated radiation or anticancer drugs (Brown 2010, Chithrani 2010) (Figure 16 and Table 3).

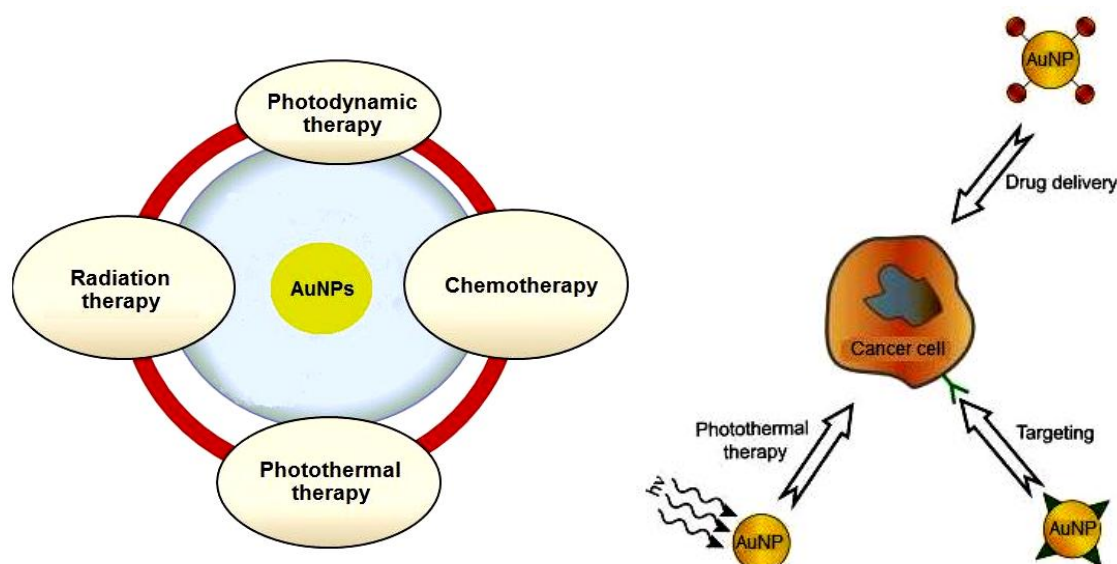


Figure 16: The possibility of combined therapies for effective therapeutics of cancer. Gold nanoparticles (AuNPs) are at the center of attention since they can be used for improving targeting, as anticancer drug enhancers through sensitizing to radiation or delivering of drugs, and for generating of heat (Adapted from Jelveh 2011 and Ghosh 2008 ).

➤ *Gold nanoparticles as drug carriers*

Functionalized AuNPs may be used as delivery vehicles to improve the dose delivery of cytotoxic or biologic agents to target tissues. They are good drug-delivery scaffolds because they are known to be biocompatible (Connor 2005). In addition, AuNPs can also be easily functionalized with targeting molecules and have shown an excellent potential for the targeted delivery of drugs. Based on recent studies, it is clear that AuNPs can enhance the therapeutic effects of some delivered drugs (Table 3).

Author	Treatment	Study type	Tumour type	Effects
Brown 2010	AuNPs conjugated to cisplatin	<i>in vitro</i>	A549 lung epithelial cancer cell line, HCT116, HCT15, HT29, RKO colon cancer cell lines	↑ cytotoxicity of cisplatin
Libutti 2010	AuNPs conjugated to TNF- $\alpha$ (CYT-6091, Aurimune®) phase I clinical study	<i>in vivo</i> (n = 30 patients)	Melanoma, colorectal, lung and pancreatic adenocarcinomas	Improving the safety of higher doses of TNF- $\alpha$
Zheng 2009	AuNPs conjugated to DNA-cisplatin complex + radiation	<i>in vitro</i>	-	Selective radiation sensitization ↑ double-strand breaks of DNA
Patra 2008	AuNPs conjugated to cetuximab and gemcitabine	- <i>in vitro</i> - <i>in vivo</i> (mice)	Pancreatic cancer	↑ inhibition of tumour cell proliferation ↑ inhibition of tumour growth
Visaria 2006 Visaria 2007	AuNPs conjugated to TNF- $\alpha$ + hyperthermic therapy	<i>in vivo</i> (mice)	SCK mammary carcinoma	Selective thermal sensitization ↑ survival rate ↓ administered dose of TNF- $\alpha$ and side effects
Paciotti 2004	AuNPs conjugated to TNF- $\alpha$	<i>in vivo</i> (mice)	MC-38 colon carcinoma	↑ tumour uptake, ↑ antitumour effect ↓ non-specific uptake ↓ administered dose of TNF- $\alpha$ and side effects

Table 3: Illustrative examples of some *in vivo* and *in vitro* studies using gold nanoparticles (AuNPs) conjugated to cytotoxic drugs. TNF- $\alpha$ : tumour necrosis factor- $\alpha$ .

Finally, AuNPs have been identified as a promising delivery platform for PDT agents and are also used to increase the efficacy of PDT. Indeed, the lack of solubility under physiological conditions constitutes a significant problem for intravenous PDT drug delivery. The PDT technique is based on the activation of photosensitizing agents with light of an appropriate wavelength (600-700 nm) and in the presence of oxygen. The light-mediated excitation of PDT agent results in the generation of reactive oxygen species (ROS) that damage the tumour tissue (Juarranz 2008, Dolmans 2003). The PDT agents conjugated to AuNPs represent an interesting tool with great versatility since it allows drug delivery, cancer therapy and monitoring of the delivery process in mice thanks to the optical properties of AuNPs (Cheng 2008).

➤ *Gold nanoparticles for photothermal therapy (PTT)*

PTT is defined as the ability to achieve hyperthermic temperatures of up to 42 °C, which can cause irreversible damages to the target tissue, render cancer cells more susceptible to the effect of radiation, and cause apoptosis to some extent. A local heating at the level of gold nanoparticle-labelled cells is produced through a local irradiation, killing cancer cells without harming surrounding healthy tissues. The interaction of light and AuNPs for subsequent heating of the local environment depend on the wavelength of light radiation, which should strongly overlap with the nanoparticle SPR absorption band. Recent studies have shown that AuNPs could effectively damage the targeted tumour tissue when irradiated with wavelengths around their absorption peak (El-Sayed 2006, Pitsillides 2003, Zharov 2003). Indeed, AuNPs can be synthesized with different sizes and shapes to tailor the absorption wavelength for generation of heat (Khlebtsov 2008, Khlebtsov 2006, Myroshnychenko 2008, Harris 2006). For example, the SPR light absorption of spherical AuNPs is in the visible region. Thus, PTT using spherical AuNPs can be achieved with visible laser, which has a shallow penetration depth in tissue. Such treatment is only suitable for superficial cancers, such as skin tumours.

By changing the shape of AuNPs from sphere to rods or nanoshells, there is a shift of their SPR absorption to NIR region (650-950 nm) (O'Neal 2004, Hirsch 2003). For instance, typically, the nanoshells with a silica core diameter of about 120 nm and a 10 nm layer of gold shell can strongly absorb NIR light and create an intense heat that is lethal to cells. It must be mentioned that although focused lasers for thermotherapy were useful, the simple heating cannot discriminate between tumours and healthy tissues. For this reason, the nanoshells conjugated with targeting molecules may be employed to specifically recognize tumour cells (Loo 2005). Indeed, the NIR laser energy can pass through the healthy tissues without causing harm and can kill only the targeted tumour cells accumulating the NPs through inducing *in vivo* thermal cytotoxicity (Gobin 2007). The NIR thermoablation is also unsuitable for treating deeper organ-based cancers due to the significant attenuation of NIR light by tissues, but it has been successfully initiated for patients with oropharyngeal malignancies and melanoma (Cherukuri 2010).

Finally, the use of radiofrequency energy to produce photothermal toxicity is not limited by tissue penetration and hence allowing to treat deeper lesions, such as hepatocellular cancer (Raouf 2011). Previous studies using cetuximab-conjugated gold nanoparticles have shown

cytotoxicity after radiofrequency field treatment. Indeed, cetuximab- conjugated gold nanoparticles are internalized in cancer cells through endocytosis with subsequent intracellular heat release and without toxicity to bystander cells that did not take up these immunonanoconjugates (Cherukuri 2010, Glazer 2010 [a], Curley 2008).

➤ *Gold nanoparticles as sensitizers in radiation therapy*

Radiotherapy is a major modality in cancer treatment. Recently, AuNPs are being used as sensitizers in radiation therapy. Previous studies tried to explain the gold-based sensitization mechanisms and hypothesised that the following effects can be combined to cause this phenomenon: enhanced localized X-ray absorption by AuNPs, effective release of low-energy electrons from AuNPs, and efficient deposition of energy in water as oxygen radicals and free electrons through creating more radicals by released electrons (Carter 2007) (Figure 17). It must be mentioned that AuNPs were in close proximity to DNA in these studies. The exact mechanisms of cell damage, when AuNPs are localized in the cytoplasm, and thus away from DNA, are not yet known (Jelveh 2011).

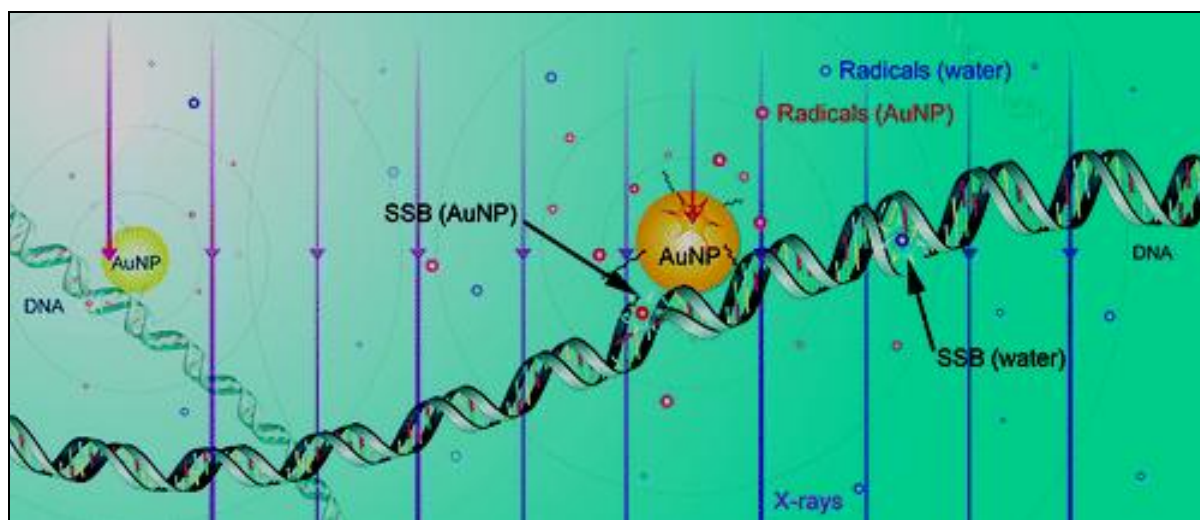


Figure 17: Hypothetical mechanisms of radiation induced DNA damage in the presence of gold nanoparticles (AuNPs). AuNPs interact with hard X-ray radiation in aqueous solution (enhanced localized X-ray absorption by AuNPs). A localized energy deposition with nanometer precision is obtained from low-energy electrons released by AuNPs. Blue spheres: radicals distributed evenly and generated from electrons produced in water; red spheres: radicals concentrated near AuNPs and generated from Auger electrons, secondary electrons and photoelectrons, which are produced by AuNPs; AuNP diameter: 3 nm; SSB: single-strand breaks of DNA (Carter 2007).

Several *in vitro* studies open the way to the possible improve of cancer irradiation therapies by using AuNPs (Liu 2010, Butterworth 2010, Rahman 2009, Kong 2008). For example, exposure cells 1 h to 1.9 nm AuNPs (10 or 100  $\mu\text{g ml}^{-1}$ ) prior to 4 Gy X- irradiation induces cellular cytotoxic response of a range of cell lines (MDA-231-MB and DU-145), including decreased clonogenic survival, increased apoptosis and induction of DNA damage which may be mediated through the production of reactive oxygen species (Butterworth 2010). These findings were confirmed by *in vivo* studies, which showed a tumour regression after X-ray irradiation of mice receiving intravenous injection of AuNPs (Hainfeld 2010, Chang 2008, Hainfeld 2004). For instance, B16F10 tumor-bearing mice received 13 nm AuNPs in conjunction with ionizing radiation (25 Gy, 24 h after injection) and showed significant delayed tumour growth and prolonged survival compared to the radiation alone (Chang 2008). It is believed that AuNPs localized into tumours enhance the X-rays absorption and subsequent cell damages (Brun 2009, Montenegro 2009). Indeed, recent studies have shown that there is an enhancement in radiosensitization when AuNPs are internalized in cancer cells (Chithrani 2010, Butterworth 2010, Rahman 2009, Kong 2008). The radiation enhancement factor seems to be dependent on the size of AuNPs, their concentration and the cell type. Moreover, the nanoparticle size plays an important role in the nanoparticle uptake at the cellular level, which leads to sensitization properties (Chithrani 2010, Chithrani 2006). For example, a recent study compared AuNPs from 14 to 74 nm and showed the highest level of cellular uptake and radiosensitization enhancement with 50 nm AuNPs irradiated with 105 kVp X-rays (Chithrani 2010). Furthermore, this study emphasized the need for optimization of nanoparticles in terms of size, shape and functionalization in order to achieve the highest level of radiation enhancement (Butterworth 2010, Chithrani 2010). In all these studies, the AuNPs accumulation into tumours is dependent on passive targeting through enhanced permeability and retention effect (EPR). Nevertheless, AuNPs can be surface modified for preferential and active targeting of cancer cells, which may lead to more radiosensitizing effect of AuNPs.

### 2.3. Strategies of tumour targeting

#### *a. Enhanced permeability and retention effect (EPR)*

NPs are accumulating passively in tumours through the leaky vasculature present in the tumours and without the aid of exogenous targeting ligands (Greish 2007). This passive

phenomenon, named EPR effect, was discovered by Matsumura and Maeda (Maeda 2009, Maeda 2001 [a], Matsumura 1986). ECs of healthy blood vessels are bound together by tight junctions that prevent any large particle in the blood from leaking out of the vessel (Sajja 2009). However, the tumour vessels are abnormal and present a high proportion of disorganized proliferating ECs, pericyte deficiency and aberrant basement membrane formation, leading to an enhanced vascular permeability (Danhier 2010, Hashizume 2000). The endothelial pores in leaky tumour vessels have sizes up to 600 nm (Schroeder 2012, Maeda 2011, Sarin 2010, Carmeliet 2000, Yuan 1995). Therefore, NPs having size less than endothelial pore size can rapidly enter into tumour sites from blood by extravasation, and are preferentially accumulated inside the interstitial space (Torchilin 2011, Pirollo 2008, Modi 2006, Iyer 2006). However, the smallest NPs easily diffuse back out (Maeda 2001 [b]). EPR effect arises from the tumour production of vascular endothelial growth factor (VEGF), which promotes the angiogenesis, and from the lack of an effective lymphatic drainage system in tumours. Indeed, the poor lymphatic vessels in tumours or their non-functional state contributes to inefficient drainage of NPs from the tumour tissue. Thus, NPs entered into the tumour are not removed efficiently and are retained there (Figure 18).

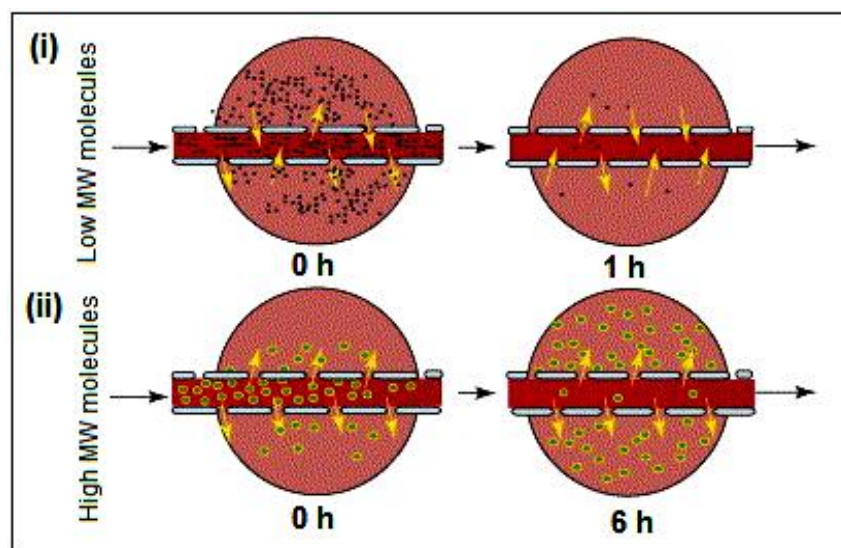


Figure 18: Schematic illustration of EPR effect: diffusion of low molecular weight (MW) molecules (i) and high MW molecules (ii) from the blood vessels into the interstitium of tumour tissue. The low MW molecules diffuse freely in and out the tumour blood vessels because of their small size and thus, their effective tumour concentration decreases after 1 h, when the high MW molecules cannot diffuse back into the bloodstream because of their large size, resulting in progressive tumour accumulation (Adapted from Iyer 2006).

### *b. Active targeting*

Despite the EPR effect that is favourable for the tumour localization of NPs of a given size, the effective uptake of NPs into the tumour mass and their homogeneous distribution may be limited because of the barriers created by the abnormal tumour physiology. Indeed many factors cause impairments regarding tumour accumulation of NPs, such as physically compromised vasculature, abnormal ECM, high interstitial fluid pressure (Heldin 2004, Jain 1987), highly variable and chaotic structure of tumour vessels, erratic blood flow in tumour vessels, formation of intratumoral vessels (Padera 2004), and possible extravasation of NPs through the extravascular barriers but impossible penetration through the tumour ECM.

For these reasons, the tumour targeting may be improved thanks to the surface modification of NPs. The ligands grafted at the NP surface, such as mAbs, allow the active targeting by binding to overexpressed receptors on cancer cells or on angiogenic ECs (Wang 2010 [a]). The targeted NPs can be successfully used as tumour high specific probes, increasing the nanoparticle-tumour interactions and the selective accumulation through the cell internalization (Popovtzer 2008, Davis 2008, Byrne 2008, Weissleder 2005). In most cases, these ligand-receptor interactions result in efficient uptake of these functionalized NPs into the tumour cells *via* receptor-mediated endocytosis. It must be mentioned that most of the conventional therapeutic agents, such as chemotherapy, are distributed non-specifically in the body, leading to systemic toxicity, serious side effects, and a loss of efficacy against tumours because of insufficient dose delivered. Therefore, the effective targeting tumour using targeted NPs might enable to provide a better pharmacokinetic profile, imaging capabilities and might contribute to deliver large doses of nanoparticles into malignant cells with minimal side effects elsewhere (Figure 19).

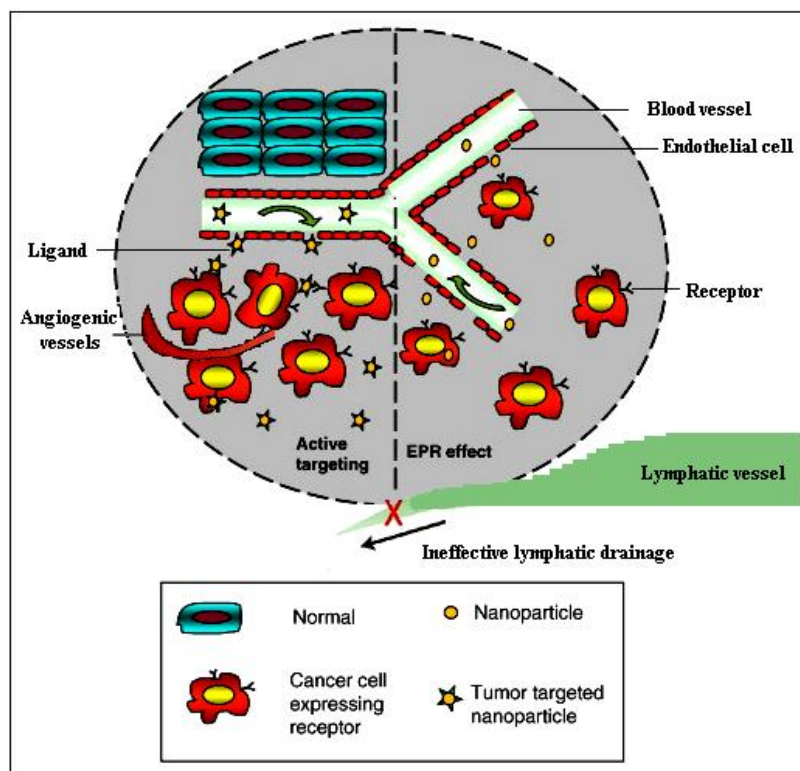


Figure 19: Schematic representation of tumour targeting. The right part of the figure depicts the increased accumulation of nanoparticles owing to the enhanced permeability and retention (EPR effect). The left part of the figure shows the active targeting mediated by targeted nanoparticles. The tumour tissues contain defective blood vessels with fenestrations, leading to a highly permeable tumour-associated neovasculature and allowing the leakage of circulating nanoparticles. The decreased of functional lymphatic vessels contributes to nanoparticle retention into the tumour site (Adapted from Misra 2010).

#### 2.4. Pharmacokinetic behaviour of gold nanoparticles

The surface coating, the shape and the size of AuNPs, as well as the route of administration, all play a role in determining *in vivo* behaviour of NPs. Many studies have provided informations regarding how these properties affect the nanoparticle biodistribution and the tumour targeting. Many improvements may be made for a favourable pharmacokinetic profile of AuNPs, such as decrease their clearance by the reticuloendothelial system (RES), extend their circulation time, ensure their *in vitro* and *in vivo* stability, and preserve their specificity regarding tumour cells (Longmire 2008).

The RES has a major role in removing foreign materials from the bloodstream mainly thanks to the macrophage activity. Indeed, the liver and the spleen have been described as the major organs of non-specific uptake of AuNPs (Douglas 1986). Modification of the surface

characteristics of AuNPs has an impact regarding the nanoparticle interaction with the RES (Bradfield 1984), and promotes the nanoparticle bioavailability. The common method to protect the nanoparticles from the opsonization and the subsequent phagocytosis consists of coating their surface with a layer of amphiphilic polymer chains, such as polyethylene glycol (PEG) (Pinto Reis 2006). PEG molecules are inert and large polymers, which have been investigated extensively as an effective means to provide hydrophilic and “stealth” properties to NPs. Indeed, the PEGylation leads to a partial avoidance of the RES uptake and a prolonged circulation time of PEGylated NPs by reducing their non-specific binding to the serum proteins and macrophages. The PEGylation creates a hydrophilic protective layer around the NPs, which increases their half-life in blood circulation. Moreover, the PEGylation imposes a steric barrier that leads to the steric repulsion forces, repelling the non-specific adsorption of opsonin proteins, and thereby blocking and delaying the opsonisation process and subsequent phagocytosis (Prencipe 2009, Owens 2006, Kaul 1992). However, the complete evasion of the RES through nanoparticle coating is not possible (Torchilin 1995, Stolnik 1995, Gref 1994). Further, the hydrophilic coating is interesting for the nanoparticle stability against aggregation since the particle aggregation is controlled by surface chemistry (Daniel 2004). Finally, the surface functionalization of AuNPs by using specific ligands has also been demonstrated to result in a rapid cellular uptake and internalization (Shenoy 2006).

The particle size and surface properties remain among the most important properties of AuNPs for effective delivery to the desired target. The large and long-circulating NPs are more retained in the tumour than smaller NPs, which easily diffuse (Pirollo 2008). The ideal nanoparticle size should be somewhere between 10 and 100 nm. Indeed, it should be much less than 400 nm for an efficient extravasation, larger than 10 nm to avoid renal filtration, but smaller than 100 nm to minimize the liver uptake (Kim 2008). The nanoparticle charge should be neutral or anionic to effectively escape to the renal elimination. Moreover, the tumour uptake through EPR effect is limited by the high interstitial fluid pressure associated with the poor lymphatic drainage (Heldin 2004, Jain 1987) and by the degree of tumour vascularization (Bae 2009), which explains the nanoparticle size relationship with the EPR effect. Further, the EPR effect will be optimal if NPs can evade immune surveillance and circulate for a long period in the blood. It is known that the plasma retention of the NPs is one of the primary driving forces for tumour accumulation through EPR effect (Modi 2006). Finally, the active targeting increases also the tumour accumulation through improving the

cellular uptake of NPs and especially through enhanced cellular internalization. Indeed, the uptake of AuNPs is consistent with the receptor-mediated endocytosis (Chen 2009). The ability of NPs to be internalized after binding to target cells is an important criterion in the selection of proper targeting ligands (Cho 2008). Therefore, the NP surface functionalization is an interesting way to improve tumour targeting since the active targeting is particularly attractive for the intracellular delivery of NPs and for increasing the antitumour effect.

## 2.5. Toxicity

Although there is a significant progress in the development of nanomaterials for biomedical applications, nanotoxicological studies have thus far lagged behind (Fischer 2007). While bulk gold is potentially biosafe, the gold nanoparticle toxicity should be assessed. Increasing number of reports has appeared with the goal of understanding the interactions between different types of nanoparticles and cells (Alkilany 2010, Lewinski 2008, Murphy 2008). However, no simple conclusions have emerged due to the variability of parameters, such as the the physical and chemical properties of AuNPs, cell type, gold concentration and incubation time, and the assay used to measure the cell health. Moreover, most nanotoxicological screening studies are done *in vitro*, on cell cultures, and are far from the real *in vivo* situation (Alkilany 2010).

Although *in vitro* studies may not accurately predict *in vivo* toxicity, they provide informations to understand the mechanisms of toxicity of nanoparticle accumulated at the cellular level (Gu 2009, Pernodet 2006). Most preclinical studies indicated that AuNPs are harmless to cultured cells. Indeed, several groups have examined the cellular uptake and the cytotoxicity of AuNPs, and showed that AuNPs are not toxic (Villiers 2009, Shukla 2005, Connor 2005). Some studies even showed that AuNPs reduce the level of harmful ROS in the cells (Shukla 2005). In contrast to these results, other groups have found that AuNPs are toxic. For instance, some experiments showed that the cytotoxicity depends on the cell type (Patra 2007, Pan 2007). Others have attributed the nanoparticle toxicity to their nanosize and have shown the size-dependent toxicity of AuNPs (Pan 2009, Pan 2007). Further, the nanoparticle toxicity due to the surface properties is rarely discussed. It seemed that cationic NPs are toxic at much lower concentrations than anionic NPs, which is related to the electrostatic interactions between the cationic NPs and the negatively charged cell membranes (Goodman 2004). Moreover, the nanoparticle coating type is able to modulate the cytotoxicity of AuNPs (Crespin

2011, Pan 2009). It is not easy to compare the results of all these *in vitro* studies because the quantification method of AuNPs varies widely across different research groups, and because the number of cells exposed to these AuNPs at a given concentration is often not specified. Finally, regarding the nanoparticle immunogenicity, the available informations are diverging. Some studies indicated that AuNPs are nonimmunogenic, and others showed that they are able to induce an antibody response in mice, regardless of their own cytotoxicity (Shukla 2005). Illustrative *in vitro* results of gold nanoparticle cytotoxicity are presented in Table 4.

Author	Size (nm)	Surface group	Cell line	Au concentration*; Incubation time	Toxicity results
Pan 2009	1.4, 15	TPMS, GSH	HeLa cells	5.6 mM; 48 h	1.4 nm AuNPs induced necrosis by oxidative stress, where 15 nm AuNPs are not toxic; GSH-capped AuNPs are less toxic than TPMS-capped AuNPs
Villiers 2009	10	citrate	Dendritic mouse cells	0.5 mM; 4-48 h	10 nm AuNPs are not toxic and did not induce dendritic cell activation
Gu 2009	3.7	PEG	HeLa cells	0.08-100 $\mu$ M; 6-72 h	3.7 nm AuNPs entered nucleus and did not induce toxicity
Pan 2007	0.8, 1.2, 1.4, 1.8, 15	TPMS, TPTS	Epithelial HELA cells Endothelial SK-ME1-28 cells Fibroblast L929 cells Phagocytes j774A1 cells	Up to 5.6 $\mu$ M; 72 h	Smallest AuNPs are toxic; 15 nm AuNPs non toxic Toxicity is not cell line dependent
Khan 2007	18	citrate	HeLa cells	0.2-2 nM; 3-6 h	18 nm AuNPs are not toxic
Patra 2007	33	CTAB, citrate	BHK21 hamster kidney cells, Hep2G human liver carcinoma cells, A549 human carcinoma lung cells	0-120 nM; 36-72 h	33 nm AuNPs non toxic to BHK21 and Hep2G cells, but toxic to A549
Pernodet 2006	13	citrate	Human dermal fibroblast	0-4 mM; 24-144 h	13 nm AuNPs $\downarrow$ cell proliferation rate, adhesion and motility
Shukla 2005	3.5	Lysine, poly(lysine)	RAW264.7 mouse macrophage cells	10-100 $\mu$ M ; 24-72 h	3.5 nm AuNPs are not toxic and not immunogenic
Connor 2005	4, 12, 18	CTAB, citrate, cysteine, glucose, biotin	K562 human leukemia	0.001-0.25 $\mu$ M; 72 h	Non toxic effect whatever size
Goodman 2004	2	Quaternary ammonium carboxylic acid	COS-1 mammalian cells, red blood cells	0.38-3 $\mu$ M ; 1-24 h	Cationic 2 nm AuNPs are toxic, while anionic not

Table 4: Illustrative examples of *in vitro* preclinical studies investigating the cytotoxicity of nanospheres gold nanoparticles (AuNPs). TPMS: triphenylphosphine monosulfonate; GSH: glutathione; PEG: polyethylene glycol; TPTS: triphenylphosphine trisulfonate; CTAB: cetyl trimethylammonium bromide; \*Doses are calculated from original papers in term of gold atom concentrations (Adapted from Alkilany 2010).

It is essential to investigate *in vivo* toxicity of AuNPs before any potential therapeutic application. Recent studies have shown the size-dependent biodistribution and toxicity of

AuNPs (Cho 2009). Some AuNPs that didn't appear toxic *in vitro*, showed toxicity *in vivo* (Chen 2009, De Jong 2008, Sonavane 2008, Hillyer 2001). These findings highlight that *in vitro* experiments, may not lead to good predictions regarding *in vivo* results. Moreover, no long-term studies on AuNPs have been reported. Illustrative *in vivo* results of gold nanoparticle cytotoxicity are presented in Table 5.

Author	Size (nm)	Surface group	Animal (n)	Dose (route of administration; time of exposure)	Toxicity results
Chen 2009	3, 5, 8, 12, 17, 37, 50, 100	citrate	Mice (6)	8 mg Au/kg (intraperitoneal; > 1200 h)	Lethalite induced by only 8-37 nm AuNPs
Cho 2009	13	PEG	Mice (9)	Up to 4.26 mg Au/kg (intravenous; up to 168 h)	Liver toxicity: inflammation and apoptosis
Bar-Ilan 2009	3, 10, 50, 100	citrate	Zebrafish (12)	0.25, 2.5, 25, 250 $\mu$ M (exposure in water; 120 h)	No toxicity
Zhang 2009	20, 40, 80	PEG	Mice (8)	34-2210 mg Au/kg (intravenous; 48 h)	Biodistribution and tumour accumulation of AuNPs is size-dependent; smaller NPs have longer blood circulation time and more tumour accumulation
Sonavane 2008	15, 50, 100, 200	citrate	Mice (3)	1000 mg Au/kg (intravenous; 24 h)	All sizes were found in liver, spleen, lung; 15 and 50 nm AuNPs were found also in heart, stomach, kidney, brain
De Jong 2008	10, 50, 100, 250	ND	Rats (4)	77-108 Au/kg (intravenous; 24 h)	Most AuNPs were found in spleen and liver; 10 nm AuNPs were found also in brain, heart, kidney, testis, thymus; no side effects
Kattumuri 2007	15, 20	Arabic gum	Pigs (3)	0.8-1.88 mg Au/kg (intravenous; 0.5-24 h)	Accumulation in lung and liver; no hematological or renal side effects
Hillyer 2001	4, 10, 28, 58	citrate	Mice (ND)	200 mg Au/kg water (oral; 168 h)	Gastrointestinal uptake

Table 5: Illustrative examples of ***in vivo* preclinical studies** investigating the cytotoxicity of nanospheres gold nanoparticles (AuNPs). PEG: polyethylene glycol; ND: not determined; \*Doses are calculated from original papers in terms of gold atom concentrations (Adapted from Alaaldin 2010).

In summary, the complete characterization of size (Pan 2007), shape (Powers 2007), charge (Jiang 2009), surface chemistry (Clift 2008) and material properties seems to be essential for reliable informations about the nanoparticle toxicity. Although AuNPs are known for their good biocompatibility and good synthetic size control, their toxicity is still a concern. The high diversity of AuNPs and the different design of conducted studies might lead to diverging outcomes.



## IV. Radiolabelled antibody-targeted gold nanoparticles

### 1. Synthesis of radiolabelled antibody-conjugated gold nanoparticles

There are two approaches of functionalizing AuNPs with targeting ligands, such as mAbs: the non-covalent and the covalent immobilization techniques (Figure 20). The non-covalent strategy includes the spontaneous physical adsorption of mAbs onto the particle surface. This method involves the passive immobilization of the antibody through two types of interactions: hydrophobic interactions due to the attraction between the hydrophobic sites of the antibody and the gold surface, or through ionic interactions that are formed between the positively charged amino acid groups abundant in mAbs and the negatively charged surface of AuNPs. The covalent coupling strategy involves the conjugation of AuNPs to mAbs using the chemical functions present on specific regions of both mAbs and coated nanoparticle surface (Masereel 2011). The polymer coating enables to modify the nanoparticle surface properties for easy nanoparticle functionalization. It must be mentioned that the properties of the polymer coating and the targeting ligands (mAbs) greatly influence the total particle size, and thus the size distribution *in vivo*. Further, the covalent coupling provides immunonanoconjugates more stable than those obtained using physical adsorption, and prevents the competitive displacement of the adsorbed antibodies (Arruebo 2009, Wilson 2002).

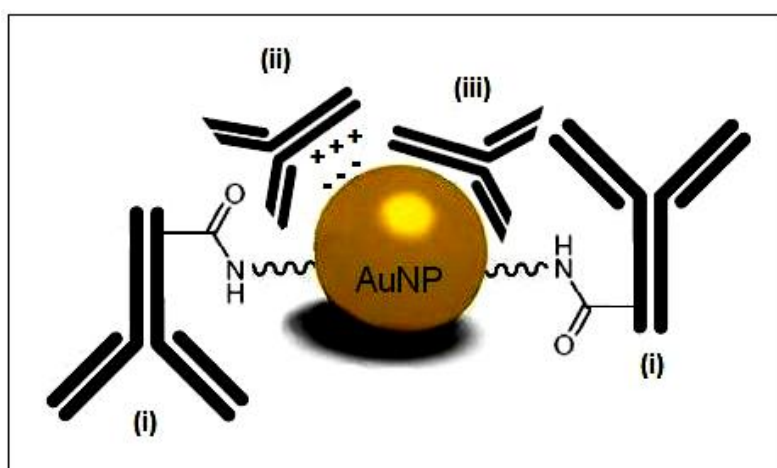


Figure 20: Coupling strategies: covalent coupling immobilization (i), non-covalent electrostatic coupling immobilization (ii) and non-covalent adsorption immobilization (iii).

The common covalent approach used for conjugation of mAbs to AuNPs involves the carbodiimide cross-linking (Hermanson 1996). The EDC\* cross-linker reacts with the carboxylic functions of C-terminal chains of the antibody in the presence of sulfo-NHS<sup>†</sup>, and then condensed with the amino acid end groups of the coating layer, such as PPAA stabilizer layer, to form amine-reactive sulfo-NHS esters. In short, the subsequent addition of gold nanoparticle solution to antibody solution results in coupling between the activated carboxylic functions of mAbs and the primary amines on the nanoparticle surface *via* a covalent amide bond (Thorek 2009) (Figure 21).

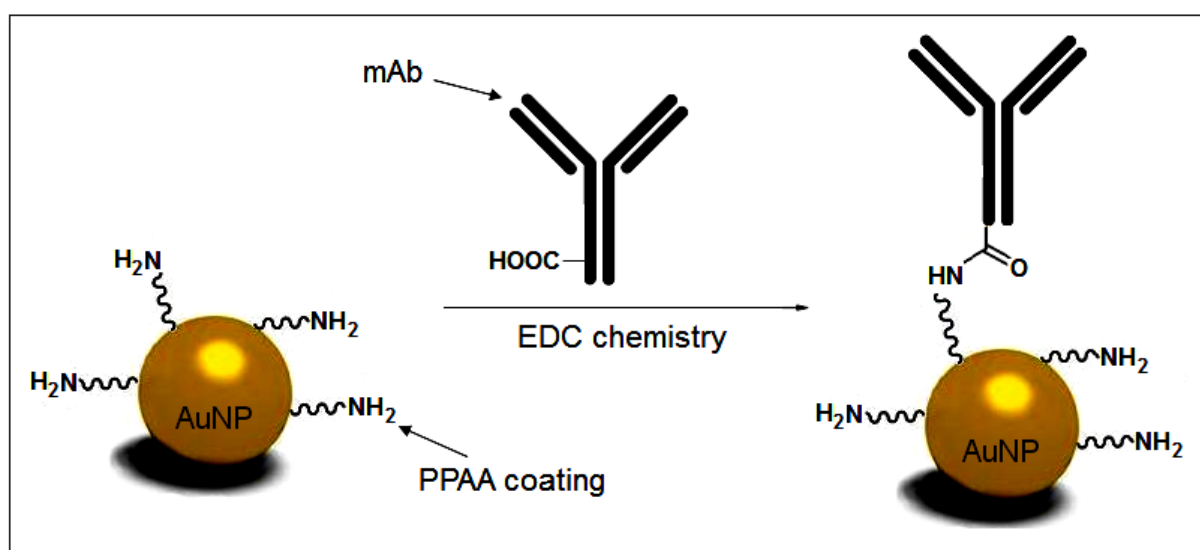


Figure 21: Synthetic pathway of covalent immobilization technique (carbodiimide reaction), resulting in antibody-conjugated gold nanoparticles. The monoclonal antibodies (mAbs) were firstly radiolabelled before their conjugation to coated gold nanoparticles in order to trace these immunonanoconjugates *in vivo*.

## 2. Influence of targeting ligands on tumour uptake of conjugated gold nanoparticles

The surface modification of AuNPs by grafting tumour-targeting molecules, such as mAbs, may improve *in vivo* targeting efficacy. Indeed, monoclonal antibody-targeted nanoparticles may exhibit a focused targeting, and may improve the pharmacokinetic profile of nonfunctionalized nanoparticles, which is dependent on passive EPR effect (Julien 2011). These immunonanoconjugates offer the promise of selective drug delivery to tumour cells, including their internalization within targeted cells (Majidi 2009, Liu 2003) (Figure 22). For

\* EDC : 1-ethyl-3-(3-dimethylaminopropyl) carbodiimide hydrochloride

<sup>†</sup> sulfo-NHS : N-hydroxysulfosuccinimide

instance, cetuximab-conjugated gold nanoparticles may enhance the tumour uptake through antibody-induced EGFR endocytosis (Bhattacharya 2010).

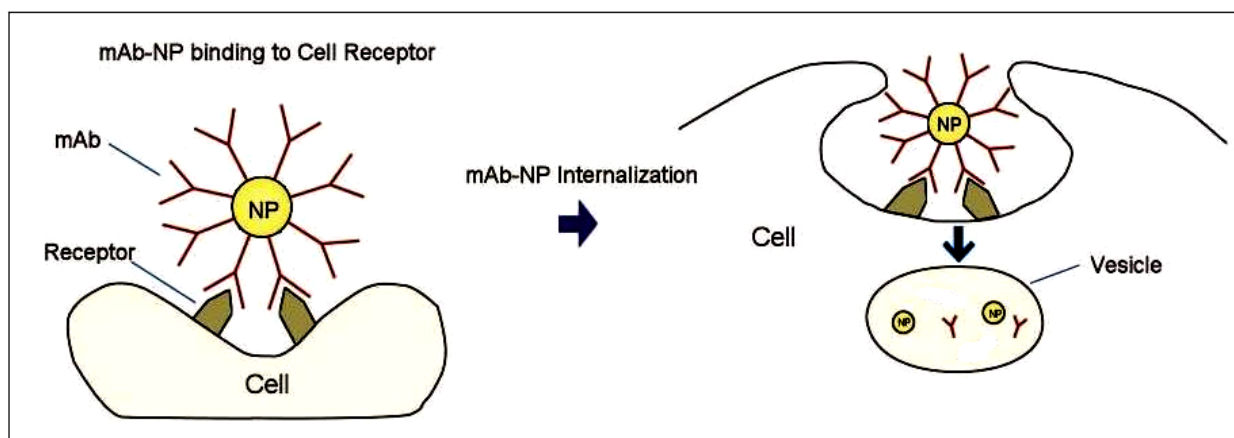


Figure 22: Cellular uptake of monoclonal antibody-conjugated nanoparticle (mAb-NP), which can be recognized by receptors on the cell membrane: internalization of these immunonanoconjugates and their trafficking along intracellular transport pathways (Adapted from Julien 2011).

There is a controversy about the role of targeting ligands in tumour uptake. Previous reports have indicated that the ligands play a role in the selective tumour accumulation of these nanocomplexes through the specific recognition of the tumour target (Pirollo 2008). In this case, the tumour localization of these complexes still depends to the contribution of the EPR effect. However, other papers have suggested that the primary function of targeting ligands was not to improve tumour targeting of these complexes by directing them to the tumour site, but to increase the intracellular uptake of these nanocomplexes (Kirpotin 2006).

In addition, the modified-surface gold nanoparticles may remain in circulation longer than uncoated AuNPs. Therefore, they have more time to accumulate in tumours thanks to the EPR effect, but also take longer to leave the tumour and return in circulation. This extended time of contact with tumour tissue enables more of ligand-grafted gold nanoparticles to bind to tumour cells. Once the functionalized nanoparticles are present in the tumour space, the ligand binds to the tumour receptor target, and thus immobilizing the nanoparticles within the tumour. This is not the case for nonfunctionalized gold nanoparticles, which can rapidly return to the circulation (Pirollo 2008) (Table 6).

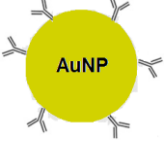
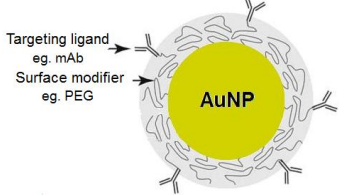
Nanoparticle design	Nanoparticle description	Blood clearance rate	Tumour localization
	“Naked” nanoparticle (no surface modifier, no ligand)	Rapid	Low (some EPR effect)
	Ligand-grafted nanoparticle (no surface modifier)	Rapid	Enhanced, owing to EPR effect and ligand binding to tumour cell receptor
	Surface-modified nanoparticle (eg. PEG)	Extended circulation time	Enhanced, owing to EPR effect and extended time in circulation
	Ligand-grafted and surface-modified nanoparticle (eg. PEG + mAbs)	Extended circulation time	Enhanced, owing to EPR effect, extended time in circulation and ligand binding to tumour cell receptor

Table 6: Surface parameters that influence the pharmacokinetic behaviour and the tumour localization of gold nanoparticles (AuNPs). PEG: polyethylene glycol; mAb: monoclonal antibody; EPR: enhanced permeability and retention (Adapted from Pirollo 2008).

### 3. Potential biomedical applications

Commercial antibodies are already on the market either attached to radioisotopes, such as Zevalin<sup>®</sup> (<sup>90</sup>Y-ibritumomab tiuxetan) for the treatment of NHL, or to drugs, such as Mylortag<sup>®</sup>, which is an antibody-chemotherapeutic conjugate, consisting of a humanized anti-CD33 mouse monoclonal antibody (Gemtuzumab ozogamicin) linked to a potent cytotoxic agent (calicheamicin derivative toxin) for the treatment of acute myeloid leukemia. The strategies to conjugate the mAbs to chemotherapeutic drugs, toxins or therapeutic radioactive isotopes are intended to improve the efficacy of cancer therapy. On the other hand, the strategy to combine gold nanoparticles and antibodies have been developed for diagnostic and therapeutic purposes based on the targeting properties of antibodies and the photophysical properties of AuNPs. Moreover, antibody-targeted gold nanoparticles can offer high molecular specificity. However, to date, there are no commercial antibodies conjugated to nanoparticles applied in therapy (Arruebo 2009). Here, some examples illustrating the potential biomedical applications of antibody-conjugated gold nanoparticles.

➤ *Antibody-conjugated gold nanoparticles for cancer detection*

AuNPs are widely used in optical sensing due to their photophysical properties, and have been used as contrast agents for biomedical imaging. Various immunoassays have been designed using AuNPs functionalized with immunosensors, such as mAbs (Tiwari 2011, Tanaka 2006). For example, an immunoassay using anti-prostate specific antibodies conjugated to AuNPs was developed for the detection of a prostate cancer biomarker (prostate specific antigen, PSA). Indeed, AuNPs was used as optical probes coupled with dynamic light scattering measurements in order to quantify the amount of PSA (Arruebo 2009, Liu 2008). Further, cetuximab-conjugated gold nanoparticles have been developed for optoacoustic imaging using AuNPs as contrast agents (Mallidi 2007). This *in vitro* study makes possible to differentiate cells preincubated with conjugated AuNPs and those preincubated with nonfunctionalized AuNPs (Fay 2011). Moreover, the cancer cells and tissues, which accumulate cetuximab-targeted gold nanoparticles, can also be molecularly imaged, and can be visualized by the SPR scattering of AuNPs through optical microscopy (El-Sayed 2005, Sokolov 2003 [b]). All these findings might offer potential techniques for cancer diagnosis.

➤ *Antibody-conjugated gold nanoparticles for cancer therapy*

Antibody-targeted gold nanoparticles may be used for therapeutic purposes, such as photothermal therapy, as drug delivery carriers and as sensitizers in radiation therapy. For instance, *in vitro* studies demonstrated the selective thermoablation of cancer cells, which accumulate cetuximab-conjugated gold nanoparticles, and after exposure to the visible laser. The method is selective since the malignant human head and neck cancer cells required less than half the laser energy to be killed, as compared with the benign cells. In addition, no photothermal destruction was observed for cells without nanoparticle labelling, even at four times the energy required to kill the labelled malignant cells (El-Sayed 2006). The selective photodamage of cancer cells is a result of the high functionalized nanoparticle loading in cancer cells overexpressing EGFR. This selective technique can be used for a variety of cancers by conjugating AuNPs with various antibodies specific to a particular cancer (Huang 2007, Huang 2006 [b]). Moreover, *in vitro* studies investigated the efficacy of tumour targeting by these immunonanoconjugates, compared with that of unconjugated nanoparticles. Cetuximab-conjugated gold nanoparticles were internalized by pancreatic and colorectal cancer cells expressing EGFR. The cells were then treated with noninvasive RF energy,

which causes a heat production from AuNPs, resulting in cell death (Curley 2008). More recently, *in vivo* explorations in mice have shown that cetuximab-conjugated gold nanoparticles may be associated with nonionizing radiofrequency radiation to specifically target and kill cells overexpressing EGFR. While the therapy is dependent on the specificity of the targeting antibody, normal tissues were spared despite systemic therapy and whole-body RF field exposure (Glazer 2010 [a]).

On the other hand, *in vitro* and *in vivo* studies demonstrated the targeting efficacy of AuNPs used as vehicles for anticancer chemotherapeutic (gemcitabine) and targeting agent (cetuximab), and showed cell proliferation inhibition of pancreatic cancer cells expressing EGFR after treating mice with gold nanoparticles conjugated with both cetuximab and gemcitabine, compared to mice receiving gemcitabine alone (Patra 2008). Finally, *in vivo* studies have investigated the potential utility of unconjugated gold nanoparticles for cancer radiotherapy and showed that AuNPs enhance the radiation therapy efficacy (Hainfeld 2010, Chang 2008, Hainfeld 2004). Given that nanoparticle conjugation with targeting antibodies can improve the tumour targeting, future studies using these conjugates for radioenhancement purposes might be promising.

These applications highlighted the interest of gold nanoparticle vectorization for improving the efficacy of cancer detection and therapy, compared with nonfunctionalized gold nanoparticles. However, no studies have investigated the preservation of the recognition properties of the targeting ligands after the nanoparticle conjugation. Indeed, the immunotargeting approach may be limited by pharmacokinetic and immunological aspects. Therefore, these more fundamental aspects of using mAbs as targeting agent need to be explored in order to investigate the influence of the structural modulations of antibodies on their biological properties.

## **Chapter 2: Aims of the thesis**

Gold nanoparticles conjugated to antibodies have been recently suggested as an interesting strategy to improve the management of cancer. Indeed, recent advances have shown that the functionalization of gold nanoparticles with antibodies enables to combine the targeting properties of mAbs and the photophysical properties of AuNPs, with improving targeted delivery of nanoparticles. **The originality of this work is to address the question of how the nanoparticle conjugation to specific mAbs affects the antibody properties, and particularly the antibody specificity. The answer to this question requires accurate characterization of such immunonanoconjugates *in vitro* and *in vivo*.** These aspects have been yet poorly documented. Our goal was not to demonstrate that the antibody conjugation to gold nanoparticles improves the pharmacokinetics of nanoparticles. Previous studies have demonstrated the interest of active targeting through grafting mAbs on nanoparticle surface and the specific concentration of these immunonanoconjugates in the tumour site. Furthermore, many studies have described the biological distribution of various gold nanoparticles according to their size, shape and surface charge, but few reports are available about the biodistribution profile of antibody-functionalized nanoparticles. **For this purpose, the aim of this work was to investigate the impact of nanoparticle conjugation to antibodies (cetuximab and anti-endoglin mAbs) on their target recognition properties and on their biodistribution profile.** For conjugation reaction to gold nanoparticles, we chose cetuximab (Erbix<sup>®</sup>), a known human monoclonal antibody, which is approved for the treatment of colorectal and head and neck cancers, and the antiangiogenic anti-CD105 monoclonal antibodies. In order to trace these immunonanoconjugates *in vivo*, the antibodies were firstly radiolabelled with <sup>125</sup>I or <sup>89</sup>Zr before nanoparticle conjugation.

This thesis was actually a part of a broader project named “TARGAN”. The main goal of this project was to develop AuNPs doped with several radionuclides through PVD process. These nanoparticles were functionalized with mAbs for targeting a specific tumour marker. The obtained nanometric sized conjugates might have a high specific activity, which enables to improve the detection threshold for imaging, and the delivered local dose for therapy. Several groups collaborated as part of this interuniversity project between UCL and University of Namur:

- The research centre for the physics of matter and radiation (PMR-LARN-University of Namur-NARILIS, Professor S. Lucas) for synthesis and characterization of gold nanoparticles.
- The pharmacology and therapeutics unit (FATH-UCL, Professor O. Feron) for anti-endoglin antibody production and purification, as well as for the screening of tumour models. Preliminary studies validated that endoglin is interesting as a tumour vascular target.

- 
- The Namur research college and department of chemistry (NARC-University of Namur, Professor D. Bonifazi) and the department of pharmacy (University of Namur, Professor B. Masereel) for optimizing the antibody-nanoparticle conjugation reaction.
  - The research unit of cell biology (URBC-University of Namur-NARILIS, Professor C. Michiels) for *in vitro* toxicity assessment of gold nanoparticles.
  - The specific task of our group was to explore the value of these immunonanoconjugates in animal models, particularly in terms of tumour uptake.
  - Finally, the clinical assessment of these immunonanoconjugates is planned (Division of Nuclear Medicine of Mont-Godinne University Hospital-NARILIS-MIRO, Professor T. Vander Borgh).

In this context, the present thesis addressed the question of how nanoparticle conjugation to antibodies affects the antibody properties *in vitro* and *in vivo*, especially the impact on tumour targeting. The steps of this work were divided into three parts:

- The first part focuses on radiolabelling of antibodies before coupling them to gold nanoparticles. This step enables to optimize the radiolabelling conditions of mAbs and their purification. We characterized radiolabelled mAbs before and after the nanoparticle conjugation in terms of radiolabelling yield, radiochemical purity, substitution rate with radionuclides, antibody integrity, coupling reaction yield and *in vitro* stability over time, including the stability in plasma.

Introducing structural changes to mAbs may hamper their ability to recognize their target and their pharmacokinetic behaviour.

- The second part was thus dedicated to the assessment of the antibody recognition properties after the nanoparticle conjugation by *in vitro* cell-based ELISA tests and through *in vivo* blocking experiments.
- The third part investigated the biodistribution profiles of radiolabelled mAbs before and after the nanoparticle conjugation. According to the radiolabel ( $^{125}\text{I}$  and  $^{89}\text{Zr}$ ), we studied *in vivo* distribution of the tracers in different organs, with a focusing on tumour uptake, and through *ex-vivo* studies, imaging techniques (SPECT/CT and PET/CT), and ICP-MS analysis for gold quantification (Appendix 5).

Overall, the ultimate objective of this work was to qualify the cetuximab- and anti-endoglin antibody-functionalized gold nanoparticles as new tools for imaging of cancer, prior to considering using them for therapeutic purposes. Therefore, it is important to provide first answers to fundamental questions such as:

- What is *in vivo* behaviour of such immunonanoconjugates?
- What is the effect of nanoparticle conjugation on the antibody efficacy in tumour targeting?
- Does these immunonanoconjugates are efficient for cancer imaging, and could we expect a final therapeutic benefit?



## **Chapter 3: RESULTS**

---

Results are presented in four chapters and are detailed as scientific publications

## **I. Targeting cancer cells using <sup>125</sup>I-labelled anti-EGFR antibody-conjugated gold nanoparticles**

The first study characterized the produced gold nanoparticles (size and morphology), the iodinated antibodies (integrity after radiolabelling, substitution rate and *in vitro* stability), and the cetuximab-conjugated gold nanoparticles (number of antibodies grafted per nanoparticle and *in vitro* specificity), and compared the biodistribution profiles of <sup>125</sup>I-labelled cetuximab before and after the nanoparticle conjugation.

**Antibody-functionalized polymer-coated gold nanoparticles targeting cancer cells: an *in vitro* and *in vivo* study**

Riccardo Marega<sup>†</sup>, **Linda Karmani**<sup>†</sup>, Lionel Flamant<sup>†</sup>, Praveen Ganesh Nageswaran, Vanessa Valembois, Bernard Masereel, Olivier Feron, Thierry Vander Borgh, Stephane Lucas, Carine Michiels, Bernard Gallez and Davide Bonifazi.

*J Mater Chem.* 2012;22:21305-21312.

---

<sup>†</sup> These authors equally contributed to this work.



# Journal of Materials Chemistry

Cite this: *J. Mater. Chem.*, 2012, **22**, 21305

www.rsc.org/materials

PAPER

## Antibody-functionalized polymer-coated gold nanoparticles targeting cancer cells: an *in vitro* and *in vivo* study

Riccardo Marega,<sup>†a</sup> Linda Karmani,<sup>†b</sup> Lionel Flamant,<sup>†c</sup> Praveen Ganesh Nageswaran,<sup>a</sup> Vanessa Valembois,<sup>d</sup> Bernard Masereel,<sup>e</sup> Olivier Feron,<sup>f</sup> Thierry Vander Borcht,<sup>f</sup> Stephane Lucas,<sup>\*d</sup> Carine Michiels,<sup>\*c</sup> Bernard Gallez,<sup>\*h</sup> and Davide Bonifazi<sup>\*ag</sup>

Received 30th May 2012, Accepted 29th July 2012

DOI: 10.1039/c2jm33482h

Gold nanoparticles (~5 nm) coated with plasma-polymerized allylamine were produced through plasma vapor deposition and bioconjugated with a monoclonal antibody targeting the epidermal growth factor receptor. The resulting nanoconjugates displayed an antibody loading of about 1.7 nmol mg<sup>-1</sup> and efficiently target epidermal growth factor receptor overexpressing cell lines, as ascertained by ELISA and Western blot assays. The *in vitro* targeting properties were also confirmed *in vivo*, where a similar biodistribution profile of what was experienced for the unconjugated antibody was observed. Thanks to the possibility of doping the gold nanoparticles with radionuclides during plasma vapor deposition, the proposed functionalization strategy represents a very suitable platform for the *in vivo* cancer targeting with nanosized multifunctional particles.

### Introduction

Among the different technological fields, gold nanostructures such as particles,<sup>1</sup> rods,<sup>2</sup> nanoshells<sup>3</sup> and nanocubes<sup>4</sup> have thoroughly been investigated for biomedical purposes.<sup>5,6</sup> In fact, thanks to their tuneable size, shape and optical absorption properties,<sup>5,7</sup> along with good biocompatibility profiles,<sup>8</sup> these nanomaterials have been proposed as sensors,<sup>9</sup> imaging<sup>10</sup> and drug-delivery platforms.<sup>11–13</sup> Most of these applications require

surface modification of Au nanostructures, which can be easily done either through adsorption of (bio)molecules bearing thiol or amino functional groups,<sup>14</sup> or by polymer coating.<sup>15</sup> In some instances, the resulting nanomaterials showed improved water dispersability/solubility properties, therefore the assessment of the interaction of such functional nanostructures with living systems is of paramount importance for both biological properties and safety evaluation.<sup>13</sup> Both the assessment of biodistribution profiles and toxicity of naked or functionalized gold nanostructures has become a field of intensive research,<sup>16</sup> as recently summarized in an excellent review by Khlebtsov and Dykman.<sup>17</sup> It is clear that the biodistribution profiles depend on several factors, such as particle shape, size and surface coating properties, each one affecting the resulting pharmacokinetic profile.<sup>17</sup> One of the major fields of research for application of gold nanoparticles (AuNPs) is cancer treatment, where a selective accumulation of (multi)functional nanomaterials in the tumor is desired. In this respect, several reports about nanoparticle surface modifications aimed at cancer targeting have been reported in the last few years,<sup>18</sup> among others, those describing antibody-coupling represent a major interest.<sup>19,20</sup> In particular, antibodies (Abs) targeting the epidermal growth factor receptor (EGFR),<sup>21</sup> a membrane protein overexpressed in several kinds of solid tumors, have been conjugated to AuNPs and efficiently employed for imaging,<sup>19,22</sup> photothermal treatment<sup>23</sup> and drug delivery.<sup>12,24</sup> Additionally, it has been shown that this “nanoconjugation” uniformly enhances the antibody-induced EGFR endocytosis for several cancer cell lines.<sup>25</sup> Aiming at maximizing the cancer uptake of such nanoconjugates, it is of great importance to determine the biodistribution of antibody-functionalized AuNPs (AuNPs-Ab) in murine models

<sup>a</sup>Namur Research College (NARC) and Department of Chemistry, University of Namur (FUNDP), Rue de Bruxelles 61, 5000 Namur, Belgium. E-mail: davide.bonifazi@fundp.ac.be

<sup>b</sup>Biomedical Magnetic Resonance Unit (REMA), Louvain Drug Research Institute, University of Louvain (UCL), Place de l'Université 1, 1348 Louvain-la-Neuve, Belgium. E-mail: bernard.gallez@uclouvain.be

<sup>c</sup>Unité de Recherche en Biologie Cellulaire (URBC), Namur Research Institute for Life Sciences (NARILIS), University of Namur (FUNDP), Rue de Bruxelles 61, 5000 Namur, Belgium. E-mail: carine.michiels@fundp.ac.be

<sup>d</sup>Research Centre for the Physics of Matter and Radiation (PMR-LARN), Namur Research Institute for Life Sciences (NARILIS), University of Namur (FUNDP), Rue de Bruxelles 61, 5000 Namur, Belgium. E-mail: stephane.lucas@fundp.ac.be

<sup>e</sup>Department of Pharmacy, Namur Medicine & Drug Innovation (NAMEDIC), Namur Research Institute for Life Sciences (NARILIS), University of Namur (FUNDP), Rue de Bruxelles 61, 5000 Namur, Belgium. E-mail: bernard.masereel@fundp.ac.be

<sup>f</sup>Institut de Recherche Expérimentale et Clinique (IREC), University of Louvain (UCL), Place de l'Université 1, 1348 Louvain-la-Neuve, Belgium. E-mail: olivier.feron@uclouvain.be; thierry.vanderborcht@uclouvain.be

<sup>g</sup>Department of Chemical and Pharmaceutical Sciences, University of Trieste, Piazzale Europa 1, Trieste, 34127, Italy

<sup>†</sup> These authors equally contributed to this work.

xenografted with human cancers. Thus, in the present work, we took advantage of the amino functionalities exohedrally exposed on relatively small sized ( $\sim 5$  nm) polymer-coated AuNPs (AuNPs-PPAA), synthesized through simultaneous plasma vapor deposition of Au (core) and allylamine (which leads to a plasma-polymerized-allylamine shell, PPAA),<sup>26</sup> to covalently immobilize *via* an amide linkage an EGFR-targeting Ab Cetuximab,<sup>27</sup> either in its native or <sup>125</sup>I-radiolabelled form. The resulting nanoconjugates have been thus tested to assess EGFR targeting both *in vitro* and *in vivo* murine models. *In vitro* studies showed the preferential binding of the nanoconjugate to EGFR overexpressing cancer cells (A431), with very low aspecific binding to EGFR non expressing cell lines (CHO and EAhy926), and the blocking of the EGF-induced biochemical effects, as assessed through Western blot analysis. *In vivo* results showed that tumor uptake was not significantly different between free and nanoconjugated Cetuximab, highlighting the preservation of antibody recognition after the bioconjugation step.

## Results and discussion

### AuNPs-PPAA synthesis and bioconjugation with Ab and Ab-<sup>125</sup>I

Fig. 1 reports the synthetic pathway toward the preparation of the bioconjugates between AuNPs-PPAA and purified Cetuximab, either in its native (Ab) or <sup>125</sup>I-bearing form (Ab-<sup>125</sup>I), generating AuNPs-PPAA-Ab and AuNPs-PPAA-Ab-<sup>125</sup>I, respectively. The amino groups present in the polymeric shell of AuNPs-PPAA were exploited for amide bond formation with carboxyl groups located on Cetuximab, through carbodiimide chemistry in buffer solution (Fig. 1a). By repeating the same reaction, but without the use of the carbodiimide, a physical mixture between AuNPs-PPAA and Cetuximab (AuNPs-PPAA/Ab) was also prepared, as a reference compound (Fig. 1b).

To determine both morphology and size distribution of the pristine nanostructures, AuNPs-PPAA were directly deposited onto a TEM grid, revealing the presence of spherical objects with an average size between 3 and 5 nm (Fig. 2a). After a diafiltration step, necessary to remove excess, unbound PPAA left from PVD cycles, spherical objects with diameters ranging from 3 to 15 nm

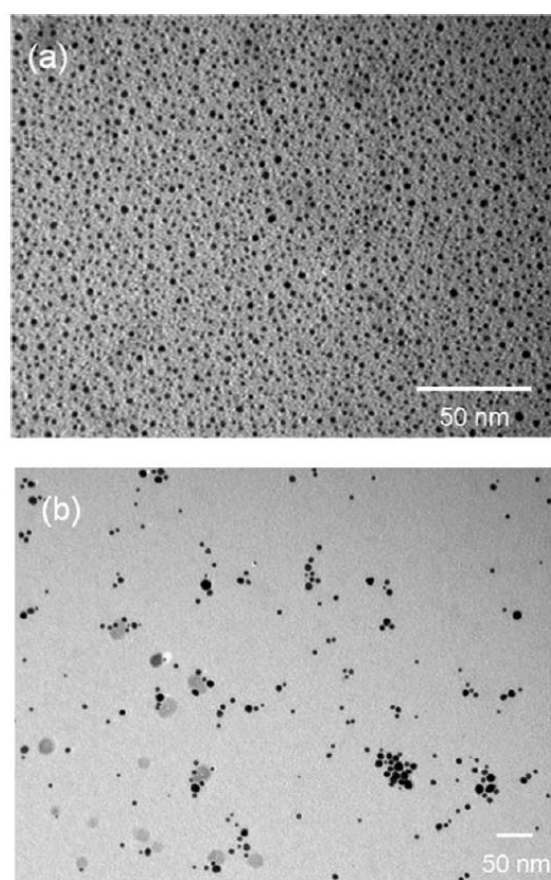


Fig. 2 Bright-field TEM images of AuNPs-PPAA on Cu grids: (a) as produced and (b) after dispersion and diafiltration.

(mean =  $4.83 \pm 1.69$  nm, Fig. 2b), as a consequence of occasional AuNPs agglomeration induced by the diafiltration process, were clearly detected by TEM imaging. Diafiltered samples containing

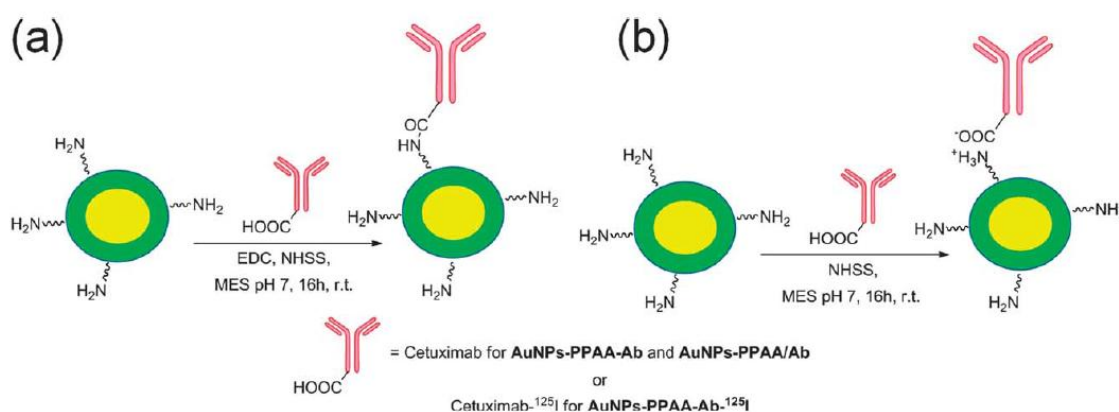
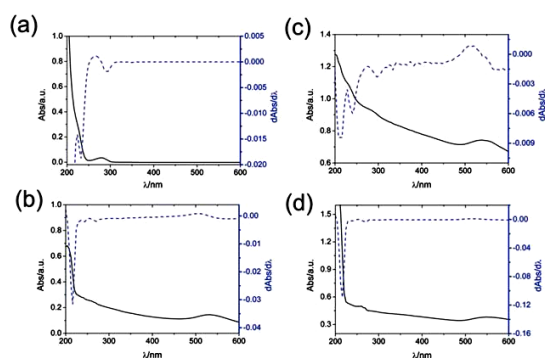


Fig. 1 Synthetic pathway for the synthesis of covalent AuNPs-PPAA-Ab (a) and physisorbed AuNPs-PPAA/Ab bioconjugates (b). Yellow: AuNPs, green: PPAA coating. EDC = 1-Ethyl-3-(3-dimethylaminopropyl)carbodiimide hydrochloride, NHSS = *N*-Hydroxysulfosuccinimide sodium salt and MES = 2-(*N*-morpholino)ethanesulfonic acid.



**Fig. 3** Steady-state UV-Vis absorption spectra (—) and derivative plots (dAbs/dλ, ---) for Ab (a), AuNPs-PPAA (b), AuNPs-PPAA-Ab (c) and AuNPs-PPAA/Ab (d).

AuNPs-PPAA-Ab, AuNPs-PPAA/Ab and reference starting materials (*i.e.*, AuNPs and Ab) were first analyzed by steady-state UV-Vis spectroscopy (Fig. 3). The absorption spectrum of Cetuximab shows the typical proteinic signature at 280 nm, which belongs to the aromatic groups-bearing aminoacidic residues (*i.e.*, phenylalanine, tyrosine, tryptophane and histidine), and the peptidic feature at 220 nm, as also clearly displayed in the dAbs/dλ plot (Fig. 3a). On the other hand, the AuNPs-PPAA absorption spectrum shows a surface plasmon absorption feature at 530 nm, characteristic of small-sized AuNPs,<sup>7</sup> and then a steady absorbance increase towards the UV region, the latter providing a characteristic peak centered at 208 nm in the dAbs/dλ plot (Fig. 3b). The dAbs/dλ plot for samples containing AuNPs-PPAA-Ab clearly shows a very good overlap with both Cetuximab- and AuNPs-PPAA-centered signatures (Fig. 3c), suggesting the simultaneous presence of the two moieties in the bioconjugate and thus their covalent linkage.

In contrast, the dAbs/dλ plot for AuNPs-PPAA/Ab only shows the presence of the AuNPs-PPAA-centered features (Fig. 3d), thus suggesting the efficient elimination of the non-covalently linked Ab counterpart by discontinuous diafiltration.

To evaluate AuNPs-PPAA-Ab composition, thermogravimetric analysis under inert atmosphere was carried out (Fig. 4). Under these conditions we expected to determine the pyrolytic

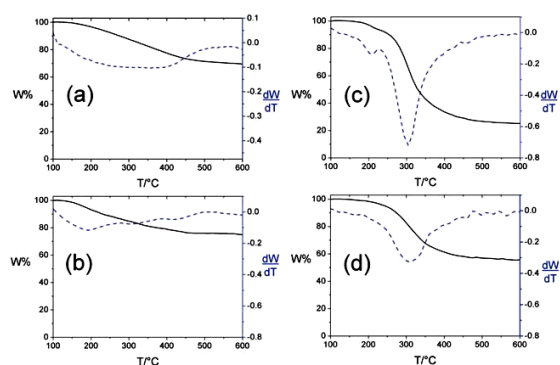


**Fig. 4** Temperature-modulated (—) and derivative (dW/dT, ---) plots of PPAA (a), AuNPs-PPAA (b), Ab (c) and AuNPs-PPAA-Ab (d), recorded under N<sub>2</sub> atmosphere.

behaviour of the single components (Ab, PPAA and AuNPs) constituting the bioconjugate AuNPs-PPAA-Ab. PPAA (Fig. 4a) showed a main pyrolysis event in the range between 100 and 500 °C, with a weight loss at 600 °C of 30.53 wt%. AuNPs-PPAA also showed a main pyrolysis occurring between 100 and 500 °C, with a weight loss at 600 °C of 25.30 wt% (Fig. 4b). Since Au has a high thermal stability (melting point at about 1060 °C), we can assume that the observed weight loss in AuNPs-PPAA is due to the decomposition of the PPAA layer, allowing for compositional estimation that gives 17.13 and 82.87 wt% for Au and PPAA, respectively. By looking at Ab pyrolysis behaviour (Fig. 4c), there is also a weight loss in the range between 100 and 500 °C, with a clear maximum at about 300 °C (Ab decomposition thermal signature) and a related weight loss of 74.92 wt% at 600 °C.

AuNPs-PPAA-Ab conjugate plots (Fig. 4d) showed the thermal signature of Ab decomposition at about 300 °C, further suggesting that the Ab coupling has occurred, and an increased weight loss of 19.23 wt% compared to AuNPs-PPAA. Considering the residual weights observed for each compound at 600 °C (74.70 wt% for AuNPs-PPAA, 25.08 wt% for Ab) and the additional weight loss after Ab immobilization, it is possible to estimate the AuNPs-PPAA-Ab composition, which was 12.73 wt% for Au, 61.60 wt% for PPAA and 25.67 wt% for Ab (*i.e.*, about 1.7 nmols of Ab per mg of material).

For the preparation of AuNPs-PPAA-Ab-<sup>125</sup>I a known radiolabeling procedure based on the Iodo-Gen method was employed. The radioiodination yield for Ab was typically 70–80%, whereas the radiochemical purity immediately after purification was greater than 99%. The resulting specific activity was 7.4 kBq per μg Ab. The <sup>125</sup>I-to-Ab ratio was about 0.014, which means that roughly one out of seventy Ab carries one <sup>125</sup>I atom. Samples were stored several days at 4 °C and analyzed for overall *in vitro* stability. The amount of free iodide in purified Ab-<sup>125</sup>I remained below 2% even after 25 days at 4 °C.

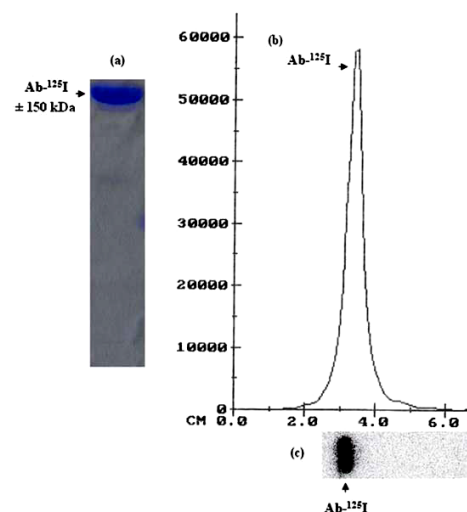


**Fig. 5** Electrophoresis gel profile of Ab-<sup>125</sup>I using SDS-PAGE 8% under non-reducing conditions (a). The migration gel was scanned by a Bioscan (b) and Phosphor Imager (c).

**Table 1** Measured radioactivity of aliquots (1 mL) of the conjugate at various time intervals

$t$ (h)	Measured activity <sup>a</sup> (csec <sup>-1</sup> )	$V_{\text{tot}}$ (mL)	Activity (csec <sup>-1</sup> )
$t_0$	133	6.4	851
$t_{1\text{h}}$	85.4	9.4	803
$t_{24\text{h}}$	11.8	9.4	111
$t_{\text{Final}}$	24.7	5.0	125

<sup>a</sup> As the purification through diafiltration proceeded, a reduction of radioactivity due to  $\text{Ab-}^{125}\text{I}$  elimination occurred, until a steady value of radioactivity ( $t_{\text{Final}}$ ), consistent with partial  $\text{Ab-}^{125}\text{I}$  immobilization, was assessed.

Electrophoresis of  $\text{Ab-}^{125}\text{I}$  under non-reducing conditions followed by autoradiography showed the 150 kDa Ab band and a single peak of radioactivity (Fig. 5), which means that antibody integrity remained preserved after the labelling procedure.

The conjugation reaction between  $\text{AuNPs-PPAA}$  and  $\text{Ab-}^{125}\text{I}$  was then performed under the same conditions as those employed for unlabeled Cetuximab (Fig. 1a). Reaction progress was monitored by measuring the total activity (csec<sup>-1</sup>) of aliquots sampled at periodic intervals (Table 1), which allowed estimating an  $\text{Ab-}^{125}\text{I}$  immobilization efficiency of about 20%.

#### *In vitro* evaluation of EGFR targeting

At first, the relative binding affinity of  $\text{AuNPs-PPAA-Ab}$  toward an EGFR overexpressing cell line has been determined by a cell based ELISA study. To this aim, we have selected the A431 cell line, since these cells express high amounts of EGFR (EGFR+).<sup>28</sup> As a negative control, cells that do not express EGFR, Chinese hamster ovary (CHO) cells, have been selected (EGFR-). Consequently, different concentrations of Ab and of  $\text{AuNPs-PPAA-Ab}$  were tested both on EGFR+ and EGFR- cells (Fig. 6). As expected, Ab bound to EGFR+ cells in a concentration-dependent manner, but not to EGFR- cells. Interestingly,  $\text{AuNPs-PPAA-Ab}$  also bound to EGFR+ cells in a concentration-dependent way, suggesting the retention of the correct Ab conformation for the epitope selection and interaction in  $\text{AuNPs-PPAA-Ab}$  conjugates. A very slight unspecific binding of

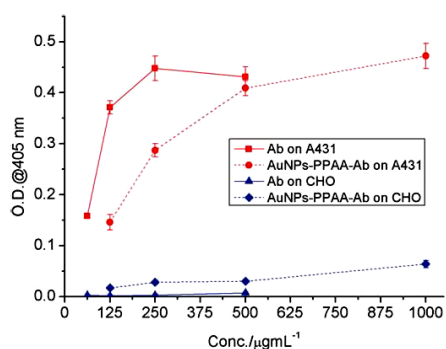


**Fig. 6** Surface ELISA for Ab and  $\text{AuNPs-PPAA-Ab}$  on EGFR+ (A431) and EGFR- (CHO) cells. Different concentrations of Ab and of  $\text{AuNPs-PPAA-Ab}$  were tested. The concentrations are expressed as  $\mu\text{g}$  of Ab per mL. Results are presented as means  $\pm$  1 S.D. ( $n = 4$ ).

$\text{AuNPs-PPAA-Ab}$  to EGFR- cells was also observed. Similar results were obtained for another EGFR- cell line, EAhy926 endothelial cells (data not shown).

From the concentration-dependent ELISA outcomes, binding affinity toward A431 cells was quantified. Half maximal effective concentration ( $\text{EC}_{50}$ ) for Ab was estimated as  $0.08 \mu\text{g mL}^{-1}$ , while the  $\text{EC}_{50}$  for  $\text{AuNPs-PPAA-Ab}$  was  $0.19 \mu\text{g mL}^{-1}$ . For the same number of antibody molecules, the spatial distribution is constrained around NPs for NP-coupled Ab in comparison to free Ab so that not all the Ab molecules are available to recognize the antigen that is distributed on the monolayer cell surface. This could explain the apparent lower affinity of the Ab when coupled to the NPs.

We then determined the capability to inhibit the EGF-induced phosphorylation of EGFR (at tyrosine 1173) through phosphorylation assays and subsequent Western Blot Analysis. Serum-starved cells (24 hours) were incubated with or without Ab or  $\text{AuNPs-PPAA-Ab}$  for 7 minutes before being stimulated or not with  $10 \text{ ng mL}^{-1}$  EGF for 10 minutes. As expected EGF stimulates EGFR phosphorylation, an effect that was inhibited if cells were pre-incubated with Ab. Negative results were obtained for both CHO and EAhy926 cells (EGFR-). Fig. 7 shows that such a competition was also observed in the presence of  $\text{AuNPs-PPAA-Ab}$ . All these binding results shows that, although slightly reduced compared to Cetuximab alone, the Ab affinity after immobilization onto  $\text{AuNPs-PPAA}$  is qualitatively preserved.

#### *In vivo* assessment of EGFR targeting

EGFR targeting was studied in NMRI nude mice bearing A431 epidermoid carcinoma tumors. Comparative pharmacokinetic

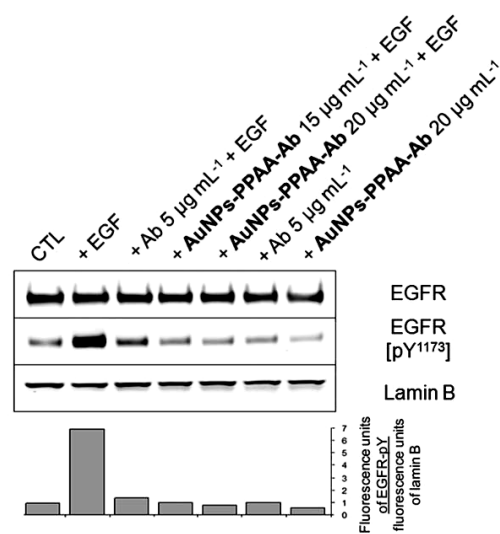


**Fig. 7** Inhibition of EGF-induced phosphorylation of EGF receptors by Ab or  $\text{AuNPs-PPAA-Ab}$ . A431 cells were incubated with Ab or  $\text{AuNPs-PPAA-Ab}$  for 7 min before being stimulated with  $10 \text{ ng mL}^{-1}$  EGF for 10 min. Lysates were separated by electrophoresis and analyzed by Western blotting using anti-EGFR or anti-phospho-EGF receptor (Tyr1173) antibodies. Lamin B was used as the loading control. The ratio between fluorescent intensity of the bands corresponding to phospho-EGFR and to Lamin B was calculated for each lane.

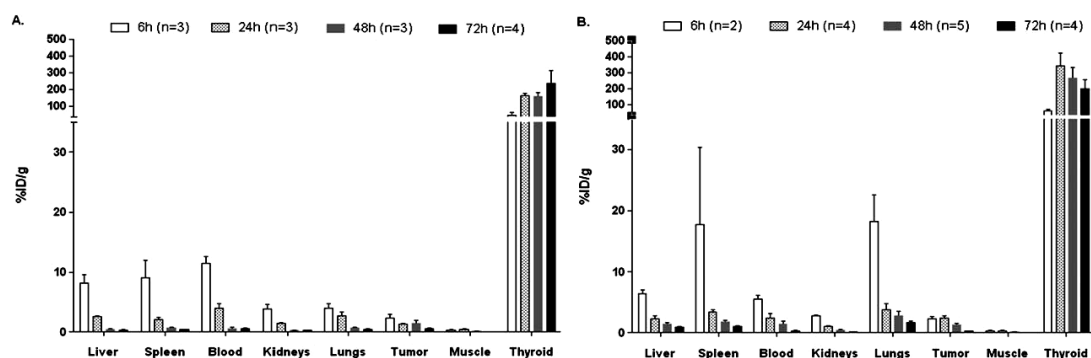


Fig. 8 Biodistribution of 60 kBq of Ab-<sup>125</sup>I (A) or AuNPs-PPAA-Ab-<sup>125</sup>I (B) (13.5–16 μg) in nude mice bearing A431 tumors at 6, 24, 48 and 72 h after injection. Columns, mean %ID per g normal tissue and tumor; bars, SEM ( $n = 2-5$ ).

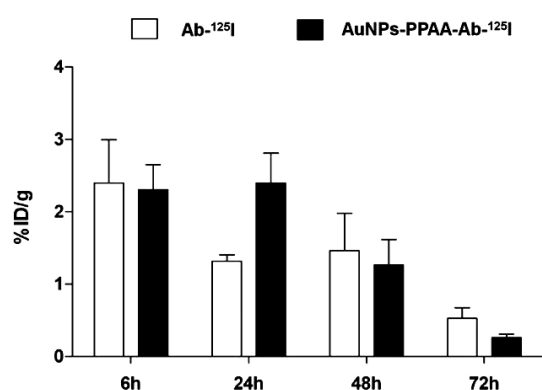


Fig. 9 Tumor uptake of 60 kBq of Ab-<sup>125</sup>I or AuNPs-PPAA-Ab-<sup>125</sup>I (13.5–16 μg) in nude mice bearing A431 tumors at 6, 24, 48 and 72 h after injection. Columns, mean; bars, SEM ( $n = 2-5$ ).

assessment of both Ab-<sup>125</sup>I and AuNPs-PPAA-Ab-<sup>125</sup>I was evaluated by *ex vivo* biodistribution studies. The biodistribution data are presented in Fig. 8. At each time post-injection, radioactivity uptake levels in tumors were not significantly different between

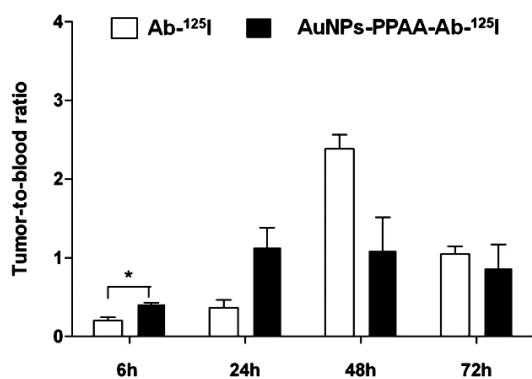


Fig. 10 Tumor to blood ratios of 60 kBq of Ab-<sup>125</sup>I or AuNPs-PPAA-Ab-<sup>125</sup>I (13.5–16 μg) in nude mice bearing A431 tumors at 6, 24, 48 and 72 h after injection. Columns mean; bars, SEM ( $n = 2-5$ ). \* $P < 0.05$ , significant differences between Ab-<sup>125</sup>I and AuNPs-Ab-<sup>125</sup>I.

the conjugates (Fig. 9). The highest tumor-to-blood ratio was observed after 48 h for both groups and was respectively  $2.38 \pm 0.18$  for Ab-<sup>125</sup>I and  $1.10 \pm 0.42$  for AuNPs-PPAA-Ab-<sup>125</sup>I.

Tumor-to-blood ratios were not significantly different between the two groups except at 6 h post-injection (Fig. 10). This difference can be explained by the blood pool activity that is significantly different between the two groups at early time. The most remarkable differences between both biodistribution patterns were observed for uptake in lungs, spleen and liver. At 6 h pi., lungs and spleen uptake levels were  $3.98 \pm 0.83$  and  $9.13 \pm 2.91$  for Ab-<sup>125</sup>I, and  $18.25 \pm 4.34$  and  $17.80 \pm 12.64$  for AuNPs-PPAA-Ab-<sup>125</sup>I, respectively. For liver, these values were  $8.18 \pm 1.39$  and  $6.42 \pm 0.61$  for Ab-<sup>125</sup>I and AuNPs-Ab-<sup>125</sup>I, respectively. Uptake levels in kidneys, thyroid and skeletal muscles were similar for both radioimmunoconjugates. The reticuloendothelial system uptake is more important for AuNPs-PPAA-Ab-<sup>125</sup>I than Ab-<sup>125</sup>I. This may explain the lower blood activity at early times. For all normal tissues (liver, spleen, kidneys, lungs and muscles), there is no specific uptake or accumulation of AuNPs-PPAA-Ab-<sup>125</sup>I compared to the control group. The radioactivity level decreased over time.

Very interestingly, despite the small decrease in binding capacity of AuNPs-PPAA-Ab-<sup>125</sup>I to the EGFR target, tumor uptake was not significantly different between the two groups. Data thus indicate that coupling nanoparticles to Cetuximab does not seem to affect the pharmacokinetic behaviour of the antibody, and particularly the tumor uptake. Therefore, an antibody conjugated to gold nanoparticles seems to maintain its targeting activity towards EGFR over-expressed on tumor cells. Nonetheless, the high thyroid uptake means an *in vivo* deiodination related to the degradation of Ab-<sup>125</sup>I, which induces a rapid free iodine clearance and a low tumor contrast expressed as a tumor-to-blood ratio.<sup>29</sup> This chemical instability may lead to errors in the estimation of the actual antibody tumor uptake.

## Conclusions

Polymer-coated AuNPs have been efficiently produced by plasma vapor deposition, through an automated batch wise procedure, and subsequently covalently decorated with native or radioiodinated Cetuximab through amide bond formation reaction. The resulting bioconjugates selectively target EGFR

overexpressing cell lines, allowing for the *in vitro* binding of cancer-like cells, as evaluated by ELISA and Western blot analysis after phosphorylation studies. Although the occurrence of the parasite deiodination of the radiolabeled Cetuximab, as detected by high thyroid uptake, certainly affects (*i.e.*, underestimating the observed value) the quantification of the accumulation in the tumor tissues, the bioconjugates showed an *in vivo* pharmacokinetic profile very similar to that of the uncoupled Ab, thus supporting our idea that such nanostructures are suitable scaffolds to be implemented for *in vivo* treatments. In particular, the possibility of further doping the AuNPs core with radioactive species during the PVD synthesis opens the way toward the development of a new generation of radioactive bioconjugates possibly displaying a theranostic activity.

## Experimental part

### Materials

All chemicals were purchased from commercial sources and used without further purification. 1-Ethyl-3-(dimethylaminopropyl)-3-carbodiimide hydrochloride (EDC·HCl), *N*-hydroxy-sulphosuccinimide sodium salt (NHSS) and 2-(*N*-morpholino)ethanesulphonic acid hydrate (MES) were obtained from Sigma-Aldrich and used without further purification. Allylamine was obtained from Sigma-Aldrich. Water was purified using a Millipore Milli-Q water production system. Commercially available Cetuximab formulation (Erbix<sup>®</sup> 2 or 5 mg mL<sup>-1</sup>, Merck & Co.) was purified by discontinuous diafiltration in centrifugal concentrators with a molecular weight cut-off (MWCO) of 10 000 g mol<sup>-1</sup> (Sartorius Vivaspin) and the purified antibody was isolated by freeze-drying (Ab). Iodo-Gen kit was obtained from Pierce Thermo scientific. <sup>125</sup>I was purchased from Best Medical Belgium and radiolabeled antibodies were purified on a Sephadex G-25 column (GE Healthcare Europe).

### Characterizations

Transmission electron microscopy (TEM) images were acquired with a Philips Tecnai 10 transmission electron microscope (TEM) operating at 80 keV and in bright-field mode. Samples for TEM analysis were obtained by depositing onto carbon-coated Cu grids directly during PVD process (Fig. 2a) or by using suitable solutions of AuNPs-PPAA in H<sub>2</sub>O (Fig 2b). All the thermogravimetric analyses were performed with a TGA Q500 instrument manufactured by TA instruments (Italy), under a N<sub>2</sub> flow of 60 mL min<sup>-1</sup> and with the following method: equilibration from room temperature to 100 °C, isothermal heating at 100 °C for 20 min, then ramp from 100 °C to 1000 °C (heating rate of 10 °C min<sup>-1</sup>). UV-Vis spectra were recorded on a Cary 5000 Spectrophotometer (Varian), using 1 cm path quartz or optical glass cuvettes. Quality controls of radiolabeled antibodies were performed by paper chromatography, Bioscan analysis (Bioscan system 200 imaging scanner), SDS-PAGE electrophoresis and by gel scanning through a Phosphor Imager (Fujifilm FLA-5100). The amount of radioactivity in tumors, blood and organs (liver, spleen, kidneys, lung, skeletal muscles and thyroid) was measured in a gamma well counter (1480 Wallac Wizard 3<sup>™</sup> automatic  $\gamma$ -counter; Perkin Elmer, Inc.).

### Synthesis of AuNPs-PPAA and antibody conjugation

Synthesis of gold nanoparticles coated with plasma-polymerized allylamine (AuNPs-PPAA) by plasma vapor deposition (PVD) was already reported.<sup>26</sup> The resulting NaCl embedded nanoparticles were then dispersed in acetate buffer (pH = 5) under 5 min of sonication and then purified from the PPAA and NaCl excess by discontinuous diafiltration in centrifugal concentrators with a molecular weight cut-off (MWCO) of 10 000 g mol<sup>-1</sup>. Ab (5 mg) was dissolved in 10 mL of 0.1 M MES buffer (190 mg in 10 mL H<sub>2</sub>O, pH = 7), and then a solution of EDC·HCl (2 mg, 0.01 mmol) and NHSS (2 mg, 0.01 mmol) in 10 mL of 0.1 M MES buffer was added. The resulting mixture was stirred at 25 °C for 15 min, after that a solution of AuNPs-PPAA (0.65 mg mL<sup>-1</sup>, 8.0 mL, 5.2 mg) in H<sub>2</sub>O was added. The reaction was stirred at 25 °C for 16 hours, after which it was purified by discontinuous diafiltration against H<sub>2</sub>O in centrifugal concentrators with MWCO of 300 000 g mol<sup>-1</sup>. Purification was completed when the electrical conductivity of the filtrate was almost equal to that of H<sub>2</sub>O. AuNPs-PPAA-Ab were isolated through freeze-drying, affording a pinkish red powder (6.5 mg).

### Radioiodination of Cetuximab

Ab radioiodination with <sup>125</sup>I was done using the Iodo-Gen method as described in instructions of use by Pierce. In brief, a mixture of sodium iodide (3700 MBq mL<sup>-1</sup>) and Cetuximab (20 mg mL<sup>-1</sup>) dissolved in 0.01 M sodium phosphate buffered saline (NaCl 0.14 M, pH 7.4) was added to an Iodo-Gen-coated reaction vial (50  $\mu$ g iodogen coating the inner surface of a 100  $\mu$ L vial) and reacted for 5 min at room temperature with stirring every 30 seconds. Protein-bound iodine was separated from free iodide by passing over a Sephadex G-25 column equilibrated with PBS 0.01 M pH 7.4. Quality control of radiolabeled Ab (Ab-<sup>125</sup>I) was performed by using paper chromatography (eluent: MeOH-H<sub>2</sub>O, 70 : 30, v/v) followed by Bioscan analysis to determine the radiochemical yield and purity. In addition, Ab-<sup>125</sup>I integrity was checked by SDS-PAGE (8%, under non-reducing conditions) and analyzed by a Bioscan and Phosphor Imager.

### Synthesis of AuNPs-PPAA-Ab-<sup>125</sup>I

2 mg of Ab-<sup>125</sup>I were redissolved in 5 mL of 0.1 M MES buffer and treated with a solution of EDC·HCl (1 mg, 0.005 mmol) and NHSS (1 mg, 0.005 mmol) in 5 mL of 0.1 M MES buffer. The mixture was stirred for 15 min at 25 °C, after which a solution of AuNPs-PPAA (0.65 mg mL<sup>-1</sup>, 2.0 mL, 1.30 mg) in H<sub>2</sub>O was added. The reaction was stirred at 25 °C for a period of 16 hours after which it was purified by diafiltration using a membrane filter of molecular weight cut-off 300 000 g mol<sup>-1</sup>. The purification was completed when the electrical conductivity of the filtrate was almost equal to that of H<sub>2</sub>O. The retentate was finally redissolved in 3.0 mL of deionized H<sub>2</sub>O by sonication affording a H<sub>2</sub>O solution of AuNPs-PPAA-Ab-<sup>125</sup>I.

### Cell culture

Human epithelial carcinoma cells A431 and Chinese hamster ovary cells CHO were maintained in culture in 75 cm<sup>2</sup>

polystyrene flasks (Corning) with respectively 15 mL of Dulbecco's modified Eagle's medium (DMEM) or Roswell Park Memorial Institute medium (RPMI 1640, Invitrogen), containing 10% of fetal calf serum (Invitrogen) and incubated under an atmosphere containing 5% CO<sub>2</sub>.

#### Surface ELISA

A431 or CHO cells (10<sup>5</sup> per well) were grown in 96 well plates (Costar) 24 hours prior to the ELISA test. Cells were rinsed once with PBS and then fixed 10 min with PBS containing 4% paraformaldehyde. After one wash with PBS, wells were blocked with 5% of non-fat dry milk in PBS for 1 hour at room temperature. Cells were rinsed one time with PBS and one time with BSA 1% in PBS for 5 min. Ab or AuNPs-PPAA-Ab were added to the cells at various concentrations for 1 hour at room temperature. Plates were washed three times with PBS-BSA, and a mouse monoclonal anti-human IgG-biotin antibody (Sigma) diluted in PBS-BSA at 1 µg mL<sup>-1</sup> was added for 1 hour at room temperature. Cells were washed three times and incubated with streptavidin-alkaline phosphatase (Sigma) for 30 min at room temperature. After three washing steps with PBS-BSA and one with PBS, alkaline phosphatase activity was revealed with 1 mg mL<sup>-1</sup> *p*-nitrophenylphosphate in 0.1 M diethanolamine pH 10.3 containing 1.5 mM levamisole hydrochloride. The reaction was stopped with NaOH 2 N and the surface expression was quantified spectrophotometrically, reading the optical density (405 nm) 45 min after addition of the substrate.

#### Phosphorylation studies

A431 cells were grown to 90% confluence in complete medium in T75 flasks, and they were starved in DMEM with 0.5% BSA (Sigma) for 24 hours prior to stimulation. Cells were incubated for 7 min with Ab or AuNPs-PPAA-Ab and then stimulated with 10 ng mL<sup>-1</sup> EGF (R&D Systems) for 10 min at 37 °C. Following stimulation, cells were washed with ice-cold PBS containing 1 mM sodium orthovanadate. Cells were lysed with a lysis buffer (Tris 20 mM pH 7.5, NaCl 150 mM, EDTA 1 mM, EGTA 1 mM, sodium deoxycholate 1%, Nonidet P40 1%, glycerol 10%) containing a protease inhibitor mixture («Complete» from Roche Molecular Biochemicals, 1 tablet in 2 mL H<sub>2</sub>O, added at a 1 : 25 dilution) and phosphatase inhibitors (NaVO<sub>3</sub> 25 mM, PNPP 250 mM, α-glycerophosphate 250 mM and NaF 125 mM, at a 1 : 25 dilution). Protein concentration in cell lysates was evaluated by Bradford protein assay (Bio-rad) and 15 µg proteins were separated by electrophoresis on a 3–8% Tris-acetate gel (NuPage, Invitrogen). After semi-dry transfer onto a low IR background PVDF (polyvinylidene fluoride) membrane (Millipore) for 2 h at 1 mA cm<sup>2</sup>, the membrane was left for 2 h in Licor blocking agent 2× diluted in PBS before incubation during 2 h with the primary antibody diluted in Odyssey blocking buffer (Licor) containing 0.1% Tween 20 (Sigma). The membrane was washed 4 × 5 min with PBS-Tween 0.1%, incubated 1 h with infrared dye specific secondary antibodies (Licor) diluted in Odyssey + Tween 0.1% and washed 4 × 5 min with PBS-Tween 0.1% and 2 × 5 min with PBS before protein detection using the Odyssey Infrared Imaging System (Licor). Fluorescence Western blot analysis by infrared technology (Licor) allows the

quantification of the fluorescent intensity of the bands corresponding to the protein of interest. Western blotting analysis was performed by infrared fluorescence with rabbit anti-phospho-EGF receptor (Tyr1173) monoclonal antibody (# 4407 Cell Signaling) used at 1/1000 dilution or rabbit anti-EGF receptor monoclonal antibody (# 4267 Cell Signaling) used at 1/5000 dilution. Goat anti-lamin B antibody (SC-6212 Santa Cruz) (final dilution 1/2000) was used for normalization. Rabbit or goat IgG infrared dye-linked antibody (Licor) was used at 1/10 000 dilution as a secondary antibody.

#### Comparative biodistribution studies in mice

NMRI nude mice (athymic nu/nu, 29–36 g, Janvier, France) were 5–8 weeks old at the time of the experiments. The human epidermoid carcinoma cell line A431 (10 × 10<sup>6</sup>) was injected subcutaneously into the flank of each mouse. Biodistribution studies were performed when tumors reached a size of approximately 7.5–8.5 mm. All animal experiments were approved by the local ethics committee for animal research in compliance with the principles of laboratory animal care. Two groups of mice were injected i.v. into the lateral tail vein with either a mixture of 74 kBq Ab-<sup>125</sup>I (control group) or with AuNPs-PPAA-Ab-<sup>125</sup>I (total of 13.5 to 16 µg of Ab per mouse). Typically, groups of 2–5 mice per time point (6, 24, 48 and 72 h after injection) were anesthetized, weighed, killed by cervical dislocation and dissected. Radioactivity uptake was expressed as the percentage of injected dose per gram of tissue (%ID g<sup>-1</sup>) and as tumor-to-blood ratios. The results were expressed as the mean ± SEM. Data calculations were performed with Prism software (GraphPad Software Inc.). The differences in tissue uptake between the two groups were considered significant if the *P* values from unpaired *t* tests were less than 0.05.

#### Acknowledgements

This work was supported by the Région Wallonne through the “TARGAN” project, the FRS-FNRS, (FRFC contracts no. 2.4.550.09 and 2.4.617.07.F and MIS no. F.4.505.10.F), Associazione Italiana Ricerca sul Cancro (AIRC), the “Loterie Nationale”, the “TINTIN” ARC project (09/14-023) and the University of Namur (internal funding). R.M. thanks FRS-FNRS for his post-doctoral fellowship. The authors thank Dr Chiara Fabbro for the TGA measurements at the University of Trieste.

#### Notes and references

- 1 R. L. Whetten, J. T. Khoury, M. M. Alvarez, S. Murthy, I. Vezmar, Z. L. Wang, P. W. Stephens, C. L. Cleveland, W. D. Luedtke and U. Landman, *Adv. Mater.*, 1996, **8**, 428; S. Chen, R. S. Ingram, M. J. Hostetler, J. J. Pietron, R. W. Murray, T. G. Schaaff, J. T. Khoury, M. M. Alvarez and R. L. Whetten, *Science*, 1998, **280**, 2098; M. C. Daniel and D. Astruc, *Chem. Rev.*, 2004, **104**, 293; Y. Lu and W. Chen, *Chem. Soc. Rev.*, 2012, **41**, 3594.
- 2 X. Huang, S. Neretina and M. A. El-Sayed, *Adv. Mater.*, 2009, **21**, 4880.
- 3 R. D. Averitt, D. Sarkar and N. J. Halas, *Phys. Rev. Lett.*, 1997, **78**, 4217.
- 4 Y. Sun and Y. Xia, *Science*, 2002, **298**, 2176.
- 5 M. Hu, J. Chen, Z. Y. Li, L. Au, G. V. Hartland, X. Li, M. Marquez and Y. Xia, *Chem. Soc. Rev.*, 2006, **35**, 1084.

- 6 R. Arvizo, R. Bhattacharya and P. Mukherjee, *Expert Opin. Drug Delivery*, 2010, **7**, 753; C. M. Copley, J. Chen, E. C. Cho, L. V. Wang and Y. Xia, *Chem. Soc. Rev.*, 2011, **40**, 44; S. Jelveh and D. B. Chithrani, *Cancers*, 2011, **3**, 1081.
- 7 S. Eustis and M. A. El-Sayed, *Chem. Soc. Rev.*, 2006, **35**, 209.
- 8 H. J. Johnston, G. Hutchison, F. M. Christensen, S. Peters, S. Hankin and V. Stone, *Crit. Rev. Toxicol.*, 2010, **40**, 328.
- 9 U. H. F. Bunz and V. M. Rotello, *Angew. Chem., Int. Ed.*, 2010, **49**, 3268; K. M. Mayer and J. H. Hafner, *Chem. Rev.*, 2011, **111**, 3828; S. J. Tan, M. J. Campolongo, D. Luo and W. Cheng, *Nanotechnol.*, 2011, **6**, 268.
- 10 C. J. Murphy, A. M. Gole, S. E. Hunyadi, J. W. Stone, P. N. Sisco, A. Alkilany, B. E. Kinard and P. Hankins, *Chem. Commun.*, 2008, **8**, 544; E. Boisselier and D. Astruc, *Chem. Soc. Rev.*, 2009, **38**, 1759; Z. Wang and L. Ma, *Coord. Chem. Rev.*, 2009, **253**, 1607.
- 11 J. D. Byrne, T. Betancourt and L. Brannon-Peppas, *Adv. Drug Deliv. Rev.*, 2008, **60**, 1615.
- 12 P. Ghosh, G. Han, M. De, C. K. Kim and V. M. Rotello, *Adv. Drug Deliv. Rev.*, 2008, **60**, 1307.
- 13 R. A. Sperling, P. Rivera Gil, F. Zhang, M. Zanella and W. J. Parak, *Chem. Soc. Rev.*, 2008, **37**, 1896.
- 14 K. G. Thomas and P. V. Kamat, *Acc. Chem. Res.*, 2003, **36**, 888; D. A. Giljohann, D. S. Seferos, W. L. Daniel, M. D. Massich, P. C. Patel and C. A. Mirkin, *Angew. Chem., Int. Ed.*, 2010, **49**, 3280; W. R. Algar, D. E. Prasuhn, M. H. Stewart, T. L. Jennings, J. B. Blanco-Canosa, P. E. Dawson and I. L. Medintz, *Bioconj. Chem.*, 2011, **22**, 825.
- 15 J. Shan and H. Tenhu, *Chem. Commun.*, 2007, 4580; D. Li, Q. He and J. Li, *Adv. Colloid Interface Sci.*, 2009, **149**, 28; B. Masereel, M. Dinguzli, C. Bouzin, N. Moniotte, O. Feron, B. Gallez, T. Vander Borgh, C. Michiels and S. Lucas, *J. Nanopart. Res.*, 2011, **13**, 1573.
- 16 G. Sonavane, K. Tomoda and K. Makino, *Colloids Surf. B*, 2008, **66**, 274; G. Zhang, Z. Yang, W. Lu, R. Zhang, Q. Huang, M. Tian, L. Li, D. Liang and C. Li, *Biomaterials*, 2009, **30**, 1928; S. K. Balasubramanian, J. Jittiwat, J. Manikandan, C. N. Ong, L. E. Yu and W. Y. Ong, *Biomaterials*, 2010, **31**, 2034; J. Lipka, M. Semmler-Behnke, R. A. Sperling, A. Wenk, S. Takenaka, C. Schleh, T. Kissel, W. J. Parak and W. G. Kreyling, *Biomaterials*, 2010, **31**, 6574; E. S. Glazer, C. Zhu, A. N. Hamir, A. Borne, C. S. Thompson and S. A. Curley, *Nanomedicine*, 2011, **5**, 459; S. Hirn, M. Semmler-Behnke, C. Schleh, A. Wenk, J. Lipka, M. Schäffler, S. Takenaka, W. Möller, G. Schmid, U. Simon and W. G. Kreyling, *Eur. J. Pharm. Biopharm.*, 2011, **77**, 407.
- 17 N. Khlebtsov and L. Dykman, *Chem. Soc. Rev.*, 2011, **40**, 1647.
- 18 X. Huang, P. K. Jain, I. H. El-Sayed and M. A. El-Sayed, *Nanomedicine*, 2007, **2**, 681; C. R. Patra, R. Bhattacharya, D. Mukhopadhyay and P. Mukherjee, *Adv. Drug Deliv. Rev.*, 2010, **62**, 346; A. Kumar, B. Mazinder Boruah and X. J. Liang, *J. Nanomater.*, 2011, **2011**, 202187; Z. Z. J. Lim, J. E. J. Li, C. T. Ng, L. Y. L. Yung and B. H. Bay, *Acta Pharmacol. Sin.*, 2011, **32**, 983; A. Llevot and D. Astruc, *Chem. Soc. Rev.*, 2012, **41**, 242.
- 19 I. H. El-Sayed, X. Huang and M. A. El-Sayed, *Nano Lett.*, 2005, **5**, 829.
- 20 E. S. Day, L. R. Bickford, J. H. Slater, N. S. Riggall, R. A. Drezek and J. L. West, *Int. J. Nanomed.*, 2010, **5**, 445; G. J. Kim, S. R. Park, G. C. Kim and J. K. Lee, *Plasma Medicine*, 2011, **1**, 45.
- 21 N. Normanno, A. De Luca, C. Bianco, L. Strizzi, M. Mancino, M. R. Maiello, A. Carotenuto, G. De Feo, F. Caponigro and D. S. Salomon, *Gene*, 2006, **366**, 2; C. M. Rocha-Lima, H. P. Soares, L. E. Razez and R. Singal, *Cancer Control*, 2007, **14**, 295.
- 22 K. Sokolov, M. Follen, J. Aaron, I. Pavlova, A. Malpica, R. Lotan and R. Richards-Kortum, *Cancer Res.*, 2003, **63**, 1999.
- 23 I. H. El-Sayed, X. Huang and M. A. El-Sayed, *Cancer Lett.*, 2006, **239**, 129.
- 24 G. Han, P. Ghosh and V. M. Rotello, *Multi-functional gold nanoparticles for drug delivery*, 2007, Vol. 620, p. 48; C. M. Copley, L. Au, J. Chen and Y. Xia, *Expert Opin. Drug Delivery*, 2010, **7**, 577.
- 25 S. Bhattacharyya, R. Bhattacharya, S. Curley, M. A. McNiven and P. Mukherjee, *Proc. Natl. Acad. Sci. U. S. A.*, 2010, **107**, 14541.
- 26 N. Moreau, C. Michiels, B. Masereel, O. Feron, B. Gallez, T. Vander Borgh and S. Lucas, *Plasma Process. Polym.*, 2009, **6**, S888.
- 27 J. Harding and B. Burtness, *Drugs Today*, 2005, **41**, 107.
- 28 E. J. Westover, D. F. Covey, H. L. Brockman, R. E. Brown and L. J. Pike, *J. Biol. Chem.*, 2003, **278**, 51125.
- 29 G. A. M. S. Van Dongen, G. W. M. Visser, M. N. Lub-De Hooge, E. G. De Vries and L. R. Perk, *Oncologist*, 2007, **12**, 1379.

## **II. *In vivo* deiodination impact of $^{125}\text{I}$ -labelled anti-CD105 antibody on tumour targeting in mice**

The second study characterized the anti-endoglin antibody (mass spectrometry of antibody fragments observed on electrophoretic gel) and the radiodinated anti-CD105 antibody (integrity after radiolabelling, substitution rate and *in vitro* stability). The biodistribution profile of radioiodinated mAbs, with a focusing on tumour targeting in two tumour models, was studied through *ex-vivo* experiments and SPECT/CT imaging. The tumour uptake profile of  $^{125}\text{I}$ -labelled anti-CD105 mAbs was compared to that of  $^{89}\text{Zr}$ -labelled anti-CD105 mAbs (a validated tracer).



**Imaging and comparative biodistribution of  $^{125}\text{I}$ - and  $^{89}\text{Zr}$ -labelled anti-endoglin antibody: impact of *in vivo* deiodination on tumour accumulation in mice**

**Linda Karmani**, Philippe Levêque, Bernard Waterlot, Caroline Bouzin, Anne Bol, Marc Dieu, Stephan Walrand, Olivier Feron, Vincent Grégoire, Carine Michiels, Stéphane Lucas, Thierry Vander Borcht and Bernard Gallez.

*Submitted to Contrast Media Mol Imaging, 2013.*



---

## Imaging and comparative biodistribution of $^{125}\text{I}$ - and $^{89}\text{Zr}$ -labelled anti-endoglin antibody: impact of *in vivo* deiodination on tumour accumulation in mice

Linda Karmani<sup>1</sup>, Philippe Levêque<sup>1</sup>, Bernard Waterlot<sup>1</sup>, Caroline Bouzin<sup>2</sup>, Anne Bol<sup>3</sup>, Marc Dieu<sup>4</sup>, Stephan Walrand<sup>5</sup>, Olivier Feron<sup>2</sup>, Vincent Grégoire<sup>3</sup>, Carine Michiels<sup>4</sup>, Stéphane Lucas<sup>6</sup>, Thierry Vander Borgh<sup>7</sup> and Bernard Gallez<sup>1</sup>.

### Authors:

1. Biomedical Magnetic Resonance Research Group (REMA), Louvain Drug Research Institute (LDRI), Université Catholique de Louvain, Avenue Mounier 73, 1200 Brussels, Belgium.
2. Pharmacology and Therapeutics Unit (FATH), Institute of Experimental and Clinical Research (IREC), Université Catholique de Louvain, Avenue Mounier 53, 1200 Brussels, Belgium.
3. Centre for Molecular Imaging, Radiotherapy and Oncology (MIRO), Institute of Experimental and Clinical Research (IREC), Université Catholique de Louvain, Avenue Hippocrate 54, 1200 Brussels, Belgium.
4. Unité de Recherche en Biologie Cellulaire (URBC), Namur Research Institute for Life Sciences (NARILIS), University of Namur, Rue de Bruxelles 61, 5000 Namur, Belgium.
5. Centre of Nuclear Medicine, Université Catholique de Louvain, Avenue Hippocrate 10, 1200 Brussels, Belgium.
6. Research Centre for the Physics of Matter and Radiation (PMR), NAMur Research Institute for Life Sciences (NARILIS), University of Namur, Rue de Bruxelles 61, 5000 Namur, Belgium.
7. Centre for Molecular Imaging, Radiotherapy and Oncology (MIRO), Institute of Experimental and Clinical Research (IREC), NAMur Research Institute for Life Sciences (NARILIS), Université Catholique de Louvain, Avenue Docteur G. Therasse 1, 5530 Yvoir, Belgium.

### Corresponding author:

Bernard Gallez, PhD  
Biomedical Magnetic Resonance Research Group  
Louvain Drug Research Institute  
Université Catholique de Louvain  
Avenue Mounier 73 - B1.73.08  
B-1200 Brussels – Belgium  
Tel: +32 2 7647391  
Fax: +32 2 7647390  
E-mail: Bernard.Gallez@uclouvain.be

## ABSTRACT

Radioiodinated antibodies, as specific tracers, were largely used to study tumour targeting. However, *in vivo* deiodination may be a limitation for assessing the potential advantage of a new tracer, such as anti-endoglin antibody, for cancer detection and therapy.

The biodistribution of  $^{125}\text{I}$ -labelled anti-endoglin antibodies and the tumour targeting profile were investigated in tumour-bearing mice through *ex-vivo* studies and *in vivo* SPECT/CT imaging. These uptake results were compared with those of  $^{89}\text{Zr}$ -anti-CD105 antibodies obtained using PET imaging.

Radioiodinated antibodies were stable *in vitro*, both in storage solution and in plasma. The most important increase of uptake was observed for thyroid ( $7.5 \pm 2.8 \text{ \%ID g}^{-1}$  at 5 min to  $341.1 \pm 58.7 \text{ \%ID g}^{-1}$  at 72 h after injection). The tumour uptake of  $^{125}\text{I}$ -anti-CD105 antibodies was not persistent and decreased over time, both for *ex-vivo* and SPECT/CT experiments. The tumour uptake of  $^{125}\text{I}$ -anti-CD105 antibodies ( $0.9 \pm 0.3 \text{ \%ID mL}^{-1}$ ) was significantly lower than that of  $^{89}\text{Zr}$ -anti-CD105 antibodies ( $6.5 \pm 0.4 \text{ \%ID mL}^{-1}$ ) 24 h after injection.

*In vivo* deiodination compromises the monitoring of pharmacokinetic profile of the anti-CD105 antibodies and the accurate characterization of tumour targeting. Radiolabelling of anti-CD105 antibodies with  $^{89}\text{Zr}$  overcomes these limitations and represents a suitable alternative for imaging of the CD105 receptor in tumours.

## INTRODUCTION

Among a variety of approaches to achieve selective accumulation of radiotracers within tumours, the radiolabelled monoclonal antibodies are highly promising, because of their high affinity and specificity [1]. Therefore, non-invasive molecular imaging of malignancies using radiolabelled antibodies as specific tracers is an attractive strategy that can improve cancer detection and therapy efficiency [2].

Very recently, monoclonal antibodies (mAbs) have been labelled with positron emitters, such as zirconium-89 ( $^{89}\text{Zr}$ ), for PET imaging; but although they present advantages, they have also drawbacks, which could be a hinder to a widespread use. It is consequently still very desirable to have validated radiotracers labelled with more common radionuclides, such as iodine, for other imaging modalities. For a long time, the radionuclides of iodine have been widely used to radiolabel mAbs, peptides and other biomolecules because they are readily available, at reasonable costs, with easy radiolabelling procedures. These radioiodinated tracers were largely used to study tumour targeting for cancer imaging ( $^{123}\text{I}$ ,  $^{124}\text{I}$ ,  $^{125}\text{I}$ ), for cancer therapy ( $^{131}\text{I}$ ) and for an approach, in which imaging is performed as a scouting procedure before radioimmunotherapy to confirm tumour targeting and to assess tissue dosimetry [3]. Many different strategies are available for radioiodination of proteins, which is often considered as a straightforward procedure. But in the context of sensitive radioiodinated biological molecules, such as antibodies, *in vivo* stability and the risk of *in vivo* deiodination and its influence on the tracer properties are not systematically investigated, especially in quantitative studies for tumour targeting.

We describe here the radiolabelling process, *in vitro* stability, *ex-vivo* distribution, *in vivo* SPECT imaging of  $^{125}\text{I}$ -labelled anti-endoglin antibody, and comparison with its analogue labelled with  $^{89}\text{Zr}$ . Endoglin (CD105) is a homodimeric cell surface glycoprotein that is mainly expressed on endothelial cells. Of particular interest is the fact that CD105 is overexpressed in tumour neovasculature [4-7] and in some cancer cells, such as melanoma [8,9]. Furthermore, the vascular density, determined using the anti-CD105 antibody, is correlated with the tumour prognosis [10], the risk of developing metastatic disease [11] and the recurrence of malignancy [12]. CD105 targeting has also been used as an antiangiogenic therapy, which is based on the attack of the new blood vessels, each of them supporting

thousands of cancer cells in the tumour mass, in addition to the directly attacking of cancer cells that overexpress CD105 [13].

It is known that antibody-based radiotracers require extended *in vivo* circulation times for optimal tumour targeting, typically 2-4 days [14]; therefore, the physical half-life of the radionuclide used for labelling must be compatible with the optimal time needed for most intact antibodies to achieve ideal tumour-to-nontumour ratio.  $^{89}\text{Zr}$  (78.41 h) is a metallic positron-emitter radionuclide, which is suitable for positron emission tomography (PET) [15], whereas  $^{125}\text{I}$  (60 days) is suitable for SPECT imaging in small animals.

Recently, we studied the biodistribution profile of  $^{89}\text{Zr}$ -labelled anti-endoglin mAbs using non-invasive immuno-PET imaging, and the effect of the antibody conjugation to gold nanoparticles [16]. In the present study, we investigated *ex vivo* and *in vivo* distribution profile of  $^{125}\text{I}$ -labelled anti-CD105 mAbs through SPECT imaging, and compared these results to that of obtained with the same antibody labelled with  $^{89}\text{Zr}$ . The tumour targeting was studied in two different tumour models (hepatocarcinoma and melanoma), which express CD105 at different levels. The tumour uptake of  $^{125}\text{I}$ -anti-CD105 mAbs was compared to that of  $^{89}\text{Zr}$ -labelled anti-CD105 mAbs, and the *in vivo* stability of the tracers was correlated with the change in imaging properties, especially regarding the tumour uptake.

## RESULTS AND DISCUSSION

### Anti-CD105 antibody radiolabelling with $^{125}\text{I}$ and quality controls

The radiolabelling of anti-CD105 mAbs with  $^{125}\text{I}$  was achieved with a mean radiochemical yield of 90% ( $n = 5$ ). The radiochemical purity as determined by radio-TLC was higher than 99% ( $n = 5$ ). Gel electrophoresis analysis under non-reducing conditions followed by radio-TLC and autoradiography revealed that at least 85% of the radioactivity was attached to the whole antibody molecule (Fig. 1), and the residual activity was attached to protein entities having immunoglobulin origin, as identified by mass spectrometry analyses (electrospray ionization time of flight mass spectrometry) and the NCBI protein database (data not shown). The specific activity was  $82 \pm 1 \text{ MBq mg}^{-1}$  of mAbs ( $n = 4$ ). The  $^{125}\text{I}$ -to-mAb ratio was about 0.2, which means that approximately one out of five mAb unit carries one  $^{125}\text{I}$  atom. *In vitro* stability of radioiodinated mAbs in storage solution showed that iodine was very slightly dissociated from the antibody in plasma over time. Starting from a solution without free iodine (100% purity), the percentage of dissociation was lower than 3% ( $n = 2-3$ ) up to 48 h after incubation in plasma. The release of free  $^{125}\text{I}$  was lower than 5% up to two months after labelling reaction.

### *Ex-vivo* biodistribution studies in mice

The biodistribution profile of  $^{125}\text{I}$ -labelled anti-CD105 mAbs was first studied in NMRI mice bearing TLT xenografts by *ex-vivo* experiments (Fig. 2). In tumour, the maximum uptake values were observed at early times after injection, and reached  $4.7 \pm 1.9 \text{ \%ID g}^{-1}$  15 min after injection, followed by a rapid decrease to  $0.5 \pm 0.1 \text{ \%ID g}^{-1}$ , 24 h after injection. In non-target organs, a similar profile was observed. At early time after tracer injection (5 min), the uptake values were  $75.8 \pm 11.8$  (lungs),  $54.4 \pm 26.7$  (spleen),  $52.1 \pm 11.01$  (liver) and  $20.3 \pm 4.7$  (kidneys)  $\text{\%ID g}^{-1}$ . These values decreased significantly to  $1.8 \pm 0.7$ ,  $1.2 \pm 0.1$ ,  $1.7 \pm 0.4$  and  $1.4 \pm 0.2 \text{ \%ID g}^{-1}$  respectively after 24 h. The uptake by stomach decreased also significantly over time. Noticeably in the stomach, a transient increase of radioactivity was observed until 6 h after injection, but followed by a rapid wash out. On the contrary, the thyroid uptake values showed a significant increase over time, from  $7.5 \pm 2.8 \text{ \%ID g}^{-1}$ , 5 min after injection to reach a quasi steady state at  $341.1 \pm 58.7 \text{ \%ID g}^{-1}$ , 72 h after injection.

Based on the long time needed for most intact antibodies to achieve optimal biodistribution and tumour targeting, we expected a slow distribution of the tracer, with an optimal tumour uptake beginning at late times after injection (2-4 days). However, the maximum TLT tumour uptake was observed at early times after injection, and was not persistent with significant decrease over time. Because the tracer accumulation in TLT tumour model was low and non persistent, a second tumour model (melanoma) was selected to investigate the tumour targeting in C57BL/6J mice and to confirm

the tumour uptake profile (17). Indeed, the immunohistochemistry analysis showed the CD105 expression only on endothelial cells of vessels in TLT tumour model (data not shown), whereas the melanoma is known for two levels of CD105 expression, by tumour cells themselves, in addition to the CD105 expression on endothelial cells (8,9). We compared the tumour uptake values, expressed as tumour-to-blood ratios (T/B), between the group of TLT-bearing mice and the group of B16-bearing mice at 5 min, 15 min, 60 min, 6 h and 24 h after injection (Fig. 3). For each time point, the T/B values of B16-bearing mice were higher than those of TLT-bearing mice. The highest T/B ratios were observed after 1 h for both groups and were respectively  $0.9 \pm 0.1$  for TLT-bearing mice and  $1.6 \pm 0.2$  for B16-bearing mice. The T/B values didn't increase over time and remained close to 1 at all times after injection. Overall no real accumulation of the tracer was noted, whatever the tumour model considered.

In conclusion for *ex-vivo* evaluation of the tracer, the kinetic profile was not in accordance with the known kinetics of most intact mAbs, most probably reflecting an intense *in vivo* metabolisation of the tracer with a rapid release of free iodine. Although the contrast, expressed as T/B ratios, were higher in B16 tumour model than in TLT tumour model (Fig. 3), the tumour uptake was only transient and the contrast at late time points was also low. Since we showed a high *in vitro* stability of radioiodinated anti-CD105 mAbs in plasma, the results suggest that *in vivo* catabolism is responsible for the important antibody dehalogenation (18).

### **Biodistribution studies using animal-SPECT/CT imaging**

In order to confirm the results of *ex-vivo* experiments, the biodistribution of  $^{125}\text{I}$ -anti-CD105 mAbs was imaged up to 24 h after injection in B16-bearing mice, by using SPECT/CT imaging modality (Fig. 4). The MIP (maximum intensity projection) images were generated for visual inspection and qualitative analysis of the global kinetics of distribution. For a more quantitative evaluation, the percentage of injected dose was computed for the tumour, thyroid, and the total body (Fig. 5). From the MIP images, it could be noted a poor tracer uptake in the tumour, with a very transient increase of activity at early times during the distribution phase and a weak tumour contrast. Only  $0.9 \pm 0.4$  %ID was found in the tumour at 1 h after injection. In liver and lungs, which are highly vascularised organs, the level of activity was much higher, particularly at early times after injection (1 and 3 h), but followed a similar kinetics with a rapid wash out of the tracer from those non specific tissues. In accordance to *ex-vivo* results, a regular and stable increase of thyroid uptake was observed, this organ being already visible after 1 h. The radioactivity trapped by the thyroid was about  $1.7 \pm 0.4$  %ID at 24 h after injection. The stomach showed a delayed increase of activity at 6 h after injection, in parallel with the thyroid uptake, but with no accumulation. This could be compatible with the uptake of free iodine rather than the intact tracer itself. Urinary excretion of the free iodine or the products of

catabolism was also noted after 6 h *via* the hot spot in the bladder. Finally, the background signal was quite low after 24 h, suggesting an almost total clearance of the radioactivity (more than 85% of the injected dose).

### Comparative *ex-vivo* biodistribution and SPECT/CT imaging of $^{125}\text{I}$ -labelled anti-CD105 mAbs

The pharmacokinetic behaviour of  $^{125}\text{I}$ -labelled anti-CD105 mAbs was assessed in mice bearing B16 xenografts. *Ex-vivo* results were confirmed by SPECT/CT imaging. We compared the tumour uptake values, expressed as tumour-to-nonspecific tissue ratios, between *ex-vivo* and SPECT/CT studies in order to evaluate the tumour contrast (Fig. 6). No significant difference was observed between the two series. There was neither any improvement of the contrast over time. As expected, the liver and spleen uptakes were observed according to the known catabolism of mAbs, these organs being the preferential sites for nonspecific uptake (19,20). Indeed, it is known that one of the limitations of antibody-based imaging is the high background signal in the reticuloendothelial system. The lung uptake may be explained by the constitutive expression of CD105 in normal blood vessels, especially in vascularized tissues. Indeed, previous studies showed that high levels of CD105 expression are seen in the distal vessels of mouse lung (21). The stomach and thyroid uptakes were related to the sodium iodide ( $\text{Na}^+/\text{I}$ ) symporter (NIS), an integral membrane protein which is expressed in thyroid epithelial cells and in stomach tissues. The NIS protein facilitates the diffusion of free iodine from the blood into the organs (22). The stomach tissue is not known to utilize iodine in any biological process. Thus, the iodine freely exits through diffusion and does not result in prolonged exposure as in the thyroid (23). The kidney and bladder uptakes most probably reflect the urinary excretion of free iodine (24). For all normal tissues (liver, lungs, spleen and kidneys), there was no specific accumulation since the radioactivity level decreased over time. Nonetheless, the increase in the thyroid uptake over time means an *in vivo* detachment of  $^{125}\text{I}$  from the antibody (Fig. 2 and 4). The antibody deiodination was important and the released iodine was rapidly cleared from the body, giving a low tumour contrast (Fig. 5 and 6). This *in vivo* chemical instability definitely leads to an underestimation of the actual antibody tumour uptake (16). In this particular case, the anti-CD105 antibody metabolism is so extended that an acceptable imaging of the tumour is not possible.

Most studies with radiohalogenated mAbs have involved the use of iodine nuclides. However, the detachment of the radiolabel probes from the antibody may raise a significant problem, especially when the radioiodine is directly attached to the antibody. Indeed, *in vivo* deiodination prevents the stable tracking of the tracer in tissues. For this reason, it is important to investigate accurately the impact of the deiodination on the tissue uptake, and particularly on the tumour uptake of novel studied tracers, such as anti-CD105 mAbs. It is of particular interest as some radioimmunotherapeutic studies have been performed with radioiodinated mAbs that were prepared *via* a direct iodination procedure

(25,26). It must be mentioned that because of these limitations, the development of a metabolically stable radioiodination reagent for coupling to mAbs was previously investigated (27-29). The indirect radiolabelling methods were developed for decreasing the loss of the nuclide from the protein *in vivo*, for decreasing the thyroid uptake of radioiodine, while retaining a tumour uptake with a suitable tumour contrast (30,31). However, many studies have continued to describe the biological distribution and the tumour targeting using directly radioiodinated mAbs without assessing the extent of the effect of *in vivo* deiodination on tissue uptake (32,33).

### Comparative *in vivo* studies of $^{125}\text{I}$ - and $^{89}\text{Zr}$ -labelled anti-CD105 mAbs

The tumour uptake results of  $^{125}\text{I}$ -anti-CD105 mAbs were compared with those of  $^{89}\text{Zr}$ -anti-CD105 mAbs. The tumour uptake of  $^{125}\text{I}$ -anti-CD105, expressed as %ID mL<sup>-1</sup> and obtained *via* SPECT/CT quantification, was significantly lower than that of  $^{89}\text{Zr}$ -anti-CD105 mAbs obtained through PET quantification, at the corresponding time points after injection (Fig. 7A). The maximum tumour uptake of  $^{89}\text{Zr}$ -anti-CD105 mAbs was about  $6.5 \pm 0.4$  %ID mL<sup>-1</sup> compared with that of iodinated mAbs ( $0.9 \pm 0.3$  %ID mL<sup>-1</sup>) at 24 h after injection. Similarly, the tumour contrast, expressed as T/Bg ratios, was significantly lower for  $^{125}\text{I}$ -anti-CD105 mAbs for all time points, with a ratio of  $0.9 \pm 0.1$  compared with  $5.4 \pm 0.3$  for  $^{89}\text{Zr}$ -anti-CD105, 24 h after injection (Fig. 7B). Moreover, the kinetics of uptake and washout from the tissue was also quite different. Whereas  $^{89}\text{Zr}$ -anti-CD105 showed a slow accumulation in tumour with a peak after 24 h (Fig. 7 and 8),  $^{125}\text{I}$ -anti-CD105 showed on a contrary a fast distribution followed by a quick washout, in contrast with the known delayed accumulation of intact antibodies (14). The tumour uptake of  $^{89}\text{Zr}$ -anti-CD105 mAbs was maintained high at late times after injection ( $5.8 \pm 0.7$  %ID mL<sup>-1</sup> until to 72 h) and with a good tumour contrast, compared with that of iodinated mAbs ( $0.9 \pm 0.3$  %ID mL<sup>-1</sup> at 24 h).

This comparison highlighted even more clearly the differences in tumour targeting profile and the impact of *in vivo* deiodination (Fig. 7 and 8).  $^{89}\text{Zr}$  is a metallic positron emitter that is suitable for PET imaging. The PET/CT images showed liver, spleen, lungs, and to a lesser extent bone uptake (Fig. 8). The bone uptake was assigned to the slight detachment of  $^{89}\text{Zr}$  from the desferal moiety. Previous studies attributed the constant bone accumulation to the strong affinity of free  $^{89}\text{Zr}$  for hydroxylapatite and phosphate constituents of bones (34-36). Despite this mild instability, the tumour uptake of  $^{89}\text{Zr}$ -anti-CD105 mAbs was significantly higher than that of  $^{125}\text{I}$ -anti-CD105 mAbs, and was extended until 72 h after injection ( $5.8 \pm 0.7$  %ID mL<sup>-1</sup>). At earlier time points after injection, the T/Bg ratios of  $^{89}\text{Zr}$ -anti-CD105 mAbs were 3.2 (3 h), 3.9 (6 h) and 5.6-fold (24 h) higher than those of  $^{125}\text{I}$ -anti-CD105 mAbs, so that  $^{89}\text{Zr}$ -anti-CD105 mAbs was more adequate for imaging purposes, whatever the time point considered. Additionally, this optimal profile was improved by the internalizing properties of antibodies and by the residualizing properties of the used isotope. Indeed,  $^{89}\text{Zr}$  is trapped inside the

cell after antibody internalization, while  $^{125}\text{I}$  is released from the tumour after internalization (15). Thus, the labelling with intracellularly retained isotopes has an advantage over released ones both in diagnosis and therapy (37). Previous *in vitro* studies showed that iodinated mAbs are intracellularly catabolized with a rapid release of iodotyrosine from the cell. In contrast, residualizing radiolabels, such as radioactive metals, are retained intracellularly longer. This also might explain the higher tumour uptake with  $^{89}\text{Zr}$  compared with  $^{125}\text{I}$ . Overall, direct radioiodination of anti-CD105 mAbs is a procedure that does not guarantee a stable labelling *in vivo*. This instability prevents reliable imaging of targeted tumours and is a serious limitation for assessing the potential advantage of the tracer for therapeutic applications.

## CONCLUSIONS

The major challenge in cancer immunodetection, imaging and therapy is to maximize the amount of antibody localizing at the tumour site, without an excessive accumulation in normal organs. Antibodies directed against endoglin were previously described as a valuable tool for imaging and/or treating cancers. The proven effectiveness of antibody therapies towards endoglin has led to increasingly focused interest on the CD105 as a cancer target. We previously studied the biodistribution of anti-CD105 mAbs radiolabelled with  $^{89}\text{Zr}$  before and after conjugation to gold nanoparticles (16). In this work, we characterized *in vivo* distribution of directly radioiodinated anti-CD105 antibodies by using *ex-vivo* experiments, which were confirmed by non-invasive SPECT/CT imaging. The antibody radiolabelling with  $^{89}\text{Zr}$  is a multi-step and a time consuming method, since the antibody is previously functionalized with a chelate before radiolabelling. Moreover,  $^{89}\text{Zr}$  has a short half-life compared with that of  $^{125}\text{I}$  and requires an animal-PET scanner and special precautions in terms of radiations. In this context, a validated radioiodinated analogue is desirable. Radioiodinated mAbs are easily prepared through a direct radioiodination procedure and have been widely used for radioimmunodiagnosis and radioimmunotherapy (38,39). However, there is some concern about the reliability of using them for the characterization of tumour targeting, with minimizing nonspecific tissue uptake. Indeed, we reported in two tumour models that the tumour uptake of radioiodinated anti-CD105 mAbs was low and not persistent compared with that of  $^{89}\text{Zr}$ -labelled anti-CD105 mAbs. These experiments indicate that the use of directly labelled anti-CD105 mAbs with radioiodine is a limitation for the accurate quantification of the biodistribution. Furthermore, the information, which may be obtained through the use of radioiodinated anti-CD105 mAbs as tracers for staging and response to therapy, may also be impaired because of the negative impact of *in vivo* deiodination. Indirect radioiodination leading to more stable tracers and preventing *in vivo* deiodination should be further investigated in order to validate the use of radioiodinated anti-CD105 mAbs for imaging. Finally,  $^{89}\text{Zr}$ -labelled mAbs are validated tracers for imaging of the CD105 receptor in tumours.

## EXPERIMENTAL

### Anti-CD105 antibody purification and radiolabelling with $^{125}\text{I}$

The rat mAb directed against mouse CD105 was produced from a hybridoma (clone MJ7/18), which was provided by the Developmental Studies Hybridoma Bank (Iowa University, Iowa City, IA, USA). First, the antibody was purified by protein G-affinity chromatography and dialysis into PBS (140 mM NaCl, 6 mM  $\text{Na}_2\text{HPO}_4$ , 3 mM KCl, 1 mM  $\text{KH}_2\text{PO}_4$ , pH 7.2), followed by size-exclusion chromatography on a Superdex 200 column (GE Healthcare Life Sciences, Belgium) using a 20 mM TRIS-HCl buffer (pH 7.5) containing 0.15 M NaCl. Then, the purified antibody was concentrated using a membrane filter device with a molecular weight cut-off of 10 kDa. Finally, the anti-CD105 mAbs were directly radiolabelled with  $^{125}\text{I}$  (3700 MBq  $\text{mL}^{-1}$ , PerkinElmer Inc., Belgium) using chloramine T as an oxidant agent. In brief, a mixture of purified anti-CD105 mAbs (200  $\mu\text{g}$ , 500  $\mu\text{L}$ ), 18.5 MBq of sodium iodide and 500  $\mu\text{L}$  of chloramine T (10 mg  $\text{mL}^{-1}$ ) was mixed and reacted for 1 min at room temperature with stirring after 30 seconds. The reaction was stopped by adding 500  $\mu\text{L}$  of sodium metabisulfite (20 mg  $\text{mL}^{-1}$ ) as a reducing agent, after which 500  $\mu\text{L}$  of cold sodium iodide (5 mg  $\text{mL}^{-1}$ ) was added. The radiolabelled antibody ( $^{125}\text{I}$ -anti-CD105 mAbs) was separated from free iodide by passing through a Sephadex G-25 column (GE Healthcare Life Sciences, Belgium), preconditioned with PBS 0.01 M, pH 7.4. All solutions were previously filtrated on 0.22  $\mu\text{m}$  filter.

The radiochemical yield and purity were performed by using thin layer chromatography (TLC) with a mixture of MeOH- $\text{H}_2\text{O}$  (70:30, v/v) as a mobile phase. The TLC migration was followed by radio-TLC detection. The integrity of the antibody after radiolabelling was checked by sodium dodecyl sulfate-polyacrylamide gel electrophoresis (8% SDS-PAGE gel, under nonreducing conditions). Detection of radioactive bands was performed with a radio-TLC analyser (Bioscan system 200 imaging scanner) and with a Phosphor Imager (Fujifilm FLA-5100).

### *In vitro* stability of $^{125}\text{I}$ -labelled anti-CD105 antibodies in storage solution and in plasma

The chemical stability of purified  $^{125}\text{I}$ -anti-CD105 mAbs, stored in a solution of PBS 0.01 M, pH 7.4 was checked for up to two months at 4°C. Samples were drawn at regular times and the proportion of free  $^{125}\text{I}$  was analyzed by radio-TLC.

*In vitro* stability of purified  $^{125}\text{I}$ -anti-CD105 mAbs was also studied in fresh mouse plasma, by incubating the solution of radiolabelled mAbs (1:10 v/v dilution at a final concentration of 2.4 MBq  $\text{mL}^{-1}$ ; sodium azide added at 0.02%) at 37°C with stirring. At different times (5 min, 15 min, 1 h, 3 h, 6 h, 24 h and 48 h), aliquots of plasma (5  $\mu\text{L}$ ) were analysed using radio-TLC.

### **Animal and tumour models**

Transplantable liver tumours (TLT hepatocarcinoma cells, ascites) were induced intramuscularly in the gastrocnemius muscle of male NMRI mice (40). Mouse melanoma cell line (B16F10-luc) was maintained in alpha minimum essential medium (MEM-alpha with glutamine, Gibco-Invitrogen, Belgium) supplemented with 10% heat-inactivated foetal bovine serum (FBS, Gibco-Invitrogen, Belgium), 1% streptomycin-penicillin (Gibco-Invitrogen, Belgium) and 1% MEM non-essential amino acids (Gibco-Invitrogen, Belgium). C57BL/6J male mice were inoculated subcutaneously in the flanks with  $1 \times 10^6$  B16F10-luc tumour cells. The mice were used for *in vivo* experiments when the diameter of tumours reached approximately 7-8.5 mm. All animal experiments were conducted in accordance with national and university animal care regulations.

### ***Ex-vivo* biodistribution studies in mice**

*Ex-vivo* experiments were carried out for biodistribution assessment of  $^{125}\text{I}$ -labelled anti-CD105 mAbs. In a first study, a group of NMRI mice bearing TLT xenografts (30-42 g, 5-7 weeks old; Janvier, France) were injected intravenously in the lateral tail vein with freshly prepared  $73 \pm 6$  kBq of  $^{125}\text{I}$ -anti-CD105 mAbs per mouse. Then, a second group of C57BL/6J mice (22-28 g, 5-6 weeks old; Janvier, France) bearing melanoma xenografts received intravenously  $43 \pm 3$  kBq of  $^{125}\text{I}$ -anti-CD105 mAbs per mouse. Typically, a group of three to four mice per time point after injection (5 min, 15 min, 60 min, 6 h, 24 h, 48 h and 72 h for NMRI mice group; 5 min, 15 min, 60 min, 3 h, 6 h and 24 h for C57BL/6J mice group) were anesthetized, weighed, killed by cervical dislocation and dissected. The blood and organs were collected, and the radioactivity uptakes were expressed as percentages of the injected dose per gram of tissue (%ID  $\text{g}^{-1}$ ) and as tumour-to-blood ratios (T/B).

### **Biodistribution studies using animal-SPECT/CT imaging**

SPECT/CT imaging was performed using a preclinical four-headed gamma-camera with integrated CT system (NanoSpect/CT, Bioscan Inc., Washington, D.C., USA) and dedicated multi-pinhole apertures, each with nine pinholes with a diameter of 1.4 mm. These apertures provide a reconstructed resolution of about 1.0 mm in a mouse-sized animal with an average sensitivity of 1800 cps/MBq across the field of view (with  $^{99\text{m}}\text{Tc}$ ). The data were acquired in a step-and-shoot helical mode to include the whole mouse within the field of view. A group of three C57BL/6J male mice (23-24 g, 5-6 weeks old; Janvier, France) bearing melanoma xenografts were injected intravenously in the lateral tail vein with a freshly prepared solution of  $^{125}\text{I}$ -anti-CD105 mAbs (3-3.7 MBq). The whole-body SPECT/CT imaging was performed under general anaesthesia by inhalation of 1.5% isoflurane (Abbott Laboratories, Belgium) mixed with 21% oxygen gas ( $2 \text{ L min}^{-1}$ ). The mice were maintained in a prone position on a heated animal bed at  $37^\circ\text{C}$  (Minerve, France). The static SPECT/CT acquisitions

were carried out at different times (1, 3, 6 and 24 h after injection). First, the SPECT images were acquired with a 20% energy window peaked at 28.4 keV, with an acquisition time varying between 20 and 70 s per projection, and with 20 projections. This acquisition time was adapted to compensate for radioiodine clearance in order to ensure significant statistics (> 10000 total counts per projection), and resulted in a total imaging time ranging between 20 and 60 min. The projection data were reconstructed with HiSPECT NG software (Scivis GmbH, Göttingen, Germany) using an iterative reconstruction algorithm with a voxel size of 0.45 mm<sup>3</sup>. After SPECT acquisition, the animal remained anesthetized and a CT image was acquired using a standard resolution with a 45 kVp voltage and 500 ms exposure time, requiring about 5 min to image a whole mouse. The CT projections were reconstructed with a voxel size of 0.15 x 0.15 x 0.15 mm<sup>3</sup> (41).

### **SPECT/CT data analyses**

After SPECT data reconstruction, the images were analyzed using PMOD software (PMOD™, version 3.4, PMOD Technologies Ltd, Zurich, Switzerland). The regions of interest (ROIs) were delineated on the SPECT/CT fused images. Before the fusion of SPECT and CT images, the SPECT images were normalized. A calibration factor was empirically determined and used to convert the ROI value (total counts) to activity (kBq). A correction was also applied for acquisition duration and physical decay during acquisition. The image scale was corrected according to the SPECT calibration factor, the physical decay at the time of injection and the injected dose. This normalization was used to parameterize images in terms of percentage of the injected dose (%ID) for expressing the tissue uptake. The 2D ROIs were drawn on consecutive transversal slices that defined a 3D volume of interest around the tissue of interest. The tracer uptake was assessed in the thyroid, tumours and total body. A background region was also drawn in the pelvic region. The same background volume was applied for all animal analyses and was representative of tissues with low nonspecific uptake. Thus, the tumour uptake was also expressed as a tumour-to-background ratio (T/Bg), calculated as the mean activity in the tumour region divided by the mean activity obtained in the background region. The tumour uptake of <sup>125</sup>I-anti-CD105 mAbs obtained through *ex-vivo* experiments for the group of dissected mice was compared with that obtained by SPECT/CT imaging for the group of imaged mice, in terms of tumour-to-nonspecific tissue ratios (T/Bg *versus* T/B).

### Comparative *in vivo* studies of <sup>125</sup>I- and <sup>89</sup>Zr-labelled anti-CD105 mAbs

In a previous study, we described the biodistribution of <sup>89</sup>Zr-anti-CD105 mAbs using PET imaging in C57BL/6J mice bearing melanoma xenografts (16). Briefly, <sup>89</sup>Zr was produced and purified in-house as previously described (42,43). <sup>89</sup>Zr-labelled anti-CD105 mAbs (<sup>89</sup>Zr-Df-Bz-NCS-anti-CD105) was prepared according to a protocol previously described (44,45). A group of five male mice (22-26 g, 5-6 weeks old; Janvier, France) were inoculated subcutaneously in the flanks with  $1 \times 10^6$  B16F10-luc cells (one or two tumours per mouse), and were injected intravenously with freshly prepared <sup>89</sup>Zr-anti-CD105 mAbs (3.4-3.9 MBq). The whole-body PET images were acquired using a dedicated small-animal PET scanner (MOSAIC, Philips Medical Systems; Cleveland, USA). The PET scans were followed by whole-body acquisitions using a helical CT scanner (NanoSpect/CT, Bioscan Inc., Washington, D.C., USA) for anatomical reference. The PET/CT acquisitions were performed at different times after tracer injection (3, 6, 24, 48 and 72 h), and the treatment of PET images were performed as previously described (19). The ROIs were delineated on the PET/CT fused images using PMOD software (PMOD™, version 3.3, PMOD Technologies Ltd, Zurich, Switzerland), and the tracer uptake was assessed in the tumours and in a background region, which was delineated in the pelvic region. The tumour uptake values of <sup>89</sup>Zr-anti-CD105 mAbs were expressed as %ID mL<sup>-1</sup> and as T/Bg ratios for the comparison with that of <sup>125</sup>I-anti-CD105 mAbs.

### Statistical Analysis

The results are given as means  $\pm$  SEM values from *n* animals. The data calculations were performed with Prism software (Graph Pad™ Software Inc., version 5.02). The differences in tissue uptake between two groups were considered significant if the p-values from unpaired t-tests (two-tailed) were  $\leq 0.05$  (\*),  $\leq 0.01$  (\*\*) or  $\leq 0.001$  (\*\*\*). The differences in tissue uptake at different times were assessed by the one-way analysis of variance and the Tukey *post-hoc* test.

**Acknowledgments** This work was supported by grants from the Region Walloon through the “TARGAN” project and the Belgian National Fund for Scientific Research (FNRS-TELEVIE). The hybridoma (clone MJ7/18) was obtained from the Developmental Studies Hybridoma Bank developed under the auspices of the NICHD and maintained by The University of Iowa, Department of Biology, Iowa City, IA 52242.

## References

1. Larson SM. Radioimmunology. Imaging and therapy. *Cancer* 1991; 67: 1253-1260.
2. Olafsen T, Kenanova VE, Wu AM. Imaging tumor xenografts using radiolabeled antibodies. In: *Antibody Engineering*, Kontermann R, Dübel S (eds). Springer-Verlag Berlin Heidelberg; 491-506, 2010.
3. Verel I, Visser GW, Vosjan MJ, et al. High-quality  $^{124}\text{I}$ -labelled monoclonal antibodies for use as PET scouting agents prior to  $^{131}\text{I}$ -radioimmunotherapy. *Eur J Nucl Med Mol Imaging* 2004; 31: 1645-1652.
4. Haruta Y, Seon BK. Distinct human leukemia-associated cell surface glycoprotein GP160 defined by monoclonal antibody SN6. *Proc. Natl. Acad. Sci. USA* 1986; 83: 7898-7902.
5. Westphal JR, Willems HW, Schalkwijk CJ, et al. A new 180-kDa dermal endothelial cell activation antigen: in vitro and in situ characteristics. *J. Invest. Dermatol* 1993; 100: 27-34.
6. Burrows FJ, Derbyshire EJ, Tazzari PL, et al. Up-regulation of endoglin on vascular endothelial cells in human solid tumors: implications for diagnosis and therapy. *Clin. Cancer Res* 1995; 1: 1623-1634.
7. Miller DW, Graulich W, Karges B, et al. Elevated expression of endoglin, a component of the TGF-beta-receptor complex, correlates with proliferation of tumor endothelial cells. *Int. J. Cancer* 1999; 81: 568-572.
8. Hussein MR. Transforming growth factor-beta and malignant melanoma: molecular mechanisms. *J. Cutan. Pathol* 2005; 32: 389-395.
9. Sun T, Sun BC, Ni CS, et al. Pilot study on the interaction between B16 melanoma cell-line and bone-marrow derived mesenchymal stem cells. *Cancer Lett.* 2008; 263:35-43. DOI: 10.1016/j.canlet.2007.12.015
10. Kumar S, Ghellal A, Li C, et al. Breast carcinoma: vascular density determined using CD105 antibody correlates with tumor prognosis. *Cancer Res* 1999; 59: 856-861.
11. Romani AA, Borghetti AF, Del Rio P, et al. The risk of developing metastatic disease in colorectal cancer is related to CD105-positive vessel count. *J. Surg. Oncol* 2006; 93: 446-455.
12. Marioni G, D'Alessandro E, Giacomelli L, et al. CD105 is a marker of tumour vasculature and a potential target for the treatment of head and neck squamous cell carcinoma. *J. Oral. Pathol. Med* 2010; 39: 361-367. DOI: 10.1111/j.1600-0714.2010.00888.x
13. Carmeliet P, Jain RK. Molecular mechanisms and clinical applications of angiogenesis. *Nature* 2011; 473: 298-307. DOI: 10.1038/nature10144
14. van Dongen GAMS, Visser GWM, Lub-de-Hooge MN, et al. Immuno-PET: A navigator in monoclonal antibody development and applications. *Oncologist* 2007; 12: 1379-1389. DOI: 10.1634/theoncologist.12-12-1379
15. Vugts DJ, van Dongen GAMS.  $^{89}\text{Zr}$ -labeled compounds for PET imaging guided personalized therapy. *Drug Discov. Today Technol* 2011; 8: e53-e61.

16. Karmani L, Bouchat V, Bouzin C, et al. <sup>89</sup>Zr-labelled anti-endoglin antibody-targeted gold nanoparticles for imaging cancer: implications for future cancer therapy. *Nanomedicine (Lond)* 2013. [In press].
17. Bredow S, Lewin M, Hofmann B, et al. Imaging of tumour neovasculature by targeting the TGF-beta binding receptor endoglin. *Eur J Cancer* 2000; 36: 675-681.
18. Siya R, Buchsbaum DJ. Radioiodination of monoclonal antibodies D612 and 17-1A with 3-iodophenylisothiocyanate and their biodistribution in tumor-bearing nude mice. *Cancer* 1994; 73: 808-815.
19. Sands H, Jones PL. Methods for the study of the metabolism of radiolabeled monoclonal antibodies by liver and tumor. *J Nucl Med* 1987; 28: 390-398.
20. van den Abbeele AD, Aaronson RA, Taube RA, et al. Preadsorption of radiolabeled monoclonal antibodies to liver and spleen tissues leads to higher tumor-to-normal-tissue ratios. *J Nucl Med Allied Sci* 1990; 34: 94-102.
21. Mahmoud M, Borthwick GM, Hislop AA, et al. Endoglin and activin receptor-like-kinase 1 are co-expressed in the distal vessels of the lung: implications for two familial vascular dysplasias, HHT and PAH. *Lab Invest* 2009; 89: 15-25. DOI: 10.1038/labinvest.2008.112
22. Filetti S, Bidart JM, Arturi F, et al. Sodium/iodide symporter: a key transport system in thyroid cancer cell metabolism. *Eur J Endocrinol* 1999; 141: 443-457.
23. Carrasco N. Iodide transport in the thyroid gland. *Biochim Biophys Acta* 1993; 1154: 65-82.
24. Cavalieri RR. Iodine metabolism and thyroid physiology: current concepts. *Thyroid* 1997; 7: 177-181.
25. Geissler F, Anderson SK, Venkatesan P, et al. Intracellular catabolism of radiolabeled anti-mu antibodies by malignant B-cells. *Cancer Res* 1992; 52: 2907-2915.
26. Meredith RF, LoBuglio AF, Plott WE, et al. Pharmacokinetics, immune response, and biodistribution of iodine-131-labeled chimeric mouse/human IgG1,k 17-1A monoclonal antibody. *J Nucl Med* 1991; 32: 1162-1168.
27. Ram S, Buchsbaum DJ. Radioiodination of monoclonal antibodies D612 and 17-1A with 3-iodophenylisothiocyanate and their biodistribution in tumor-bearing nude mice. *Cancer* 1994; 73(3 Suppl): 808-815.
28. Zalutsky MR, Narula AS. A method for the radiohalogenation of proteins resulting in decreased thyroid uptake of radioiodine. *Int J Rad Appl Instrum A* 1987; 38: 1051-1055.
29. Wilbur DS, Hadley SW, Hylarides MD, et al. Development of a stable radioiodinating reagent to label monoclonal antibodies for radiotherapy of cancer. *J Nucl Med* 1989; 30: 216-226.
30. Zalutsky MR, Garg PK, Narula AS. Labeling monoclonal antibodies with halogen nuclides. *Acta Radiol Suppl* 1990; 374: 141-145.
31. Srivastava PC, Buchsbaum DJ, Allred JF, et al. A new conjugating agent for radioiodination of proteins: low in vivo deiodination of a radiolabeled antibody in a tumor model. *Biotechniques* 1990; 8: 536-545.

- 
32. Li J, Shi L, Wang C, et al. Preliminary biological evaluation of  $^{125}\text{I}$ -labeled anti-carbonic anhydrase IX monoclonal antibody in the mice bearing HT-29 tumors. *Nucl Med Commun* 2011; 32: 1190-1193. DOI: 10.1097/MNM.0b013e32834bf3e1
33. Fonsatti E, Jekunen AP, Kairemo KJ, et al. Endoglin is a suitable target for efficient imaging of solid tumors: in vivo evidence in a canine mammary carcinoma model. *Clin Cancer Res* 2000; 6: 2037-2043.
34. Tinianow JN, Gill HS, Ogasawara A, et al. Site-specifically Zr-89-labeled monoclonal antibodies for ImmunoPET. *Nucl. Med. Biol* 2010; 37: 289-297. DOI: 10.1016/j.nucmedbio.2009.11.010
35. Mealey Jr J. Turn-over of carrier-free zirconium-89 in man. *Nature* 1957; 179: 673-674.
36. Abou DS, Ku T, Smith-Jones PM. In vivo biodistribution and accumulation of  $^{89}\text{Zr}$  in mice. *Nucl. Med. and Biol* 2011; 38: 675-681. DOI: 10.1016/j.nucmedbio.2010.12.011
37. Sharkey RM, Behr TM, Mattes MJ, et al. Advantage of residualizing radiolabels for an internalizing antibody against the B-cell lymphoma antigen, CD22. *Cancer Immunol Immunother* 1997; 44: 179-188.
38. Fan Z, Tang Z, Liu K, et al. Radioiodinated anti-hepatocellular carcinoma (HCC) ferritin. Targeting therapy, tumor imaging and anti-antibody response in HCC patients with hepatic arterial infusion. *J Cancer Res Clin Oncol* 1992; 118: 371-376.
39. Miraldi F. Monoclonal antibodies and neuroblastoma. *Semin Nucl Med* 1989; 19: 282-294.
40. Taper H, Woolley GW, Teller MN, et al. A new transplantable mouse liver tumor of spontaneous origin. *Cancer Res* 1966; 26: 143-148.
41. Forrer F, Valkema R, Bernard B, et al. In vivo radionuclide uptake quantification using a multi-pinhole SPECT system to predict renal function in small animals. *Eur J Nucl Med Mol Imaging* 2006; 33: 1214-1217.
42. Karmani L, Labar D, Valembois V, et al. Antibody-functionalized nanoparticles for imaging cancer: influence of conjugation to gold nanoparticles on the biodistribution of  $^{89}\text{Zr}$ -labeled cetuximab in mice. *Contrast Media Mol Imaging* 2013; 8: 402-408. DOI: 10.1002/cmml.1539
43. Holland JP, Sheh YC, Lewis JS. Standardized methods for the production of high specific-activity zirconium-89. *Nucl Med Biol* 2009; 36: 729-739. DOI: 10.1016/j.nucmedbio.2009.05.007
44. Vosjan MJWD, Perk LR, Visser GW, et al. Conjugation and radiolabeling of monoclonal antibodies with zirconium-89 for PET imaging using the bifunctional chelate p-isothiocyanatobenzyl-desferrioxamine. *Nat. Prot* 2010; 5: 739-743. DOI: 10.1038/nprot.2010.13
45. Perk LR, Vosjan MJWD, Visser GW, et al. p-Isothiocyanatobenzyl-desferrioxamine: a new bifunctional chelate for facile radiolabeling of monoclonal antibodies with zirconium-89 for immuno-PET imaging. *Eur J Nucl Med Mol Imaging* 2010; 37: 250-259. DOI: 10.1007/s00259-009-1263-1

## Figures

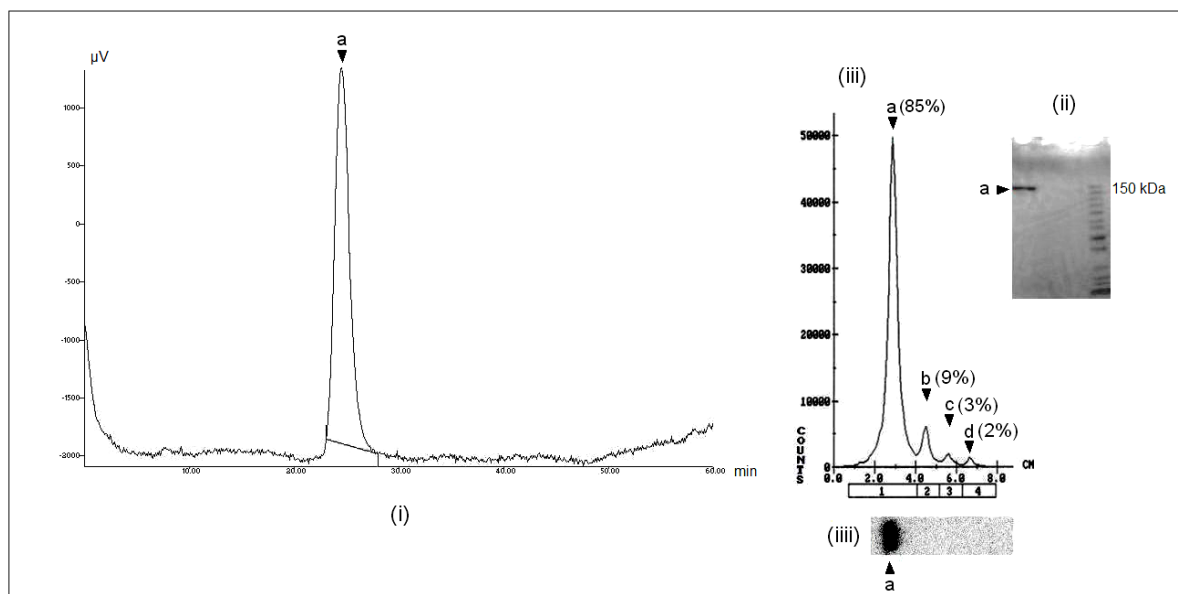


Fig. 1 Chromatographic profile of purified anti-CD105 mAbs (clone MJ7/18) using size-exclusion chromatography on a Superdex 200 column [i] and electrophoretic profile of  $^{125}\text{I}$ -anti-CD105 mAbs using SDS-PAGE 8% under non-reducing conditions [ii] followed by radioactivity scanning (iii) and Phosphor Imager (iiii) analysis. Intact antibody [a], antibody fragment [b], antibody high chain [c] and antibody light chain [d].

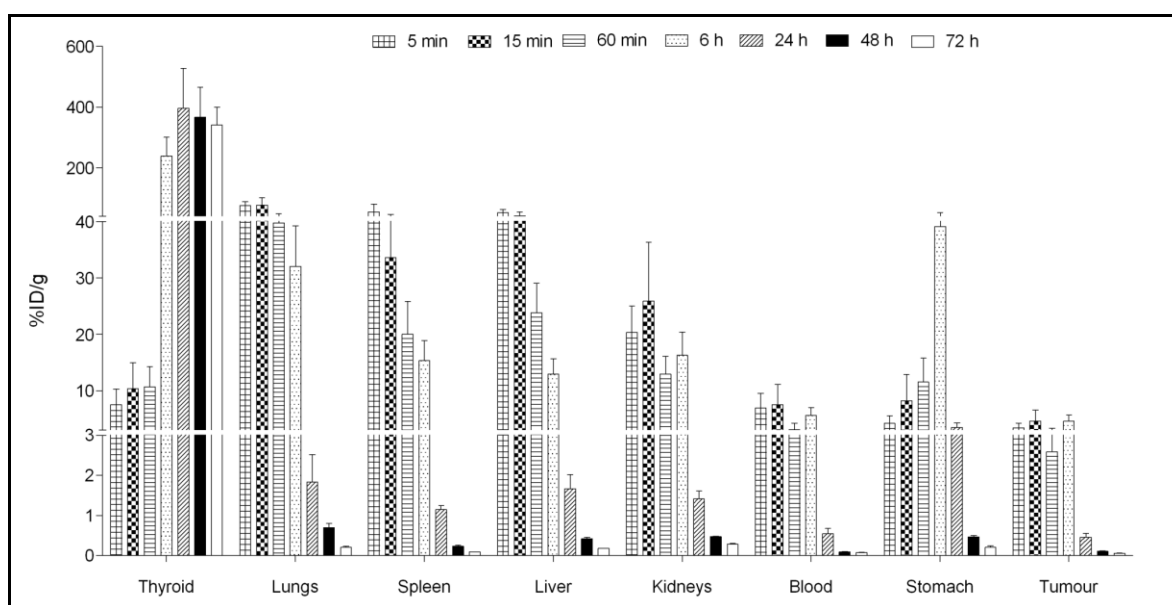


Fig. 2 Biodistribution profile of  $^{125}\text{I}$ -anti-CD105 mAbs in NMRI mice bearing TLT tumours at 5 min, 15 min, 60 min, 6 h, 24 h, 48 h and 72 h after tracer injection. The tissue uptake is expressed as  $\% \text{ID g}^{-1}$ . Each mouse was injected intravenously with  $73 \pm 6 \text{ kBq}$  of  $^{125}\text{I}$ -anti-CD105 mAbs. The results are expressed as means  $\pm$  SEM ( $n = 3-4$ ); note the axis break.

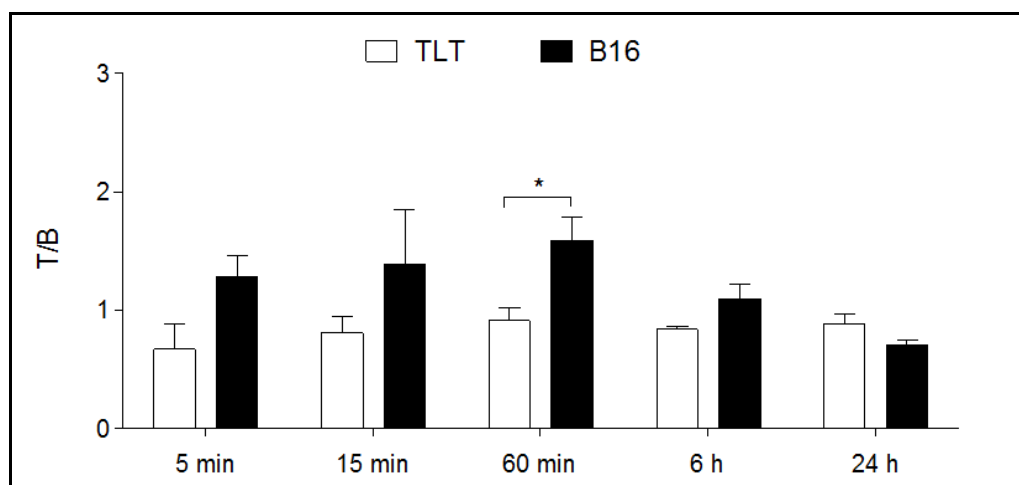


Fig. 3 Tumour to blood ratios (T/B) for TLT-bearing NMRI mice, injected with  $^{125}\text{I}$ -anti-CD105 mAbs ( $73 \pm 6$  kBq per mouse, white bars), and for B16-bearing C57BL/6J mice, injected with  $^{125}\text{I}$ -anti-CD105 mAbs ( $43 \pm 3$  kBq per mouse, black bars) at 5 min, 15 min, 60 min, 6 h and 24 h after tracer injection. The results are expressed as means  $\pm$  SEM ( $n = 3-4$ ).

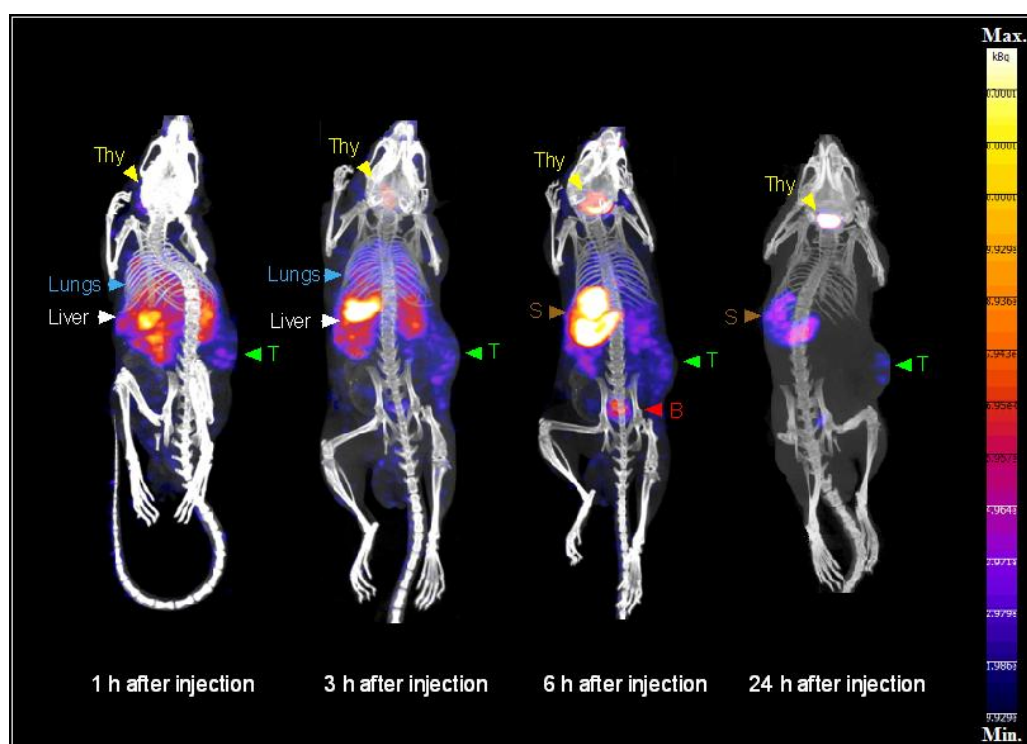


Fig. 4 Maximum intensity projection (MIP) images from SPECT/CT imaging (total imaging time between 20 and 60 min) of one mouse bearing B16 tumour, injected with  $^{125}\text{I}$ -anti-CD105 mAbs (3-3.7 MBq) at 1, 3, 6 and 24 h after injection. Thyroid [Thy], tumour inoculated subcutaneously in the right flank [T], stomach [S] and bladder [B]. MIP images were all normalized at the same maximum value.

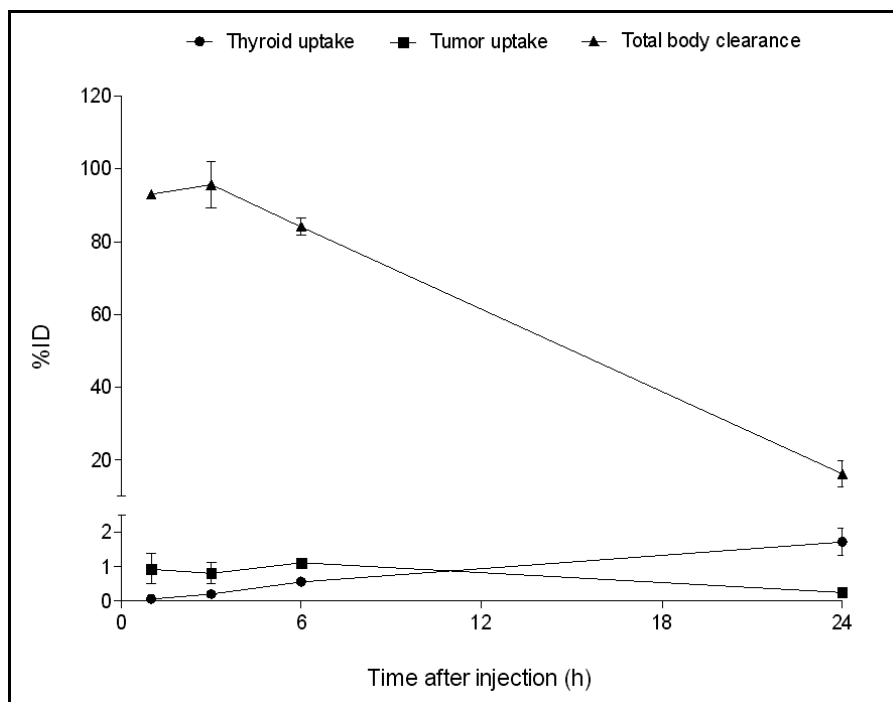


Fig. 5 Thyroid uptake (●), tumour uptake (■) and total body clearance (▲) of  $^{125}\text{I}$ -anti-CD105 mAbs (%ID) in B16-bearing C57BL/6J mice after intravenous injection (3-3.7 MBq per mouse) at 1, 3, 6 and 24 h. Results are expressed as mean  $\pm$  SEM (n = 3).

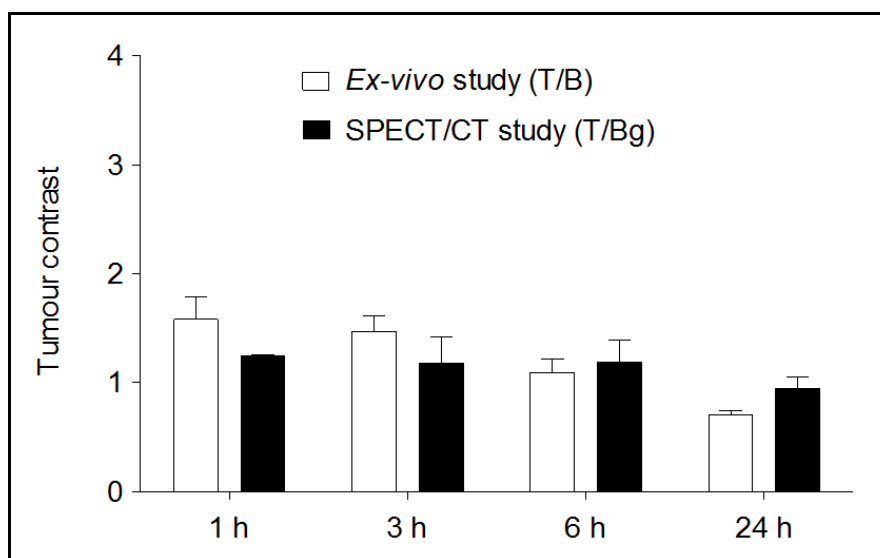


Fig. 6 Tumour contrast in B16-bearing mice, injected with  $^{125}\text{I}$ -anti-CD105 mAbs ( $43 \pm 3$  kBq per mouse for *ex-vivo* experiment, 3-3.7 MBq per mouse for SPECT/CT imaging) at 1, 3, 6 and 24 h after injection. Tumour contrast is expressed as tumour-to blood ratios (T/B, white bars) in *ex-vivo* experiment and as tumour-to-background ratios (T/Bg, black bars) in SPECT/CT imaging. The results are expressed as means  $\pm$  SEM (n = 3-4).

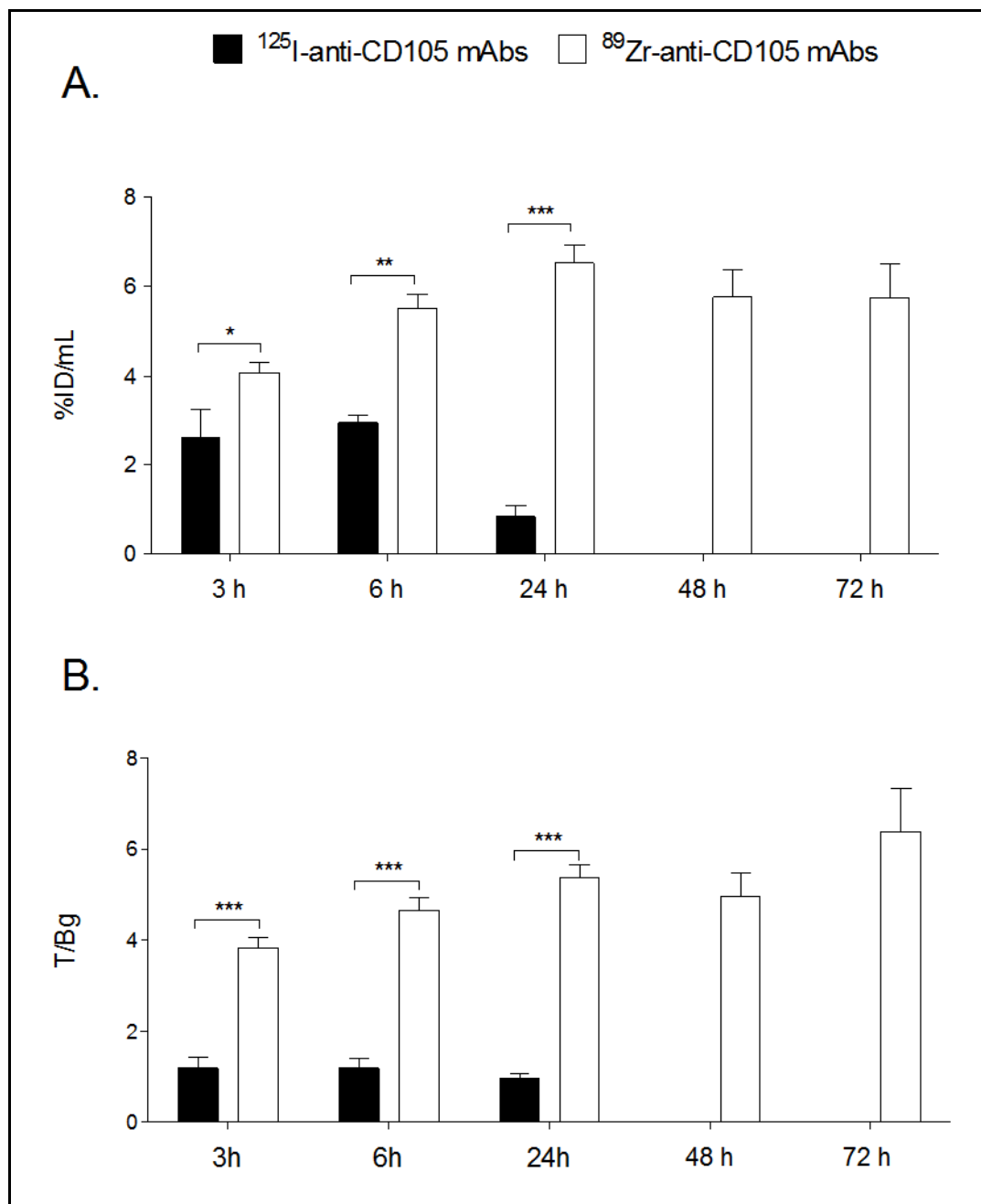


Fig. 7 Tumour uptake expressed as %ID mL<sup>-1</sup> [A] and tumour-to-background ratios (T/Bg) [B] of  $^{125}\text{I}$ -anti-CD105 mAbs (black bars) at 3, 6 and 24 h after injection or  $^{89}\text{Zr}$ -anti-CD105 mAbs (white bars) in B16-bearing C57BL/6J mice at 3, 6, 24, 48 and 72 h after injection. Injected activity ranged from 3-3.7 MBq for  $^{125}\text{I}$ -anti-CD105 mAbs, and from 3.4-3.9 MBq for  $^{89}\text{Zr}$ -anti-CD105 mAbs. Results are expressed as mean  $\pm$  SEM (n = 3-5). \* p < 0.05, \*\* p < 0.01 and \*\*\* p < 0.0001.

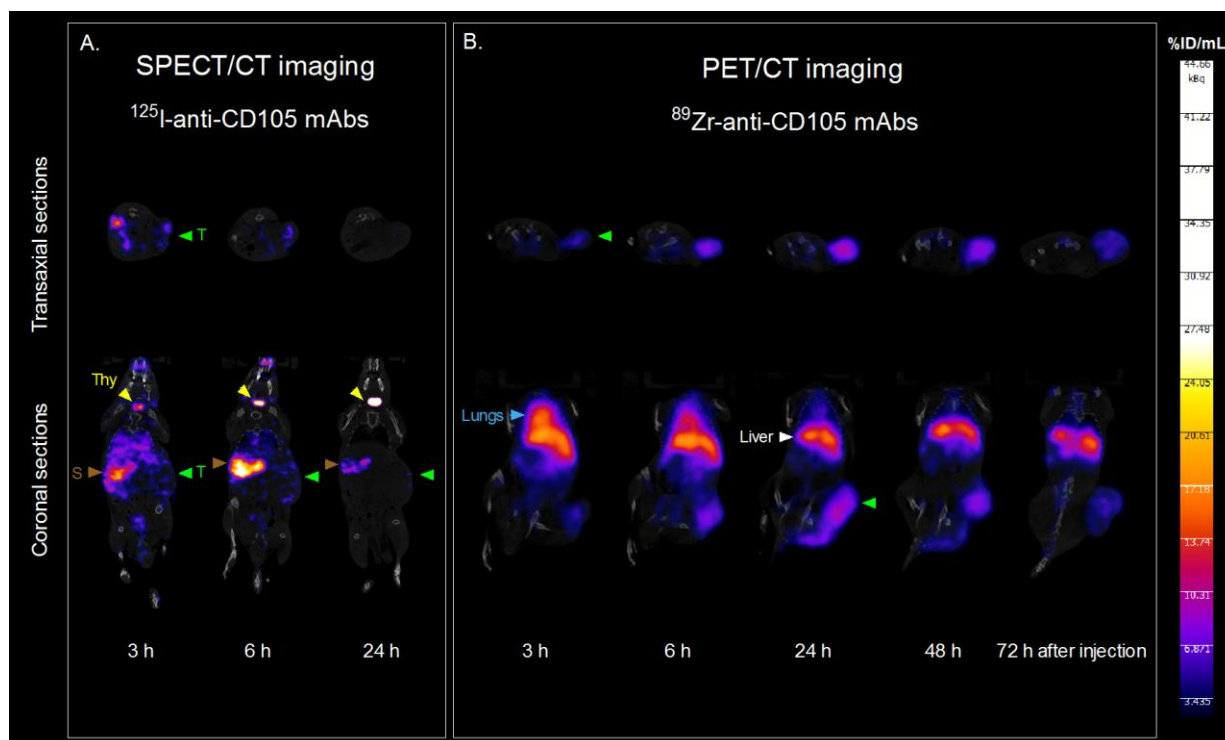


Fig. 8 B16-bearing C57BL/6J mice, injected with  $^{125}\text{I}$ -anti-CD105 mAbs [A] or  $^{89}\text{Zr}$ -anti-CD105 mAbs [B]. Transaxial (upper) and coronal (lower) SPECT/CT images were obtained at 3, 6, and 24 h after injection (total imaging time between 20 and 60 min) [A]. Transaxial (upper) and coronal (lower) PET/CT images were obtained at 3, 6, 24, 48 and 72 h after injection (total imaging time between 15 and 30 min). Color scales expressed as %ID mL<sup>-1</sup>, indicated radioactivity uptake levels in tumours (green arrows), in liver (white arrows), in lungs (blue arrows) and in stomach (brown arrows). The tumour is indicated with “T” letter and the stomach with “S” letter.

### **III. Targeting cancer cells using $^{89}\text{Zr}$ -labelled anti-EGFR antibody-conjugated gold nanoparticles**

Because of the observed limitations of direct radioiodination,  $^{89}\text{Zr}$  was used for antibody radiolabelling in our following studies. The third study describes *in vivo* distribution of  $^{89}\text{Zr}$ -labelled anti-EGFR antibody before and after conjugation to gold nanoparticles. The tissue uptakes of the tracer, with a focusing on tumour uptake, and the anti-EGFR antibody specificity after the nanoparticle conjugation were assessed through quantitative PET imaging.



**Antibody-functionalized nanoparticles for imaging cancer: influence of conjugation to gold nanoparticles on the biodistribution of  $^{89}\text{Zr}$ -labeled cetuximab in mice**

**Linda Karmani**, Daniel Labar, Vanessa Valembois, Virginie Bouchat, Praveen Ganesh Nagaswaran, Anne Bol, Jacques Gillart, Philippe Levêque, Caroline Bouzin, Davide Bonifazi, Carine Michiels, Olivier Feron, Vincent Grégoire, Stéphane Lucas, Thierry Vander Borghet and Bernard Gallez.

*Contrast Media Mol Imaging*. 2013;8:402-408.



# Antibody-functionalized nanoparticles for imaging cancer: influence of conjugation to gold nanoparticles on the biodistribution of $^{89}\text{Zr}$ -labeled cetuximab in mice

Linda Karmani<sup>a</sup>, Daniel Labar<sup>b</sup>, Vanessa Valembois<sup>c</sup>, Virginie Bouchat<sup>c</sup>, Praveen Ganesh Nagaswaran<sup>d</sup>, Anne Bol<sup>b</sup>, Jacques Gillart<sup>b</sup>, Philippe Levêque<sup>a</sup>, Caroline Bouzin<sup>e</sup>, Davide Bonifazi<sup>d</sup>, Carine Michiels<sup>f</sup>, Olivier Feron<sup>e</sup>, Vincent Grégoire<sup>b</sup>, Stéphane Lucas<sup>c</sup>, Thierry Vander Borgh<sup>b</sup> and Bernard Gallez<sup>a\*</sup>



Antibody-labeled gold nanoparticles represent a promising novel tool regarding cancer imaging and therapy. Nevertheless, the characterization of biodistribution of such immunonanocarriers has been poorly documented. In this study, the biodistribution of  $^{89}\text{Zr}$ -labeled cetuximab before and after the coupling reaction to gold nanoparticles (AuNPs) was compared and the quantitative imaging performance of  $^{89}\text{Zr}$  immuno-PET was evaluated. Cetuximab was functionalized with the desferal moiety and labeled with  $^{89}\text{Zr}$  ( $^{89}\text{Zr}$ -Df-Bz-NCS-cetuximab). AuNPs with a mean diameter of 5 nm were synthesized according a new method developed in the laboratory, and conjugated to  $^{89}\text{Zr}$ -Df-Bz-NCS-cetuximab using carbodiimide chemistry (AuNPs-PPAA-cetuximab- $^{89}\text{Zr}$ ). The two tracers were injected in A431 xenograft-bearing mice. Tumor and liver uptakes were assessed at different times after injection using quantitative PET imaging. The *in vivo* specificity of the binding was investigated using a saturating dose of unlabeled cetuximab. Radiolabeled cetuximab was conjugated to AuNPs with a coupling reaction yield >75%. All conjugates were stable *in vitro* and to a lesser extent in plasma. *In vivo* distribution studies revealed no significant difference in tumor uptake for cetuximab conjugated to nanoparticles up to 72 h after injection, compared with unconjugated cetuximab. Immuno-PET studies showed that AuNPs-PPAA-cetuximab- $^{89}\text{Zr}$  provided high tumor-to-background ratio. The liver uptake of AuNPs-PPAA-cetuximab- $^{89}\text{Zr}$  was higher, compared with  $^{89}\text{Zr}$ -Df-Bz-NCS-cetuximab. *In vivo* blocking experiments demonstrated selective tumor targeting after coupling reaction. This study showed that the conjugation of AuNPs to cetuximab did not affect its tumor accumulation and that the efficacy of EGFR-targeted nanoparticles was unaltered. The  $^{89}\text{Zr}$ -labeled cetuximab-targeted gold nanoparticles could be a valuable tool for theranostic purposes. Copyright © 2013 John Wiley & Sons, Ltd.

Supporting information may be found in the online version of this paper.

**Keywords:** immuno-PET; EGFR;  $^{89}\text{Zr}$ ; cetuximab-targeted gold nanoparticles; molecular imaging

## 1. INTRODUCTION

The emerging nanomedicines provide attractive tools that have a potential to improve cancer detection and therapy efficiency (1).

Gold nanoparticles (AuNPs) are known for their good biocompatibility profiles and their interesting properties. Owing to their optical absorption properties, gold nanoparticles have shown potential as contrast agents for optoacoustic cancer imaging (2)

\* Correspondence to: B. Gallez, Biomedical Magnetic Resonance Group, Louvain Drug Research Institute, Université Catholique de Louvain, Avenue Mounier 73, 1200 Brussels, Belgium. E-mail: Bernard.Gallez@uclouvain.be

a L. Karmani, P. Levêque, B. Gallez  
Biomedical Magnetic Resonance Group, Louvain Drug Research Institute, Université Catholique de Louvain, Avenue Mounier 73, 1200, Brussels, Belgium

b D. Labar, A. Bol, J. Gillart, V. Grégoire, T. V. Borgh  
Center for Molecular Imaging, Radiotherapy and Oncology, Institute of Experimental and Clinical Research, Université Catholique de Louvain, Avenue Hippocrate 54, 1200, Brussels, Belgium

c V. Valembois, V. Bouchat, S. Lucas  
Research Center for the Physics of Matter and Radiation, University of Namur,

Namur Research Institute for Life Sciences, Rue de Bruxelles 61, 5000, Namur, Belgium

d P. G. Nagaswaran, D. Bonifazi  
Namur Research College and Department of Chemistry, University of Namur, Rue de Bruxelles 61, 5000, Namur, Belgium

e C. Bouzin, O. Feron  
Pole of Pharmacology and Therapeutics, Institute of Experimental and Clinical Research, Université Catholique de Louvain, Avenue Mounier 53, 1200, Brussels, Belgium

f C. Michiels  
Unité de Recherche en Biologie Cellulaire, University of Namur, Namur Research Institute for Life Sciences, Rue de Bruxelles 61, 5000, Namur, Belgium

and can be used as photothermal agents in cancer therapy (3). However, their small size facilitates their entry into various cells and makes it difficult to use them for targeted delivery to specific tissues. Development of active targeting of nanoparticles, such as nanoparticle conjugation to tumor-specific ligands, may constitute the next generation of polymeric nanoparticles drug delivery systems and would be a solution to improve targeted delivery (4). The active targeting involves the incorporation of molecules that specifically bind an antigen or receptor that is either exclusively expressed or overexpressed on the tumor cell surface. Monoclonal antibodies (mAbs) have long been considered as interesting candidates for targeted cancer therapy and diagnostics, thanks to their highly specific targeting ability. Although antibodies are used successfully as intrinsic therapeutic agents, they have also the ability to be exploited as targeting agents (5). The antibody-targeted nanoparticles were expected as a strategy to enhance the efficacy of tumor targeting for nanoparticle delivery systems while reducing toxicity in normal tissues (4). To functionalize gold nanoparticles we have chosen cetuximab, a mouse-human chimeric monoclonal antibody that binds competitively and with high affinity to the epidermal growth factor receptor (EGFR). The EGFR is an attractive target for anticancer therapy (6) as this tyrosine kinase receptor is overexpressed in many epithelial solid tumors. Currently, cetuximab (Erbix<sup>®</sup>) is approved for the treatment of metastatic colorectal cancer and has been shown to inhibit ligand binding, receptor dimerization and downstream signaling by binding to extracellular domain of the EGFR (7). Several antibody-based strategies have been developed to block EGFR activation and are used clinically (8,9). Moreover, EGFR targeting has also been achieved using several immunoconjugates including cetuximab conjugated to gold nanoparticles (10–13).

Many studies have described the biological distribution of nanoparticles according to their size, shape, surface charge, mechanical properties and chemistry, as well as the route of administration (14), but few reports are available on biodistribution experiments with antibody-functionalized nanoparticles (15). For this purpose, we studied the impact of cetuximab conjugation to gold nanoparticles on their *in vivo* distribution behavior compared with unconjugated antibody. To trace these immunoconjugates, cetuximab was previously radiolabeled using zirconium-89 (<sup>89</sup>Zr). <sup>89</sup>Zr is a promising candidate for positron emission tomography (PET) (16). Immuno-PET using <sup>89</sup>Zr has been particularly applied in cancer research. In addition to numerous animal studies (17,18), the application of <sup>89</sup>Zr-labeled antibodies to detect primary tumors in human has been successfully demonstrated in several studies (19,20). In fact, antibody-based radiotracers require extended *in vivo* circulation times for optimal biodistribution and tumor targeting (21). Therefore, the long physical half-life of <sup>89</sup>Zr (78.41 h) is compatible with the time needed for most intact antibodies to achieve optimal tumor-to-nontumor ratio (typically 2–4 days). In the current study, we used the labeling of cetuximab with <sup>89</sup>Zr and animal PET imaging to monitor the influence of gold nanoparticles conjugation on the biological distribution of the antibody.

## 2. RESULTS AND DISCUSSION

### 2.1. Characterization of <sup>89</sup>Zr-labeled cetuximab and <sup>89</sup>Zr-cetuximab conjugated to AuNPs

Radiolabeling of Df-Bz-NCS-cetuximab with <sup>89</sup>Zr-oxalate was achieved with a mean radiochemical yield of 30% ( $n=6$ ),

whereas the radiochemical purity immediately after purification was >95% ( $n=6$ ). The resulting specific activity was  $50.9 \pm 9.8$  MBq mg<sup>-1</sup> of mAb ( $n=6$ ). Electrophoresis of <sup>89</sup>Zr-labeled Df-Bz-NCS-cetuximab under nonreducing conditions followed by radio-TLC and autoradiography showed a single band of 150 kDa corresponding to <sup>89</sup>Zr-Df-Bz-NCS-cetuximab and a single peak of radioactivity (see supplementary figure 1a in the online Supporting Information), which means that antibody integrity remained preserved after labeling reaction.

After coating nanoparticles with PPAA (plasma-polymerized allylamine), the nanoparticle diameters observed by transmission electron microscopy (TEM) imaging ranged from 3 to 10 nm (mean diameter of  $4.8 \pm 1.7$  nm) (22). The mean diameter of cetuximab after coupling to gold nanoparticles was determined by CPS disk centrifuge and was estimated about  $31.0 \pm 10.4$  nm (see supplementary figure 2 in the online Supporting Information). Electrophoresis of cetuximab-labeled gold nanoparticles under nonreducing conditions followed by radio-TLC showed a lower migration of AuNPs-PPAA-cetuximab-<sup>89</sup>Zr compared with <sup>89</sup>Zr-Df-Bz-NCS-cetuximab and two peaks of radioactivity corresponding to the position of the two species on the gel (see supplementary figure 1b in the online Supporting Information). The percentage of radioactivity linked to the peak of AuNPs-PPAA-cetuximab-<sup>89</sup>Zr expressed the coupling reaction yield, which was greater than 75% ( $n=3$ ). In order to enhance the coupling yield, the coupling reaction was achieved overnight. This conjugation step is quite long and inconvenient for possible future theranostic use of these nanoconjugates. The coupling reaction of antibodies to gold nanoparticles could be optimized for later studies by using another cross-linking method like click chemistry. The modern click chemistry method is known for its high coupling efficiency and shorter time of reaction compared with conventional carbodiimide chemistry (23). Thermogravimetric analysis revealed the number of coupled antibodies molecules per nanoparticle, which was estimated to be 5–10 mAbs per nanoparticle (22). Finally, a cell-based ELISA, phosphorylation assays and subsequent western blot analysis showed that the *in vitro* binding activity of cetuximab after coupling reaction to nanoparticles was quantitatively slightly reduced compared with uncoupled cetuximab but qualitatively preserved (22).

### 2.2. PET evaluation of <sup>89</sup>Zr-labeled cetuximab biodistribution in mice before and after coupling reaction to AuNPs

Two groups of A431 bearing nude mice were injected with <sup>89</sup>Zr-Df-Bz-NCS-cetuximab or AuNPs-PPAA-cetuximab-<sup>89</sup>Zr, respectively. We compared the pharmacokinetic behavior of AuNPs-PPAA-cetuximab-<sup>89</sup>Zr with that of <sup>89</sup>Zr-Df-Bz-NCS-cetuximab, as a reference compound. Figure 1 shows representative PET images of A431 xenograft bearing nude mice at 48 h after tracer injection, and compares the distributions of <sup>89</sup>Zr-Df-Bz-NCS-cetuximab (Fig. 1a) and AuNPs-PPAA-cetuximab-<sup>89</sup>Zr (Fig. 1b). The accumulation of the two tracers was most predominantly observed in the liver (red arrows) and in tumors implanted in both legs (green arrows). For both radioimmunoconjugates, a similar pattern was observed, but with a higher liver and spleen uptake for AuNPs-PPAA-cetuximab-<sup>89</sup>Zr. This distribution pattern remained constant at later time points (data not shown). 3D videos related to PET study are available online as supplementary materials 3 and 4 for <sup>89</sup>Zr-Df-Bz-NCS-cetuximab and AuNPs-PPAA-cetuximab-<sup>89</sup>Zr respectively (Supporting Information).

In the tumor, the kinetics were slow for both coupled and uncoupled <sup>89</sup>Zr-labeled cetuximab (Fig. 2a), with a maximum uptake reached

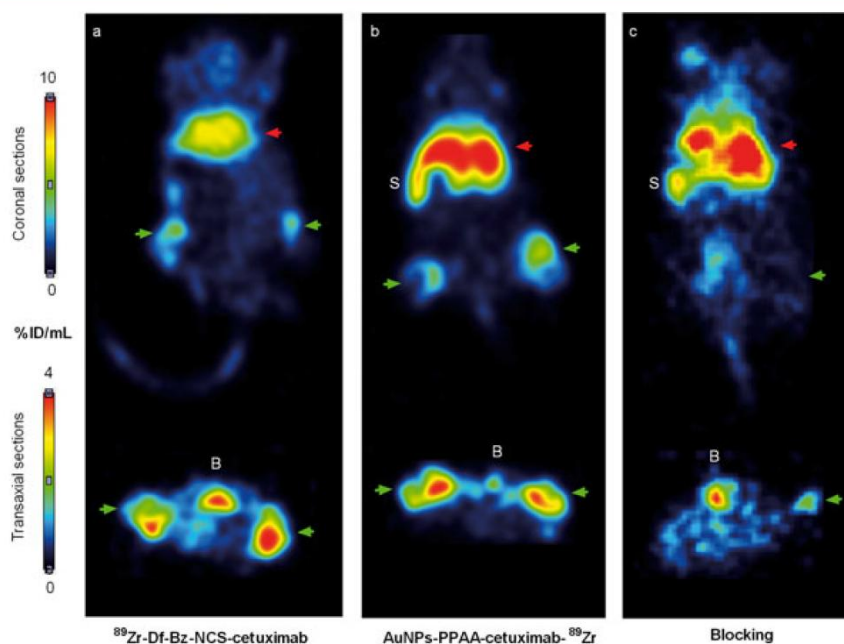


**Figure 1.** A431-bearing nude mice, injected with  $^{89}\text{Zr}$ -Df-Bz-NCS-cetuximab (a) or AuNPs-PPAA-cetuximab- $^{89}\text{Zr}$  (b) (two tumors per mouse), or AuNPs-PPAA-cetuximab- $^{89}\text{Zr}$  2 h after a blocking dose of unlabeled cetuximab (c) (one tumor per mouse). Coronal (upper) and transaxial (lower) PET images were obtained 48 h after injection. Color scales, expressed as  $\% \text{ID mL}^{-1}$ , indicate radioactivity uptake levels in tumors (green arrows) and in liver (red arrows). The bladder is indicated with 'B' and the spleen with 'S'.

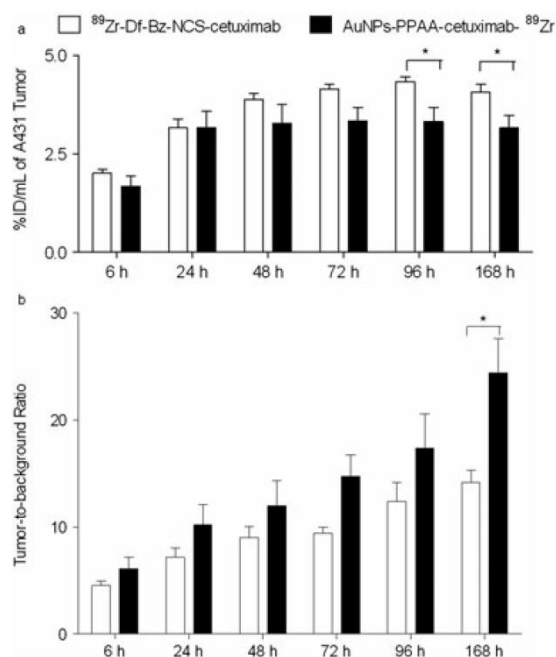


**Figure 2.** Tumor uptake (a) and tumor-to-background ratio (b) of  $^{89}\text{Zr}$ -Df-Bz-NCS-cetuximab (white bars) or AuNPs-PPAA-cetuximab- $^{89}\text{Zr}$  (black bars) in A431-bearing nude mice at 6, 24, 48, 72, 96 and 168 h after injection. Injected activity ranged from 3.3 to 4.6 MBq, corresponding to a total of 200–350  $\mu\text{g}$  mAb per mouse. Results are expressed as means  $\pm$  SEM ( $n = 3\text{--}5$ ). \*  $p < 0.05$ .

after 48 h and followed by a plateau phase ( $3.9 \pm 0.1$  for  $^{89}\text{Zr}$ -Df-Bz-NCS-cetuximab and  $3.3 \pm 0.5$  for AuNPs-PPAA-cetuximab- $^{89}\text{Zr}$ ). No difference in tumor uptake between the two groups was seen at early time points. A small, statistically significant difference of uptake was noted at 96 and 168 h. In terms of tumor-to-background ratio, a continuous increase was observed over time, with no difference between the two groups except for the latest time point (168 h) in favor of AuNPs-PPAA-cetuximab- $^{89}\text{Zr}$  (Fig. 2b). This trend suggested a lower background for mice receiving antibody conjugated to gold nanoparticles, which would probably be related to the more important tracer uptake by the reticuloendothelial system and particularly by the liver. Thus, we demonstrated that the tumor uptake of the vectorized gold nanoparticles was mostly similar to that of uncoupled cetuximab. A small difference could only be seen for late time points, the tumor uptake being then slightly lower for the AuNPs-PPAA-cetuximab- $^{89}\text{Zr}$  when expressed as percentage of the injected dose per milliliter ( $\% \text{ID mL}^{-1}$ ), but higher when expressed as tumor-to-background ratio. The preservation of high tumor contrast after nanoparticle conjugation, expressed as tumor-to-background ratio, supports the good imaging properties of AuNPs-PPAA-cetuximab- $^{89}\text{Zr}$ .

Major differences between both biodistribution patterns were observed for liver and spleen uptake (Fig. 1). For each time point considered, it must be mentioned that the liver uptake for AuNPs-PPAA-cetuximab- $^{89}\text{Zr}$  was quite important, more than twice as that of the unconjugated cetuximab (Fig. 3). The uptake by the liver was fast and the maximum uptake value was reached at 6 h after tracer injection ( $13.4 \pm 0.6$  for AuNPs-PPAA-cetuximab- $^{89}\text{Zr}$  and  $7.5 \pm 0.3$  for  $^{89}\text{Zr}$ -Df-Bz-NCS-cetuximab). One of the limitations of antibody-based imaging is the high background signal in the reticuloendothelial system, which was particularly

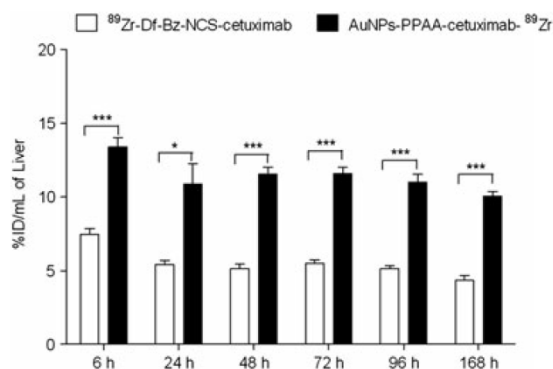


**Figure 3.** Liver uptake of <sup>89</sup>Zr-Df-Bz-NCS-cetuximab (white bars) or AuNPs-PPAA-cetuximab-<sup>89</sup>Zr (black bars) in A431 bearing nude mice at 6, 24, 48, 72, 96 and 168 h after injection. Injected activity ranged from 3.3–4.6 MBq corresponding to a total of 200–350  $\mu$ g mAb per mouse. Results are expressed as means  $\pm$  SEM ( $n = 3$ –5). \*  $p < 0.05$ ; \*\*\*  $p < 0.0001$ .

illustrated in our study by liver uptake of <sup>89</sup>Zr-Df-Bz-NCS-cetuximab. Moreover, the colloidal properties of gold nanoparticles could be the cause of the enhanced AuNPs-PPAA-cetuximab-<sup>89</sup>Zr accumulation in the reticuloendothelial system.

The specificity of tumor uptake was investigated by administering a saturating dose of unlabeled cetuximab 2 h before AuNPs-PPAA-cetuximab-<sup>89</sup>Zr injection. In this saturation experiment, the binding of AuNPs-PPAA-cetuximab-<sup>89</sup>Zr was markedly reduced in the tumor, as illustrated on images obtained 48 h after injection of the tracer (Fig. 1c). The residual activity in the tumor was significantly lower for the blocking group at each time point compared with tumor uptake in mice injected with only AuNPs-PPAA-cetuximab-<sup>89</sup>Zr (Fig. 4a). In fact, the tumor uptake value in the blocking group ( $1.5 \pm 0.1$  %ID ml<sup>-1</sup>) was reduced by a factor of 2.2 at 48 h after injection compared with mice receiving only AuNPs-PPAA-cetuximab-<sup>89</sup>Zr ( $3.3 \pm 0.5$  %ID ml<sup>-1</sup>). In terms of tumor-to-background ratio, the reduction in tumor uptake for the blocking group was more pronounced and was significant at each time point, compared with the nonsaturating group (Fig. 4b). Indeed, the tumor-to-background ratio value was equal to  $3.4 \pm 0.5$  for the blocking group and  $12.0 \pm 2.3$  for mice receiving only AuNPs-PPAA-cetuximab-<sup>89</sup>Zr, at 48 h after injection. We demonstrated that administration of unlabeled antibodies in excess before AuNPs-PPAA-cetuximab-<sup>89</sup>Zr injection induced the saturation of EGFR binding sites and decreased significantly the EGFR-binding of AuNPs-PPAA-cetuximab-<sup>89</sup>Zr in tumors. These results suggested the selective accumulation and the EGFR-specific binding of AuNPs-PPAA-cetuximab-<sup>89</sup>Zr *in vivo*. It also confirmed the preservation of the EGFR recognition by the antibody after its radiolabeling and coupling to nanoparticles in agreement with previous *in vitro* studies showing its preservation after chelation and radiolabeling (24,25). Indeed, the functionalization of cetuximab with a three-fold molar excess of Df-Bz-NCS led to a reproducible chelate:mAb substitution ratio of 1.5:1. Such a low chelate:mAb ratio was reported not to alter the pharmacokinetic nor the immunoreactivity of the antibody. In addition, our previous studies showed that the *in vitro* binding activity of AuNPs-PPAA-cetuximab-<sup>89</sup>Zr ( $EC_{50}$  0.08  $\mu$ g ml<sup>-1</sup>) remained in the same range as for <sup>89</sup>Zr-Df-Bz-NCS-cetuximab ( $EC_{50}$  0.19  $\mu$ g ml<sup>-1</sup>) (22).

Finally, it can also be emphasized that we did not observe radioactivity accumulation in other nonspecific organs, apart from

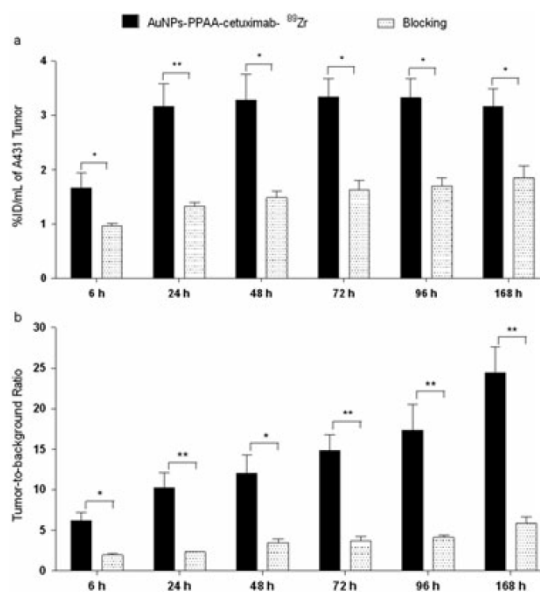


**Figure 4.** Tumor uptake (a) and tumor-to-background ratio (b) of AuNPs-PPAA-cetuximab-<sup>89</sup>Zr (3.3–4.6 MBq, total of 200–350  $\mu$ g mAb per mouse) or AuNPs-PPAA-cetuximab-<sup>89</sup>Zr (2.2–3.5 MBq, total of 200  $\mu$ g mAb per mouse) after a blocking dose of unlabeled cetuximab (2000  $\mu$ g mAb per mouse) in A431-bearing nude mice at 6, 24, 48, 72, 96 and 168 h after injection. Results are expressed as means  $\pm$  SEM ( $n = 3$ ). \*  $p < 0.05$ ; \*\*  $p < 0.01$ .

liver, spleen and bones. For the two groups of mice and starting from 24 h after injection, the maximum intensity projection images showed an accumulation of radioactivity in bones, which was particularly enhanced at 48 h after injection (Fig. 5). PET images displayed distinct hot spots in joints (shoulders and knees) and in the whole mouse backbone. A similar pattern of skeleton uptake was also reported for <sup>89</sup>Zr-labeled trastuzumab (26). The bone uptake might be assigned to the detachment of <sup>89</sup>Zr from

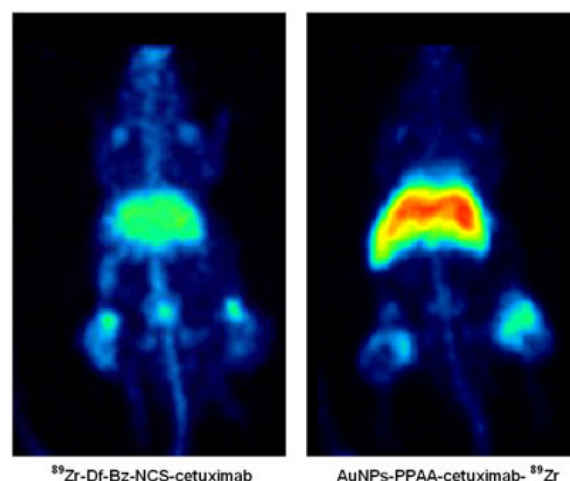


**Figure 5.** Maximum intensity projection of <sup>89</sup>Zr-Df-Bz-NCS-cetuximab (left) and AuNPs-PPAA-cetuximab-<sup>89</sup>Zr (right) 48 h after injection in A431-bearing nude mice (two tumors per mouse). Upper and lower intensity threshold were set at 100% and 0% respectively.

the desferal moiety. First, we observed that the two tracers were not fully stable in physiological conditions, a release of free  $^{89}\text{Zr}$  being observed up to 10% after 24 h of plasmatic *in vitro* incubation. Second, previous studies attributed constant bone accumulation to the strong affinity of free  $^{89}\text{Zr}^{4+}$  for hydroxylapatite and phosphate constituents of bones. In fact, zirconium is known to bind to plasma proteins and it is later deposited in mineral bone (27). Other studies hypothesized that high murine bone uptake is also due to the liver metabolism of the conjugate and the release of free  $^{89}\text{Zr}$  into the circulation (28).

### 3. CONCLUSIONS

Development of more efficient drug delivery systems is important to effectively target cancer cells. Gold nanoparticles, used as scaffolds to which antibodies are attached, were previously described as valuable tools for imaging and/or treating cancers. Nevertheless, the characterization of *in vivo* distribution of such scaffolds was poorly documented. Because our group has recently developed a method to synthesize gold nanoparticles (29), we addressed in this work the question of the nanoparticle vectorization through conjugation to cetuximab, a specific monoclonal antibody directed against EGFR. We combined the targeting properties of cetuximab and favorable imaging properties of  $^{89}\text{Zr}$  to further characterize the *in vivo* behaviour of these vectorized nanoparticles and the *in vivo* impact of nanoparticle conjugation on antibody distribution by using noninvasive PET imaging.

We demonstrated that the conjugation of cetuximab to gold nanoparticles does not significantly affect the EGFR-dependent tumor uptake in mice. However, the reticuloendothelial system uptake of  $^{89}\text{Zr}$ -labeled cetuximab conjugated to gold nanoparticles was higher than for  $^{89}\text{Zr}$ -labeled antibody alone. This could be a limitation for the use of radioactive nanoparticles for systemic metabolic radiotherapy, but not for strategies based on photothermal therapy where nanoparticle activation can be controlled. Overall, PET-imaging using  $^{89}\text{Zr}$ -labeled antibodies is a powerful tool to analyse the *in vivo* properties of complex systems like immunonanocarriers suggested for theranostic applications and more specifically for photodynamic therapy, which is an attractive alternative to surgery or radiation for the management of malignant tumors.

### 4. EXPERIMENTAL

#### 4.1. Production and purification of $^{89}\text{Zr}$

$^{89}\text{Zr}$  was produced and purified as previously described (30,31). In brief,  $^{89}\text{Zr}$  was produced in-house via a (p,n) reaction on natural yttrium ( $^{89}\text{Y}$ ) using a Cyclone<sup>®</sup> 30 cyclotron (IBA, Louvain-la-Neuve, Belgium). For this purpose, 100 mg of 100% ( $^{89}\text{Y}$ )- $\text{Y}_2\text{O}_3$  powder (Sigma-Aldrich, Belgium, 99.99% purity) was bombarded with incident proton-beam ( $E_p = 14$  MeV, 10  $\mu\text{A}$ ) for about 10 h.

The irradiated  $^{89}\text{Y}$  target was dissolved in 6 mol  $\text{L}^{-1}$  HCl (Sigma-Aldrich, Belgium) at 120 °C for 30 min, then diluted with water (>18 M $\Omega$   $\text{cm}^{-1}$ , 25 °C, Milli-Q, Millipore) to ensure a final concentration of 2 mol  $\text{L}^{-1}$  HCl. The obtained solution was loaded onto a solid-phase hydroxamate column (100 mg), which was prepared as previously reported (30,32). The column was washed with 2 mol  $\text{L}^{-1}$  HCl and Milli-Q water, respectively, to remove  $^{89}\text{Y}$  ions and other radionuclidic metal impurities.  $^{89}\text{Zr}$  was finally slowly eluted with 1 mol  $\text{L}^{-1}$  oxalic acid (Sigma-Aldrich, 99.999% purity). All used reagents and solvents were of trace analysis quality.

#### 4.2. Preparation and characterization of $^{89}\text{Zr}$ -labeled cetuximab

$^{89}\text{Zr}$ -Df-Bz-NCS-cetuximab was prepared according to a protocol previously described (33,34). First, cetuximab (Erbix<sup>®</sup> 5 mg  $\text{mL}^{-1}$ , Merck, Belgium) was purified by discontinuous filtration in centrifugal filter device with a molecular weight cut-off of 10 kDa (Vivaspin, Sartorius, Belgium). Then, the purified cetuximab was functionalized with the bifunctional chelating agent *p*-isothiocyanatobenzyl-desferrioxamine (Df-Bz-NCS, Macrocylics, Dallas, TX, USA). In short, a three-fold molar excess of Df-Bz-NCS in 20  $\mu\text{L}$  DMSO (Sigma-Aldrich, Belgium) was added to the antibody solution (2 mg in 1 ml 0.1 M  $\text{NaHCO}_3$  buffer, pH 9.0) and incubated for 30 min at 37 °C. The isothiocyanate group of the chelate agent forms a thiourea bond with a primary amine of the antibody lysine groups. Finally, the functionalized cetuximab (Df-Bz-NCS-cetuximab) was purified by size exclusion chromatography using a PD10 column (GE Healthcare Life Sciences, Belgium) and radiolabeled with produced  $^{89}\text{Zr}$  (111 MBq) at room temperature for 60 min, followed by gel filtration purification using 5 mg  $\text{mL}^{-1}$  gentisic acid in 0.25 M sodium acetate (pH 5.4–5.6) as mobile phase. During the critical steps of the antibody functionalization and radiolabeling, the pH was carefully adjusted with a pH meter (Inolab<sup>®</sup>, pH 730, WTW) equipped with a micro pH electrode (Inlab<sup>®</sup> Micro, Mettler Toledo).

The radiochemical yield and purity were determined using instant thin-layer chromatography (ITLC) and 20 mM citric acid (pH 4.9–5.1) as mobile phase. ITLC migration was followed by radio-TLC detection (Mini-Gita TLC scanner, Raytest, Germany) and showed that the radiolabeled antibody migrated with  $R_f < 0.1$ , whereas unbound  $^{89}\text{Zr}$  migrated to the solvent front ( $R_f$  is the distance that compound has traveled divided by the distance that the solvent has traveled). In addition, the integrity of the antibody after radiolabeling was checked using sodium dodecyl sulfate–polyacrylamide gel electrophoresis (10% SDS–PAGE gel, under nonreducing conditions), followed by radio-TLC detection (Bioscan system 200 imaging scanner), and by scanning gel using Phosphor Imager (Fujifilm FLA-5100) analysis.

#### 4.3. Synthesis and characterization of $^{89}\text{Zr}$ -labeled cetuximab and conjugated to AuNPs

The gold nanoparticles were synthesized and coated with PPAA by physical vapour deposition as previously described by our group (29). The coated nanoparticles (AuNPs–PPAA) were purified by discontinuous filtration in centrifugal filter device with a molecular weight cut-off of 10 kDa. Cetuximab was then coupled to coated nanoparticles using carbodiimide chemistry, as recently described (35). In summary, the amino groups present in the polymeric coating of AuNPs–PPAA were exploited to form an amide bond with the carboxyl groups of the antibody. About 1 mg of  $^{89}\text{Zr}$ -Df-Bz-NCS-cetuximab was added in 5 ml of an aqueous solution containing 95 mg of 2-(*N*-morpholino)ethanesulphonic acid hydrate (Sigma-Aldrich, Belgium), 1 mg of *N*-hydroxysulphosuccinimide (Sigma-Aldrich, Belgium) and 1 mg of 3-carbodiimide hydrochloride (Sigma-Aldrich, Belgium). The mixture was stirred for 20 min at 25 °C, after which the aqueous solution of AuNPs–PPAA (1.3 mg, 2 ml) was added. The reaction was stirred at 25 °C for a period of 16 h. The  $^{89}\text{Zr}$ -labeled antibodies conjugated to nanoparticles (AuNPs–PPAA–cetuximab– $^{89}\text{Zr}$ ) were purified by filtration, using membrane filter of molecular weight cut-off of 300 kDa (Millipore, Belgium).

Transmission electron microscopy (Philips Tecnai 10 transmission electron microscope) was carried out to assess the morphology

and size distribution of AuNPs-PPAA as previously described (35). Differential centrifugal sedimentation (DC 24000 Disc Centrifuge; CPS Instruments Inc.) was achieved to determine the size of AuNPs-PPAA-cetuximab-<sup>89</sup>Zr by measuring the time required for the radioimmunoconjugates to traverse a sucrose density gradient created in a disk centrifuge. This method uses calibrated gold nanoparticles coated layer-by-layer with polyelectrolytes to estimate the size of the tracer (35). The efficiency of conjugation reaction between gold nanoparticles and radiolabeled cetuximab was assessed using electrophoresis gel (10% SDS-PAGE gel, under nonreducing conditions), followed by a radio-TLC analysis. Thermogravimetric analysis were performed with a TGA Q500 instrument (TA instruments, Italy) to evaluate AuNPs-PPAA-cetuximab-<sup>89</sup>Zr composition as previously reported (22). A cell-based ELISA was achieved to assess the relative binding affinity. In addition, phosphorylation assays and subsequent western blot analysis were carried out to control the preservation of the cetuximab ability to inhibit the EGF-induced phosphorylation of EGFR after its conjugation to nanoparticles (22).

#### 4.4. *In vitro* stability of radioimmunoconjugates in storage solution and in plasma

Chemical stability of purified <sup>89</sup>Zr-Df-Bz-NCS-cetuximab and AuNPs-PPAA-cetuximab-<sup>89</sup>Zr in a solution of 5 mg ml<sup>-1</sup> gentisic acid in 0.25 M sodium acetate, pH 5.4–5.6, was checked in storage conditions at 4 °C. Samples were drawn at regular time points and the proportion of free <sup>89</sup>Zr was analyzed by radio-TLC. In these conditions, the release of free <sup>89</sup>Zr was lower than 20%, 2 weeks after labeling reaction.

*In vitro* plasmatic stability of both <sup>89</sup>Zr-Df-Bz-NCS-cetuximab and AuNPs-PPAA-cetuximab-<sup>89</sup>Zr was studied in fresh mouse plasma, by incubating the solution of radiolabeled antibodies (1:2 v/v dilution at a final concentration of 1.6 MBq ml<sup>-1</sup>; sodium azide added to 0.02%) at 37 °C with stirring. At different time points (6, 24, 48, 72 and 96 h), aliquots of plasma (10 µl) were analysed using radio-TLC and this showed that <sup>89</sup>Zr was slightly dissociated from the antibody over time. Starting from a solution without free <sup>89</sup>Zr (100% purity), the percentages of dissociation were <5% after 6 h, 10% after 24 h, 15% after 48 h and 20% after 72 and 96 h, for both radioimmunoconjugates.

#### 4.5. Comparative biodistribution studies in mice using animal-PET imaging

For the biodistribution and PET studies, NMRI male nude mice (32–37 g, 5–7 weeks old; Janvier, France) bearing human epithelial carcinoma xenografts (A431) were used. A431 cancer cell line was maintained in appropriate medium Dulbecco's modified Eagle's medium (glucose 4.5 g l<sup>-1</sup> without pyruvate, Gibco-Invitrogen, Belgium), supplemented with 10% heat inactivated fetal bovine serum (Gibco-Invitrogen, Belgium) and 1% streptomycin-penicillin (Gibco-Invitrogen, Belgium). A431 cells (10 × 10<sup>6</sup>) were inoculated subcutaneously into flanks of NMRI nude mice (two tumors per mouse). Mice were used for *in vivo* experiments when the diameter of tumors reached 7–8.5 mm. All animal experiments were conducted in accordance with national and university animal care regulations.

To compare the pharmacokinetic behavior of radiolabeled antibody conjugated to gold nanoparticles and uncoupled radiolabeled antibody, two groups of three to five mice were injected intravenously into the lateral tail vein with either freshly prepared <sup>89</sup>Zr-Df-Bz-NCS-cetuximab or with AuNPs-PPAA-

cetuximab-<sup>89</sup>Zr, (3.3–4.6 MBq, total of 200–350 µg mAb per mouse). Additionally, to assess the *in vivo* specificity of cetuximab-conjugated gold nanoparticles, a group of three A431 tumor-bearing mice (blocking group, one tumor per mouse) was injected with an excess of unlabeled cetuximab (2 mg mAb per mouse) 2 h before the injection of AuNPs-PPAA-cetuximab-<sup>89</sup>Zr (2.2–3.5 MBq, total of 200 µg mAb per mouse) as previously described (36). The blocking group was compared with the group of mice who received only AuNPs-PPAA-cetuximab-<sup>89</sup>Zr without a saturating dose.

PET imaging was performed using a dedicated small-animal PET scanner (MOSAIC, Philips Medical Systems; Cleveland, USA) with a spatial resolution of 2.5 mm (full width at half maximum) (37). Mice were imaged under anesthesia by inhalation of 1.5% isoflurane (Abbott Laboratories, Belgium)-oxygen gas mixture (2 l min<sup>-1</sup>). The PET acquisitions were carried out with an energy window of 410–660 keV. Static acquisitions were performed at different time points (6, 24, 48, 72, 96 and 168 h after tracer injection). For emission scans, acquisition time was adapted to compensate for decay in order to ensure significant statistics. Before reconstruction, raw data were corrected for random and scattered coincidences, as well as for system dead time. For attenuation correction of emission data, transmission scans were acquired using a 370 MBq <sup>137</sup>Cs source. All images were reconstructed with a fully 3D iterative algorithm (3D-RAMLA). The reconstructed matrix consisted of 120 transverse images of 128 × 128 voxels, with a voxel size of 1 mm<sup>3</sup>.

#### 4.6. PET data analyses

PET data were analyzed using PMOD software (PMOD™, version 3.3, PMOD Technologies Ltd, Zurich, Switzerland). Regions of interest (ROIs) were delineated after image normalization. An empirically determined system calibration factor for mice was used to convert the ROI value (counts per pixel per minute) to activity concentration (nCi ml<sup>-1</sup>). Image scale was first corrected according to the PET calibration factor, including the positron branching ratio, the physical decay to the time of injection, the acquisition period and the injected dose. This normalization was used to parameterize images in terms of percentage of the injected dose per milliliter.

The 2D ROIs were established on consecutive transversal slices using a 50% isocontour tool (ROI including the pixel values greater than 50% of the maximum pixel) that semiautomatically defined a 3D volume of interest around the tissue of interest. The tracer uptake was assessed in liver and tumors. Moreover, a background region was drawn in the pelvic region. The same background volume was applied for all animal analyses and it was representative for tissues with low nonspecific uptake. The tumor uptake was also expressed as tumor-to-background ratio, calculated as the mean activity in tumor region divided by the mean activity obtained in the background region.

#### 4.7. Statistical analysis

Results are given as means ± SEM values from n animals. Data calculations were performed with Prism software (Graph Pad™ Software Inc., version 5.02). The differences in tissue uptake between two groups were considered significant if the *p*-values from unpaired *t*-tests were ≤0.05 (\*), ≤0.01 (\*\*) or ≤0.001 (\*\*\*). The differences in tissue uptake at different time points were assessed by the one-way analysis of variance and Tukey *post-hoc* test.

## Supporting Information

Supporting information can be found in the online version of this article.

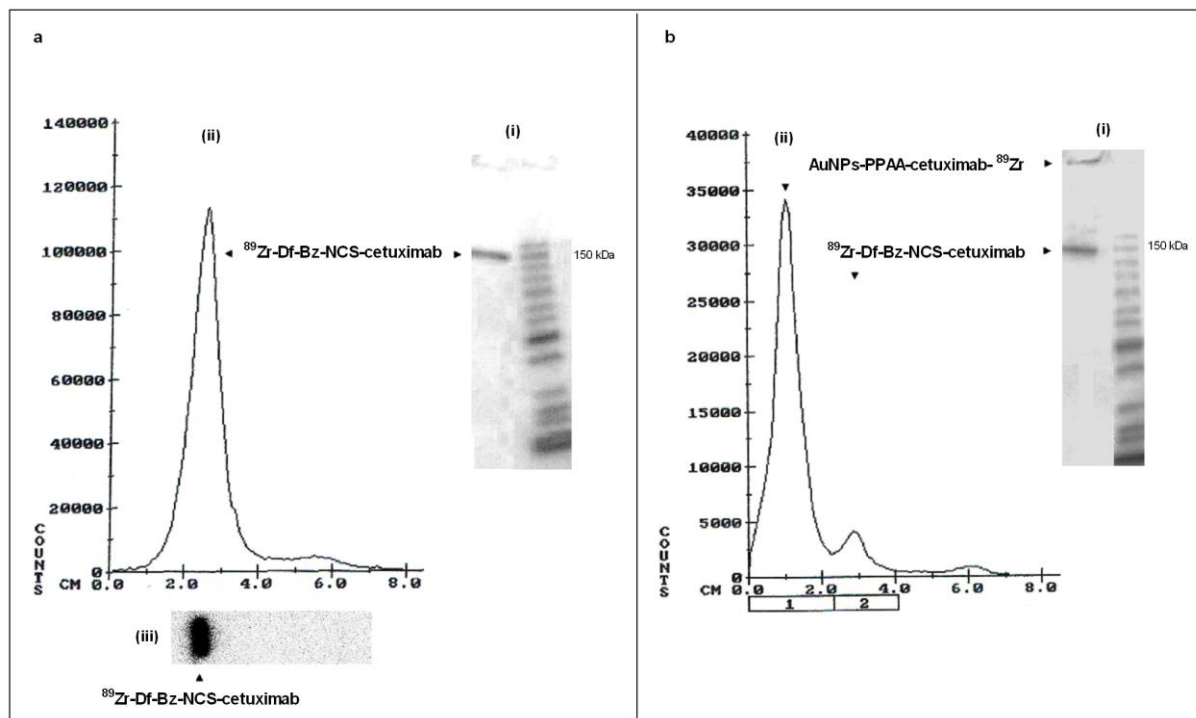
## Acknowledgments

This work was supported by grants from the Region Wallone through the 'TARGAN' project and the Belgian National Fund for Scientific Research (FNRS-TELEVE).

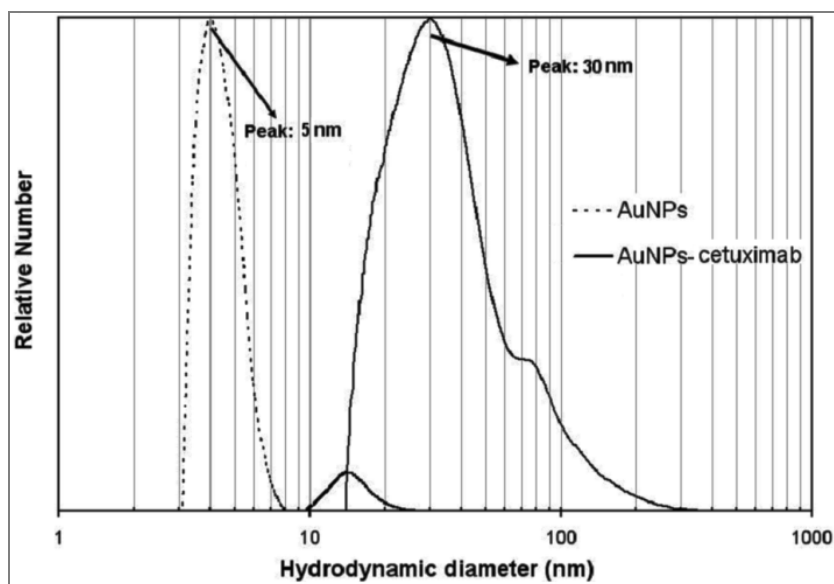
## REFERENCES

- Bharali DJ, Mousa SA. Emerging nanomedicines for early cancer detection and improved treatment: current perspective and future promise. *Pharmacol Ther* 2010;128:324–335.
- Mallidi S, Larson T, Aaron J, Sokolov K, Emelianov S. Molecular specific optoacoustic imaging with plasmonic nanoparticles. *Opt Express* 2007;15:6583–6588.
- Glaser ES, Massey KL, Zhu C, Curley SA. Pancreatic carcinoma cells are susceptible to noninvasive radio frequency fields after treatment with targeted gold nanoparticles. *Surgery* 2010;148:319–324.
- Tiwari PM, Vig K, Dennis VA, Singh R. Functionalized gold nanoparticles and their biomedical applications. *Nanomaterials* 2011;1:31–63; doi: 10.3390/nano1010031
- Fay F, Scott CJ. Antibody-targeted nanoparticles for cancer therapy. *Immunotherapy* 2011;3:381–394.
- Mendelsohn J, Baselga J. Epidermal growth factor receptor targeting in cancer. *Semin Oncol* 2006;33:369–385.
- Li S, Schmitz KR, Jeffrey PD, Wiltzius JJ, Kussie P, Ferguson KM. Structural basis for inhibition of the epidermal growth factor receptor by cetuximab. *Cancer Cell* 2005;7:301–311.
- Tejani MA, Cohen RB, Mehra R. The contribution of cetuximab in the treatment of recurrent and/or metastatic head and neck cancer. *Biologics* 2010;4:173–185; PMID: 20714355
- Fakih M, Wong R. Efficacy of the monoclonal antibody EGFR inhibitors for the treatment of metastatic colorectal cancer. *Curr Oncol* 2010;17 suppl 1:S3–17.
- El-Sayed IH, Huang X, El-Sayed MA. Selective laser photo-thermal therapy of epithelial carcinoma using anti-EGFR antibody conjugated gold nanoparticles. *Cancer Lett* 2006;239:129–135.
- Sokolov K, Follen M, Aaron J, Pavlova I, Malpica A, Lotan R, Richards-Kortum R. Real-time vital optical imaging of precancer using anti-epidermal growth factor receptor antibodies conjugated to gold nanoparticles. *Cancer Res* 2003;63:1999–2004.
- Kah JCY, Olivo MC, Lee CGL, Sheppard CJR. Molecular contrast of EGFR expression using gold nanoparticles as a reflectance-based imaging probe. *Mol Cell Probes* 2008;22:14–23.
- El-Sayed IH, Huang X, El-Sayed MA. Surface Plasmon resonance scattering and absorption of anti-EGFR antibody conjugated gold nanoparticles in cancer diagnostics: application in oral cancer. *Nano Lett* 2005;5:829–834; doi: 10.1021/nl050074e
- Sonavane G, Tomoda K, Makino K. Biodistribution of colloidal gold nanoparticles after intravenous administration: effect of particle size. *Colloids Surf B Biointerfaces* 2008;66:274–280.
- Schroeder A, Heller DA, Winslow MM, Dahlman JE, Pratt GW, Langer R, Jacks T, Anderson DG. Treating metastatic cancer with nanotechnology. *Nat Rev Cancer* 2012;12:39–50; doi: 10.1038/nrc3180
- Vugts DJ, van Dongen GAMS. <sup>89</sup>Zr-labeled compounds for PET imaging guided personalized therapy. *Drug Discov Today Technol* 2011;8:e53–e61; doi: 10.1016/j.ddtec.2011.12.004.
- Meijs WE, Haisma HJ, Klok RP, van Gog FB, Kievit E, Pinedo HM, Herscheid JD. Zirconium-labeled monoclonal antibodies and their distribution in tumor-bearing nude mice. *J Nucl Med* 1997;38:112–118.
- Dijkers ECF, Kosterink JGW, Rademaker AP, Perk LR, van Dongen GAMS, Bart J, de Jong JR, de Vries EG, Lub-de Hooge MN. Development and characterization of clinical-grade Zr-89-trastuzumab for HER2/neu immunoPET imaging. *J Nucl Med* 2009;50:974–981; doi: 10.2967/jnumed.108.060392
- Borjesson PK, Jauw YW, Boellaard R, de Bree R, Comans EF, Roos JC, Castelijns JA, Vosjan MJ, Kummer JA, Leemans CR, Lammertsma AA, van Dongen GA. Performance of immuno-positron emission tomography with zirconium-89-labeled chimeric monoclonal antibody U36 in the detection of lymph node metastases in head and neck cancer patients. *Clin Cancer Res* 2006;12:2133–2140.
- Borjesson PKE, Jauw YWS, de Bree R, Roos JC, Castelijns JA, Leemans CR, van Dongen GA, Boellaard R. Radiation dosimetry of zirconium-89-labeled chimeric monoclonal antibody U36 as used for immuno-PET in head and neck cancer patients. *J Nucl Med* 2009;50:1828–1836.
- van Dongen GAMS, Visser GWM, Lub-de-Hooge MN, De Vries EG, Perk LR. Immuno-PET: A navigator in monoclonal antibody development and applications. *Oncologist* 2007;12:1379–1389.
- Marrega R, Karmani L, Flamant L, Nageswaran PG, Valembois V, Masereel B, Feron O, Vander Borgh T, Lucas S, Michiels C, Gallez B and Bonifazi D. Antibody-functionalized polymer-coated gold nanoparticles targeting cancer cells: an in vivo and in vitro study. *J Mater Chem* 2012;22:21305–21312.
- Thorek DLJ, Elias DR and Tsourkas A. Comparative analysis of nanoparticle-antibody conjugations: carbodiimide versus click chemistry. *Mol Imag* 2009;8:221–229.
- van Gog FB, Visser GWM, Klok RP, van der Schors R, Snow GB, van Dongen GAMS. Monoclonal antibodies labeled with rhenium-186 using the MAG3 chelate: relationship between the number of chelated groups and biodistribution characteristics. *J Nucl Med* 1996;37:352–362.
- Kukis DL, DeNardo GL, DeNardo SJ, Mirick GR, Miers LA, Greiner DP, Meares CF. Effect of the extent of chelate substitution on the immunoreactivity and biodistribution of 2IT-BAT-Lym-1 immunoconjugates. *Cancer Res* 1995;55:878–884.
- Tinianow JN, Gill HS, Ogasawara A, Flores JE, Vanderbilt AN, Luis E, Vandlen R, Darwish M, Junutula JR, Williams SP, Marik J. Site-specifically Zr-89-labeled monoclonal antibodies for ImmunoPET. *Nucl Med Biol* 2010;37:289–297.
- Mealey Jr J. Turn-over of carrier-free zirconium-89 in man. *Nature* 1957;179:673–674; doi: 10.1038/179673a0
- Abou DS, Ku T, Smith-Jones PM. In vivo biodistribution and accumulation of <sup>89</sup>Zr in mice. *Nucl Med Biol* 2011;38:675–681.
- Moreau N, Michiels C, Masereel B, Feron O, Gallez B, Vander Borgh T, Lucas S. PVD synthesis and transfer into water-based solutions of functionalized gold nanoparticles. *Plasma Process Polymer* 2009;6: S888–S892; doi: 10.1002/ppap.200932210
- Holland JP, Sheh YC, Lewis JS. Standardized methods for the production of high specific-activity zirconium-89. *Nucl Med Biol* 2009;36:729–739.
- Kandil SA, Scholten B, Saleh ZA, Youssef AM, Qaim SM, Coenen HH. A comparative study on the separation of radiozirconium via ion-exchange and solvent extraction techniques, with particular reference to the production of <sup>88</sup>Zr and <sup>89</sup>Zr in proton induced reactions on yttrium. *J Radioanal Nucl Chem* 2007;274:45–52; doi: 10.1007/s10967-006-6892-2
- Serel I, Visser GWM, Boellaard R, Stigter-van Walsum M, Snow GB, van Dongen GAMS. <sup>89</sup>Zr immuno-PET: Comprehensive procedures for the production of <sup>89</sup>Zr-labeled monoclonal antibodies. *J Nucl Med* 2003;44:1271–1281.
- Vosjan MJWD, Perk LR, Visser GW, Budde M, Jurek P, Kiefer GE, van Dongen GA. Conjugation and radiolabeling of monoclonal antibodies with zirconium-89 for PET imaging using the bifunctional chelate p-isothiocyanatobenzyl-desferrioxamine. *Nat Prot* 2010;5:739–743.
- Perk LR, Vosjan MJWD, Visser GW, Budde M, Jurek P, Kiefer GE, van Dongen GA. p-Isothiocyanatobenzyl-desferrioxamine: a new bifunctional chelate for facile radiolabeling of monoclonal antibodies with zirconium-89 for immuno-PET imaging. *Eur J Nucl Med Mol Imag* 2010;37:250–259.
- Masereel B, Dinguizli M, Bouzin C, Moniotte N, Feron O, Gallez B, Vander Borgh T, Michiels C, Lucas S. Antibody immobilization on gold nanoparticles coated layer-by-layer with polyelectrolytes. *J Nanopart Res* 2011;13:1573–1580.
- Hong H, Yang Y, Zhang Y, Engle JW, Barnhart TE, Nickles RJ, Leigh BR, Cai W. Positron emission tomography imaging of CD105 expression during tumor angiogenesis. *Eur J Nucl Med Mol Imag* 2011;38:1335–1343.
- Huisman MC, Reder S, Weber AW, Ziegler SI, Schwaiger M. Performance evaluation of the Philips MOSAIC small animal PET scanner. *Eur J Nucl Med Mol Imag* 2007;34:532–540.

## Supplementary material



Online Resource 1: Electrophoretic profiles of  $^{89}\text{Zr}$ -Df-Bz-NCS-cetuximab (a) and AuNPs-PPAA-cetuximab- $^{89}\text{Zr}$  (b) using SDS-PAGE 10% under non-reducing conditions (i) followed by radio-TLC (ii) and Phosphor Imager (iii) analysis.



Online Resource 2: Size distribution given by differential centrifugal sedimentation (CPS Instruments, Inc.) for AuNPs (dashed line) and AuNPs-PPAA-cetuximab (solid line).

---

#### **IV. Targeting cancer cells using $^{89}\text{Zr}$ -labelled anti-endoglin antibody-conjugated gold nanoparticles**

The last study describes the pharmacokinetic profile of anti-endoglin antibodies conjugated to gold nanoparticles for the first time. The biodistribution of  $^{89}\text{Zr}$ -labelled anti-CD105 mAbs before and after the nanoparticle conjugation was assessed through PET/CT imaging. The tissue uptakes, and particularly the tumour uptake, were quantified through PET/CT imaging. *In vitro* binding studies, *in vivo* blocking experiments and ICP-MS analysis were carried out to determine the antibody specificity after the nanoparticle conjugation.



**<sup>89</sup>Zr-labelled anti-endoglin antibody-targeted gold nanoparticles for  
imaging cancer: implications for future cancer therapy**

**Linda Karmani**, Virginie Bouchat, Caroline Bouzin, Philippe Levêque, Daniel Labar, Anne Bol, Gladys Deumer, Riccardo Marega, Davide Bonifazi, Vincent Haufroid, Carine Michiels, Vincent Grégoire, Olivier Feron, Stéphane Lucas, Thierry Vander Borcht and Bernard Gallez.

*Nanomedicine. 2013; in press.*



---

## **<sup>89</sup>Zr-labelled anti-endoglin antibody-targeted gold nanoparticles for imaging cancer: implications for future cancer therapy**

Linda Karmani<sup>1</sup>, Virginie Bouchat<sup>2</sup>, Caroline Bouzin<sup>3</sup>, Philippe Levêque<sup>1</sup>, Daniel Labar<sup>4</sup>, Anne Bol<sup>4</sup>, Gladys Deumer<sup>5</sup>, Riccardo Marega<sup>6</sup>, Davide Bonifazi<sup>6</sup>, Vincent Haufroid<sup>5</sup>, Carine Michiels<sup>7</sup>, Vincent Grégoire<sup>4</sup>, Olivier Feron<sup>3</sup>, Stéphane Lucas<sup>2</sup>, Thierry Vander Borght<sup>4</sup> and Bernard Gallez<sup>1</sup>

1. Biomedical Magnetic Resonance Group (REMA), Louvain Drug Research Institute, Université Catholique de Louvain, Avenue Mounier 73, 1200 Brussels, Belgium.
2. Research Centre for the Physics of Matter and Radiation (PMR-LARN), Namur Research Institute for Life Sciences (NARILIS), University of Namur, Rue de Bruxelles 61, 5000 Namur, Belgium.
3. Pharmacology and Therapeutics Unit (FATH), Institute of Experimental and Clinical Research (IREC), Université Catholique de Louvain, Avenue Mounier 53, 1200 Brussels, Belgium.
4. Centre for Molecular Imaging, Radiotherapy and Oncology (MIRO), Institute of Experimental and Clinical Research (IREC), Université Catholique de Louvain, Avenue Hippocrate 54, 1200 Brussels, Belgium.
5. Laboratory of Analytical Biochemistry and Louvain Centre for Toxicology and Applied Pharmacology (LTAP), Avenue Hippocrate 10, 1200 Brussels, Belgium.
6. Department of Chemistry and Namur Research College (NARC), University of Namur, Rue de Bruxelles 61, 5000 Namur, Belgium.
7. Unité de Recherche en Biologie Cellulaire (URBC), Namur Research Institute for Life Sciences (NARILIS), University of Namur, Rue de Bruxelles 61, 5000 Namur, Belgium.

### **Corresponding author:**

Prof. Bernard Gallez

Louvain Drug Research Institute

Université Catholique de Louvain

Avenue Mounier 73 - B1.73.08

B-1200 Brussels - Belgium

Phone: +32 2 7647391

Fax: +32 2 7647390

Email: Bernard.Gallez@uclouvain.be

## Abstract

**Aims:** Antibody-labelled gold nanoparticles represent an attractive tool for cancer imaging and therapy. In this study, the anti-CD105 antibody was conjugated with gold nanoparticles (AuNPs) for the first time. The antibody biodistribution in mice before and after conjugation to AuNPs was studied, with a focusing on tumour targeting.

**Materials and methods:** Antibodies were radiolabelled with  $^{89}\text{Zr}$  before conjugation to AuNPs (5 nm). Immunonanoconjugates were characterized *in vitro* in terms of size, stability in plasma and binding to the target. Quantitative PET imaging and ICP-MS analysis assessed *in vivo* distribution and specific tumour targeting of tracers.

**Results:** The tumour uptake of immunoconjugates was preserved up to 24 h after injection, with high tumour contrast and selective tumour targeting. No major tracer accumulation was observed over time in nonspecific organs. ICP-MS analysis confirmed the antibody specificity after nanoparticle conjugation.

**Conclusion:** The anti-CD105 antibody conjugation to AuNPs did not greatly affect the CD105-dependent tumour uptake and the efficacy of tumour targeting for cancer detection.

## Introduction

Immunotargeted gold nanomaterials represent an attractive tool for cancer imaging and treatment [1]. During the past decade, the biomedical use of gold nanoparticles (AuNPs) has piqued interest owing to their good biocompatibility and their interesting optical properties, which can be used to improve the management of cancer [2]. Recently, promising applications of AuNPs-based systems as contrast agents for cancer imaging [3] or therapeutic agents for photothermal therapy have been reported [4]. Interestingly, AuNPs can be easily modified with various ligands, including specific monoclonal antibodies (mAbs). Functionalization of AuNPs surface with mAbs enables them to have an adequate biodistribution as well as to specifically target and be accumulated in cells that express or overexpress a specific surface membrane antigen. Thus, the resulting gold immunonanoconjugates is expected to be a good strategy for enhancing the efficacy of tumour targeting while reducing toxicity in normal tissues [5].

In this study, we functionalized AuNPs by choosing mAbs directed against endoglin (CD105), a homodimeric cell surface glycoprotein that is overexpressed on angiogenic vascular endothelial cells [6-13] and in some cancer cells, such as melanoma [14, 15] and choriocarcinoma cells [16]. Furthermore, vascular density of CD105, determined using the anti-CD105 mAbs, is correlated with the tumour prognosis [17], the risk of developing metastatic disease [18] and the recurrence of malignancy [19]. Recently, several studies have indicated that CD105 represents a more specific and sensitive marker for tumour angiogenesis and tumour progression than the commonly used pan-endothelial markers, such as CD34 and CD31 in various types of human malignancies [17, 20-22]. Thus, CD105 targeting has been used as an antiangiogenic therapy based on attacking both of the tumour neovasculature, in addition to directly attacking cancer cells that overexpress CD105 [23]. Nevertheless, tumours may still become resistant to antiangiogenic therapy [24]. Preclinical studies indicate that combining these agents with conventional cytotoxic agents or radiation therapy results in an additive or even synergistic antitumor effect [25]. Other approaches are to provide immunoconjugates with either immunotoxins or radioantibodies, which are effective for suppression of tumour growth [26-31] and metastasis [32]. Although anti-endoglin mAbs are successfully used as intrinsic therapeutic agents, they can also be used as targeting agents. Within this context, antibody-targeted gold nanoparticles may represent an interesting

combined approach for improving the efficacy of the standard inhibitors of angiogenesis thanks to the photophysical properties of gold.

The main goal of this work is to characterize the impact of nanoparticle conjugation reaction on target recognition properties of anti-CD105 mAbs *in vitro* and *in vivo*. Recently, we described the synthesis and characterization of cetuximab-targeted gold nanoparticles. We investigated the impact of nanoparticle conjugation on cetuximab biodistribution and tumour targeting through *ex-vivo* biodistribution study [33] and *in vivo* noninvasive PET imaging [34]. We demonstrated that the conjugation of cetuximab to AuNPs did not significantly affect the EGFR-dependent tumour uptake in mice. The present study was designed to assess the *in vivo* distribution of anti-endoglin mAbs conjugated to AuNPs compared to that of unconjugated mAbs, and to explore the effect of nanoparticle conjugation on tumour targeting. To trace these immunoconjugates, anti-CD105 mAbs were radiolabelled in advance using zirconium-89 ( $^{89}\text{Zr}$ ).  $^{89}\text{Zr}$  has an ideal long physical half-life (78.41 h) for positron emission tomography (PET) imaging [35] of intact mAbs, which require time (typically 2-4 days) to reach optimal biodistribution and tumour targeting [36].

## Materials and methods

### Production and characterization of $^{89}\text{Zr}$ -labelled anti-CD105 mAbs

$^{89}\text{Zr}$  was produced and purified in-house as previously described [34, 37, 38]. The rat anti-mouse CD105 mAb was produced from an hybridoma (clone MJ7/18), which was provided by the Developmental Studies Hybridoma Bank (Iowa University, Iowa City, IA, USA).  $^{89}\text{Zr}$ -labelled anti-CD105 mAbs ( $^{89}\text{Zr}$ -Df-Bz-NCS-anti-CD105) was prepared according to a protocol previously described [39,40]. First, the antibody was purified by protein G-affinity chromatography and dialysis into PBS (140 mM NaCl, 6 mM  $\text{Na}_2\text{HPO}_4$ , 3 mM KCl, 1 mM  $\text{KH}_2\text{PO}_4$ , pH 7.2) followed by size-exclusion chromatography on a Superdex 200 column (GE Healthcare Life Sciences, Belgium) using a 20 mM TRIS-HCl buffer (pH 7.5) containing 0.15 M NaCl. Then, the purified mAbs was functionalized with the bifunctional chelating agent p-isothiocyanatobenzyl-desferrioxamine (Df-Bz-NCS, Macrocyclics, Dallas, TX, USA) as previously described [34]. Finally, the functionalized antibody (Df-Bz-NCS-anti-CD105) was purified by size exclusion chromatography using a PD10 column (GE Healthcare Life Sciences, Belgium) and radiolabelled with the produced  $^{89}\text{Zr}$ -oxalate (74-111 MBq).

The radiochemical yield and purity were determined by using instant thin-layer chromatography (ITLC) and 20 mM citric acid (pH 4.9-5.1) as the mobile phase. ITLC migration was followed by radio-TLC detection (Mini-Gita TLC scanner, Raytest, Germany) which showed that the radiolabelled antibody migrated with  $R_f < 0.1$ , whereas unbound  $^{89}\text{Zr}$  migrated to the solvent front. In addition, the integrity of the antibody after radiolabelling was checked by sodium dodecyl sulfate-polyacrylamide gel electrophoresis (10% SDS-PAGE gel, under nonreducing conditions), followed by radio-TLC detection (Bioscan system 200 imaging scanner), or by gel scanning using Phosphor Imager (Fujifilm FLA-5100) analysis.

### Synthesis and characterization of $^{89}\text{Zr}$ -labelled anti-CD105 mAbs conjugated to AuNPs

AuNPs were synthesized and coated with plasma-polymerized allylamine (PPAA) through physical vapour deposition technique (PVD) as previously described by our group [41]. The coated nanoparticles (AuNPs-PPAA) were purified as previously reported [33]. Anti-CD105 mAbs were conjugated to AuNPs-PPAA using carbodiimide chemistry and purified as previously described in our latest works [33-34]. The efficiency of the conjugation reaction between AuNPs-PPAA and  $^{89}\text{Zr}$ -labelled anti-CD105 mAbs was assessed using gel

electrophoresis (10% SDS-PAGE gel, under nonreducing conditions), followed by a radio-TLC analysis.

Physicochemical characterizations of AuNPs-PPAA and the immunonanoconjugates were performed as previously detailed [33, 34, 41, 42]. In brief, transmission electron microscopy (TEM, Philips Tecnai 10 transmission electron microscope) was carried out to assess the morphology and size distribution of AuNPs-PPAA. Differential centrifugal sedimentation (DCS; DC 24000 Disk Centrifuge; CPS Instruments, Inc.) was performed to determine the size of  $^{89}\text{Zr}$ -labelled mAbs conjugated to AuNPs ( $^{89}\text{Zr}$ -anti-CD105-AuNPs-PPAA) by measuring the time required for these immunonanoconjugates to traverse a sucrose density gradient created in a disk centrifuge. This method used calibrated gold nanoparticles coated layer-by-layer with polyelectrolytes to estimate the size of the tracer [33].

### **Cell culture and cell surface ELISA**

Mouse melanoma cell line (B16F10-luc) and embryonic endothelial progenitor cells (eEPC) were maintained in alpha minimum essential medium (MEM-alpha with glutamine, Gibco-Invitrogen, Belgium) supplemented with 10% heat-inactivated foetal bovine serum (FBS, Gibco-Invitrogen, Belgium), 1% streptomycin-penicillin (Gibco-Invitrogen, Belgium) and 1% MEM non-essential amino acids (Gibco-Invitrogen, Belgium), or in Dulbecco's modified Eagle's medium (DMEM glucose  $4.5 \text{ g l}^{-1}$  without pyruvate, Gibco-Invitrogen, Belgium), supplemented with 10% foetal bovine serum and 1% streptomycin-penicillin respectively.

B16F10-luc or eEPC cells ( $10^4$  cells per well) were grown in 96-well plates (Thermo Fisher Scientific, Belgium) 24 h prior to the ELISA test. Cells were washed once with PBS for cell culture (Lonza, Belgium), then fixed for a 10 min strict with PBS containing 4% paraformaldehyde. After one wash with PBS, wells were blocked with 5% non-fat dry milk in PBS for 1 h at room temperature. Cells were rinsed twice with PBS and once with PBS containing 1% BSA (1% BSA-PBS) for 5 min. Anti-CD105 mAbs and anti-CD105-AuNPs-PPAA were added to the cells at various concentrations for 1 h at room temperature. Wells were washed six times with 1% BSA-PBS. Then, goat anti-rat IgG conjugated to peroxidase (Jackson Immunoresearch Laboratories, Belgium) diluted in 1% BSA-PBS at  $0.32 \text{ mg ml}^{-1}$  was added for 30 min at room temperature. After three washing steps with 1% BSA-PBS, the enzyme activity was revealed by adding 100  $\mu\text{l}$  of TMB substrate (Merck Chemicals,

Belgium) to each well for 20 min in the dark. The reaction was stopped with 250 mM HCl and the cell binding was quantified spectrophotometrically at 450 nm.

### ***In vitro* stability of radioimmunoconjugates in plasma**

*In vitro* stability of both purified  $^{89}\text{Zr}$ -Df-Bz-NCS-anti-CD105 and  $^{89}\text{Zr}$ -anti-CD105-AuNPs-PPAA was studied in fresh mouse plasma, by incubating the solution of radiolabelled mAbs (1:2 v/v dilution at a final concentration of 1.1 MBq ml<sup>-1</sup>; sodium azide added at 0.02%) at 37 °C with stirring. At different times after incubation (6, 24, 48 and 72 h), aliquots of plasma (10 µl) were analysed using radio-ITLC.

### **Comparative biodistribution studies in mice using animal PET/CT imaging**

For the biodistribution assessment using PET imaging, C57BL/6J male mice (22-26 g, 5-6 weeks old; Janvier, France) bearing melanoma xenografts were used. The mice were inoculated subcutaneously in the flanks with  $1 \times 10^6$  B16F10-luc cells (one or two tumours per mouse). After about ten days, the diameter of the tumours had reached 7.5-8.5 mm and the mice were ready for *in vivo* experiments. All animal experiments were conducted in accordance with national and university animal care regulations.

To compare the pharmacokinetic profiles of native radiolabelled mAbs and those conjugated to AuNPs, two groups of three to five mice were injected intravenously in the lateral tail vein with either freshly prepared  $^{89}\text{Zr}$ -Df-Bz-NCS-anti-CD105 or with  $^{89}\text{Zr}$ -anti-CD105-AuNPs-PPAA (2.9-4.1 MBq, total of 350-400 µg mAbs per mouse). Additionally, to assess the *in vivo* specificity of anti-CD105 mAbs conjugated to AuNPs, a group of three B16 melanoma-bearing mice (blocking group, two tumours per mouse) was injected with an excess of unlabelled anti-CD105 mAbs (2 mg mAbs per mouse) 2 h before the injection of  $^{89}\text{Zr}$ -anti-CD105-AuNPs-PPAA (3.6-4.1 MBq, total of 200 µg mAbs per mouse) as previously described [43]. The blocking group was compared with the group of mice who received only  $^{89}\text{Zr}$ -anti-CD105-AuNPs-PPAA without a saturating dose.

Whole-body PET images were acquired using a dedicated small-animal PET scanner (MOSAIC, Philips Medical Systems; Cleveland, USA) with an intrinsic spatial resolution of 2.5 mm (full width at half maximum) [44]. The PET scans were followed by whole-body acquisitions using a helical CT scanner (NanoSpect/CT, Bioscan Inc., Washington, D.C., USA) for anatomical reference. The PET/CT acquisitions were performed at different times

after tracer injection (3, 6, 24, 48 and 72 h). All imaging procedures were performed under anaesthesia with 1.5% isoflurane (Abbott Laboratories, Belgium) / oxygen gas mixture (2 l min<sup>-1</sup>). Mice were maintained in a prone position on a heated animal bed at 37 °C (Minerve, France). The PET acquisition durations were adapted to compensate for decay and ensure significant statistics (above 10000 total counts). The emission scans were followed by transmission scans using a 370 MBq <sup>137</sup>Cs source for attenuation correction. All PET scans were reconstructed with a fully 3D iterative algorithm (3D-RAMLA) in a 128 x 128 x 120 matrix, with a voxel size of 1 mm<sup>3</sup>. After PET acquisition, the animal remained anesthetized and was transferred on the same bed from the PET scanner to the CT scanner (spatial resolution 48 µm, X-ray tube voltage 55 kVp, X-ray tube current 145 µA, number of projections 180, exposure time 1000 ms). The CT projections were reconstructed with a voxel size of 0.221 x 0.221 x 0.221 mm<sup>3</sup>.

Before the PET and CT images were fused, the PET images were normalized according to a PET calibration factor including the positron branching ratio, the physical decay to the time of injection, the acquisition duration and the injected dose. This normalization was used to parameterize images in terms of percentage of the injected dose per millilitre. Regions of interest (ROIs) were delineated on the PET/CT fused images. The 2D ROIs were drawn on consecutive transversal slices using PMOD software (PMOD™, version 3.3, PMOD Technologies Ltd, Zurich, Switzerland) as previously described [34]. The tracer uptakes were assessed in the liver, lungs and tumours. Moreover, we defined a ROI, called background region, which was representative of tissues with low nonspecific uptake. The same background volume was drawn in the pelvic region of all animals, far from hot spots (organs with high uptake). The background signal was used to assess the specific-to-nonspecific tissue uptake, and particularly to estimate the tumour contrast, which was also expressed as tumour-to-background ratio, and which was calculated as the mean activity in the tumour region divided by the mean activity obtained in the background region. Finally, we quantified the blood activity over time by drawing ROIs within the ventricular cavity of heart, based on anatomical CT images fused with PET images (see online supplementary figure 1).

## Quantification of gold (Au) in tumours by ICP-MS

To compare the gold distribution of free nanoparticles to that of conjugated mAbs, two groups of four B16 melanoma-bearing mice were injected intravenously in the lateral tail vein with either freshly prepared AuNPs-PPAA (a total of 36  $\mu\text{g}$  Au per mouse) or with  $^{89}\text{Zr}$ -anti-CD105-AuNPs-PPAA (a total of 18  $\mu\text{g}$  Au per mouse, corresponding to 100  $\mu\text{g}$  mAbs per mouse). Moreover, to confirm the *in vivo* specificity of anti-CD105 mAbs conjugated to AuNPs, a group of four B16 melanoma-bearing mice (blocking group) was injected with an excess of unlabelled anti-CD105 mAbs (2 mg mAbs per mouse) 2 h before the injection of anti-CD105-AuNPs-PPAA (a total of 22  $\mu\text{g}$  Au per mouse, corresponding to a total of 200  $\mu\text{g}$  mAbs per mouse). The blocking group was compared to the group of mice which received only anti-CD105-AuNPs-PPAA without a saturating dose. After 6 h, the animals were sacrificed. The blood and tumours were collected, weighed, freeze-dried and processed for gold content determination. The samples were hydrolyzed using 4 ml of pure 65% nitric acid (Merck chemicals, Belgium) in a water bath at 60 °C until complete solubilization of tissues. The analytical determination of gold ( $^{197}\text{Au}$ ) in the samples was performed by inductively coupled plasma mass spectrometry (ICP-MS, type Agilent 7500cx, Agilent Technologies, Germany). The homogenized samples were diluted 100 times in a basic diluent (2% butanol, 0.05% EDTA, 1%  $\text{NH}_4\text{OH}$  and 0.05% triton) containing iridium ( $^{193}\text{Ir}$ ) as an internal standard. The gold content of the samples was quantified by plotting the calibration curve with known concentrations of a gold standard solution (Merck Chemicals, Belgium) used for the external calibration. The amount of Au detected in the tumours was expressed as a percentage of the injected dose and as a tumour-to-blood ratio.

## Statistical Analysis

Data calculations were performed with Prism software (Graph Pad™ Software Inc., version 5.02). The differences in tissue uptake of radioactivity between two groups were considered significant if the p-values from non-parametric two-tailed Mann-Whitney tests were  $\leq 0.05$  (\*) or  $\leq 0.01$  (\*\*). The differences in tissue uptake of radioactivity at different times were assessed by one-way analysis of variance and the Tukey *post-hoc* test. The differences in tissue uptake of gold between two groups were considered significant if the p-values from unpaired t-tests (two-tailed) were  $\leq 0.05$  (\*) or  $\leq 0.01$  (\*\*).

## Results

### Characterization of radioimmunoconjugates before and after nanoparticle conjugation

Df-Bz-NCS-anti-CD105 was radiolabelled with  $^{89}\text{Zr}$  with a mean radiochemical yield of  $49.7 \pm 13.2\%$  ( $n = 3$ ), whereas the radiochemical purity immediately after purification was  $> 95\%$ . The resulting specific activity was  $55.5 \pm 14.3\text{ MBq mg}^{-1}$  of mAbs ( $n = 3$ ). Electrophoresis of  $^{89}\text{Zr}$ -labelled anti-CD105 mAbs under nonreducing conditions followed by radio-TLC and autoradiography showed a single band of 150 kDa corresponding to  $^{89}\text{Zr}$ -Df-Bz-NCS-anti-CD105 and a single peak of radioactivity (see online supplementary figure 2A), which means that the antibody integrity was preserved after the labelling reaction. Electrophoresis of antibody-labelled gold nanoparticles under nonreducing conditions followed by radio-TLC showed a lower migration of  $^{89}\text{Zr}$ -anti-CD105-AuNPs-PPAA compared to that of  $^{89}\text{Zr}$ -Df-Bz-NCS-anti-CD105 and two peaks of radioactivity corresponding to the positions of the two species on the gel (see supplementary online figure 2B). The percentage of radioactivity linked to the peak of  $^{89}\text{Zr}$ -anti-CD105-AuNPs-PPAA expressed the coupling reaction yield, which was  $> 75\%$ . The nanoparticle diameters observed by TEM imaging ranged from 3 to 10 nm (mean diameter of  $4.8 \pm 1.7\text{ nm}$ ) [33]. The mean diameter of anti-CD105-AuNPs-PPAA was determined by differential centrifugal sedimentation and was estimated at about  $102.6 \pm 4.0\text{ nm}$  (Fig. 1). This technique gives an “apparent diameter”, which may be affected by the non-perfect spherical shape of analyzed particle and by the nanoparticle coating. The size of anti-CD105-AuNPs-PPAA was not available through TEM imaging because the contrast was dominated by AuNPs, so that the nanoparticle coating was not visible. Moreover, it is likely that the carbodiimide reaction produces to some extent polymerized mAbs, which would increase the apparent diameter of the conjugates. Finally, the *in vitro* stability of radioimmunoconjugates in plasma showed that  $^{89}\text{Zr}$  was slightly dissociated from the antibody over time. Starting from a solution without free  $^{89}\text{Zr}$  (100% purity), the percentages of dissociation were lower by 5% after 6 h, 10% after 24 h, 15% after 48 and 72 h for both radioimmunoconjugates.

### ***In vitro* assessment of CD105 targeting**

A cell-based ELISA study investigated the relative binding affinity of anti-CD105 mAbs towards endoglin overexpressing cells before and after antibody conjugation to AuNPs. For this purpose, we chose the B16F10-luc melanoma cell line, known for its CD105 overexpression (CD105+) [14, 15]. The eEPC cell line was selected as negative control cells that do not express CD105, based on qualitative immunohistochemistry results and *in vitro* quantitative ELISA tests (data not shown). Different concentrations of anti-CD105 mAbs and anti-CD105-AuNPs-PPAA were tested on both CD105+ and CD105- cells (Fig. 2). As expected, anti-CD105 mAbs bound to CD105+ cells in a concentration-dependent way, but not to CD105- cells. Interestingly, anti-CD105-AuNPs-PPAA also bound to CD105+ cells in a concentration-dependent manner, suggesting retention of the target recognition property after nanoparticle conjugation. The relative binding affinity of anti-CD105 mAbs before and after conjugation to AuNPs was quantified as a half-maximal effective concentration (EC<sub>50</sub>). The EC<sub>50</sub> value was reduced from 1 µg ml<sup>-1</sup> (for anti-CD105 mAbs) to 5 µg ml<sup>-1</sup> (for anti-CD105-AuNPs-PPAA). The relative binding affinity remains on the same range (less than 1 log) before and after antibody conjugation to gold nanoparticles. This lower CD105 binding affinity of conjugated antibody was confirmed *in vivo* by blocking experiments as described below.

### **PET evaluation of <sup>89</sup>Zr-labelled anti-CD105 mAbs biodistribution in mice before and after coupling reaction to AuNPs**

Two groups of B16 melanoma-bearing mice were injected with <sup>89</sup>Zr-Df-Bz-NCS-anti-CD105 or with <sup>89</sup>Zr-anti-CD105-AuNPs-PPAA respectively. We compared the pharmacokinetic behaviour of <sup>89</sup>Zr-anti-CD105-AuNPs-PPAA with that of <sup>89</sup>Zr-Df-Bz-NCS-anti-CD105, as a reference compound. Figure 3 shows representative PET/CT images of mice bearing B16 tumour xenografts at different times after tracer injection (3, 6, 24, 48 and 72 h), and compares the distribution of <sup>89</sup>Zr-Df-Bz-NCS-anti-CD105 (Fig. 3A) and <sup>89</sup>Zr-anti-CD105-AuNPs-PPAA (Fig. 3B) respectively. At the different times after injection, accumulation of the two tracers was predominantly observed in the liver (red arrows) and in tumours implanted in the legs (yellow arrows). The lung uptake (green arrows) was observed only at early times (3 and 6 h). A similar pattern was observed for both radioimmunoconjugates, but with visually higher liver, spleen and lung uptakes for <sup>89</sup>Zr-anti-

CD105-AuNPs-PPAA than for  $^{89}\text{Zr}$ -Df-Bz-NCS-anti-CD105 (Fig. 3). This distribution pattern remained constant at later times for the liver and spleen. 3D videos representing PET/CT fusion MIP (maximum intensity projection) of mice that received  $^{89}\text{Zr}$ -Df-Bz-NCS-anti-CD105 or  $^{89}\text{Zr}$ -anti-CD105-AuNPs-PPAA are available online as supplementary materials 3 and 4, respectively.

For each time point considered, it must be mentioned that quantification of liver and lung uptakes showed no significant difference between the two groups (Fig. 4), despite the visually more pronounced tracer uptake observed on PET/CT images for  $^{89}\text{Zr}$ -anti-CD105-AuNPs-PPAA compared to unconjugated antibody (Fig. 3). The liver and lung uptakes were fast, with maximum values observed 3 h after tracer injection. The maximum liver uptake was about  $14.9 \pm 2.8 \text{ \%ID ml}^{-1}$  for  $^{89}\text{Zr}$ -anti-CD105-AuNPs-PPAA and  $11.7 \pm 1.1 \text{ \%ID ml}^{-1}$  for  $^{89}\text{Zr}$ -Df-Bz-NCS-anti-CD105 (Fig. 4A), whereas the maximum lung uptake was about  $15.2 \pm 3.6 \text{ \%ID ml}^{-1}$  for  $^{89}\text{Zr}$ -anti-CD105-AuNPs-PPAA and  $11.61 \pm 1.0 \text{ \%ID ml}^{-1}$  for  $^{89}\text{Zr}$ -Df-Bz-NCS-anti-CD105 (Fig. 4B).

The major differences between the biodistribution patterns were observed for tumour uptake (Fig. 5). In the tumour, the kinetics were relatively fast for both conjugated and unconjugated mAbs (Fig. 5A), with a maximum uptake reached after 24 h, followed by a plateau phase ( $6.5 \pm 0.4 \text{ \%ID ml}^{-1}$  for  $^{89}\text{Zr}$ -Df-Bz-NCS-anti-CD105 and  $4.6 \pm 0.1 \text{ \%ID ml}^{-1}$  for  $^{89}\text{Zr}$ -anti-CD105-AuNPs-PPAA). A decrease in tumour uptake was observed starting 24 h after injection in favour of unconjugated mAbs. However, a continuous increase in tumour-to-background ratio was observed over time, with no difference between the two groups (Fig. 5A). Finally, the specificity of tumour uptake was investigated by administering a saturating dose of unlabelled anti-CD105 mAbs 2 h before  $^{89}\text{Zr}$ -anti-CD105-AuNPs-PPAA injection. This saturation experiment showed that the CD105 binding of  $^{89}\text{Zr}$ -anti-CD105-AuNPs-PPAA was markedly reduced in the tumour up to 24 h after injection (Fig. 6). In fact, the residual activity in the tumour was significantly lower for the blocking group at 3, 6 and 24 h after injection compared with the tumour uptake in mice injected with only  $^{89}\text{Zr}$ -anti-CD105-AuNPs-PPAA. The tumour uptake value in the blocking group 6 h after injection ( $1.9 \pm 0.2 \text{ \%ID ml}^{-1}$ ) was reduced by a factor of 2.5 compared to that for mice receiving only  $^{89}\text{Zr}$ -anti-CD105-AuNPs-PPAA ( $4.7 \pm 0.2 \text{ \%ID ml}^{-1}$ ).

### Assessment of gold content in tumours by ICP-MS

Gold content was measured in blood and tumours by ICP-MS at 6 h after tracer injection. In the normal situation, the presence of Au is detectable without background in the body. Figure 7A shows that the amount of Au expressed as a percentage of the injected dose in tumours was significantly higher for mice receiving anti-CD105-AuNPs-PPAA ( $3.3 \pm 0.4$  %ID) than for those receiving AuNPs-PPAA ( $1.8 \pm 0.1$  %ID). Moreover, the tumour-to-blood ratio was also significantly higher for the group of mice injected with anti-CD105-AuNPs-PPAA compared to the group of mice receiving free AuNPs (Fig. 7B). The specificity of anti-CD105 mAbs after nanoparticle conjugation was confirmed by repeating the blocking experiment. The gold quantification in tumours after injecting a saturating dose of anti-CD105 mAbs 2 h before the anti-CD105-AuNPs-PPAA injection showed a significant decrease in gold content ( $1.3 \pm 0.1$  %ID) compared to the group of mice receiving only anti-CD105-AuNPs-PPAA ( $3.3 \pm 0.4$  %ID) at 6 h after injection (Fig. 7A). The tumour-to-blood ratio values for the blocking group reached those for free nanoparticles and were significantly lower than those of mice receiving anti-CD105-AuNPs-PPAA without a prior saturating dose (Fig. 7B).

## Discussion

Because our group has recently developed a method for synthesizing AuNPs [41] and has successfully investigated the *in vivo* distribution of cetuximab conjugated to AuNPs [34], we have expanded our studies of nanoparticle vectorization through conjugation to mAbs by choosing the anti-CD105 mAb, which is still little-known but seems to be promising for targeting tumour cells and angiogenic vascular endothelial cells. We combined the targeting properties of anti-CD105 mAbs and the favourable imaging properties of  $^{89}\text{Zr}$ . Our major goal was to further characterize the *in vivo* distribution of these antibody-targeted gold nanoparticles, with a focusing on tumour targeting, and to assess the *in vivo* impact of nanoparticle conjugation on the antibody target recognition by using noninvasive PET imaging.

The biodistribution pattern of  $^{89}\text{Zr}$ -anti-CD105-AuNPs-PPAA and that of  $^{89}\text{Zr}$ -Df-Bz-NCS-anti-CD105 showed liver, spleen and lung uptakes (Fig. 3). First, the liver uptake quantification was not significantly different between the two groups (Fig. 4A). It is known that one of the limitations of antibody-based imaging is the high background signal in the reticuloendothelial system (RES), which was particularly illustrated in our study by the liver uptake of the tracers. Furthermore, the large nanoparticles (100 nm) are not excreted in urine, which causes their extended presence in the circulation. Thus, the nanoparticles are eliminated from the blood by the RES and are accumulated in the spleen and liver [45]. On the other hand, the vascular endothelium structure of liver and spleen are discontinuous with large fenestrations, thus allowing nanomaterials (up to 100 nm) to pass through the endothelium and to be accumulated in these tissues [46]. Visually, the PET images showed that the liver uptake seemed to be increased after antibody conjugation to AuNPs (Fig. 3). The colloidal properties of AuNPs could be the cause of this effect.

The same finding was observed for the lungs. Visually, the PET images showed that the lung uptake seemed to be higher for  $^{89}\text{Zr}$ -anti-CD105-AuNPs-PPAA than for  $^{89}\text{Zr}$ -Df-Bz-NCS-anti-CD105 only at early times (3 and 6 h after injection) (Fig. 3). However, the lung uptake quantification showed no significant difference between the two groups at each time after injection (Fig. 4B). First, no increase in lung accumulation was observed over time. The conjugates were cleared from lungs starting 24 h after injection. The alveolar macrophage activity of lungs might be the mechanism by which the conjugates were cleared [47]. The

translocation of nanoparticles out of the lungs through lymphatic vessels was also described [48]. Further studies should be done to explore the lung clearance of our synthesized conjugates because the particle size, shape, surface properties and formulation affect the nanoparticle entrapment and the subsequent efficient uptake by macrophages [49]. Then, the constitutive expression of CD105 in vascularised organs like lungs may explain the lung uptake. Moreover, previous studies showed that high levels of CD105 expression are seen in the distal vessels of mouse lung [50]. Other studies described the size-dependent biodistribution of AuNPs and showed that nanoparticles sized 100 nm were only significantly deposited in the liver, spleen and blood [51]. Finally, our blocking experiments showed the decrease of the immunonanoconjugates uptake in lungs, liver and spleen for mice receiving a saturating dose of unlabelled mAbs (data not shown). However, we cannot exclude some aggregation of the conjugates *in vivo* after intravenous injection, which might increase the lung uptake without observed any obvious respiratory problem, such as pulmonary embolism. In this regard, a special attention should be paid if these nanoconjugates are injected at higher doses, such as for therapeutic purposes.

It must be mentioned that no major accumulation of radioactivity was observed in nonspecific organs, aside from liver, spleen, lungs, and to a lesser extent bones. Starting 24 h after injection, PET images displayed distinct hot spots in joints (shoulders and knees) that might be assigned to the detachment of  $^{89}\text{Zr}$  from the desferal moiety (Fig. 3). In fact, we observed that the two tracers were not fully stable under physiological conditions, with a release of up to 10% free  $^{89}\text{Zr}$  being observed after 24 h of tracer incubation in plasma. Previous studies, including our latest study with cetuximab conjugated to gold nanoparticles [34, 52], reported a similar pattern of skeleton uptake and attributed the constant bone accumulation to the strong affinity of free  $^{89}\text{Zr}$  ions for hydroxylapatite and phosphate constituents of bones. In fact, zirconium is known to bind to plasma proteins and it is later deposited in mineral bone [53]. Other studies hypothesized that high murine bone uptake is also due to the liver metabolism of the conjugate and the release of free  $^{89}\text{Zr}$  into the circulation [54].

With regard to tumour targeting, we observed that the tumour uptake expressed as  $\%ID\text{ ml}^{-1}$  was significantly decreased after nanoparticle conjugation, starting one day after injection. This decrease was confirmed by the results of *in vitro* ELISA test. Nevertheless, the tumour-to-background ratio remained good without a significant difference before and after nanoparticle

conjugation. Thus, the preservation of high tumour contrast after nanoparticle conjugation supports the good imaging properties of these radioimmunonanoconjugates.

We compared current data with those obtained previously with cetuximab conjugated to AuNPs [34]. For  $^{89}\text{Zr}$ -cetuximab-AuNPs-PPAA, the tumour uptake was not significantly lower than for  $^{89}\text{Zr}$ -Df-Bz-NCS-cetuximab up to 72 h after injection, with preserved tumour contrast. Indeed, our previous studies showed that *in vitro* binding activity of  $^{89}\text{Zr}$ -cetuximab-AuNPs-PPAA ( $\text{EC}_{50}$  value of  $0.19 \mu\text{g ml}^{-1}$ ) was reduced by a factor of two compared to  $^{89}\text{Zr}$ -Df-Bz-NCS-cetuximab ( $\text{EC}_{50}$  value of  $0.08 \mu\text{g ml}^{-1}$ ) [33], while the  $\text{EC}_{50}$  value of  $^{89}\text{Zr}$ -anti-CD105-AuNPs-PPAA was about five times higher than that of  $^{89}\text{Zr}$ -Df-Bz-NCS-anti-CD105. The larger size of conjugated anti-CD105 mAbs (100 nm) compared with that of conjugated cetuximab (30 nm) suggests a higher grafting rate of mAbs molecules onto the nanoparticle surface (Fig. 1), and might explain the observed decrease in tumour targeting (Fig. 5A).

Despite the decrease in tumour uptake starting one day after injection, the maintained specificity of conjugated anti-CD105 mAbs was confirmed by *in vivo* saturation experiment, suggesting the selective accumulation of  $^{89}\text{Zr}$ -anti-CD105-AuNPs-PPAA in tumours and the preservation of the CD105 recognition property of the antibody after radiolabelling and coupling to AuNPs. In fact, the administration of unlabelled mAbs in excess before  $^{89}\text{Zr}$ -anti-CD105-AuNPs-PPAA injection induced the saturation of CD105 binding sites, and significantly decreased the CD105 binding of  $^{89}\text{Zr}$ -anti-CD105-AuNPs-PPAA in tumours (Fig. 6). These results confirmed the antigen-specific binding and the partial preservation of antibody immunoreactivity.

On the other hand, ICP-MS analysis quantified the tumour uptake of functionalized AuNPs, functionalized AuNPs after a saturating dose of unlabelled anti-CD105 mAbs (blocking group) and free AuNPs, by determining gold content at 6 h after injection (Fig. 7). The significant decrease of gold content in tumours belonging to the blocking group (dashed column) compared with mice receiving anti-CD105-AuNPs-PPAA without saturating target receptors (white column) also confirmed the preservation of the antibody specificity after nanoparticle conjugation, since the saturation of CD105 binding sites led to a significant decrease in gold in tumours (Fig. 7A). Moreover, the significant higher amount of Au in tumours for mice receiving anti-CD105-AuNPs-PPAA (white column) compared with those receiving AuNPs-PPAA (black column) highlighted the improved tumour uptake of

functionalized nanoparticles. Indeed, the presence of grafted mAbs on the nanoparticle surface might be favourable to directing the nanoimmunoconjugate to the tumour. These ligand-receptor interactions result in improved uptake of the nanocomplex into the tumour. Further studies are actually needed to assess the interest of active targeting by conjugating nanoparticles to nonspecific antibodies. Moreover, figure 7B showed the significant higher tumour-to-blood ratio for mice injected with antibody-targeted nanoparticles (white column) compared to those receiving free AuNPs (black column). This statement was supported by the significantly lower gold concentration in circulation for mice receiving anti-CD105-AuNPs-PPAA compared to that of mice receiving uncoupled nanoparticles (data not shown). This result is probably related to the greater uptake of anti-CD105-AuNPs-PPAA by the RES, as seen on PET images (Fig. 3).

This study highlights the potential of anti-CD105-antibody-labelled gold nanoparticles in tumour detection and demonstrates the preservation of the antibody specificity after nanoparticle conjugation. Regarding cancer therapy, the anticancer effect of anti-CD105 mAbs due to their antiangiogenic properties might be boosted thanks to the photophysical properties of AuNPs. Indeed, previous studies have shown that AuNPs have interesting anticancer properties through photothermolysis of cancer cells and enhancement of the efficacy of radiotherapy. It must be mentioned that a sufficient amount of gold delivered to tumours is required for these applications. For imaging purpose, as is the case of this study, we injected trace amounts of immunonanoconjugates, which are sufficient for diagnostic applications with a minimal risk of toxicity. However, we should consider increasing the amount of injected conjugates for therapeutic purposes [55, 56, 57, 58], and thus assessing the potential toxicity of high amounts of injected AuNPs. Furthermore, the photothermal therapy using visible lasers is adequate for superficial tumours, such as melanoma, but not for deeper lesions, for which the shortwave radiofrequency field treatment is most suitable [59]. Finally, as it is possible to locally and specifically activate AuNPs accumulated in malignant tissues, the nonspecific uptake of immunonanoconjugates by the RES may be overcome thanks to the local radiation exposure of AuNPs. These encouraging results present new opportunities for nanoparticle-based drug delivery systems in future theranostic applications.

## Conclusion and future prospects

Antibody-based targeting of angiogenesis represents a new promising diagnostic and therapeutic tool. Among these tools, anti-CD105 mAbs have shown anticancer benefit in recent clinical studies [60]. Indeed, the proven value of endoglin as the most suitable marker for evaluating tumour angiogenesis [61, 62] has led to increasingly focused interest on CD105 as a target for immunoconjugates. On the other hand, AuNPs are the subject of intensive studies in biomedical applications. No studies have investigated the biomedical potential of anti-CD105 mAbs conjugated to AuNPs as immunonanocarriers for vascular targeting detection and therapy of cancer. Moreover, development of more efficient drug delivery systems is important in effectively targeting cancer. For these reasons, we were interested in AuNPs as scaffolds to which anti-CD105 mAbs are attached as an attractive diagnostic and/or therapeutic tool. These immunonanoconjugates might combine the therapeutic properties of anti-CD105 mAbs with those of AuNPs and might improve antitumor efficacy. In this study, we have demonstrated that despite decreased tumour uptake after nanoparticle conjugation, the *in vivo* antibody specificity and the tumour contrast in PET imaging are preserved. CD105-dependent tumour targeting was also confirmed by the quantification of gold in tumours. Thus, our studies validate anti-endoglin antibody-functionalized gold nanoparticles as a new tool for diagnostic and imaging of cancer. The nonspecific RES uptake of immunonanoconjugates could be a limitation in the use of radioactive nanoparticles for systemic metabolic radiotherapy, but not for therapeutic strategies, such as photothermal therapy, where nanoparticle activation can be locally controlled. Overall,  $^{89}\text{Zr}$  immuno-PET imaging is a powerful tool for characterizing the *in vivo* properties of such nanocomplex systems and can present new opportunities for drug delivery guided by *in vivo* imaging. These observations lay the groundwork for further theranostic applications and give further credence to the probability of future effective nanoparticle-based therapy systems.

## Executive Summary

### Characterization of radioimmunoconjugates and *in vitro* assessment of CD105 targeting

- Anti-CD105 mAbs conjugated to AuNPs were characterized *in vitro* in terms of size, plasmatic stability and binding to the target before *in vivo* experiments.
- The nanoparticle diameters observed by TEM imaging ranged from 3 to 10 nm. The mean diameter of anti-CD105 mAbs after coupling to AuNPs was estimated at about  $102.6 \pm 4.0$  nm by differential centrifugal sedimentation.
- The *in vitro* stability in plasma of both radioimmunoconjugates showed that the percentages of dissociation were lower by 10% after 24 h.
- The  $EC_{50}$  value was reduced from  $1 \mu\text{g ml}^{-1}$  (for anti-CD105 mAbs) to  $5 \mu\text{g ml}^{-1}$  (for anti-CD105-AuNPs-PPAA). The relative binding affinity remains on the same range (less than 1 log) before and after antibody conjugation to AuNPs.

### PET evaluation of $^{89}\text{Zr}$ -labelled anti-CD105 mAbs biodistribution in mice before and after coupling reaction to AuNPs

- The tumour uptake of  $^{89}\text{Zr}$ -labelled anti-CD105 mAbs was quantified before and after nanoparticle conjugation using noninvasive PET imaging in mice. The decreased tumour uptake after conjugation reaction is in accordance with the results obtained with *in vitro* ELISA study. Blocking experiments confirmed the specific tumour targeting of conjugated mAbs.
- The tumour-to-background ratio remained good after conjugation reaction. The high tumour contrast after nanoparticle conjugation supports the good imaging properties of the radioimmunonanoconjugates.
- The tumour uptake of antibody-targeted gold nanoparticles was also quantified using ICP-MS analysis by determining gold content in tumours, and was compared with the tumour uptake of free nanoparticles. Results highlighted the improved tumour uptake for functionalized nanoparticles. The specificity of anti-CD105 mAbs conjugated to AuNPs was confirmed through ICP-MS by repeating blocking experiments.
- No major accumulation of radioactivity was observed in nonspecific organs, aside from liver, spleen, lungs, and to a lesser extent bones.
- These results present new opportunities for nanoparticle-based imaging and therapy systems in future theranostic applications.

**Acknowledgments:** This work was supported by grants from the Walloon Region through the “TARGAN” project, and from the Belgian National Fund for Scientific Research (FNRS-TELEVIE). The hybridoma (clone MJ7/18) was obtained from the Developmental Studies Hybridoma Bank developed under the auspices of the NICHD and maintained by The University of Iowa, Department of Biology, Iowa City, IA 52242.

## References

Especially noteworthy papers have been marked as:

\* of interest

\*\* of considerable interest

1. Julien DC, Behnke S, Wang G, Murdoch GK, Hill RA. Utilization of monoclonal antibody-targeted nanomaterials in the treatment of cancer. *MAbs*. 3(5), 467–478 (2011). \* This review discusses the broad range of nanomaterials including AuNPs that are under investigation as potential platforms for the presentation of mAbs either as single or combined therapeutics, and their advantages and limitations in specifically targeting cancer.
2. Dykman L, Khlebtsov N. Gold nanoparticles in biomedical applications: recent advances and perspectives. *Chem. Soc. Rev.* 41(6), 2256–2282 (2012).
3. Mallidi S, Larson T, Aaron J, Sokolov K, Emelianov S. Molecular specific optoacoustic imaging with plasmonic nanoparticles. *Opt. Express*. 15(11), 6583–6588 (2007).
4. Glaser ES, Massey KL, Zhu C, Curley SA. Pancreatic carcinoma cells are susceptible to noninvasive radio frequency fields after treatment with targeted gold nanoparticles. *Surgery*. 148(2), 319–324 (2010).
5. Tiwari PM, Vig K, Dennis VA, Singh R. Functionalized gold nanoparticles and their biomedical applications. *Nanomaterials*. 1, 31–63 (2011). \* This review describes the recent advances in the field of functionalization of AuNPs and their potential biomedical applications.
6. Haruta Y, Seon BK. Distinct human leukemia-associated cell surface glycoprotein GP160 defined by monoclonal antibody SN6. *Proc. Natl. Acad. Sci. USA*. 83(20), 7898–7902 (1986).
7. Westphal JR, Willems HW, Schalkwijk CJ, Ruiter DJ, de Waal RM. A new 180-kDa dermal endothelial cell activation antigen: *in vitro* and *in situ* characteristics. *J. Invest. Dermatol.* 100(1), 27–34 (1993).
8. Burrows FJ, Derbyshire EJ, Tazzari PL *et al.* Up-regulation of endoglin on vascular endothelial cells in human solid tumors: implications for diagnosis and therapy. *Clin. Cancer Res.* 1(12), 1623–1634 (1995).
9. Miller DW, Graulich W, Karges B *et al.* Elevated expression of endoglin, a component of the TGF-beta-receptor complex, correlates with proliferation of tumor endothelial cells. *Int. J. Cancer*. 81(4), 568–572 (1999).
10. Fonsatti E, Nicolay HJ, Altomonte M, Covre A, Maio M. Targeting cancer vasculature via endoglin/CD105: a novel antibody-based diagnostic and therapeutic strategy in solid tumours. *Cardiovasc. Res.* 86(1), 12–19 (2010).
11. Wang JM, Kumar S, Pye D, van Agthoven AJ, Krupinski J, Hunter R.D. A monoclonal antibody detects heterogeneity in vascular endothelium of tumours and normal tissues. *Int. J. Cancer*. 54(3), 363–370 (1993).
12. Clasper S, Royston D, Baban D *et al.* A novel gene expression profile in lymphatics associated with tumor growth and nodal metastasis. *Cancer Res.* 68(18), 7293–7303 (2008).

13. Yoshitomi H, Kobayashi S, Ohtsuka M *et al.* Specific expression of endoglin (CD105) in endothelial cells of intratumoral blood and lymphatic vessels in pancreatic cancer. *Pancreas*. 37(3), 275–281 (2008).
14. Hussein MR. Transforming growth factor-beta and malignant melanoma: molecular mechanisms. *J. Cutan. Pathol.* 32(6), 389–395 (2005).
15. Sun T, Sun BC, Ni CS *et al.* Pilot study on the interaction between B16 melanoma cell-line and bone-marrow derived mesenchymal stem cells. *Cancer Lett.* 263(1), 35–43 (2008).
16. Letamendía A, Lastres P, Almendro N *et al.* Endoglin, a component of the TGF-beta receptor system, is a differentiation marker of human choriocarcinoma cells. *Int. J. Cancer.* 76(4), 541–546 (1998).
17. Kumar S, Ghellal A, Li C *et al.* Breast carcinoma: vascular density determined using CD105 antibody correlates with tumor prognosis. *Cancer Res.* 59(4), 856–861 (1999).
18. Romani AA, Borghetti AF, Del Rio P, Sianesi M, Soliani P. The risk of developing metastatic disease in colorectal cancer is related to CD105-positive vessel count. *J. Surg. Oncol.* 93(6), 446–455 (2006).
19. Marioni G, D'Alessandro E, Giacomelli L, Staffieri A. CD105 is a marker of tumour vasculature and a potential target for the treatment of head and neck squamous cell carcinoma. *J. Oral. Pathol. Med.* 39(5), 361–367 (2010).
20. Tanaka F, Otake Y, Yanagihara K *et al.* Evaluation of angiogenesis in non-small cell lung cancer: comparison between anti-CD34 antibody and anti-CD105 antibody. *Clin. Cancer Res.* 7(11), 3410–3415 (2001).
21. Li C, Gardy R, Seon BK *et al.* Both high intratumoral microvessel density determined using CD105 antibody and elevated plasma levels of CD105 in colorectal cancer patients correlate with poor prognosis. *Br. J. Cancer.* 88(9), 1424–1431 (2003).
22. Charpin C, Dales JP, Garcia S *et al.* Tumor neoangiogenesis by CD31 and CD105 expression evaluation in breast carcinoma tissue microarrays. *Clin. Cancer Res.* 10(17), 5815–5819 (2004).
23. Carmeliet P, Jain RK. Molecular mechanisms and clinical applications of angiogenesis. *Nature.* 473(7347), 298–307 (2011).
24. Mitchell DC, Bryan BA. Anti-angiogenic therapy: adapting strategies to overcome resistant tumors. *J. Cell. Biochem.* 111(3), 543–553 (2010).
25. Gasparini G, Longo R, Fanelli M, Teicher BA. Combination of antiangiogenic therapy with other anticancer therapies: results, challenges, and open questions. *J. Clin. Oncol.* 23(6), 1295–1311 (2005).
26. Seon BK, Matsuno F, Haruta Y, Kondo M, Barcos M. Long-lasting complete inhibition of human solid tumors in SCID mice by targeting endothelial cells of tumor vasculature with anti-human endoglin immunotoxin. *Clin. Cancer Res.* 3(7), 1031–1044 (1997).
27. Matsuno F, Haruta Y, Kondo M, Tsai H, Barcos M, Seon BK. Induction of lasting complete regression of preformed distinct solid tumors by targeting the tumor vasculature using two new anti-endoglin monoclonal antibodies. *Clin. Cancer Res.* 5(2), 371–382 (1999).

28. Tabata M, Kondo M, Haruta Y, Seon BK. Antiangiogenic radioimmunotherapy of human solid tumors in SCID mice using  $^{125}\text{I}$ -labeled anti-endoglin monoclonal antibodies. *Int. J. Cancer*. 82(5), 737–742 (1999).
29. Takahashi N, Haba A, Matsuno F, Seon BK. Antiangiogenic therapy of established tumors in human skin/severe combined immunodeficiency mouse chimeras by anti-endoglin (CD105) monoclonal antibodies, and synergy between anti-endoglin antibody and cyclophosphamide. *Cancer Res*. 61(21), 846–854 (2001).
30. Tsujie M, Uneda S, Tsai H, Seon BK. Effective anti-angiogenic therapy of established tumors in mice by naked anti-human endoglin (CD105) antibody: differences in growth rate and therapeutic response between tumors growing at different sites. *Int. J. Oncol*. 29(5), 1087–1094 (2006).
31. Tsujie M, Tsujie T, Toi H *et al*. Anti-tumor activity of an anti-endoglin monoclonal antibody is enhanced in immunocompetent mice. *Int. J. Cancer*. 122(10), 2266–2273 (2008).
32. Uneda S, Toi H, Tsujie T *et al*. Anti-endoglin monoclonal antibodies are effective for suppressing metastasis and the primary tumors by targeting tumor vasculature. *Int. J. Cancer*. 125(6), 1446–1453 (2009).
33. Marega R, Karmani L, Flamant L *et al*. Antibody-functionalized polymer-coated gold nanoparticles targeting cancer cells: an in vivo and in vitro study. *J. Mater. Chem*. 22(39), 21305–21312 (2012). \*\* Describes the characterization of gold nanoparticles and cetuximab conjugated to gold nanoparticles before *in vivo* experiments and assesses the biodistribution of iodinated cetuximab before and after nanoparticle conjugation by *ex-vivo* studies.
34. Karmani L, Labar D, Valembois V *et al*. Antibody-functionalized nanoparticles for imaging cancer: influence of conjugation to gold nanoparticles on the biodistribution of  $^{89}\text{Zr}$ -labeled cetuximab in mice. *Contrast Media Mol Imaging*. 8(5), 402–408 (2013). \*\* Compares the biodistribution pattern of cetuximab-targeted gold nanoparticles and unconjugated cetuximab in mice using non invasive  $^{89}\text{Zr}$  immuno-PET studies.
35. Vugts DJ, van Dongen GAMS.  $^{89}\text{Zr}$ -labeled compounds for PET imaging guided personalized therapy. *Drug Discov. Today Technol*. 8(2-4), e53–e61 (2011).
36. van Dongen GAMS, Visser GWM, Lub-de-Hooge MN, De Vries EG, Perk LR. Immuno-PET: A navigator in monoclonal antibody development and applications. *Oncologist*. 12(12), 1379–1389 (2007).
37. Holland JP, Sheh YC, Lewis JS. Standardized methods for the production of high specific-activity zirconium-89. *Nucl. Med. Biol*. 36(7), 729–739 (2009).
38. Kandil SA, Scholten B, Saleh ZA, Youssef AM, Qaim SM, Coenen HH. A comparative study on the separation of radiozirconium via ion-exchange and solvent extraction techniques, with particular reference to the production of  $^{88}\text{Zr}$  and  $^{89}\text{Zr}$  in proton induced reactions on yttrium. *J. Radioanal. Nucl. Chem*. 274(1), 45–52 (2007).
39. Vosjan MJWD, Perk LR, Visser GW *et al*. Conjugation and radiolabeling of monoclonal antibodies with zirconium-89 for PET imaging using the bifunctional chelate p-isothiocyanatobenzyl-desferrioxamine. *Nat. Prot*. 5(4), 739–743 (2010).

40. Perk LR, Vosjan MJWD, Visser GW *et al.* p-Isothiocyanatobenzyl-desferrioxamine: a new bifunctional chelate for facile radiolabeling of monoclonal antibodies with zirconium-89 for immuno-PET imaging. *Eur. J. Nucl. Med. Mol. Imaging.* 37(2), 250–259 (2010).
41. Moreau N, Michiels C, Masereel B *et al.* PVD synthesis and transfer into water-based solutions of functionalized gold nanoparticles. *Plasma Process Polymer.* 6(1), S888–S892 (2009). \* Describes the synthesis and the coating of AuNPs by PVD techniques and highlights the crucial role of the coating to prevent the AuNPs aggregation when transferred into liquid solutions in order to facilitate their functionalization for future studies.
42. Masereel B, Dinguizli M, Bouzin C *et al.* Antibody immobilization on gold nanoparticles coated layer-by-layer with polyelectrolytes. *J. Nanopart. Res.* 13(4), 1573–1580 (2011).
43. Hong H, Yang Y, Zhang Y *et al.* Positron emission tomography imaging of CD105 expression during tumor angiogenesis. *Eur. J. Nucl. Med. Mol. Imaging.* 38(7), 1335–1343 (2011).
44. Huisman MC, Reder S, Weber AW, Ziegler SI, Schwaiger M. Performance evaluation of the Philips MOSAIC small animal PET scanner. *Eur. J. Nucl. Med. Mol. Imaging.* 34(4), 532–540 (2007).
45. Alkilany AM, Murphy CJ. Toxicity and cellular uptake of gold nanoparticles: what we have learned so far? *J Nanopart Res.* 12(7), 2313–2333 (2010).
46. Garnett MC, Kallinteri P. Nanomedicines and nanotoxicology: some physiological principles. *Occup Med (Lond).* 56(5), 307–311 (2006).
47. Hirota K, Hasegawa T, Hinata H *et al.* Optimum conditions for efficient phagocytosis of rifampicin-loaded PLGA microspheres by alveolar macrophages. *J Control Release.* 119(1), 69–76 (2007).
48. Videira MA, Botelho MF, Santos AC, Gouveia LF, de Lima JJ, Almeida AJ. Lymphatic uptake of pulmonary delivered radiolabelled solid lipid nanoparticles. *J Drug Target.* 10(8), 607–613 (2002).
49. He C, Hu Y, Yin L, Tang C, Yin C. Effects of particle size and surface charge on cellular uptake and biodistribution of polymeric nanoparticles. *Biomaterials.* 31(13), 3657–3666 (2010).
50. Mahmoud M, Borthwick GM, Hislop AA, Arthur HM. Endoglin and activin receptor-like-kinase 1 are co-expressed in the distal vessels of the lung: implications for two familial vascular dysplasias, HHT and PAH. *Lab Invest.* 89(1), 15–25 (2009).
51. De Jong WH, Hagens WI, Krystek P, Burger MC, Sips AJ, Geertsma RE. Particle size-dependent organ distribution of gold nanoparticles after intravenous administration. *Biomaterials.* 29(12), 1912–1919 (2008).
52. Tinianow JN, Gill HS, Ogasawara A *et al.* Site-specifically <sup>89</sup>Zr-labeled monoclonal antibodies for ImmunoPET. *Nucl. Med. Biol.* 37(3), 289–297 (2010).
53. Mealey Jr J. Turn-over of carrier-free zirconium-89 in man. *Nature.* 179(4561), 673–674 (1957).
54. Abou DS, Ku T, Smith-Jones PM. In vivo biodistribution and accumulation of <sup>89</sup>Zr in mice. *Nucl. Med. and Biol.* 38(5), 675–681 (2011).

- 
55. Glazer ES, Curley SA. Radiofrequency field-induced thermal cytotoxicity in cancer cells treated with fluorescent nanoparticles. *Cancer*. 116(13), 3285–3293 (2010).
56. Moran CH, Wainerdi SM, Cherukuri TK et al. Size-dependent joule heating of gold nanoparticles using capacitively coupled radiofrequency fields. *Nano Res*. 2(5), 400–405 (2009).
57. Chang MY, Shiau AL, Chen YH, Chang CJ, Chen HH, Wu CL. Increased apoptotic potential and dose-enhancing effect of gold nanoparticles in combination with single-dose clinical electron beams on tumor-bearing mice. *Cancer Sci*. 99(7), 1479–1484 (2008).
58. Hainfeld JF, Slatkin DN, Smilowitz HM. The use of gold nanoparticles to enhance radiotherapy in mice. *Phys Med Biol*. 49(18), N309–N315. (2004).
59. Raof M, Curley SA. Non-invasive radiofrequency-induced targeted hyperthermia for the treatment of hepatocellular carcinoma. *Int J Hepatol*. 2011, 676957 (2011).
60. Rosen LS, Hurwitz HI, Wong MK et al. A phase I first-in-human study of TRC105 (Anti-Endoglin Antibody) in patients with advanced cancer. *Clin. Cancer Res*. 18(17), 4820–4829 (2012). \*\* Reports the first-in-human, phase I study using anti-endoglin antibody (TRC105) in order to investigate its safety, pharmacokinetics and antitumor activity in patients with advanced refractory solid tumors.
61. Fonsatti E, Del Vecchio L, Altomonte M et al. Endoglin: an accessory component of the TGF-beta-binding receptor-complex with diagnostic, prognostic, and bioimmunotherapeutic potential in human malignancies. *J. Cell. Physiol*. 188(1), 1–7 (2001).
62. Wang JM, Kumar S, Pye D, van Agthoven AJ, Krupinski J, Hunter RD. A monoclonal antibody detects heterogeneity in vascular endothelium of tumours and normal tissues. *Int. J. Cancer*. 54(3), 363–370 (1993).

## Figures

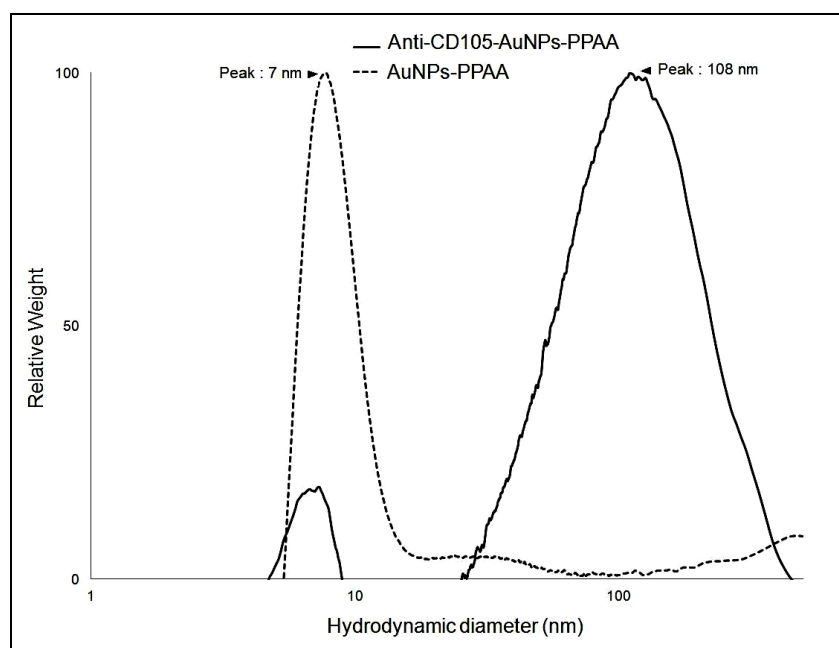


Fig. 1 Size distributions given by differential centrifugal sedimentation for AuNPs (dashed line) and anti-CD105-AuNPs-PPAA obtained after conjugation reaction (solid line).

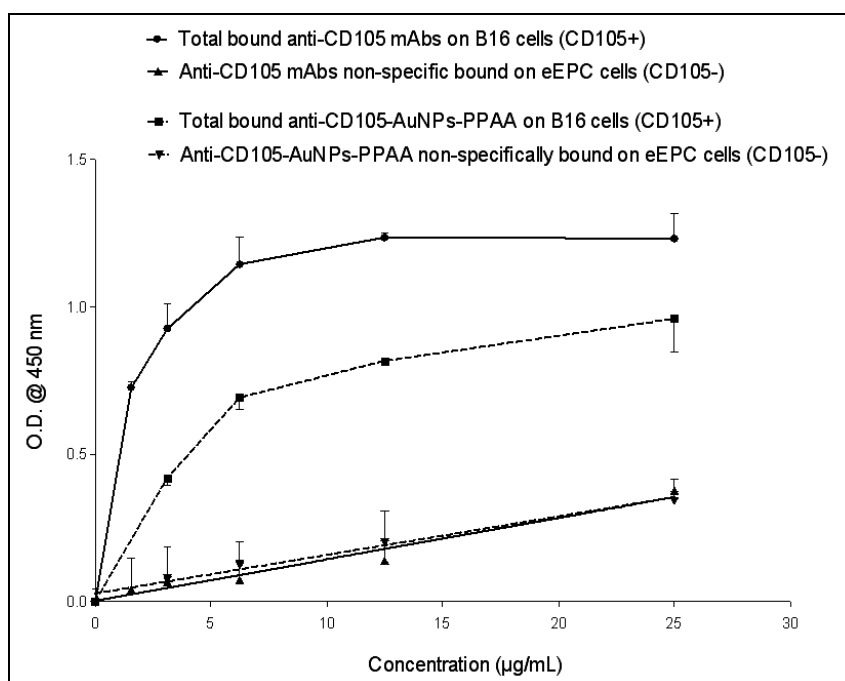


Fig. 2 Surface ELISA for anti-CD105 mAbs and anti-CD105-AuNPs-PPAA on CD105+ (B16F10-luc) and CD105- (eEPC) cells. Different concentrations of mAbs and mAbs conjugated to AuNPs were tested. The concentration is expressed as  $\mu\text{g}$  of mAbs  $\text{mL}^{-1}$ . Results are presented as means  $\pm$  SEM. (n = 2-4).

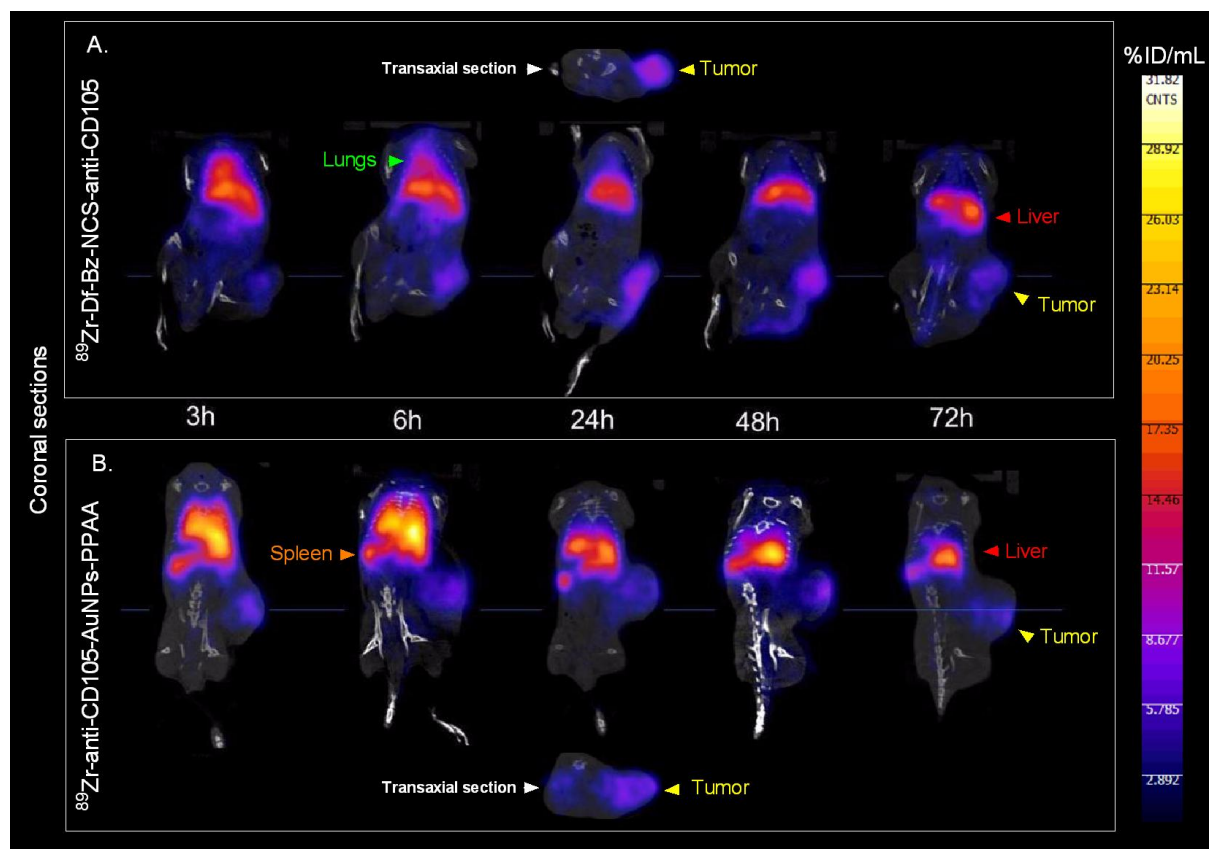


Fig. 3 B16 melanoma-bearing C57BL/6J mice, injected with  $^{89}\text{Zr}$ -Df-Bz-NCS-anti-CD105 [A] or  $^{89}\text{Zr}$ -anti-CD105-AuNPs-PPAA [B] (one tumour per mouse). PET/CT images were obtained at different times after injection (3, 6, 24, 48 and 72 h). Colour scale expressed as a percentage of the injected dose per millilitre (%ID  $\text{ml}^{-1}$ ), indicated the radioactivity uptake levels in tumours (yellow arrows), in liver (red arrows), in spleen (orange arrows) and in lungs (green arrows).

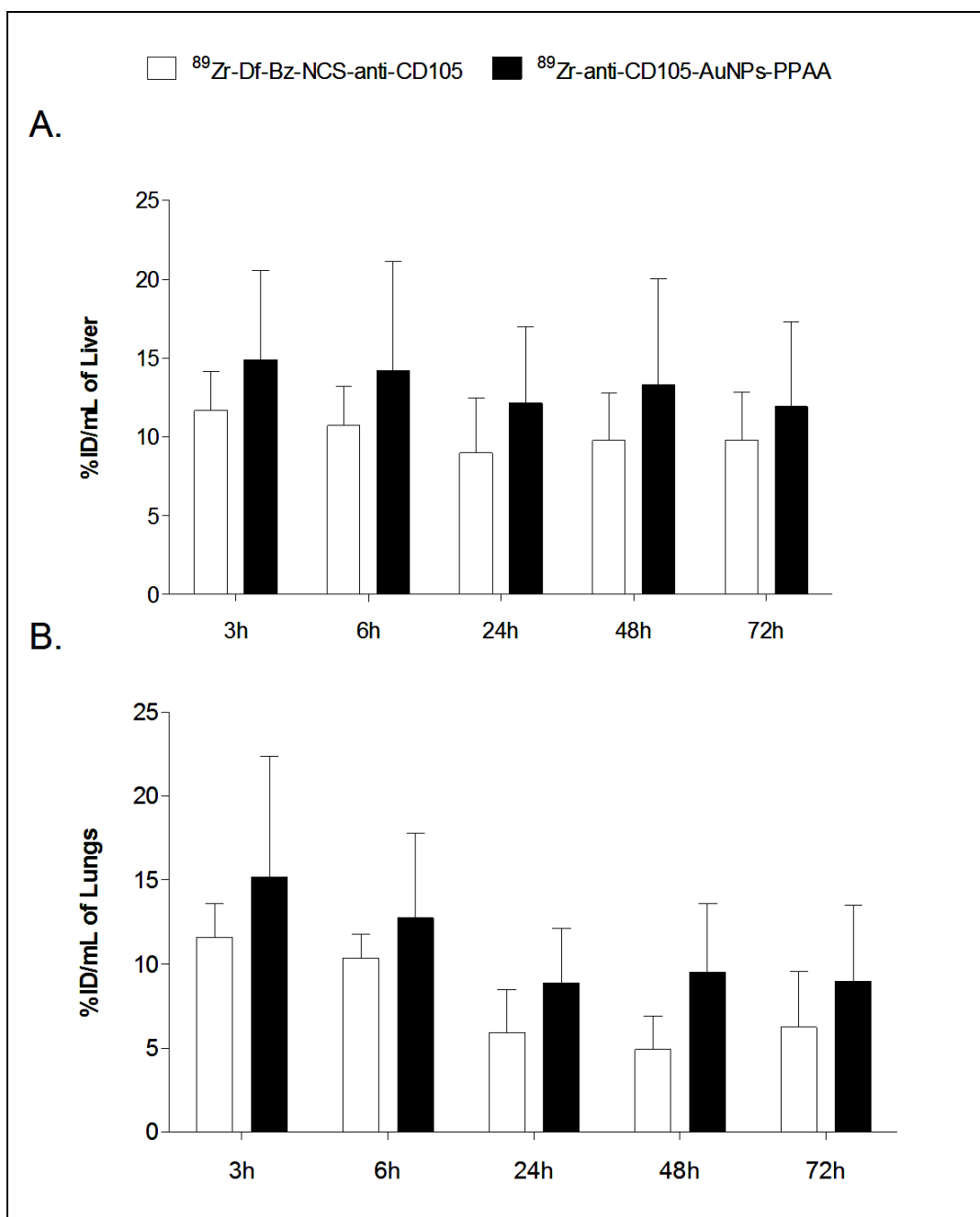


Fig. 4 B16 melanoma-bearing C57BL/6J mice, injected with  $^{89}\text{Zr}$ -Df-Bz-NCS-anti-CD105 (white bars) or  $^{89}\text{Zr}$ -anti-CD105-AuNPs-PPAA (black bars). Injected activity ranged from 2.9-4.1 MBq, corresponding to a total of 350-400  $\mu\text{g}$  mAbs per mouse. Liver [A] and lung [B] uptakes were quantified at 3, 6, 24, 48 and 72 h after injection. Results are expressed as means  $\pm$  SD ( $n = 4-5$  animals).

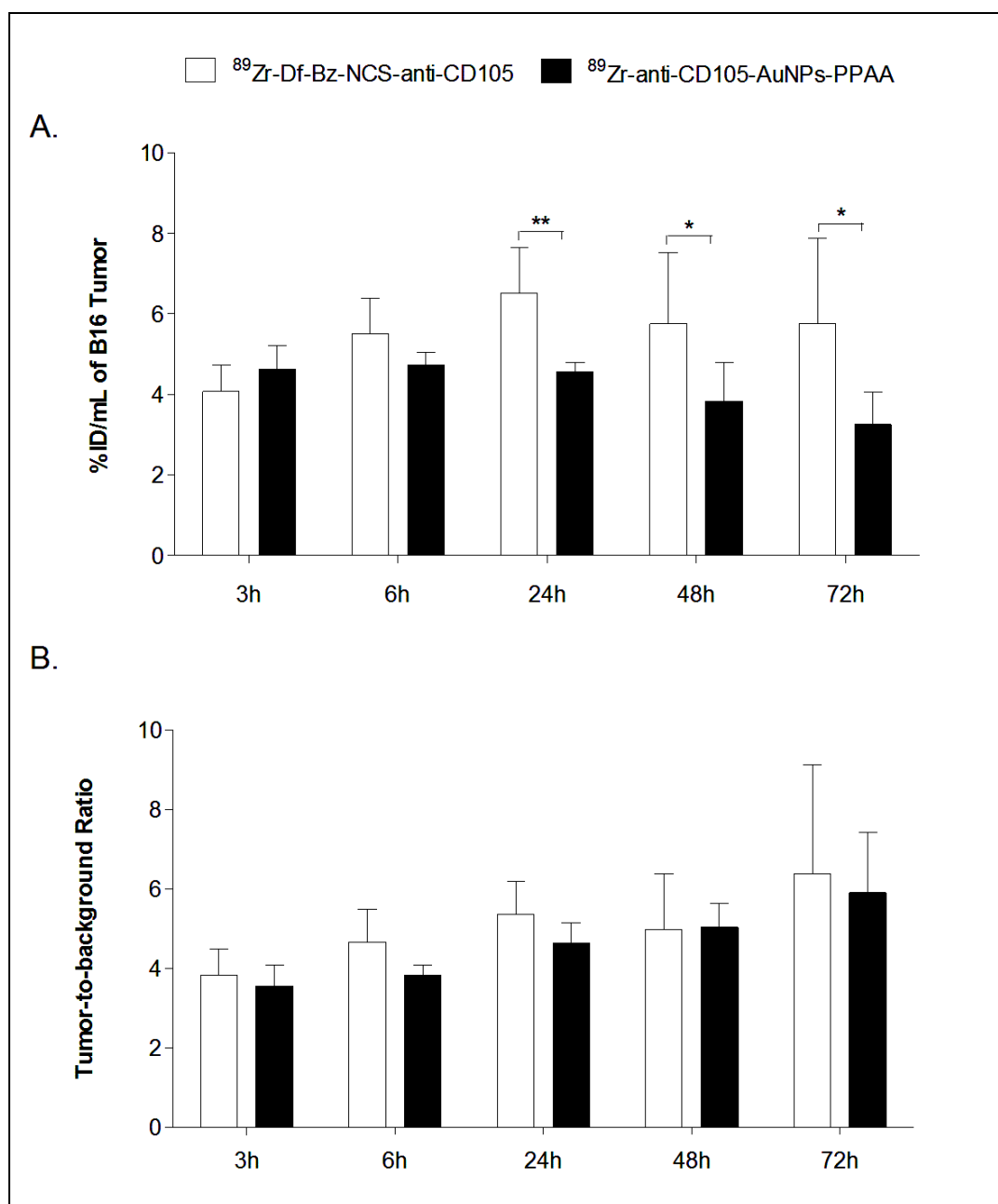


Fig. 5 Tumour uptake [A] and tumour-to-background ratio [B] of  $^{89}\text{Zr}$ -Df-Bz-NCS-anti-CD105 (white bars) or  $^{89}\text{Zr}$ -anti-CD105-AuNPs-PPAA (black bars) in B16 melanoma-bearing C57BL/6J mice at 3, 6, 24, 48 and 72 h after injection. Injected activity ranged from 2.9-4.1 MBq, corresponding to a total of 350-400  $\mu\text{g}$  mAbs per mouse. Results are expressed as means  $\pm$  SD (n = 3-5 animals; 4-8 tumours). \* p < 0.05; \*\* p < 0.01.

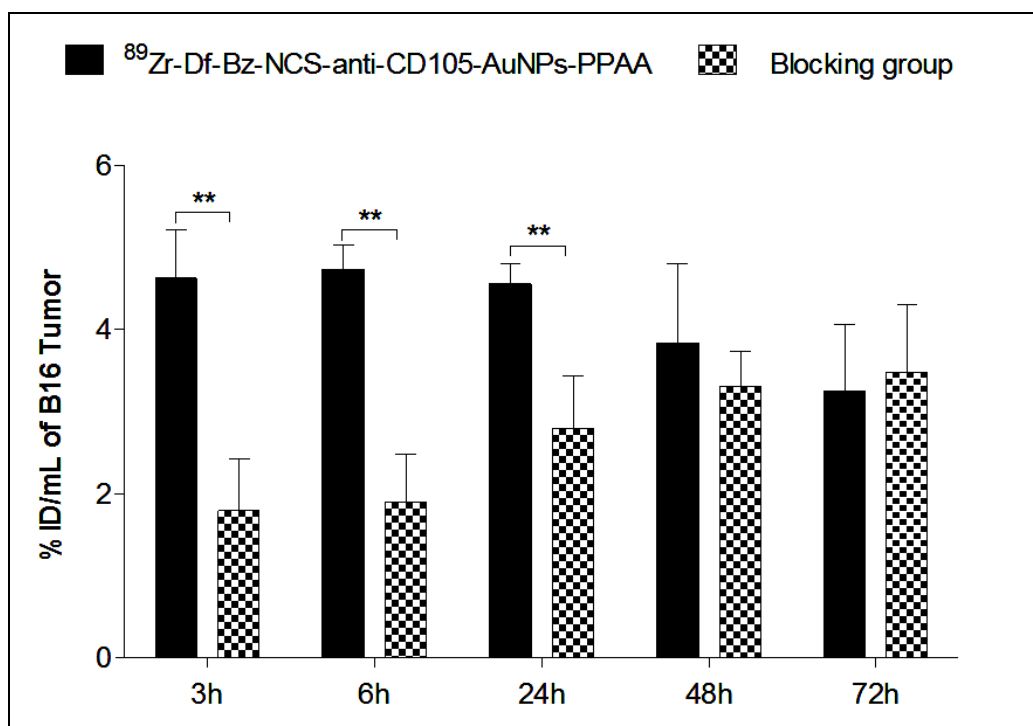


Fig. 6 Tumour uptake of  $^{89}\text{Zr}$ -anti-CD105-AuNPs-PPAA (2.9-4.1 MBq, a total of 350-400  $\mu\text{g}$  mAbs per mouse) or  $^{89}\text{Zr}$ -anti-CD105-AuNPs-PPAA (3.6-4.1 MBq, a total of 200  $\mu\text{g}$  mAbs per mouse) after a blocking dose of unlabelled anti-CD105 mAbs (2000  $\mu\text{g}$  mAbs per mouse) in B16 melanoma-bearing C57BL/6J mice at 3, 6, 24, 48 and 72 h after injection. Results are expressed as means  $\pm$  SD (n = 3 animals; 4-6 tumours). \*\* p < 0.01.

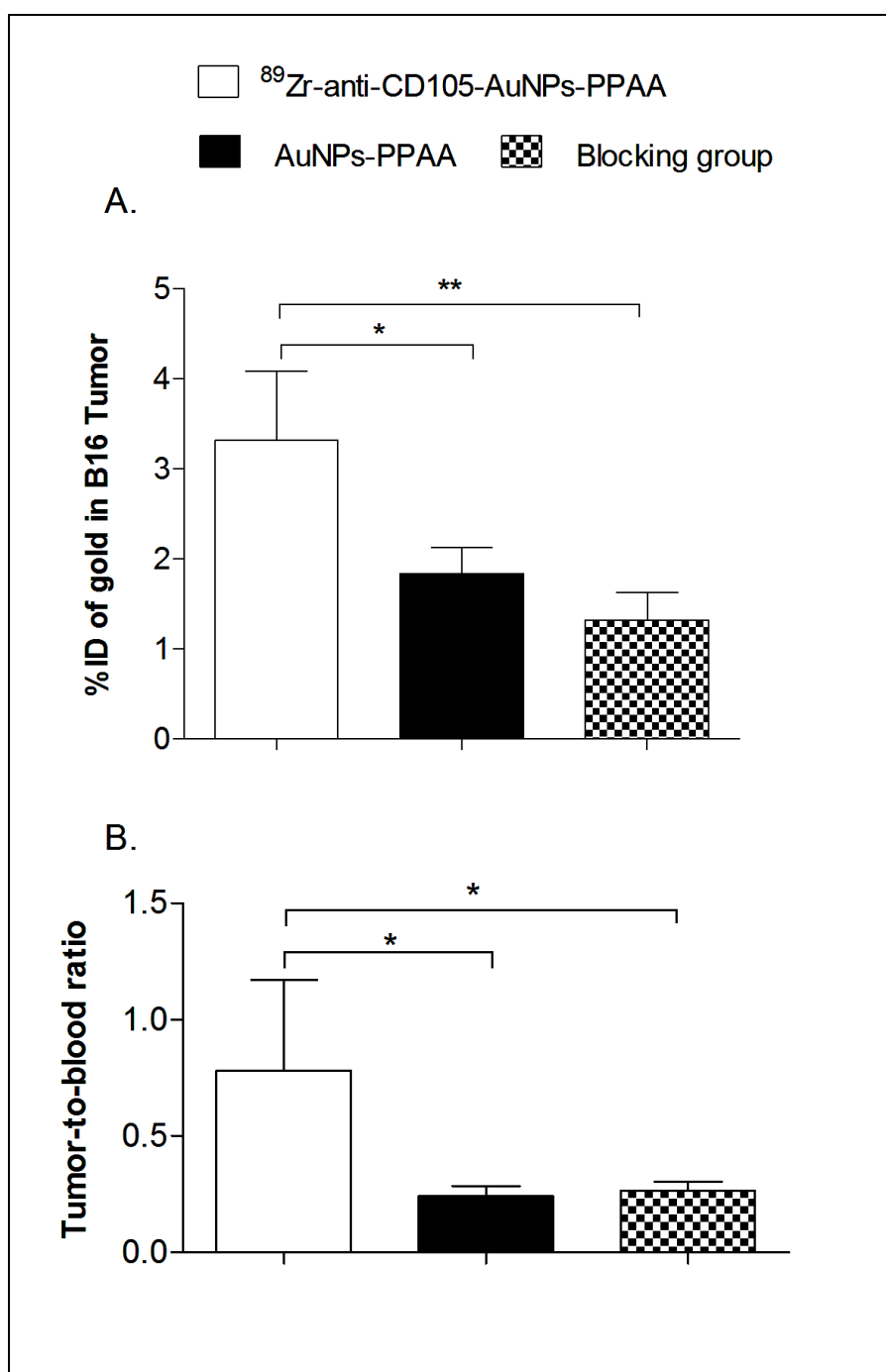
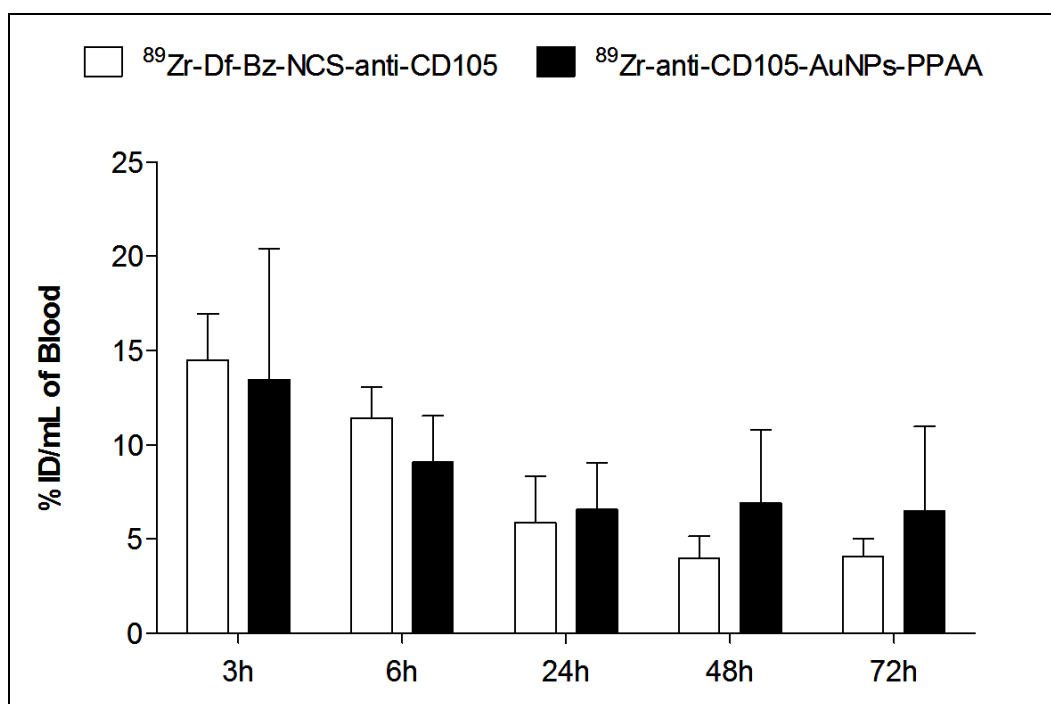
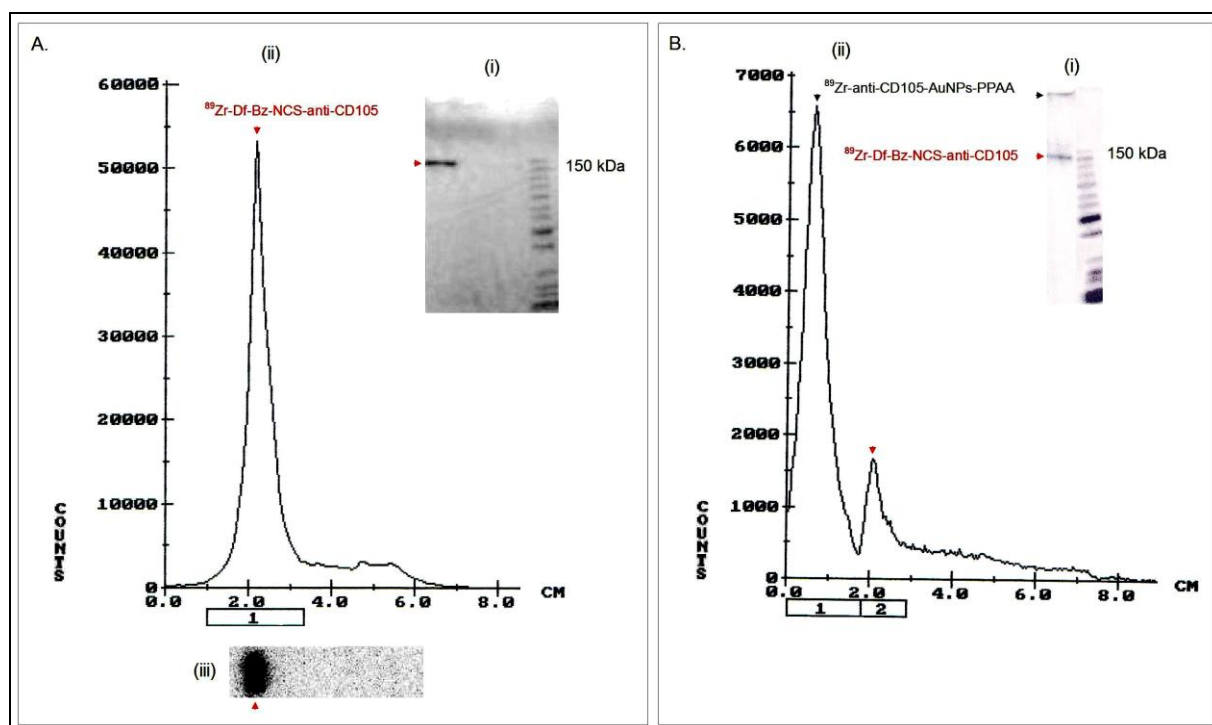


Fig. 7 Gold content in tumours [A] and tumour-to-background ratio [B] after intravenous injection of free AuNPs (a total of 36  $\mu\text{g}$  Au per mouse) or anti-CD105-AuNPs-PPAA (a total of 18  $\mu\text{g}$  Au per mouse, corresponding to 100  $\mu\text{g}$  mAbs per mouse) or anti-CD105-AuNPs-PPAA (a total of 22  $\mu\text{g}$  Au per mouse, corresponding to a total of 200  $\mu\text{g}$  mAbs per mouse) after a blocking dose of anti-CD105 mAbs (2 mg mAbs per mouse) in B16 melanoma-bearing C57BL/6J mice 6 h after injection. Gold content as measured by ICP-MS is expressed as a percentage of the given dose (%ID). Data are expressed as means  $\pm$  SD ( $n = 3-4$  animals; 3-4 tumours). \*  $p < 0.05$ ; \*\*  $p < 0.01$ .

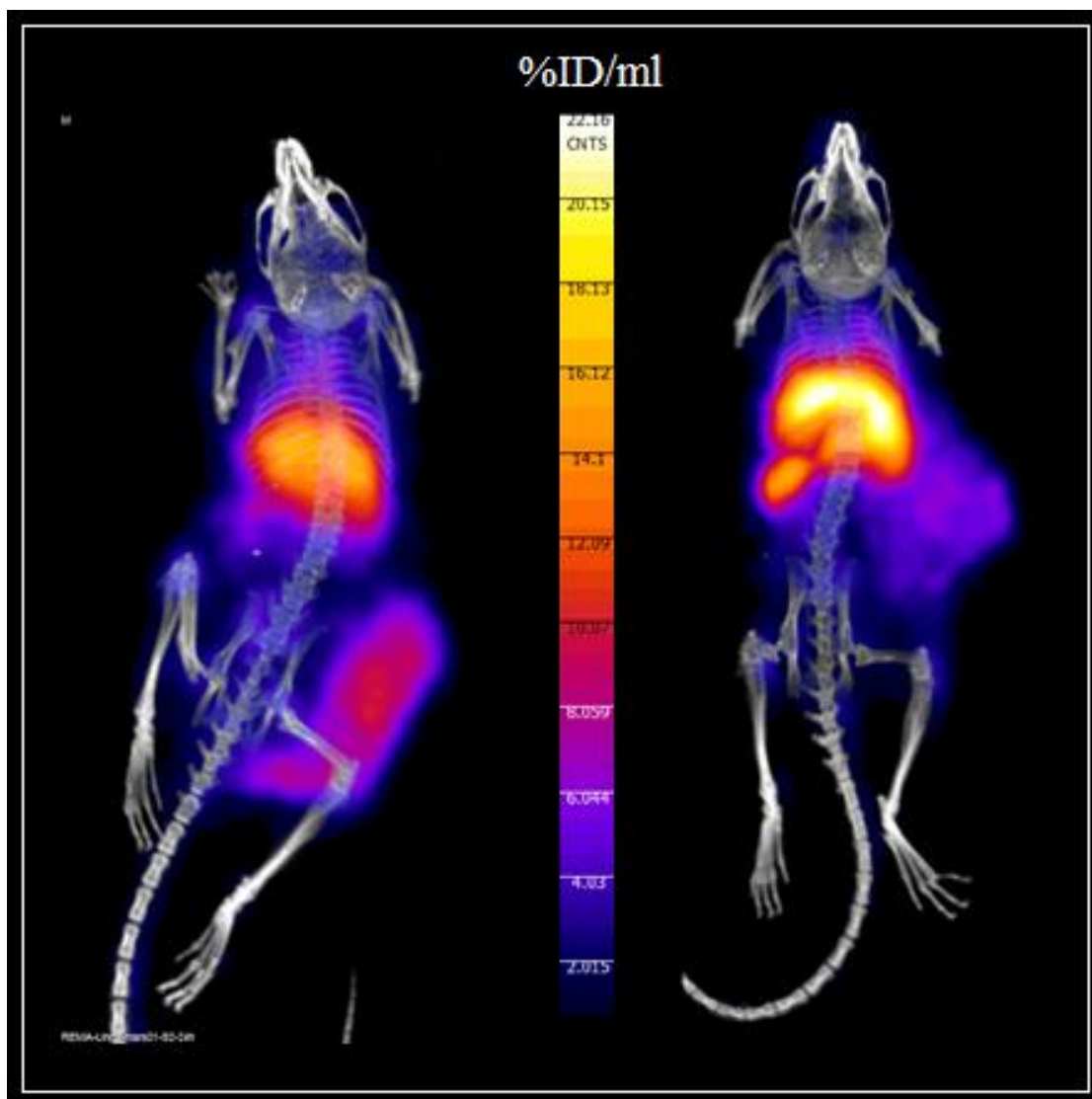
## Supplementary material



Online Resource 1 Blood concentration of  $^{89}\text{Zr}$ -Df-Bz-NCS-anti-CD105 (white bars) or  $^{89}\text{Zr}$ -anti-CD105-AuNPs-PPAA (black bars) in B16 melanoma-bearing C57BL/6J mice at 3, 6, 24, 48 and 72 h after injection. Injected activity ranged from 2.9-4.1 MBq, corresponding to a total of 350-400  $\mu\text{g}$  mAbs per mouse. Results are expressed as means  $\pm$  SD (n = 4-5 animals).

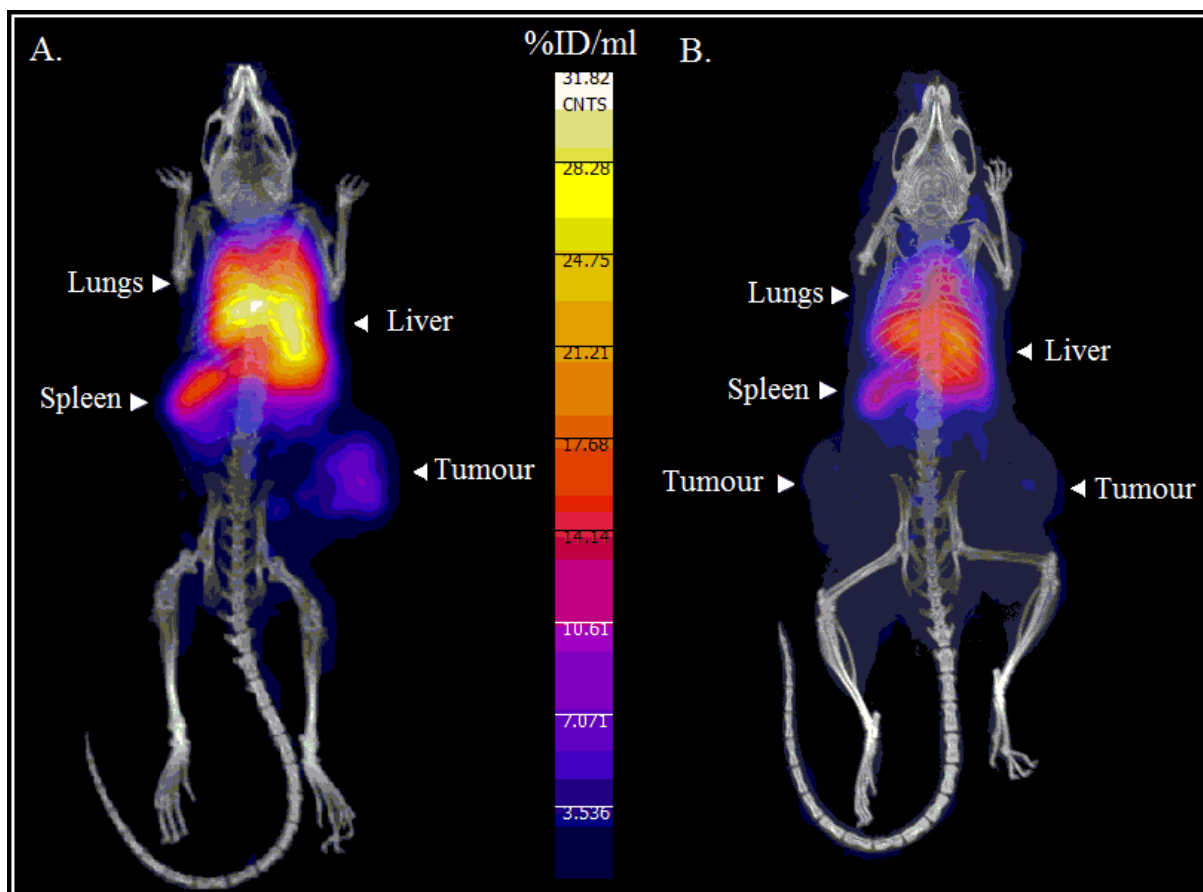


Online Resource 2 Electrophoretic profiles of  $^{89}\text{Zr}$ -Df-Bz-NCS-anti-CD105 [A] and  $^{89}\text{Zr}$ -anti-CD105-AuNPs-PPAA [B] using SDS-PAGE 10% under nonreducing conditions (i) followed by radio-TLC (ii) and Phosphor Imager (iii) analysis.



Online Resource 3 3D video of a PET/CT fusion MIP of  $^{89}\text{Zr}$ -Df-Bz-NCS-anti-CD105 24 h after injection in B16 melanoma-bearing C57BL/6J mice (one tumour per mouse).

Online Resource 4 3D video of a PET/CT fusion MIP of  $^{89}\text{Zr}$ -anti-CD105-AuNPs-PPAA 24 h after injection in B16 melanoma-bearing C57BL/6J mice (one tumor per mouse).



Data not shown: PET/CT fusion MIP of  $^{89}\text{Zr}$ -anti-CD105-AuNPs-PPAA (2.9-4.1 MBq, corresponding to a total of 350-400  $\mu\text{g}$  mAbs) 3 h after injection in B16 melanoma-bearing mice, before [A] and after [B] injection of a saturating dose of unlabelled mAbs (2000  $\mu\text{g}$  mAbs). White arrows indicate the decrease of radioactivity signal after blocking CD105 receptor [B] in lungs, liver, spleen and tumours.

## **Chapter 4: DISCUSSION AND PROSPECTS**



## I. Main findings

The first study characterized the produced gold nanoparticles and cetuximab-conjugated gold nanoparticles. *Ex-vivo* experiments assessed the biodistribution profile of iodinated anti-EGFR antibody before and after the nanoparticle conjugation. The main results are:

- Coupling nanoparticles to cetuximab does not affect the pharmacokinetic behaviour of the anti-EGFR mAbs, and particularly the tumour uptake, except a relative increased RES uptake without accumulation.
- After the nanoparticle conjugation, cetuximab preserves its specific targeting activity towards EGFR overexpressed on tumour cells, in accordance with the results of *in vitro* binding studies.
- The maximum tumour uptake was observed at a relatively early time after injection (about 2.3 %ID g<sup>-1</sup>; 24 h after injection) and was not persistent over time, with a low tumour contrast (T/B less than 2.4). *In vivo* deiodination, which is suspected because of the thyroid accumulation, might affect the quantification of the tumour uptake (underestimation of tumour uptake values).

Based on these first results, the second study highlights the limitations of using direct labelling of anti-CD105 mAbs with radioiodine on monitoring the pharmacokinetics of iodinated antibodies. The effects of *in vivo* dehalogenation of anti-CD105 mAbs on the assessment of tumour targeting were described thanks to *ex-vivo* studies, and were confirmed through SPECT/CT imaging. The tumour uptake of <sup>125</sup>I-labelled anti-CD105 mAbs was compared with that of <sup>89</sup>Zr-labelled anti-CD105 mAbs. The main results are:

- The high *in vitro* stability of <sup>125</sup>I-anti-CD105 mAbs in plasma suggests that *in vivo* catabolism is probably responsible for the important antibody dehalogenation.
- The tumour uptake kinetics of <sup>125</sup>I-anti-CD105 mAbs was rapid with a significant decrease over time (%ID g<sup>-1</sup> less than 1; 24 h after injection). This non persistent tumour uptake was similar for two tumour models (hepatocarcinoma and melanoma) and was not in accordance with the delayed tumour accumulation, which is expected for most intact mAbs.
- The most remarkable uptake by nonspecific tissues was observed for lungs, spleen, liver, stomach and kidneys without any accumulation. The most significant increase of nonspecific accumulation was observed for the thyroid (from 7.5 ± 2.8 %ID g<sup>-1</sup>, 5 min after injection to 341.1 ± 58.7 %ID g<sup>-1</sup>, 72 h after injection), suggesting *in vivo* deiodination.
- *In vivo* chemical instability of iodinated mAbs leads to a rapid clearance of the radiolabel probes, and an unsuitable weak tumour contrast for SPECT imaging (T/Bg close to 1).

- The tumour targeting profile over time was different for  $^{89}\text{Zr}$ -labelled anti-CD105 mAbs and  $^{125}\text{I}$ -labelled anti-CD105 mAbs. The maximum tumour uptake was higher for  $^{89}\text{Zr}$ -anti-CD105 mAbs (6.5 %ID ml<sup>-1</sup>; 24 h after injection), and remained high at late times after injection (5.8 %ID ml<sup>-1</sup>; 72 h after injection) with a high tumour contrast (T/Bg about 5.6-fold higher).  $^{89}\text{Zr}$  seems to be a more suitable alternative for the anti-CD105 antibody radiolabelling than the direct labelling with  $^{125}\text{I}$ .
- In summary, *in vivo* deiodination has a negative impact on the monitoring of the anti-CD105 antibody pharmacokinetic profile, and compromises the stable tracking of the tracer in tissues, and thus the accurate characterization of tumour targeting. Therefore, we chose  $^{89}\text{Zr}$ , as a known validated radiolabel for the anti-CD105 mAbs labelling in order to study the biodistribution of our immunonanoconjugates.

The third study characterized *in vivo* distribution of  $^{89}\text{Zr}$ -labelled cetuximab before and after the nanoparticle conjugation by using the quantitative PET imaging:

- There was no significant difference in tumour uptake of cetuximab before and after the nanoparticle conjugation. The same kinetic profile was observed with a slow tumour uptake (maximum %ID ml<sup>-1</sup> of 3.3; 48 h after injection), and with a continuous high tumour contrast (T/Bg more than 10 starting from 24 h).
- The liver and spleen uptake were enhanced after the nanoparticle conjugation, with a significant increase in liver uptake (more than twice high).
- The bone accumulation was due to the detachment of  $^{89}\text{Zr}$  from the antibody, and started from 24 h after injection, in accordance with the results of the tracer stability in plasma.
- *In vivo* specificity of cetuximab after the coupling reaction was preserved, with a selective tumour targeting (a significant decrease in tumour uptake after the saturation of EGFR binding sites).
- In summary, conjugation cetuximab to AuNPs does not significantly affect the tumour uptake in mice.  $^{89}\text{Zr}$ -labelled cetuximab-targeted gold nanoparticles enable to effectively target cancer cells, with preserving favourable imaging properties.

The last study characterized *in vivo* distribution of  $^{89}\text{Zr}$ -labelled anti-CD105 mAbs before and after the nanoparticle conjugation by using the quantitative PET imaging and ICP-MS analysis. The anti-CD105 mAbs were conjugated to AuNPs for the first time:

- After the nanoparticle conjugation, the anti-CD105 antibody preserves its selective targeting activity towards CD105 overexpressed on tumour cells, in accordance with the results of *in vitro* binding studies.

- The tumour uptake of these immunonanoconjugates was preserved up to 24 h after injection, suggesting a partial retention of the target recognition properties of conjugated antibodies. The maximum tumour uptake was about 4.6 %ID ml<sup>-1</sup> at 24 h after injection, with a high tumour contrast (T/Bg more than 4.5 starting from 24 h).
- No major tracer accumulation of these conjugates was observed over time in nonspecific tissues, aside from liver, spleen, lungs and bones.
- *In vivo* specificity of anti-CD105 mAbs after the nanoparticle conjugation was preserved, with a selective tumour targeting (a significant decrease in tumour uptake after the saturation of CD105 binding sites).
- In summary, conjugation the anti-CD105 antibody to AuNPs does not greatly affect the CD105-dependent tumour uptake and the efficacy of tumour targeting for cancer detection.

Overall, the two latest studies have characterized *in vivo* properties of antibody-functionalized gold nanoparticles, and have qualified these immunonanoconjugate systems, as potential new tools for imaging of cancer. These radiolabelled conjugates might represent new opportunities for effective nanoparticle-based therapy guided by *in vivo* imaging.



## II. Methodological considerations

### 1. Relevance of selected tumour model for targeting endoglin (CD105)

Although anti-CD105 mAbs are used successfully as intrinsic antiangiogenic agents, they can also be exploited as targeting agents. Within this context, the anti-CD105 antibody-targeted gold nanoparticles might represent an interesting combined approach for improving the efficacy of the standard inhibitors of angiogenesis thanks to the targeting properties of mAbs and the photophysical properties of AuNPs. While CD105 is a marker of neovessels originating from the angiogenic process, it should be noted that CD105 is also overexpressed by some tumour cells. Indeed, we used in our study the melanoma tumour model (B16F10-luc), which is expressing CD105 in tumour cells. This feature has two important consequences. First, that means that the used antibodies directed against CD105 are not “*stricto sensu*” markers of the angiogenic process. Second, that means also that the use of anti-CD105 mAbs may reach two targets in tumours, namely tumour cells and vessels. This particular feature could represent an advantage when considering the use of anti-CD105 mAbs as a targeting moiety for delivering associated anti-cancer treatment.

On the other hand, negative controls are required for full characterization of CD105 targeting *in vivo*. Two approaches are possible. Choosing tumour models, which don't express the target (CD105). In this case, we should consider the heterogeneity between the tumour models, such as the variability in perfusion and in the vascular structure. The most suitable approach involves using a non-specific antibody, which doesn't recognize the tumour target.

### 2. Limitations of techniques for determining nanoparticle size

The mean diameter of synthesized gold nanoparticles is about 5 nm, and the size of antibodies is about 15 nm (Bouchat 2007) (Figure 23). The “apparent mean diameters” of cetuximab- and anti-CD105 antibody-conjugated gold nanoparticles are stated to be about 30 nm and 100 nm respectively. The size characterization of the antibody-conjugated gold nanoparticles was assessed through two techniques:

- The differential centrifugal sedimentation (CPS disc centrifuge), which is based on measuring the time required for these immunonanoconjugates to cross over a sucrose density gradient created in a disc centrifuge

- The laser light scattering (Zetasizer Nano instrument), which is based on the principle of dynamic light scattering.

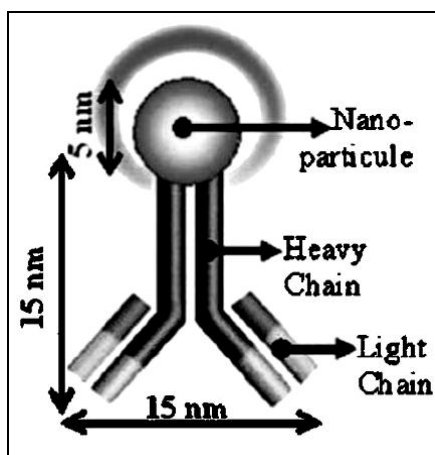


Fig. 23: Representation of a nanoparticle of 5 nm diameter conjugated with an antibody of 15 nm height (Bouchat 2007).

The mean diameter of anti-CD105 antibody-conjugated gold nanoparticles (100 nm) might suggest an aggregation. However, the measurement through dynamic light scattering is consistent with the result obtained with differential centrifugal sedimentation (Figures 24 and 25). It must be mentioned that these techniques have limitations regarding the accurate determination of particle size and give a result, which is an “apparent equivalent diameter” of a perfect sphere that would have the same behaviour as the analyzed particle under the same conditions. AuNPs are perfect spheres. However, the gold nanoparticles conjugated to a biomaterial, such as antibodies, are not. The transmission electron microscopy (TEM) is an absolute technique to characterize the particle size, and was used to measure the size of AuNPs. However, in the case of the immunonanoconjugates, the contrast was dominated by AuNPs, so that the nanoparticle coating was not visible, hence the size of conjugated gold nanoparticles was not available through this technique.

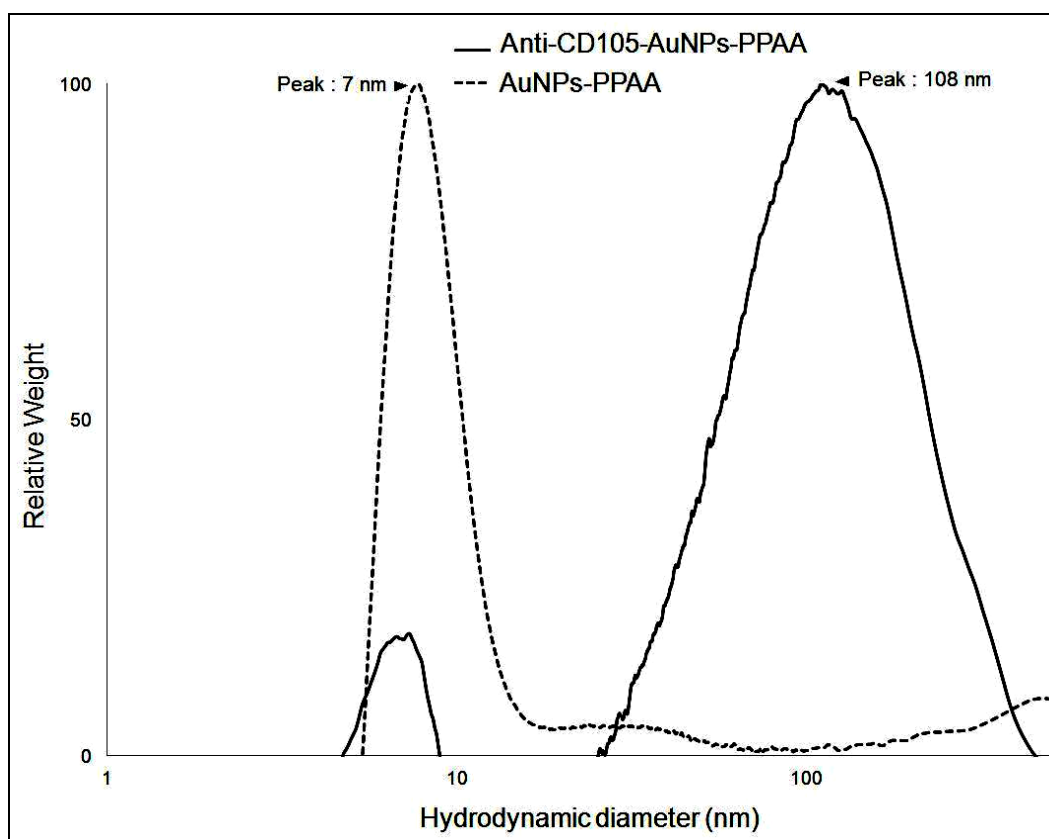


Fig. 24: Size distribution report of anti-CD105-AuNPs-PPAA using differential centrifugal sedimentation (CPS Instruments, Inc.).

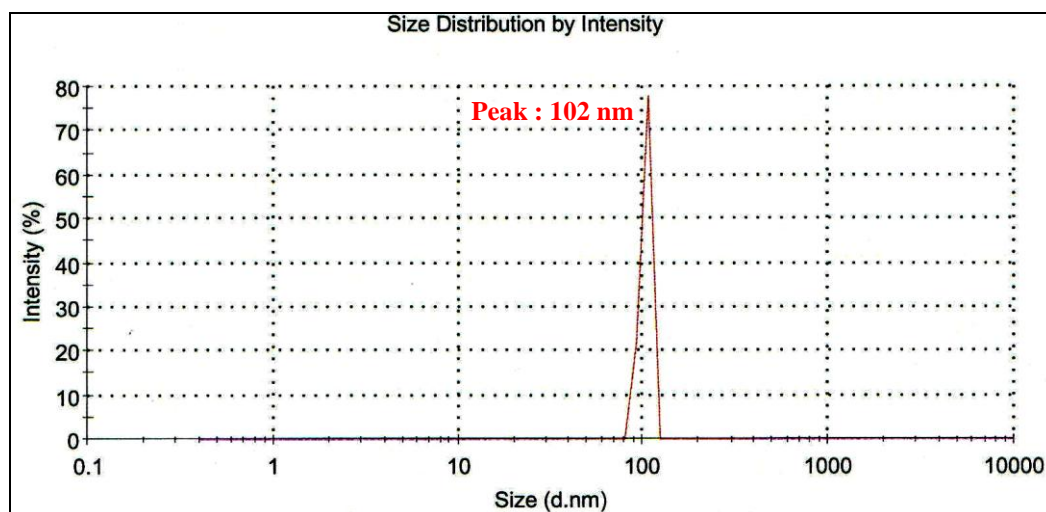


Fig. 25: Size distribution report of anti-CD105-AuNPs-PPAA using Zetasizer (Malvern Instruments Ltd.).

On the other hand, the produced nanoparticles were also coated with a PPAA stabilizer layer. The PPAA molecules, such as PEG molecules, are inert and large polymers. The nanoparticle coating may affect the sedimentation properties of the immunonanoconjugates,

so that the “apparent diameter” may probably increase. Finally, it is possible that the carbodiimide reaction produces to some extent polymerized antibodies, which would increase the apparent diameter of the conjugates (Figures 26). Therefore, we can hypothesize that the larger size of anti-CD105 antibody-conjugated gold nanoparticles (100 nm) compared with that of conjugated cetuximab (30 nm) might suggest a higher grafting rate of antibody molecules onto the nanoparticle surface. The grafting rate might impact the antibody recognition properties. Further accurate characterizations of these immunonanoconjugates are required, such as the thermogravimetric analysis, which may be suggested to estimate the number of anti-CD105 antibody molecules grafted per nanoparticle. The grafting rate may be controlled by optimizing the reagent ratios employed for the conjugation reaction or by controlling the number of amino groups onto the nanoparticle surface. On the other hand, later studies are required in order to optimize the conjugation reaction. The total time for conjugation of the radiolabeled antibodies onto the gold nanoparticles, and consequent purification is quite long (16 h). In order to enhance the coupling yield, the coupling reaction was achieved overnight. This conjugation step is quite long and inconvenient for a possible future theranostic use of these nanoconjugates. The coupling reaction of antibodies to gold nanoparticles could be optimized by using another cross-linking method like click chemistry. The modern click chemistry method is known for its high coupling efficiency and a less time of reaction compared to conventional carbodiimide chemistry (Thorek 2009).

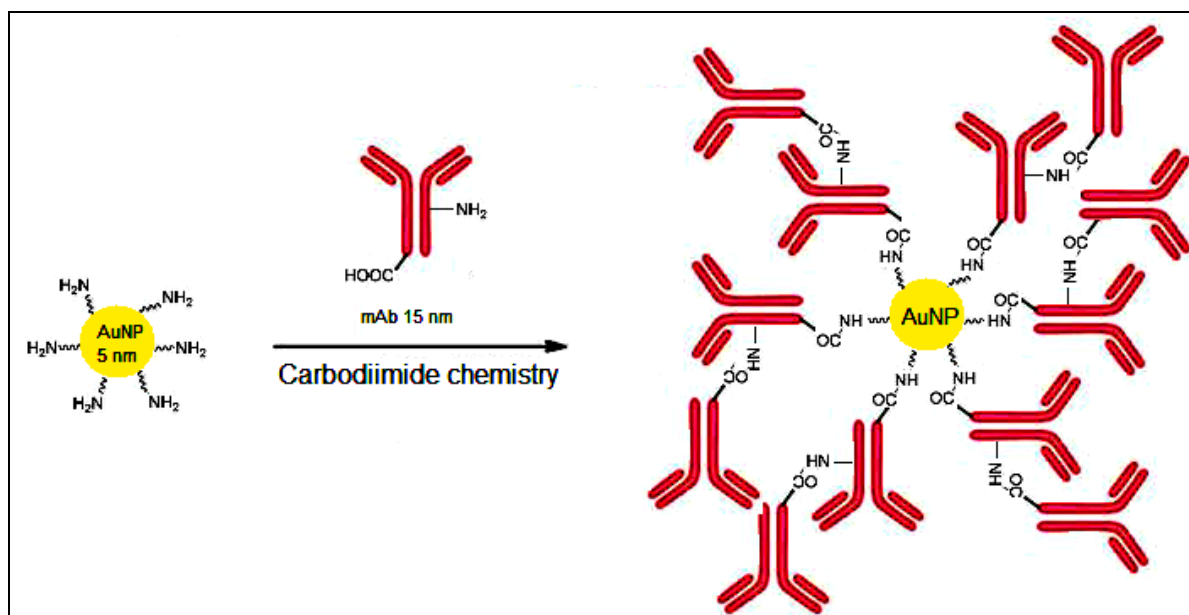


Fig. 26: The hypothetical model of anti-CD105 antibodies conjugated to gold nanoparticles.

### 3. Aggregation risk

Metallic nanoparticles, such as AuNPs, tend to agglomerate when exposed to physiological environment (Julien 2011). Moreover, the conjugation of mAbs to AuNPs involves most often the antibody coupling through carboxylic or amino groups. This often gives rise to a neutral linkage and to a decrease in antibody solubility, resulting in aggregation and precipitation (Julien 2011, Pietersz 1987). For these reasons, the risk of aggregation is a recurrent question in size analysis of such nonmaterials, and may impact their biodistribution profile. An internal quality control of the size distribution through differential centrifugal sedimentation showed a large distribution of the particle sizes around the mean size of 108 nm (Figure 24), which may suggest some aggregation. The shape of the distribution is normal (Gauss-like curve), but wide. This may reflect a random degree of antibody conjugation to AuNPs, with nanoparticles highly substituted and others with a lower degree of substitution, and consequently conjugates of various sizes. Further, the presence of a quite different population, such as aggregates, would have strongly modified the shape of the distribution of the raw data, and a Gauss-like curve would not have been observed. On the other hand, the uncoated AuNPs are known to strongly aggregate, whereas the coated AuNPs show a decreased risk of aggregation. The improved stability of the PPAA-coated gold nanoparticles suspension can be explained by the strong hydrophilic character of the coating layer. Nevertheless, to some extent, *in vivo* aggregation can not be ruled out. In summary, a careful attention should be paid to the nanoparticle conjugation process for producing constructs suitable for *in vivo* studies, because the size of these nanoconstructs is likely a strong contributing factor to the tissue distribution, with a risk of off-target effects.

### 4. The selected radiotracer for radiolabelling of conjugates

The radioiodinated tracers were largely used to study tumour targeting for cancer imaging (Verel 2004). Our preliminary experiments studied the biodistribution of immunoconjugates, which are directly radiolabelled with  $^{125}\text{I}$ .  $^{125}\text{I}$  is a common radiohalogen widely used in laboratory thanks to its availability, reasonable cost, and easy radiolabelling procedures. These first studies have underscored the negative impact of *in vivo* deiodination on the reliability of using radioiodinated antibodies, and especially  $^{125}\text{I}$ -labelled anti-CD105 mAbs, for the characterization of tumour targeting. Indeed, the comparison of the tumour uptake profile of  $^{125}\text{I}$ -labelled anti-CD105 mAbs and that of  $^{89}\text{Zr}$ -labelled anti-CD105 mAbs highlights that the dehalogenation prevents the stable tracking of the tracer. Finally, the radiolabelling of

anti-CD105 mAbs with  $^{89}\text{Zr}$  overcomes these limitations and represents a suitable tracer for imaging of the CD105 receptor in tumours.

Therefore, for subsequent studies, we used  $^{89}\text{Zr}$ , a metallic positron emitter, to trace our immunoconjugates through PET imaging.  $^{89}\text{Zr}$  is an ideal isotope for labelling intact mAbs, because its physical half-life matches with the biological half-life of mAbs and the time needed to reach optimal target-to-non target ratios. Moreover, the internalizing properties of antibodies and the residualizing properties of  $^{89}\text{Zr}$  support the optimal biodistribution profile of the conjugates. Indeed,  $^{89}\text{Zr}$  is trapped inside the cell after antibody internalization, while iodotyrosine is released from the tumour after internalization (Vugts 2011, Sharkey 1997). However,  $^{89}\text{Zr}$  has a short half-life compared with  $^{125}\text{I}$  and requires an animal-PET scanner and special precautions in terms of radiations. Moreover, the radiolabelling process using  $^{89}\text{Zr}$  is a multi-step and a time consuming method, since the antibody is previously functionalized with a chelate before radiolabelling. Therefore, future studies are required to investigate other techniques for anti-CD105 antibody radioiodination, notably the indirect radiolabelling methods, which were developed for decreasing the loss of the nuclide from the antibody *in vivo*, decreasing the thyroid uptake of radioiodine, while retaining the tumour uptake with a suitable tumour contrast (Ram 1994, Wilbur 1988, Zalutsky 1987). Indeed, previous studies described the development of a metabolically stable radioiodination reagent for coupling to mAbs. For instance, the radioiodination of mAbs with 3-iodophenylisothiocyanate has been investigated. This new ligand forms a stable thiourea linkage *via* a reaction of the isothiocyanate moiety with the amino group of lysine (Ram 1994).

Finally, our experiments showed that  $^{89}\text{Zr}$  may constitute a suitable alternative for the immunonanoconjugate radiolabelling for imaging purposes. Therefore,  $^{89}\text{Zr}$ -labelled immunonanoconjugates may be used as a scouting procedure before radioimmunotherapy to confirm the tumour targeting by the immunonanoconjugates and to allow the estimation of radiation dose delivery to tumours and normal tissues (Zhang 2011, Perk 2005). Hence,  $^{89}\text{Zr}$ -labelled immunonanoconjugates could serve as a surrogate for scouting the biodistribution of  $^{90}\text{Y}$ -labelled immunoconjugates (Zhang 2011).

### III. Challenges of conjugating monoclonal antibodies to gold nanoparticles

The design and the development of carefully validated nanoparticle-based systems for biomedical imaging requires a wide range of expertise ranging from chemistry to cell biology, as well as imaging techniques (Nune 2009). The two major goals in the development of improved anticancer immunonanoconjugates are to ensure greater selective targeting and better delivery efficiency (Julien 2011). Thereby, these immunonanoconjugates addressed many challenges, and the development of such immunonanoconjugates is complex and involves rigorous characterizations. A number of factors must be considered when designing antibody-targeted gold nanoparticles, including the conjugate stability *in vitro* and *in vivo*, notably the colloidal system stability and the bound ligand stability, which need to be investigated. Moreover, the retention of the antibody specificity after the nanoparticle conjugation in order to preserve the antibody recognition for a specific target, while minimizing the potential toxicity to non-target cells, need also to be determined.

Further, to design effective immunonanoconjugates, their escape from vasculature and their accumulation into target tissue is an important consideration. The size of the conjugates may affect the efficacy of tumour uptake and the significance of nonspecific uptake. Indeed, the increased size of conjugates makes them more likely to be cleared by the RES, or inhibits their extravasation and their access to target tissues (Julien 2011, Sarin 2010). A careful attention should thus be paid about the number of antibody molecules grafted to each nanoparticle. Indeed, our studies showed that the higher size of anti-CD105 antibody-conjugated gold nanoparticles (100 nm), by comparison with cetuximab-conjugated gold nanoparticles (30 nm), may suggest a higher grafting rate of anti-CD105 mAbs molecules onto the nanoparticle surface with the risk to affect the antibody immunoreactivity. This may explain the significant decrease in tumour uptake of anti-CD105 antibody-conjugated gold nanoparticles, starting from 24 h after injection. In contrast, the tumour uptake of conjugated cetuximab does not significantly decrease up to 72 h after injection. Moreover, the tumour uptake profile of conjugated cetuximab was similar to that of unconjugated cetuximab over time by comparison with the significant decrease over time of the tumour uptake of conjugated anti-CD105 mAbs. These findings suggested a partial loss of anti-CD105 antibody immunoreactivity after the nanoparticle conjugation (Figure 27).

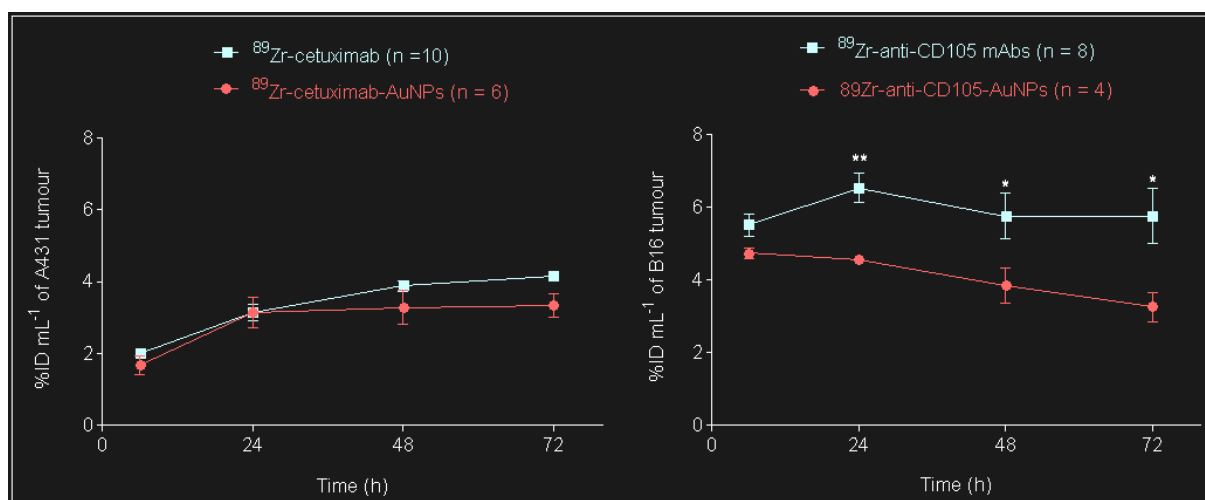


Fig. 27: The tumour uptake profile of cetuximab [left] and anti-CD105 antibodies [right], before [■] and after [●] the nanoparticle conjugation in tumour-bearing mice at different times after trace injection (6, 24, 48 and 72 h). Injected activity ranged from 2.9-4.6 MBq, corresponding to a total of 200-400 µg mAbs per mouse. Results are expressed as means of %ID mL<sup>-1</sup> ± SEM (n = 3-5 animals; 4-10 tumours). \* p < 0.05; \*\* p < 0.01.

### About the affinity of the immunonanoconjugates to the targeted receptors

The antibody should retain an acceptable level of specificity after the nanoparticle conjugation. In our studies, the receptor-ligand interactions of these immunonanoconjugates were characterized through binding experiments. For the two antibodies (cetuximab and anti-CD105 mAbs) and in comparison with the native antibody, the affinity was apparently slightly decreased after the nanoparticle conjugation ( $EC_{50}$  decreased less than 1 log). Moreover, *in vivo* blocking experiments confirmed the preservation of the antigen-specific binding after the antibody conjugation. *In vitro* binding activity of cetuximab-conjugated gold nanoparticles ( $EC_{50}$  value of 0.19 µg mL<sup>-1</sup>) was reduced by a factor of two compared with unconjugated cetuximab ( $EC_{50}$  value of 0.08 µg mL<sup>-1</sup>), while the relative binding affinity of anti-CD105-antibody conjugated gold nanoparticles ( $EC_{50}$  value of 5 µg mL<sup>-1</sup>) was about five times lower than that of unconjugated anti-CD105 mAbs ( $EC_{50}$  value of 1 µg mL<sup>-1</sup>). It should be noticed that these binding curves express the results in terms of **antibody concentration** (Figure 28).

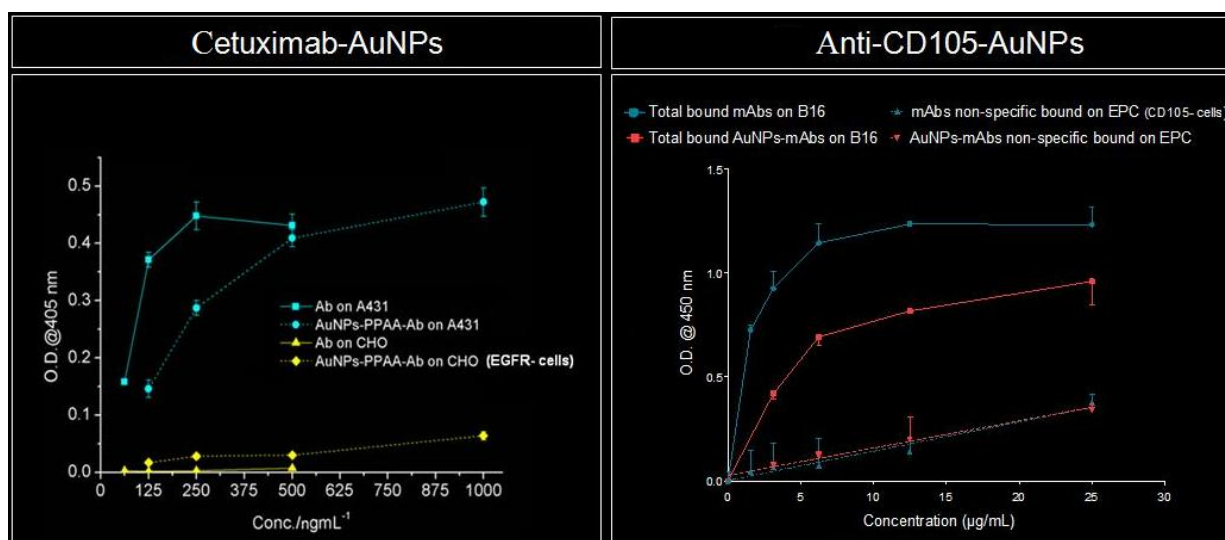


Fig. 28: Surface ELISA for cetuximab and cetuximab-AuNPs on EGFR+ (A431) and EGFR- (CHO) cells [left], and anti-CD105 mAbs and anti-CD105-AuNPs on CD105+ (B16F10-luc) and CD105- (eEPC) cells [right]. Different concentrations of mAbs and mAbs conjugated to AuNPs were tested in quadruplicate. The concentration is expressed as the amount of antibody ( $\text{ng ml}^{-1}$  or  $\mu\text{g ml}^{-1}$ ).

However, these *in vitro* binding curves (Figure 28) do not consider the multivalency structure of the immunonanoconjugates. In our studies, the AuNPs were indeed bearing several antibodies. Due to steric constraints and stiffness of the immunonanoconjugates, all antibodies linked to the nanoparticle have not the capability to bind receptors present on the cell surface layer (Figure 29).

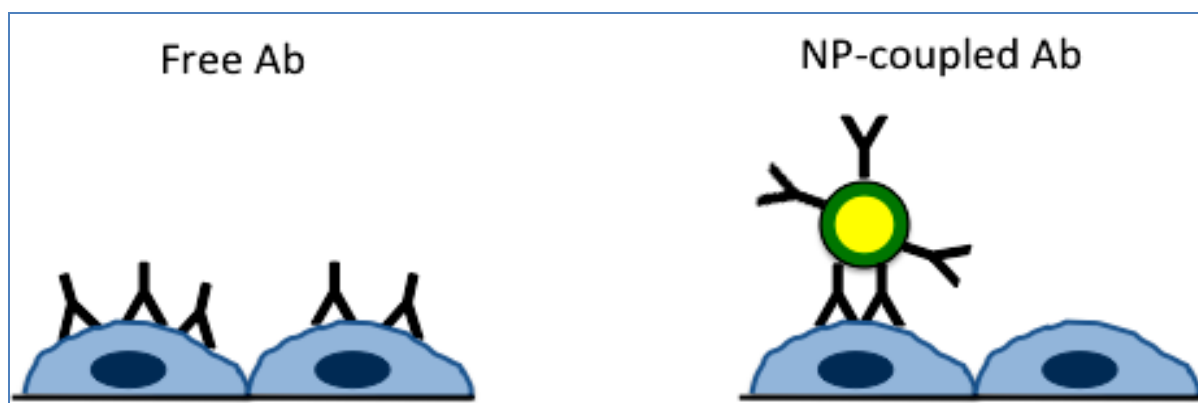


Fig. 29: Recognition of the cell target by free antibodies [left] and by antibodies conjugated to a gold nanoparticle [right].

In order to consider the effect of the multivalency on the binding properties, the conjugate concentration may also be expressed in terms of **nanoparticle concentration** instead of antibody concentration (Figure 30). According to thermogravimetric analysis, we considered roughly five antibody molecules conjugated per nanoparticle for cetuximab-conjugated gold nanoparticles (5 mAbs = 1 NP), and 10 antibody molecules conjugated per nanoparticle for anti-CD105-conjugated gold nanoparticles (10 mAbs = 1 NP). In this case, *in vitro* binding activity of antibody-conjugated gold nanoparticles was higher than that of unconjugated antibody. The relative binding affinity cetuximab-conjugated gold nanoparticles ( $EC_{50}$  value of  $0.04 \mu\text{g ml}^{-1}$ ) was slightly higher compared with unconjugated cetuximab ( $EC_{50}$  value of  $0.07 \mu\text{g ml}^{-1}$ ), while that of anti-CD105-antibody conjugated gold nanoparticles ( $EC_{50}$  value of  $0.5 \mu\text{g ml}^{-1}$ ) was about two times higher than that of unconjugated anti-CD105 mAbs ( $EC_{50}$  value of  $1.3 \mu\text{g ml}^{-1}$ ).

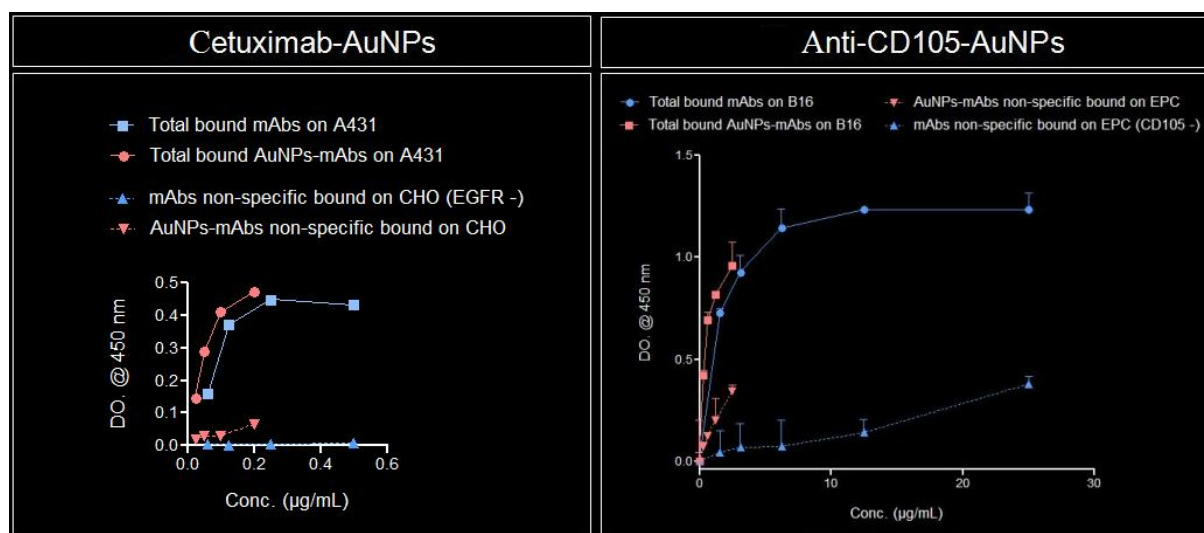


Fig. 30: Surface ELISA for cetuximab and cetuximab-AuNPs on EGFR+ (A431) and EGFR- (CHO) cells [left], and anti-CD105 mAbs and anti-CD105-AuNPs on CD105+ (B16F10-luc) and CD105- (eEPC) cells [right]. Different concentrations of mAbs and mAbs conjugated to AuNPs were tested in quadruplicate. The concentration expresses the gold nanoparticle concentration ( $\mu\text{g ml}^{-1}$ ).

As shown above, the differences in expression of concentration (antibody versus nanoparticle) may lead to differences in interpretation. Both interpretations shade some light on the consequence of the grafting of antibodies on nanoparticles. On the one hand, when using the antibody concentration as a variable, we may consider that there is an apparent loss of affinity of the nanoimmunoconjugate, a feature that is explained by the steric hindrance and the incapacity for some immobilized antibodies to bind the receptor at the surface of the cell.

This rigid structure maximizes the risk of unfavorable interactions between some ligands and receptors. On the other hand, when using the nanoparticle concentration as a variable, we may consider that there is an apparent increase in affinity when using a nanoimmunoconjugate. This feature is consistent with the multivalent theory. A multivalent ligand includes several copies of ligands conjugated to scaffolds, allowing the simultaneous binding of multivalent ligands to multiple binding sites or receptors (Chittasupho 2012, Krishnamurthy 2006). Actually, the multivalent ligands involve multiple interactions, which could result in the amplification of the avidity and the apparent affinity of the nanocomplex. Moreover, the multiple ligand site of recognition is supported by entropic effects, which may affect the affinity. Indeed, the loss of degrees of freedom is greater for the monovalent ligands than for the multivalent ligands. Another way to explain this phenomenon is to consider that the probability of dissociation of a ligand with multiple binding sites is lower compared to a ligand with a single binding site. Many multivalent ligands have been designed and synthesized to increase the binding affinity, avidity and specificity of the ligand to the receptor. Many factors affect the multivalent interactions, including the size and shape of the ligand, geometry and the arrangement of ligands on the scaffold, linker length, thermodynamic, and kinetics of the interactions (Chittasupho 2012). For example, a bivalent ligand directed against opioid receptors, with a spacer of optimal length exhibit greater potency than that derived from the sum of its two monovalent pharmacophores (Wei-Sheng Lee 2013, Portoghese 1985). This multivalent theory, initially described for small molecules, is also likely true for immunonanoconjugates. We can conclude that the antibody grafting on the nanoparticle surface does not greatly affect the antibody recognition properties.

Finally, the formulation approach to develop new therapeutic drugs is often parallel to the prior exploration of their value as biomedical imaging agents. Indeed, we reported the preservation of the targeting properties of the antibodies after their conjugation to AuNPs. We hope that these immunonanoconjugates might be exploited for therapy thanks to the antitumour properties of targeting antibodies, which might be boosted by the photophysical properties of AuNPs. For this purpose, future studies are required to assess if conjugated antibodies preserves their anticancer activity after their conjugation to AuNPs.



#### **IV. Antibody-targeted gold nanoparticles: molecular aspects**

Due to their ability to specifically bind to a particular biological target, mAbs are able to influence the cellular function at a molecular level (Julien 2011). On the other hand, previous studies have investigated the mechanisms by which AuNPs enter into cells and showed that endocytosis of AuNPs is dependent on the nanoparticle surface coating and the particle size (Nativo 2008, Jiang 2008, Giljohann 2007, Chithrani 2007, Chithrani 2006, Shenoy 2006). The active targeting involving the introduction of targeting ligands on the nanoparticle surface facilitates the homing, the binding to the target, and the internalization of the nanoconjugates in targeted cells (Fay 2011). For example, AuNPs coated with specific antibodies can regulate the process of membrane receptor internalization. The binding and activation of membrane receptors and subsequent protein expression strongly depend on nanoparticle size. Further, the nanoparticles within the 2-100 nm size range were found to alter signalling processes essential for cell functions, including cell death (Jiang 2008). Moreover, some mAbs have been shown to be effective in allowing cell-specific uptake of targeted nanoparticles, such as cetuximab-conjugated gold nanoparticles (Julien 2011). The cell-specific-receptor mediated endocytosis of these immunonanoconjugates and the receptor activation make possible to trigger the receptor-activated signalling (Wang 2010 [b], Huang 2009). Finally, the multivalent presentation of antibodies results in a relatively strong interaction between functionalized nanoparticles and the intended cells. However, the ligand density on the nanoparticle surface is a critical factor, which should be optimized in order to preserve the ligand functionalities (Nune 2009). It must be mentioned that the use of small molecules, such as multivalent small organic molecules, as an alternative to antibodies, allows further optimisation of the binding affinity and specificity by adjusting the density of targeting molecules, which may impart a precise biological targeting (Nune 2009, Weissleder 2005).

Previous studies showed that the anti-EGFR mAbs were involved in the EGFR internalization into cancer cells, and the subsequent degradation of active EGFR (Prewett 1996). Moreover, cetuximab is known for its high rate of internalization (Perk 2010). Recent studies described how the nanoconjugation modulates the mechanism of antibody-induced receptor endocytosis. The nanoconjugation induces faster endocytosis of EGFR and may alter the cellular processes. Thus, nanoconjugation cannot be considered as an innocuous reaction (Bhattacharyya 2010). Further studies are required to investigate these issues with our immunonanoconjugates. On the other hand, the internalization of the antibody-receptor

complex is followed by the sequestration of metallic radiolabels, such as  $^{89}\text{Zr}$ , inside tumour cells (Holland 2010). This residualizing phenomenon may also probably explain the better tumor contrast, which was observed with our conjugates, and supports the interesting imaging properties of cetuximab-conjugated gold nanoparticles. These aspects should also be investigated for anti-CD105 antibodies.

Finally, the internalization of these immunonanoconjugates is important for improvement cancer response, notably for hyperthermia therapy. Further, it is also important that AuNPs and mAbs remain conjugated until intracellular delivery (Glazer 2010 [a]). Therefore, future investigations are required for the characterization of *in vivo* stability of the amide link between the antibody and the nanoparticle. This may validate the results of the biodistribution profile obtained with our immunoconjugates, but also may predict the efficacy of future therapeutic applications. In our case, there is some evidence about the stability of our immunonanoconjugates until injection, because of the favourable results regarding *in vitro* stability of the conjugates in plasma and those of ICP-MS analyses. However, further studies remain necessary for accurately exploring these aspects.

## **V. Antibody-targeted gold nanoparticles: towards future theranostic applications**

We demonstrated that radiolabelled cetuximab- and radiolabelled anti-CD105 antibody-functionalized gold nanoparticles are able to detect cancer cells and have suitable imaging properties. In addition to cancer imaging, these immunonanoconjugates might be exploited for therapy, particularly thanks to the anticancer properties of AuNPs. Previous reports showed a potential for novel cancer therapies associating gold nanoparticles, based on noninvasively hyperthermia therapy or radiotherapy enhancement. A selective damage of cancer cells is the result of high gold nanoparticle loading in target cells owing to the tumour target overexpression on cell surface (Huang 2007). Therefore, the major challenge for gold nanoparticle-based therapy is to deliver a sufficient amount of gold to tumours. Hence, two questions are raised:

### **1. Does the amount of antibody-targeted gold nanoparticles in the tumour achieve an appropriate gold concentration for therapy?**

Previous studies showed that targeting of AuNPs has the potential to further improve both the therapy efficacy at the the tumour site, whilst reducing off-target effects (Fay 2011). Indeed, in order to deliver a targeted therapy to tumour cells and to enhance the specific tumour uptake, the nanoparticles may be conjugated to mAbs (Huang 2006 [b], El-Sayed 2006). Our studies didn't investigate if active targeting maximizes the concentration of these immunonanoconjugates at the tumour site. Previous studies investigated the interest of gold nanoparticles functionalization with anti-EGFR mAbs (Raouf 2011). Nevertheless, the anti-CD105 mAbs were conjugated to AuNPs for the first time. Thus, it is interesting to investigate the potential of conjugating the anti-CD105 mAbs to AuNPs by comparison with the unconjugated AuNPs, in terms of improving tumour targeting, and thus the increase of gold content in tumours. It must be mentioned that previous reports indicated that the targeting ligands play a role in the selective tumour accumulation of these nanocomplexes through the specific recognition of the tumour target (Pirollo 2008). In this case, the tumour localization of these nanocomplexes still depends to the contribution of the EPR effect. However, recent papers have suggested that the primary function of targeting ligands was not only in targeting the complexes to the tumour, but to increase the intracellular nanocomplexes uptake (Kirpotin 2006). This hypothesis supports that the inclusion of ligands on nanoparticle

surface in order to direct nanoparticles to target tissues is not the main mechanism of tumour uptake.

For future studies, there is a need to investigate the therapeutic potential of our immunonanoconjugates by exposing tumours to a noninvasive electromagnetic energy in order to produce cytotoxicity. Our studies have assessed the amount of gold found in tumours for anti-CD105 antibody-conjugated gold nanoparticles through ICP-MS analysis. However, other experiments are required to determine the dose-effect relationship. Regarding the amount of AuNPs that has to be delivered to the tumour, previous studies showed that different concentrations of spherical AuNPs induce hyperthermic cytotoxicity when exposed to visible laser radiation or to radiofrequency energy. For photothermal therapy, a relatively low concentration of AuNPs [ $\mu\text{g}$  range] is reported to be sufficient to induce cytotoxicity and cell death (Glazer 2010 [b], Moran 2009, von Maltzahn 2009). These gold concentrations are in the same range of those we quantified in tumours after injection of anti-CD105 antibody-conjugated gold nanoparticles to mice. However, we have not quantified the amount of gold in tumours after injection of cetuximab-conjugated gold nanoparticles. Future ICP-MS analyses are required to this end, although previous studies provided favourable results with cetuximab-conjugated gold nanoparticles, but with immunonanoconjugates synthesized differently and in other tumour models (Glazer 2010 [a]).

On the other hand, other studies showed that AuNPs may improve the therapeutic efficacy of external beam ionizing radiation in preclinical models (Chang 2008). However, the radioenhancement requires here a significant amount of gold in the tumour site [ $\text{mg}$  range] (Hainfeld 2004). For imaging purposes, as is the case of our studies, we injected trace amounts of immunonanoconjugates, which are sufficient for diagnostic purposes, with probably a low risk of toxicity. For radioenhancement purposes, we should consider increasing significantly the amount of injected immunonanoconjugates, which could be limited by systemic toxicity.

The PTT using spherical AuNPs can be achieved with visible laser, which has a shallow penetration depth in tissue. Such treatment is only suitable for superficial cancers, such as skin tumours. Indeed, the thermoablation using visible laser is not suitable for deeper lesions given the limited penetration of optical photons into tissues. On the other side, the use of radiofrequency energy for heating of AuNPs is not limited by tissue penetration, and hence makes it possible to treat deeper lesions, such as hepatocellular cancer (Raouf 2011). Finally,

it must be mentioned that by using heat to treat targeted tumour cells, the drug resistance is no longer a constraint (Julien 2011, Carpin 2011).

## **2. What about the toxicity associated to gold nanoparticle uptake by nonspecific tissues?**

Although the systemic toxicity of AuNPs is beyond the scope of this thesis, this question is quite important, especially if injected doses have to be increased for therapy. For this purpose, it is important to accurately assess the biodistribution of AuNPs and to quantify it in various tissues. The immunonanoconjugates are new entities different from unconjugated AuNPs, which are already well characterized in terms of *in vivo* distribution in several studies (De Jong 2008, Sonavane 2008, Hillyer 2001). Therefore, ICP-MS analyses are required in order to fully characterize the gold content in nonspecific tissues, in which these immunonanoconjugates may be accumulated, and which may be analyzed by histopathologic evaluation.

An obvious challenge in utilizing antibody-conjugated gold nanoparticles for therapeutic purposes is to decrease the nonspecific tissue uptake. Our studies showed that these conjugates were particularly trapped by the RES. As it is possible to locally and specifically activate gold nanoparticles accumulated in malignant tissues, the nonspecific uptake of these immunonanoconjugates may be overcome thanks to the local radiation exposure of AuNPs accumulated in the target tissue. Nevertheless, the development of nonspecific tissue toxicity, and particularly liver toxicity, will need to be closely monitored in the future. In this regard, previous studies demonstrated that there was no evidence of liver injury despite clear presence of AuNPs and under RF field exposure, and suggested that the regenerative characteristics of the normal hepatocytes tolerate hyperthermia more than tumour tissues (Glazer 2010 [a], Du 2009, Fausto 2006). Furthermore, there is evidence that the majority of splenic and hepatic uptake of AuNPs is by macrophages cells, without major induction of proinflammatory cytokines (Glazer 2010 [a], Cho 2010, Shukla 2005). Moreover, the macrophages cells in these organs might be affected by photothermic treatment, but these cells are rapidly repopulated from circulating macrophage population (Glazer 2010 [a], Yamamoto 1996). Finally, it must be mentioned that while photothermal therapy efficiency is dependent on the specificity of the targeting antibody and despite the potential side systemic effects, normal tissues tolerate hyperthermia at higher temperatures and for longer periods of time than malignant tissues (Storm 1979). Indeed, previous studies showed that antibody-targeted gold

nanoparticles used for hyperthermic therapy leads to effective destruction of tumour cells with a minimal toxicity for normal cells (Glazer 2010 [a]).

Overall, the potential toxicity of these immunonanoconjugates to non-target cells in both *in vitro* and *in vivo* systems need to be carefully studied in order to assess how these conjugates will interact with cells and tissues. The concern regarding the use of noble-metal nanomaterials *in vivo*, such as AuNPs, remains their elimination from the body, because they are not biodegradable and thus may have a long-term effect on cellular functions (Bawarski 2008).

## VI. Challenges towards clinical use (Danhier 2010, Nune 2009)

Recent research on the encouraging use of antibody-targeted gold nanoparticles in cancer diagnostic and therapy has already set the stage for the development of future clinical applications (Huang 2007). The highlighted preclinical efficacies with these nanosystems might provide interesting opportunities for future commercialization. Although antibody-modified gold nanoparticles have found success in targeting cancer cells *in vitro* and *in vivo* in mice, some key questions remain before considering the translation of antibody-targeted gold nanoparticles to an effective clinical use. Therefore, many challenges in bringing the use of these immunonanoconjugates from bench to clinic may be discussed.

This thesis enabled to explore the biodistribution of immunonanoconjugates, as imaging probes, and before considering therapeutic applications. As with any product for use in humans, extensive safety and toxicology studies will be needed in parallel to pharmacokinetic and biodistribution studies in early stage clinical trials. The metabolism is another aspect, which should be explored. Moreover, translating this technology to clinical application may be very challenging because of the limited stability and the high costs associated with synthetic nanoparticle functionalization with targeting antibodies (Nune 2009). Further, the formulation aspects, such as aggregation and storage in clinical setting, remain a challenge (Nune 2009). Finally, the reproducible large-scale production of these nanoconjugates according a good manufacturing practice and in a cost effective way needs to be addressed.

Some practical limitations exist to expand the use of these nanomedecines in clinic (Danhier 2010):

- The major limitation impeding the entry of targeted nanomaterials onto the market is that innovative ideas within academia are not usually exploited in collaboration with the pharmaceutical industry.
- A new subdiscipline of nanotechnology, called nanotoxicology, has emerged. Indeed, *in vivo* nanosystems are extremely complex and the interactions of nanocarriers with biological components are vast. More data are needed to understand their structure-property relationships. Further, standardized methods are required for investigating their toxicity. Moreover, more studies and clearer regulations are necessary in order to fully define the biocompatibility of nanocarriers in humans.

- Finally, clinical trials of combined treatments are difficult to conduct, particularly because the proof of principle and the complete toxicology data of these complex nanosystems are difficult to establish.

Regarding the growing number of clinical trials of nanomedecines combined with radiotherapy or chemotherapy, there is an evidence of the possible success of these therapies (Danhier 2010, Ruenraroengsak 2010). Indeed, the combination of treatments seems to be the future of the management of cancer. Before a new drug delivery system is approved, it is already being tested in combination with other treatments, such as radiotherapy or conventional chemotherapy. Furthermore, nanomedecines can associate drug delivery with different targeting strategies, and thus may be multifunctional nanomaterial systems. Finally, emerging concepts using gold nanoparticles combined both with imaging and therapeutic functions should thoroughly consider the regulatory complexity of this type of theranostic approach. However, the multifunctional nanodivices are still at a proof of concept stage and the progress has been slow.

## VII. Outlook and future directions

The complex goal of nanomedecines is to devise agents that selectively target tumour sites, provide imaging capabilities, and deliver specific therapy with minimal untoward effects elsewhere (Sajja 2009). Our studies have shown the potential of antibody-targeted gold nanoparticles for cancer imaging, and have underscored the complexity of such nanodevices and the need to be fully characterized. In this context, there are still numerous hurdles that must be overcome before such immunonanoconjugates may be more universally implemented in order to expand their field of application:

- Further studies are required to complete the characterization of our immunonanoconjugates, such as exploring the internalization process, characterizing *in vivo* stability and metabolism, investigating the potential toxicity profile, assessing the interest of active targeting through conjugation of anti-CD105 mAbs to AuNPs, and determining if the anticancer functions of conjugated mAbs are preserved after the nanoparticle conjugation.
- Future investigations are needed to study the therapeutic potential of our immunonanoconjugates by exposing tumours to a noninvasive electromagnetic energy for producing cytotoxicity. Furthermore, AuNPs may be conjugated to other ligands in addition to the targeting antibody, such as toxins or cytotoxic drugs, in order to potentiate the hyperthermic effect and to impede cell repair mechanisms. Therefore, we can expect the emergence of many nanotechnology platforms for drug delivery applications, such as AuNPs, which may act as a scaffold for many targeting and therapeutic agents.
- The radioimmunoimaging can provide targeting and dosimetry informations that can guide therapy. Our experiments showed that  $^{89}\text{Zr}$  may constitute a suitable choice for radiolabelling of conjugates. Therefore,  $^{89}\text{Zr}$ -labelled immunonanoconjugates may be used as a scouting procedure before radioimmunotherapy to confirm the tumour targeting and to allow the estimation of radiation dose delivery to tumours and normal tissues (Zhang 2011, Perk 2005). Hence,  $^{89}\text{Zr}$ -labelled immunonanoconjugates could serve as a surrogate for scouting the biodistribution of  $^{90}\text{Y}$ -labelled immunonanoconjugates (Zhang 2011).

- It may be interesting to extend the panel of chosen targeting antibodies for the nanoparticle conjugation in order to investigate other tumour models or other disorders besides cancer. Indeed, antibody-targeted gold nanoparticles may become an enabling technology for personalized medicine, in which cancer detection and therapy are tailored to each individual's tumour molecular profile.
- Advances in cancer biology are critical for improving the efficacy of nanodevices. A greater efficiency of lower doses of nanoconjugates, killing solely the cancer cells, could be achieved by selective targeting of unique biomolecular surface signatures on tumour cells. The rational design of nanoconjugates requires the knowledge of tumour-specific biomarkers that facilitate the identification of cancers, and tumour-specific receptors that enable endocytosis of conjugated nanoparticles and that can enable their selective uptake into cells or accumulation in tumour microenvironments (Sajja 2009).
- Other studies exploring the use of anti-endoglin fragments may be interesting. We have begun to produce anti-CD105 F(ab')<sub>2</sub> fragments in order to investigate their pharmacokinetic profile. Previous studies using anti-CD105 Fab fragments and anti-CD105 nanobodies showed the much faster tumour uptake of these fragments compared with intact anti-CD105 mAbs, and thus may be translated into the same-day immuno-PET imaging for clinical investigation (Zhang 2013, Ahmadvand 2008). Moreover, the early pharmacokinetic profile of these fragments has an impact on the choice of the radiotracer. Indeed, radionuclides with shorter physical half-life than that of <sup>89</sup>Zr, such as <sup>99m</sup>Tc, may be chosen for the radiolabelling of these fragments. The F(ab')<sub>2</sub> fragments are bivalent and are able to bind to two antigens with high affinity and high retention times (avidity). Moreover, the absence of the Fc domain avoids the recruitment of the cytotoxic effector functions through FcγR, and decreases the serum half-lives through interaction with the FcRn, which acts as a salvage receptor. Finally, the antibody fragment-based molecular imaging may enable early imaging of malignant lesions that will accelerate the evaluation of patient care and treatment.
- It could be also interesting to assess the tumour uptake in different tumour models before and after anticancer therapy (anti-EGFR mAbs and anti-CD105 mAbs conjugated or not to AuNPs) in order to assess the value of these radiolabelled conjugates, as a biomarker of response to a treatment.

- The directly radiolabelled nanoparticles represent a new class of agents with an interesting potential for cancer management. Recently, several reports have indicated the use of gold nanoparticles labelled with  $\gamma$ -emitters or  $\beta^+$ -emitters for multimodal imaging, such as PET/CT imaging (Guerrero 2012, Xie 2011, Agarwal 2011, Shao 2011). This approach takes advantage of high PET sensitivity and an accurate localization of AuNPs provided by X-ray CT (de Barros 2012). The challenges encountered in producing radioactive nanoparticles and the trouble to synthesize nanoparticles with a high specific activity led us to radiolabel the antibodies before their conjugation to AuNPs in order to detect our immunonanoconjugates *in vivo*.

To conclude, current cancer treatments (surgery, radiotherapy and conventional chemotherapy) lead to side effects and toxicity to healthy cells. Recent developments in cancer research have shown the introduction of gold nanoparticles into these standard protocols for enhancing the tumour cell killing. The promises of nanotechnology, as innovative strategy, lie in the potential to decrease harm to healthy tissues and might change the very foundations of cancer diagnosis and treatment.



## References

- Aerts HJ, Dubois L, Perk L, Vermaelen P, van Dongen GA, Wouters BG, Lambin P. Disparity between in vivo EGFR expression and <sup>89</sup>Zr-labeled cetuximab uptake assessed with PET. *J Nucl Med*. 2009;50:123-131.
- Agarwal A, Shao X, Rajian JR, Zhang H, Chamberland DL, Kotov NA, Wang X: Dual-mode imaging with radiolabeled gold nanorods. *J Biomed Opt* 2011;16:051307.
- Ahmadvand D, Rasaei MJ, Rahbarizadeh F, Mohammadi M. Production and characterization of a high-affinity nanobody against human endoglin. *Hybridoma (Larchmt)*. 2008;27:353-360.
- Alkilany AM, Murphy CJ. Toxicity and cellular uptake of gold nanoparticles: what we have learned so far? *J Nanopart Res*. 2010;12:2313–2333.
- Allabashi R, Stach W, de la Escosura-Munniz A., Liste-Calleja L, Merkoci A. ICP-MS: a powerful technique for quantitative determination of gold nanoparticles without previous dissolving. *J Nanopart Res*. 2009;11:2003-2011.
- Arruebo M, Valldares M, Gonzalez-Fernandez A. Antibody-conjugated nanoparticles for biomedical applications. 2009. DOI:10.1155/2009/439389.
- Bae YH. Drug targeting and tumor heterogeneity. *J Control Release*. 2009;133:2-3.
- Barbieri MA, Roberts RL, Gumusboga A, Highfield H, Alvarez-Dominguez C, Wells A, Stahl PD. Epidermal growth factor and membrane trafficking. EGF receptor activation of endocytosis requires Rab5a. *J Cell Biol*. 2000;151:539-550.
- Bar-Ilan O, Albrecht RM, Fako VE, Furgeson DY. Toxicity assessments of multisized gold and silver nanoparticles in zebrafish embryos. *Small*. 2009;5:1897-1910.
- Baselga J, Mendelsohn J. Receptor blockade with monoclonal antibodies as anti-cancer therapy. *Pharmacol Ther*. 1994;64:127-154.
- Bawarski WE, Chidlow E, Bharali DJ, Mousa SA. Emerging nanopharmaceuticals. *Nanomedicine*. 2008;4:273-282.
- Beresford MJ, Harris AL, Ah-See M, Daley F, Padhani AR, Makris A. The relationship of the neo-angiogenic marker, endoglin, with response to neoadjuvant chemotherapy in breast cancer. *Br J Cancer*. 2006;95: 1683-1688.
- Bernabeu C, Conley BA, Vary CPH. Novel biochemical pathways of endoglin in vascular cell physiology. *J Cell Biochem* 2007;102:1375-1388.

- Bernabeu C, Lopez-Novoa JM, Quintanilla M. The emerging role of TGF-beta superfamily coreceptors in cancer. *Biochim Biophys Acta*. 2009;1792:954-973.
- Bhattacharyya S, Bhattacharyya R, Curley S, McNiven MA, Mukherjee P. Nanoconjugation modulates the trafficking and mechanism of antibody induced receptor endocytosis. *Proc Natl Acad Sci USA*. 2010;107:14541-14546.
- Bird RE, Hardman KD, Jacobson JW, Johnson S, Kaufman BM, Lee SM, Pope SH, Riordan GS, Whitlow M. Single-chain antigen-binding proteins. *Science*. 1988;242:423-426.
- Blumenthal RD, Kashi R, Sharkey RM, Goldenberg DM. Quantitative and qualitative effects of experimental radioimmunotherapy on tumor vascular permeability. *Int J Cancer*. 1995;61:557-566.
- Borjesson PK, Jauw YW, Boellaard R, de Bree R, Comans EF, Roos JC, Castelijns JA, Vosjan MJ, Kummer JA, Leemans CR, Lammertsma AA, van Dongen GA. Performance of immuno-positron emission tomography with zirconium-89-labeled chimeric monoclonal antibody U36 in the detection of lymph node metastases in head and neck cancer patients. *Clin Cancer Res*. 2006; 12: 2133-2140.
- Boswell CA, Brechbiel MW. Development of radioimmunotherapeutic and diagnostic antibodies: an inside-out view. *Nucl Med Biol*. 2007;34:757-778.
- Bouchat V, Moreau N, Valembois V, Abbas K, Feron O, Gallez B, Holzwarth U, Masereel B, Michiels C, Simonelli F, Vander Borgh T, Lucas S. On the use of radioisotopes to study the possible synthesis by magnetron sputtering of bimetallic nanoparticles. *Surface and Coatings Technology*. 2011;205:4934-4940.
- Bouchat V, Nuttens VE, Lucas S, Michiels C, Masereel B, Féron O, Gallez B, Vander Borgh T. Radioimmunotherapy with radioactive nanoparticles: first results of dosimetry for vascularized and necrosed solid tumors. *Med Phys*. 2007;34:4504-4513.
- Boudaïffa B, Cloutier P, Hunting D, Huels MA, Sanche L. Resonant formation of DNA strand breaks by low-energy (3 to 20 eV) electrons. *Science*. 2000;287:1658-1660.
- Bradfield WBJ. In: Davis SS, Illum L, McVie JG, Tomlinson E, editors. *Microspheres and Drug Therapy*. Elsevier, Amsterdam; 1984. p. 25-37.
- Bredow S, Lewin M, Hofmann B, Marecos E, Weissleder R. Imaging of tumour neovasculature by targeting the TGF-beta binding receptor endoglin. *Eur J Cancer* 2000; 36: 675-681.
- Brewer CA, Setterdahl JJ, Li MJ, Johnston JM, Mann JL, McAsey ME. Endoglin expression as a measure of microvessel density in cervical cancer. *Obstet Gynecol*. 2000;96:224-228.

- Brown SD, Nativo P, Smith JA, Stirling D, Edwards PR, Venugopal B, Flint DJ, Plumb JA, Graham D, Wheate NJ. Gold nanoparticles for the improved anticancer drug delivery of the active component of oxaliplatin. *J Am Chem Soc.* 2010;132:4678-4684.
- Brun E, Cloutier P, Sicard-Roselli C, Fromm M, Sanche L. Damage induced to DNA by low-energy (0-30 eV) electrons under vacuum and atmospheric conditions. *J Phys Chem B.* 2009;113:10008-10013.
- Brust M, Fink J, Bethell D, Schiffrin DJ, Kiely C. Synthesis and reactions of functionalised gold nanoparticles. *J Chem Soc Chem Comm.* 1995;21:1655-1656.
- Brust M, Walker M, Bethell D, Schiffrin DJ, Whyman R. Synthesis of thiol-derivatized gold nanoparticles in a 2-phase liquid-liquid system. *J Chem Soc Chem Comm.* 1994;7:801-802.
- Burrows FJ, Derbyshire EJ, Tazzari PL et al. Up-regulation of endoglin on vascular endothelial cells in human solid tumors: implications for diagnosis and therapy. *Clin. Cancer Res.* 1995;1:1623-1634.
- Butterworth KT, Coulter JA, Jain S, Forker J, McMahon SJ, Schettino G, Prise KM, Currell FJ, Hirst DG. Evaluation of cytotoxicity and radiation enhancement using 1.9 nm gold particles: potential application for cancer therapy. *Nanotechnology.* 2010;21:295101.
- Byrne JD, Betancourt T, Brannon-Peppas L. Active targeting schemes for nanoparticle systems in cancer therapeutics. *Adv Drug Deliv Rev.* 2008;60:1615-1626.
- Carmeliet P, Jain RK. Molecular mechanisms and clinical applications of angiogenesis. *Nature.* 2011;473:298-307.
- Carmeliet P. Mechanisms of angiogenesis and arteriogenesis. *Nat Med.* 2000;6:389-395.
- Carpin LB, Bickford LR, Agollah G, Yu TK, Schiff R, Li Y, Drezek RA. Immunoconjugated gold nanoshell-mediated photothermal ablation of trastuzumab-resistant breast cancer cells. *Breast Cancer Res Treat.* 2011;125:27-34.
- Carrot G, Valmalette JC, Plummer CJG, Scholz SM, Dutta J, Hofmann H, Hilborn JG. Gold nanoparticle synthesis in graft copolymer micelles. *Colloid and Polymer Science.* 1998;10: 853-859.
- Carter JD, Cheng NN, Qu Y, Suarez GD, Guo T. Nanoscale energy deposition by X-ray absorbing nanostructures. *J Phys Chem B.* 2007;111:11622-11625.
- Carter P. Improving the efficacy of antibody-based cancer therapies. *Nat Rev Cancer.* 2001;1:118-129.
- Chang MY, Shiau AL, Chen YH, Chang CJ, Chen HH, Wu CL. Increased apoptotic potential and dose-enhancing effect of gold nanoparticles in combination with single-dose clinical electron beams on tumor-bearing mice. *Cancer Sci.* 2008;99:1479-1484.

- Charpin C, Dales JP, Garcia S, Carpentier S, Djemli A, Andrac L, Lavaut MN, Allasia C, Bonnier P. Tumor neoangiogenesis by CD31 and CD105 expression evaluation in breast carcinoma tissue microarrays. *Clin Cancer Res.* 2004;10:5815-5819.
- Chen YS, Hung YC, Liao I, Huang GS. Assessment of the In Vivo Toxicity of Gold Nanoparticles. *Nanoscale Res Lett.* 2009;4:858-864.
- Cheng Y, C Samia A, Meyers JD, Panagopoulos I, Fei B, Burda C. Highly efficient drug delivery with gold nanoparticle vectors for in vivo photodynamic therapy of cancer. *J Am Chem Soc.* 2008;130:10643-10647.
- Cherukuri P, Glazer ES, Curley SA. Targeted Hyperthermia Using Metal Nanoparticles. *Adv Drug Deliv Rev.* 2010;62:339-345.
- Chithrani BD, Chan WCW: Elucidating the mechanism of cellular uptake and removal of protein-coated gold nanoparticles of different sizes and shapes. *Nano Lett.* 2007;7:1542-1550.
- Chithrani BD, Ghazani AA, Chan WC. Determining the size and shape dependence of gold nanoparticle uptake into mammalian cells. *Nano Lett.* 2006;6:662-668.
- Chithrani DB, Jelveh S, Jalali F, van Prooijen M, Allen C, Bristow RG, Hill RP, Jaffray DA. Gold nanoparticles as radiation sensitizers in cancer therapy. *Radiat Res.* 2010;173:719-728.
- Chittasupho C. Multivalent ligand: design principle for targeted therapeutic delivery approach. *Ther Deliv.* 2012;3:1171-1187.
- Cho K, Wang X, Nie S, Chen ZG, Shin DM. Therapeutic nanoparticles for drug delivery in cancer. *Clin Cancer Res.* 2008;14:1310-1316.
- Cho WS, Cho M, Jeong J, Choi M, Han BS, Shin HS, Hong J, Chung BH, Jeong J, Cho MH. Size-dependent tissue kinetics of PEG-coated gold nanoparticles. *Toxicol Appl Pharmacol.* 2010;245:116-123.
- Cho WS, Cho MJ, Jeong J, et al. Acute toxicity and pharmacokinetics of 13 nm-sized PEG-coated gold nanoparticles. *Toxicol Appl Pharmacol.* 2009;236:16-24.
- Choi SH, Zhang YP, Gopalan A, Lee KP, Kang HD. Preparation of catalytically efficient precious metallic colloids by  $\gamma$ -irradiation and characterization. *Colloids Surf A Physicochem Eng Asp.* 2005;256:165-170.
- Clift MJ, Rothen-Rutishauser B, Brown DM, Duffin R, Donaldson K, Proudfoot L, Guy K, Stone V. The impact of different nanoparticle surface chemistry and size on uptake and toxicity in a murine macrophage cell line. *Toxicol Appl Pharmacol.* 2008;232:418-427.
- Connor EE, Mwamuka J, Gole A, Murphy CJ, Wyatt MD. Gold nanoparticles are taken up by human cells but do not cause acute cytotoxicity. *Small.* 2005;1:325-327.

- Cortez-Retamozo, Lahoutte T, Caveliers V, Gainkam LO, Hernot S, Packeu A, De Vos F, Vanhove C, Muyltermans S, De Baetselier P, Revets H. <sup>99m</sup>Tc-labeled nanobodies: A new type of targeted probes for imaging antigen expression. *Curr Radiopharm.* 2008;1:37-41.
- Costello B, Li C, Duff S, Butterworth D, Khan A, Perkins M, Owens S, Al-Mowallad AF, O'Dwyer S, Kumar S. Perfusion of <sup>99m</sup>Tc-labeled CD105 Mab into kidneys from patients with renal carcinoma suggests that CD105 is a promising vascular target. *Int J Cancer* 2004;109:436-441.
- Crespin M, Moreau N, Masereel B, Feron O, Gallez B, Vander Borgh T, Michiels C, Lucas S. Surface properties and cell adhesion onto allylamine-plasma and amine-plasma coated glass coverslips. *J Mater Sci Mater Med.* 2011;22:671-682.
- Curley SA, Cherukuri P, Briggs K, Patra CR, Upton M, Dolson E, Mukherjee P. Noninvasive radiofrequency field-induced hyperthermic cytotoxicity in human cancer cells using cetuximab-targeted gold nanoparticles. *J Exp Ther Oncol.* 2008;7:313-326.
- Danhier F, Feron O, Pr at V. To exploit the tumor microenvironment: Passive and active tumor targeting of nanocarriers for anti-cancer drug delivery. *J Control Release.* 2010;148:135-146.
- Daniel MC, Astruc D. Gold nanoparticles: assembly, supramolecular chemistry, quantum-size-related properties, and applications toward biology, catalysis, and nanotechnology. *Chem Rev.* 2004;104:293-346.
- Davis ME, Chen ZG, Shin DM. Nanoparticle therapeutics: an emerging treatment modality for cancer. *Nat Rev Drug Discov.* 2008;7:771-782.
- de Barros AB, Tsourkas A, Saboury B, Cardoso VN, Alavi A. Emerging role of radiolabeled nanoparticles as an effective diagnostic technique. *EJNMMI Res.* 2012;2:39.
- De Jong WH, Hagens WI, Krystek P, Burger MC, Sips AJ, Geertsma RE. Particle size-dependent organ distribution of gold nanoparticles after intravenous administration. *Biomaterials.* 2008;29:1912-1919.
- Dolmans DE, Fukumura D, Jain RK. Photodynamic therapy for cancer. *Nat Rev Cancer.* 2003;3:380-387.
- Douglas S J, Davis SS, Illum L. Biodistribution of poly(butyl 2-cyanoacrylate) nanoparticles in rabbits. *Int J Pharm.* 1986;34:145-152.
- Dreesen L, Cecchet F, Lucas S. DC Magnetron Sputtering Deposition of Titanium Oxide Nanoparticles: Influence of Temperature, Pressure and Deposition Time on the Deposited Layer Morphology, the Wetting and Optical Surface Properties. *Plasma Processes and Polymers.* 2009;6:S849-S854.
- Du SS, Zeng ZC, Tang ZY, Zhang ZY, Shi LS, Wu Z, Qiang M, Liu ZS. Regenerative capacity of normal and irradiated liver following partial hepatectomy in rats. *Int J Radiat Biol.* 2009;85:1114-1125.

- Dykman L, Khlebtsov N. Gold nanoparticles in biomedical applications: recent advances and perspectives. *Chem. Soc. Rev.* 2012;41:2256-2282.
- Elghanian R, Storhoff JJ, Mucic RC, Letsinger RL, Mirkin CA. Selective colorimetric detection of polynucleotides based on the distance-dependent optical properties of gold nanoparticles. *Science.* 1997;277:1078-1081.
- El-Gohary YM, Silverman JF, Olson PR, Liu YL, Cohen JK, Miller R, Saad RS. Endoglin (CD105) and vascular endothelial growth factor as prognostic markers in prostatic adenocarcinoma. *Am J Clin Pathol.* 2007;127:572-579.
- El-Rayes BF, LoRusso PM. Targeting the epidermal growth factor receptor. *Br J Cancer.* 2004;91:418-424.
- El-Sayed IH, Huang X, El-Sayed MA. Selective laser photo-thermal therapy of epithelial carcinoma using anti-EGFR antibody conjugated gold nanoparticles. *Cancer Lett.* 2006;239:129-135.
- El-Sayed IH, Huang X, El-Sayed MA. Surface plasmon resonance scattering and absorption of anti-EGFR antibody conjugated gold nanoparticles in cancer diagnostics: applications in oral cancer. *Nano Lett.* 2005;5:829-834.
- El-Sayed MA. Some interesting properties of metals confined in time and nanometer space of different shapes. *Acc Chem Res.* 2001;34:257-264.
- Fagerberg J, Frödin JE, Ragnhammar P, Steinitz M, Wigzell H, Mellstedt H. Induction of an immune network cascade in cancer patients treated with monoclonal antibodies. *Cancer Immunol Immunother.* 1994;38:149-159.
- Fass L. Imaging and cancer: a review. *Mol Oncol.* 2008;2:115-152.
- Fausto N, Campbell JS, Riehle KJ. Liver regeneration. *Hepatology.* 2006;43:S45-S53.
- Fay F, Scott CJ. Antibody-targeted nanoparticles for cancer therapy. *Immunotherapy.* 2011;3:381-394.
- Fischer HC, Chan WC. Nanotoxicity: the growing need for in vivo study. *Curr Opin Biotechnol.* 2007;18:565-571.
- Fonsatti E, Jekunen AP, Kairemo KJ, Coral S, Snellman M, Nicotra MR, Natali PG, Altomonte M, Maio M. Endoglin is a suitable target for efficient imaging of solid tumors: in vivo evidence in a canine mammary carcinoma model. *Clin Cancer Res* 2000;6:2037-2043.
- Fonsatti E, Nicolay HJ, Altomonte M, Covre A, Maio M. Targeting cancer vasculature via endoglin/CD105: a novel antibody-based diagnostic and therapeutic strategy in solid tumours. *Cardiovasc. Res.* 2010;86:12-19.

- Frens G. Controlled Nucleation for the Regulation of the Particle Size in Monodisperse Gold Suspensions. *Nature Physical Science*. 1973;241:20-22.
- Friedman M, Stahl S. Engineered affinity proteins for tumour-targeting applications. *Biotechnol Appl Biochem*. 2009;53:1-29.
- G.T. Hermanson, *Bioconjugate Techniques*, 1<sup>st</sup> ed. Academic Press, London;1996. p. 169-172.
- Gasparini G, Longo R, Fanelli M, Teicher BA. Combination of antiangiogenic therapy with other anticancer therapies: results, challenges, and open questions. *J Clin Oncol*. 2005;23:1295-1311.
- Gebauer M, Skerra A. Engineered protein scaffolds as next-generation antibody therapeutics. *Curr Opin Chem Biol*. 2009;13:245-255.
- Gerion D, Pinaud F, Williams SC, Parak WJ, Zanchet D, Weiss S, Alivisatos AP. Synthesis and Properties of Biocompatible Water-Soluble Silica-Coated CdSe/ZnS Semiconductor Quantum Dots. *J Phys Chem B*. 2001;105:8861-8871.
- Ghosh P, Han G, De M, Kim CK, Rotello VM. Gold nanoparticles in delivery applications. *Adv Drug Deliv Rev*. 2008;60:1307-1315.
- Giljohann DA, Seferos DS, Patel PC, Millstone JE, Rosi NL, Mirkin CA: Oligonucleotide loading determines cellular uptake of DNA-modified gold nanoparticles. *Nano Lett*. 2007;7:3818-3821.
- Glazer ES, Curley SA. Radiofrequency field-induced thermal cytotoxicity in cancer cells treated with fluorescent nanoparticles. *Cancer*. 2010;116:3285-3293 [b].
- Glazer ES, Zhu C, Massey KL, Thompson CS, Kaluarachchi WD, Hamir AN, Curley SA. Noninvasive radiofrequency field destruction of pancreatic adenocarcinoma xenografts treated with targeted gold nanoparticles. *Clin Cancer Res*. 2010;16:5712-5721 [a].
- Gobin AM, Lee MH, Halas NJ, James WD, Drezek RA, West JL. Near-infrared resonant nanoshells for combined optical imaging and photothermal cancer therapy. *Nano Lett*. 2007;7:1929-1934.
- Goldenberg DM. Targeted therapy of cancer with radiolabeled antibodies. *J Nucl Med*. 2002;43:693-713.
- Goldstein NI, Prewett M, Zuklys K, Rockwell P, Mendelsohn J. Biological efficacy of a chimeric antibody to the epidermal growth factor receptor in a human tumor xenograft model. *Clin Cancer Res*. 1995;1:1311-1318.
- Goodman CM, McCusker CD, Yilmaz T, Rotello VM. Toxicity of gold nanoparticles functionalized with cationic and anionic side chains. *Bioconjug Chem*. 2004;15:897-900.

- Gougos A, Letarte M. Primary structure of endoglin, an RGD-containing glycoprotein of human endothelial cells. *J Biol Chem* 1990;265:8361-8364.
- Goumans MJ, Liu Z, ten Dijke P. TGF-beta signaling in vascular biology and dysfunction. *Cell Res* 2009;19:116-127.
- Goumans MJ, Valdimarsdottir G, Itoh S, Rosendahl A, Sideras P, ten Dijke P. Balancing the activation state of the endothelium via two distinct TGF-beta type I receptors. *EMBO J* 2002;21:1743-1753.
- Green MC, Murray JL, Hortobagyi GN. Monoclonal antibody therapy for solid tumors. *Cancer Treat Rev.* 2000;26:269-286.
- Gref R, Minamitake Y, Peracchia MT, Trubetskoy V, Torchilin V, Langer R. Biodegradable long-circulating polymeric nanospheres. *Science*. 1994;263:1600-1603.
- Greish K. Enhanced permeability and retention of macromolecular drugs in solid tumors: a royal gate for targeted anticancer nanomedicines. *J Drug Target*. 2007;15:457-464.
- Gu YJ, Cheng JP, Lin CC, Lam YW, Cheng SH, Wong WT. Nuclear penetration of surface functionalized gold nanoparticles. *Toxicol Appl Pharmacol*. 2009;237:196-204.
- Guerrero S, Herance JR, Rojas S, Mena JF, Gispert JD, Acosta GA, Albericio F, Kogan MJ: Synthesis and in vivo evaluation of the biodistribution of a <sup>18</sup>F-labeled conjugate gold-nanoparticle-peptide with potential biomedical applications. *Bioconjugate Chem* 2012;23:399-408.
- Guerrero-Esteo M, Sanchez-Elsner T, Letamendia A, Bernabeu C. Extracellular and cytoplasmic domains of endoglin interact with the transforming growth factor-beta receptors I and II. *J Biol Chem* 2002;277:29197-29209.
- Hainfeld JF, Dilmanian FA, Zhong Z, Slatkin DN, Kalef-Ezra JA, Smilowitz HM. Gold nanoparticles enhance the radiation therapy of a murine squamous cell carcinoma. *Phys Med Biol*. 2010 ;55:3045-3059.
- Hainfeld JF, Slatkin DN, Focella TM, Smilowitz HM. Gold nanoparticles: a new X-ray contrast agent. *Br J Radiol*. 2006;79:248-253.
- Hainfeld JF, Slatkin DN, Smilowitz HM. The use of gold nanoparticles to enhance radiotherapy in mice. *Phys Med Biol*. 2004;49:N309-315.
- Hamerli P, Weigel T, Groth T, Paul D. Surface properties of and cell adhesion onto allylamine-plasma-coated polyethyleneterephthalat membranes. *Biomaterials*. 2003;24:3989-3999.
- Harari PM, Huang SM. Modulation of molecular targets to enhance radiation. *Clin Cancer Res*. 2000;6:323-325.

- Harari PM. Epidermal growth factor receptor inhibition strategies in oncology. *Endocr Relat Cancer*. 2004;11:689-708.
- Harris N, Ford MJ, Cortie MB. Optimization of plasmonic heating by gold nanospheres and nanoshells. *J Phys Chem B*. 2006;110:10701-10707.
- Haruta Y, Seon BK. Distinct human leukemia-associated cell surface glycoprotein GP160 defined by monoclonal antibody SN6. *Proc. Natl. Acad. Sci. USA*. 1986;83:7898-7902.
- Hashizume H, Baluk P, Morikawa S, McLean JW, Thurston G, Roberge S, Jain RK, McDonald DM. Openings between defective endothelial cells explain tumor vessel leakiness. *Am J Pathol*. 2000;156:1363-1380.
- Heldin CH, Rubin K, Pietras K, Ostman A. High interstitial fluid pressure - an obstacle in cancer therapy. *Nat Rev Cancer*. 2004;4:806-813.
- Herbst RS, Shin DM. Monoclonal antibodies to target epidermal growth factor receptor-positive tumors: a new paradigm for cancer therapy. *Cancer*. 2002;94:1593-1611.
- Hillyer JF, Albrecht RM. Gastrointestinal persorption and tissue distribution of differently sized colloidal gold nanoparticles. *J Pharm Sci*. 2001;90:1927-1936.
- Hines MA, Guyot-Sionnest P. Synthesis and Characterization of Strongly Luminescing ZnS-Capped CdSe Nanocrystals. *J Phys Chem-US*. 1996;100:468-471.
- Hirsch LR, Stafford RJ, Bankson JA, Sershen SR, Rivera B, Price RE, Hazle JD, Halas NJ, West JL. Nanoshell-mediated near-infrared thermal therapy of tumors under magnetic resonance guidance. *Proc Natl Acad Sci USA*. 2003;100:13549-13554.
- Holland JP, Divilov V, Bander NH, Smith-Jones PM, Larson SM, Lewis JS.  $^{89}\text{Zr}$ -DFO-J591 for immunoPET of prostate-specific membrane antigen expression in vivo. *J Nucl Med*. 2010; 51:1293-1300.
- Huang F, Kirkpatrick D, Jiang X, Gygi S, Sorkin A. Differential regulation of EGF receptor internalization and degradation by multiubiquitination within the kinase domain. *Mol Cell*. 2006;21:737-748 [a].
- Huang L, Gainkam LO, Cavelliers V, Vanhove C, Keyaerts M, De Baetselier P, Bossuyt A, Revets H, Lahoutte T. SPECT imaging with  $^{99\text{m}}\text{Tc}$ -labeled EGFR-specific nanobody for in vivo monitoring of EGFR expression. *Mol Imaging Biol*. 2008;10:167-175.
- Huang X, El-Sayed MA. Gold nanoparticles: Optical properties and implementations in cancer diagnosis and photothermal therapy. *Journal of Advanced Research*. 2010;1:13-28.

- Huang X, Jain PK, El-Sayed IH, El-Sayed MA. Determination of the minimum temperature required for selective photothermal destruction of cancer cells with the use of immunotargeted gold nanoparticles. *Photochem Photobiol.* 2006;82:412-417 [b].
- Huang X, Jain PK, El-Sayed IH, El-Sayed MA. Gold nanoparticles: interesting optical properties and recent applications in cancer diagnostics and therapy. *Nanomedicine (Lond).* 2007;2:681-693.
- Huang YF, Liu H, Xiong X, Chen Y, Tan W. Nanoparticle-mediated IgE-receptor aggregation and signaling in RBL mast cells. *J Am Chem Soc.* 2009;131:17328-17334.
- Hunter WM, Greenwood FC. Preparation of iodine-131 labelled human growth hormone of high specific activity. *Nature.* 1962;194:495-496.
- Hussein MR. Transforming growth factor-beta and malignant melanoma: molecular mechanisms. *J. Cutan. Pathol.* 2005;32:389-395.
- Hynes NE, Horsch K, Olayioye MA, Badache A. The ErbB receptor tyrosine family as signal integrators. *Endocr Relat Cancer.* 2001;8:151-159.
- Iyer AK, Khaled G, Fang J, Maeda H. Exploiting the enhanced permeability and retention effect for tumor targeting. *Drug Discov Today.* 2006;11:812-818.
- Jaffer FA, Weissleder R. Molecular imaging in the clinical arena. *JAMA.* 2005;293:855-862.
- Jain RK. Transport of molecules in the tumor interstitium: a review. *Cancer Res.* 1987;47:3039-3051.
- Janmaat ML, Kruyt FA, Rodriguez JA, Giaccone G. Response to epidermal growth factor receptor inhibitors in non-small cell lung cancer cells: limited antiproliferative effects and absence of apoptosis associated with persistent activity of extracellular signal-regulated kinase or Akt kinase pathways. *Clin Cancer Res.* 2003;9:2316-2326.
- Jelveh S, Chithrani DB. Gold nanostructures as a platform for combinational therapy in future cancer therapeutics. *Cancers.* 2011;3:1081-1110.
- Jiang W, Kim BYS, Rutka JT, Chan WCW: Nanoparticle-mediated cellular response is size-dependent. *Nature Nanotech.* 2008;3:145-150.
- Jiang, JK; Oberdorster, G; Biswas, P Characterization of size, surface charge, and agglomeration state of nanoparticle dispersions for toxicological studies. *J Nanopart Res.* 2009;11:77-89.
- Jin Y, Wang P, Yin D, Liu J, Qin L, Yu N, Xie G, Li B. Gold nanoparticles prepared by sonochemical method in thiol-functionalized ionic liquid. *Colloids Surf A Physicochem Eng Asp.* 2007;302:366-370.

- John R, Rezaeiipoor R, Adie SG, Chaney EJ, Oldenburg AL, Marjanovic M, Haldar JP, Sutton BP, Boppart SA. In vivo magnetomotive optical molecular imaging using targeted magnetic nanoprobe. *Proc Natl Acad Sci U S A*. 2010;107: 8085-8090.
- Joshi A, Narsingi KY, Manasreh MO, Davis EA, Weaver BD. Temperature dependence of the band gap of colloidal CdSe/ZnS core/shell nanocrystals embedded into an ultraviolet curable resin. *Appl. Phys. Lett.* 2006;89:131907.
- Juarranz A, Jaén P, Sanz-Rodríguez F, Cuevas J, González S. Photodynamic therapy of cancer. Basic principles and applications. *Clin Transl Oncol*. 2008;10:148-154.
- Julien DC, Behnke S, Wang G, Murdoch GK, Hill RA. Utilization of monoclonal antibody-targeted nanomaterials in the treatment of cancer. *MAbs*. 2011;3:467-478.
- Kattumuri V, Katti K, Bhaskaran S, et al. Gum arabic as a phytochemical construct for the stabilization of gold nanoparticles: in vivo pharmacokinetics and X-ray-contrast-imaging studies. *Small*. 2007;3:333-341.
- Kaul G, Amiji M. Long-circulating poly(ethylene glycol)-modified gelatin nanoparticles for intracellular delivery. *Pharm. Res*. 2002;19:1061-1067.
- Khlebtsov BN, Zharov VP, Melnikov AG, Tuchin VV, Khlebtsov NG. Optical amplification of photothermal therapy with gold nanoparticles and nanoclusters. *Nanotechnology*. 2006;17:5167-5179.
- Khlebtsov NG. Optics and biophotonics of nanoparticles with a plasmon resonance. *Quantum Electron*. 2008;38:504-529.
- Kiesewetter DO, Krämer-Marek G, Ma Y, Capala J. Radiolabeling of HER2 specific Affibody<sup>®</sup> molecule with F-18. *J Fluor Chem*. 2008;129:799-805.
- Kim D, Park S, Lee JH, Jeong YY, Jon S. Antibiofouling polymer-coated gold nanoparticles as a contrast agent for in vivo X-ray computed tomography imaging. *J Am Chem Soc*. 2007;129:7661-7665.
- Kim JH, Kim YS, Park K, Lee S, Nam HY, Min KH, Jo HG, Park JH, Choi K, Jeong SY, Park RW, Kim IS, Kim K, Kwon IC. Antitumor efficacy of cisplatin-loaded glycol chitosan nanoparticles in tumor-bearing mice. *J Control Release*. 2008;127:41-49.
- Kimling J, Maier M, Okenve B, Kotaidis V, Ballot H, Plech A. Turkevich method for gold nanoparticle synthesis revisited. *J Phys Chem B*. 2006;110:15700-15707.
- Kirpotin DB, Drummond DC, Shao Y, Shalaby MR, Hong K, Nielsen UB, Marks JD, Benz CC, Park JW. Antibody targeting of long-circulating lipidic nanoparticles does not increase tumor localization but does increase internalization in animal models. *Cancer Res*. 2006;66:6732-6740.

- Kocher DC. Radioactive decay data tables, a handbook of decay data for application to radiation dosimetry and radiological assessments. Washington, DC; U.S. Department of Energy Technical Information Center; DOE/TIC-11026; 1981.
- Kong T, Zeng J, Wang X, Yang X, Yang J, McQuarrie S, McEwan A, Roa W, Chen J, Xing JZ. Enhancement of radiation cytotoxicity in breast-cancer cells by localized attachment of gold nanoparticles. *Small*. 2008;4:1537-1543.
- Korpanty G, Carbon JG, Grayburn PA, Fleming JB, Brekken RA. Monitoring response to anticancer therapy by targeting microbubbles to tumor vasculature. *Clin Cancer Res*. 2007;13:323-330.
- Korpanty G, Grayburn PA, Shohet RV, Brekken RA. Targeting vascular endothelium with avidin microbubbles. *Ultrasound Med Biol*. 2005;31:1279-1283.
- Kramer-Marek G, Bernardo M, Kiesewetter DO, Bagci U, Kuban M, Aras O, Zielinski R, Seidel J, Choyke P, Capala J. PET of HER2-positive pulmonary metastases with  $^{18}\text{F}$ -ZHER2:342 affibody in a murine model of breast cancer: comparison with  $^{18}\text{F}$ -FDG. *J Nucl Med*. 2012;53:939-946.
- Kreibig U, Vollmer M. Optical Properties of Metal Clusters. Springer; 1995.
- Krishnamurthy VM. Multivalency in Ligand Design 2006. p. 11-53. DOI: 10.1002/3527608761.ch2.
- Kuan CT, Wikstrand CJ, Bigner DD. EGF mutant receptor vIII as a molecular target in cancer therapy. *Endocr Relat Cancer*. 2001;8:83-96.
- Kumar S, Ghellal A, Li C, Byrne G, Haboubi N, Wang JM, Bundred N. Breast carcinoma: vascular density determined using CD105 antibody correlates with tumor prognosis. *Cancer Res*. 1999;59:856-861.
- Kurai J, Chikumi H, Hashimoto K, Yamaguchi K, Yamasaki A, Sako T, Touge H, Makino H, Takata M, Miyata M, Nakamoto M, Burioka N, Shimizu E. Antibody-dependent cellular cytotoxicity mediated by cetuximab against lung cancer cell lines. *Clin Cancer Res*. 2007;13:1552-1561.
- Lebrin F, Goumans MJ, Jonker L, Carvalho RL, Valdimarsdottir G, Thorikay M et al. Endoglin promotes endothelial cell proliferation and TGF-beta/ALK1 signal transduction. *EMBO J* 2004;23:4018-4028.
- Lee CM, Tannock IF. The distribution of the therapeutic monoclonal antibodies cetuximab and trastuzumab within solid tumors. *BMC Cancer*. 2010;10:255.
- Letamendía A, Lastres P, Almendro N, Raab U, Bühring HJ, Kumar S, Bernabéu C. Endoglin, a component of the TGF-beta receptor system, is a differentiation marker of human choriocarcinoma cells. *Int. J. Cancer*. 1998;76:541-546.
- Lewinski N, Colvin V, Drezek R. Cytotoxicity of nanoparticles. *Small*. 2008;4:26-49.

- Li C, Gardy R, Seon BK, Duff SE, Abdalla S, Renehan A, O'Dwyer ST, Haboubi N, Kumar S.. Both high intratumoral microvessel density determined using CD105 antibody and elevated plasma levels of CD105 in colorectal cancer patients correlate with poor prognosis. *BrJ Cancer*. 2003;88:1424-1431.
- Li S, Schmitz KR, Jeffrey PD, Wiltzius JJ, Kussie P, Ferguson KM. Structural basis for inhibition of the epidermal growth factor receptor by cetuximab. *Cancer Cell*. 2005;7:301-311.
- Libutti SK, Paciotti GF, Byrnes AA, Alexander HR Jr, Gannon WE, Walker M, Seidel GD, Yuldasheva N, Tamarkin L. Phase I and pharmacokinetic studies of CYT-6091, a novel PEGylated colloidal gold-rhTNF nanomedicine. *Clin Cancer Res*. 2010;16:6139-6149.
- Limage H, Tichelaar FD, Closset R, Delvaux S, Cloots R, Lucas S. Study of the effect of a silver nanoparticle seeding layer on the crystallisation temperature, photoinduced hydrophilic and catalytic properties of TiO<sub>2</sub> thin films deposited on glass by magnetron sputtering. *Surface and Coatings Technology*. 2011;205:3774-3778.
- Link S, El-Sayed MA. Optical properties and ultrafast dynamics of metallic nanocrystals. *Annu Rev Phys Chem*. 2003;54:331-366.
- Link S, El-Sayed MA. Shape and size dependence of radiative, non-radiative and photothermal properties of gold nanocrystals. *Int Rev Phys Chem*. 2000;19:409-453.
- Link S, El-Sayed MA. Spectral properties and relaxation dynamics of surface plasmon electronic oscillations in gold and silver nanodots and nanorods. *J. Phys. Chem. B*. 1999;103:8410-8426.
- Liu CJ, Wang CH, Chen ST, Chen HH, Leng WH, Chien CC, Wang CL, Kempson IM, Hwu Y, Lai TC, Hsiao M, Yang CS, Chen YJ, Margaritondo G. Enhancement of cell radiation sensitivity by pegylated gold nanoparticles. *Phys Med Biol*. 2010;55:931-945.
- Liu X, Dai Q, Austin L, Coutts J, Knowles G, Zou J, Chen H, Huo Q. A one-step homogeneous immunoassay for cancer biomarker detection using gold nanoparticle probes coupled with dynamic light scattering. *J Am Chem Soc*. 2008;130:2780-2782.
- Liu X, Wang X, Wei D, Cai M, Li G. [Internalization of antibody-targeted immunonanoparticles into human hepatoma cells and its reversal effect on MDR] *Sichuan Da Xue Xue Bao Yi Xue Ban*. 2003;34:431-434.
- Longmire M, Choyke PL, Kobayashi H. Clearance properties of nano-sized particles and molecules as imaging agents: considerations and caveats. *Nanomedicine (Lond)*. 2008;3:703-717.
- Loo C, Lowery A, Halas N, West J, Drezek R. Immunotargeted nanoshells for integrated cancer imaging and therapy. *Nano Lett*. 2005;5:709-711.

- Lucas S, Genard G, Michiels C, Masereel B, Feron O, Gallez B, Vander Borgh T, Moreau N. Production and preliminary characterization of DC Plasma Polymerized Allylamine film (PPAA) by NRA, ERD and XPS. *Nucl Instrum Meth Phys Res B*. 2008;266:2494-2497.
- Luwor RB, Lu Y, Li X, Mendelsohn J, Fan Z. The antiepidermal growth factor receptor monoclonal antibody cetuximab/C225 reduces hypoxia-inducible factor-1 alpha, leading to transcriptional inhibition of vascular endothelial growth factor expression. *Oncogene*. 2005;24:4433-4441.
- Maeda H, Bharate GY, Daruwalla J. Polymeric drugs for efficient tumor-targeted drug delivery based on EPR-effect. *Eur J Pharm Biopharm*. 2009;71:409-419.
- Maeda H, Matsumura Y. EPR Effect Based Drug Design and Clinical Outlook for Enhanced Cancer Chemotherapy. In: Maeda H, Matsumura Y, editors. *Adv Drug Deliv Rev*. 2011;63:129-130.
- Maeda H, Sawa T, Konno T. Mechanism of tumor-targeted delivery of macromolecular drugs, including the EPR effect in solid tumor and clinical overview of the prototype polymeric drug SMANCS. *J Control Release*. 2001;74:47-61 [a].
- Maeda H. The enhanced permeability and retention (EPR) effect in tumor vasculature: the key role of tumor-selective macromolecular drug targeting. *Adv Enzyme Regul*. 2001;41:189-207 [b].
- Maier JA, Delia D, Thorpe PE, Gasparini G. In vitro inhibition of endothelial cell growth by the antiangiogenic drug AGM-1470 (TNP-470) and the anti-endoglin antibody TEC-11. *Anticancer Drugs* 1997;8:238-244.
- Maio M, Altomonte M, Fonsatti E. Is it the primetime for endoglin (CD105) in the clinical setting? *Cardiovasc Res*. 2006;69:781-783.
- Majidi J, Barar J, Baradaran B, Abdolalizadeh J, Omid Y. Target therapy of cancer: implementation of monoclonal antibodies and nanobodies. *Hum Antibodies*. 2009;18:81-100.
- Mallick K, Wang ZL, Pal T. Seed-mediated successive growth of gold particles accomplished by UV irradiation: a photochemical approach for size-controlled synthesis. *J Photochem Photobiol A: Chem*. 2001;140:75-80.
- Mallidi S, Larson T, Aaron J, Sokolov K, Emelianov S. Molecular specific optoacoustic imaging with plasmonic nanoparticles. *Opt Express*. 2007;15:6583-6588.
- Marioni G, D'Alessandro E, Giacomelli L, Staffieri A. CD105 is a marker of tumour vasculature and a potential target for the treatment of head and neck squamous cell carcinoma. *J Oral Pathol. Med*. 2010;39:361-367.
- Masereel B, Dinguizli M, Bouzin C et al. Antibody immobilization on gold nanoparticles coated layer-by-layer with polyelectrolytes. *J. Nanopart. Res*. 2011;13:1573-1580.

- Matsumura Y, Maeda H. A new concept for macromolecular therapeutics in cancer chemotherapy: mechanism of tumorotropic accumulation of proteins and the antitumor agent smancs. *Cancer Res.* 1986;46:6387-6392.
- Matsuno F, Haruta Y, Kondo M, Tsai H, Barcos M, Seon BK. Induction of lasting complete regression of preformed distinct solid tumors by targeting the tumor vasculature using two new anti-endoglin monoclonal antibodies. *Clin Cancer Res.* 1999;5:371-382.
- Meijs W. E., Herscheid J. D. M., Haisma H. J. and Pinedo H. M. Evaluation of desferal as a bifunctional chelating agent for labelling antibodies with Zr-89. *Appl. R&at. Isot.* 1992;43:1443-1447.
- Meijs W. E., Herscheid J. D. M., Haisma H. J., Wijbrandts R., van Langevelde F., van Leuffen P. J., Mooy R. and Pinedo H. M. Production of highly pure no-carrier added <sup>89</sup>Zr for the labelling of antibodies with a positron emitter. 1994;45:1142-1147.
- Mie G. Contributions to the optics of turbid media, particularly of colloidal metal solutions. Tech. Rep. Library Translation 1873, RAE-Lit-Trans-1873, Royal Aircraft Establishment (1976). <http://diogenes.iwt.uni-bremen.de/vt/laser/papers/RAE-LT1873-1976-Mie-1908-translation.pdf>
- Milenic DE, Brady ED, Brechbiel MW. Antibody-targeted radiation cancer therapy. *Nat Rev Drug Discov.* 2004;3:488-499.
- Miller DW, Graulich W, Karges B et al. Elevated expression of endoglin, a component of the TGF-beta-receptor complex, correlates with proliferation of tumor endothelial cells. *Int. J. Cancer.* 1999;81:568-572.
- Misra R, Acharya S, Sahoo SK. Cancer nanotechnology: application of nanotechnology in cancer therapy. *Drug Discov Today.* 2010;15:842-850.
- Mitchell DC, Bryan BA. Anti-angiogenic therapy: adapting strategies to overcome resistant tumors. *J Cell Biochem.* 2010;111:543-553.
- Modi S, Prakash Jain J, Domb AJ, Kumar N. Exploiting EPR in polymer drug conjugate delivery for tumor targeting. *Curr Pharm Des.* 2006;12:4785-4796.
- Montenegro M, Nahar SN, Pradhan AK, Huang K, Yu Y. Monte Carlo simulations and atomic calculations for Auger processes in biomedical nanotheranostics. *J Phys Chem A.* 2009;113:12364-12369.
- Moran CH, Wainerdi SM, Cherukuri TK, Kittrell C, Wiley BJ, Nicholas NW, Curley SA, Kanzius JS, Cherukuri P. Size-dependent joule heating of gold nanoparticles using capacitively coupled radiofrequency fields *Nano Res.* 2009;2:400-405.

- Moreau N, Feron O, Gallez B, Masereel B, Michiels C, Vander Borgh T, Rossig F, Lucas S, hChemical reactivity of plasma polymerized allylamine (PPAA) thin films on Au and Si: Study of the thickness influence and aging of the films *Surface and Coatings Technology*. 2011;205:S462–S465.
- Moreau N, Michiels C, Masereel B et al. PVD synthesis and transfer into water-based solutions of functionalized gold nanoparticles. *Plasma Process Polymer*. 2009;6:S888-S892.
- Müller C, Schibli R. Single photon emission computed tomography tracer. *Recent Results Cancer Res*. 2013;187:65-105.
- Mukherjee P, Bhattacharya R, Wang P, Wang L, Basu S, Nagy JA, Atala A, Mukhopadhyay D, Soker S. Antiangiogenic properties of gold nanoparticles. *Clin Cancer Res*. 2005;11:3530-3534.
- Muñoz R, Arias Y, Ferreras JM, Rojo MA, Gayoso MJ, Nocito M, Benitez J, Jiménez P, Bernabéu C, Girbés T. Targeting a marker of the tumour neovasculature using a novel anti-human CD105-immunotoxin containing the non-toxic type 2 ribosome-inactivating protein nigrin b. *Cancer Lett*. 2007;256:73-80.
- Murphy CJ, Gole AM, Stone JW, Sisco PN, Alkilany AM, Goldsmith EC, Baxter SC. Gold nanoparticles in biology: beyond toxicity to cellular imaging. *Acc Chem Res*. 2008;41:1721-1730.
- Murphy K, editor. *Janeway's Immunobiology*. 8th ed. London and New York: Garland Science; 2012.
- Myroshnychenko V, Rodríguez-Fernández J, Pastoriza-Santos I, Funston AM, Novo C, Mulvaney P, Liz-Marzánb LM, García de Abajo FJ. Modelling the optical response of gold nanoparticles. *Chem. Soc. Rev*. 2008;37:1792-1805.
- Narita T, Taga T, Sugita K, Nakazawa S, Ohta S. The autocrine loop of epidermal growth factor receptor-epidermal growth factor / transforming growth factor- $\alpha$  in malignant rhabdoid tumor cell lines: heterogeneity of autocrine mechanism in TTC549. *Jpn J Cancer Res*. 2001;92:269-278.
- Nativo P, Prior IA, Brust M: Uptake and intracellular fate of surface-modified gold nanoparticles. *ACS Nano*. 2008;2:1639-1644.
- Nune SK, Gunda P, Thallapally PK, Lin YY, Forrest ML, Berkland CJ. Nanoparticles for biomedical imaging. *Expert Opin Drug Deliv*. 2009;6:1175-1194.
- Nuttall SD, Walsh RB. Display scaffolds: protein engineering for novel therapeutics. *Curr Opin Pharmacol*. 2008;8:609-615.
- O'Mahony D, Bishop MR. Monoclonal antibody therapy. *Front biosci*. 2006;11:1620-1635.
- O'dwyer PJ, Benson AB 3rd. Epidermal growth factor receptor-targeted therapy in colorectal cancer. *Semin Oncol*. 2002;29:10-17.

- Olafsen T, Betting D, Kenanova VE, Salazar FB, Clarke P, Said J, Raubitschek AA, Timmerman JM, Wu AM. Recombinant anti-CD20 antibody fragments for small animal PET imaging of B-cell lymphomas. *J Nucl Med.* 2009;50:1500-1508.
- Olafsen T, Wu AM. Novel Antibody Vectors for Imaging. *Semin Nucl Med.* 2010;40:167-181.
- Olayioye MA, Neve RM, Lane HA, Hynes NE. The ErbB signaling network: receptor heterodimerization in development and cancer. *EMBO J.* 2000;19:3159-3167.
- O'Neal DP, Hirsch LR, Halas NJ, Payne JD, West JL. Photo-thermal tumor ablation in mice using near infrared-absorbing nanoparticles. *Cancer Lett.* 2004;209:171-176.
- Orendorff CJ, Sau TK, Murphy CJ. Shape-dependent plasmon-resonant gold nanoparticles. *Small.* 2005;2:636-639.
- Oriuchi N, Higuchi T, Hanaoka H, Iida Y, Endo K. Current status of cancer therapy with radiolabeled monoclonal antibody. *Ann Nucl Med.* 2005;19:355-365.
- Ortaldo JR, Woodhouse C, Morgan AC, Herberman RB, Cheresch DA, Reisfeld R. Analysis of effector cells in human antibody-dependent cellular cytotoxicity with murine monoclonal antibodies. *J Immunol.* 1987;138:3566-3572.
- Owens DE 3rd, Peppas NA. Opsonization, biodistribution, and pharmacokinetics of polymeric nanoparticles. *Int J Pharm.* 2006;307:93-102.
- Paciotti GF, Myer L, Weinreich D, Goia D, Pavel N, McLaughlin RE, Tamarkin L. Colloidal gold: a novel nanoparticle vector for tumor directed drug delivery. *Drug Deliv.* 2004;11:169-183.
- Padera TP, Stoll BR, Tooredman JB, Capen D, di Tomaso E, Jain RK. Pathology: cancer cells compress intratumour vessels. *Nature.* 2004;427:695.
- Pan Y, Leifert A, Ruau D, et al. Gold nanoparticles of diameter 1.4 nm trigger necrosis by oxidative stress and mitochondrial damage. *Small.* 2009;5:2067-2076.
- Pan Y, Neuss S, Leifert A, Fischler M, Wen F, Simon U, Schmid G, Brandau W, Jahnke-Dechent W. Size-dependent cytotoxicity of gold nanoparticles. *Small.* 2007;3:1941-1949.
- Park JE, Atobe M, Fuchigami T. Synthesis of multiple shapes of gold nanoparticles with controlled sizes in aqueous solution using ultrasound. *Ultrason Sonochem.* 2006;13:237-241.
- Patra CR, Bhattacharya R, Wang E, Katarya A, Lau JS, Dutta S, Muders M, Wang S, Buhrow SA, Safgren SL, Yaszemski MJ, Reid JM, Ames MM, Mukherjee P, Mukhopadhyay D. Targeted delivery of gemcitabine to pancreatic adenocarcinoma using cetuximab as a targeting agent. *Cancer Res.* 2008;68:1970-1978.

- Patra HK, Banerjee S, Chaudhuri U, Lahiri P, Dasgupta AK. Cell selective response to gold nanoparticles. *Nanomedicine*. 2007;3:111-119.
- Paus E, Bromer O, Nustad K. Radioiodination of proteins with the IODOGEN method. *Radioimmunoassay in Related Procedures in Medicine. Proc Int Symp*, 161-171 (1982).
- Pedersen MW, Jacobsen HJ, Koefoed K, Hey A, Pyke C, Haurum JS, Kragh M. Sym004: a novel synergistic anti-epidermal growth factor receptor antibody mixture with superior anticancer efficacy. *Cancer Res*. 2010;70:588-597.
- Pérez-Gómez E, Eleno N, López-Novoa JM, Ramirez JR, Velasco B, Letarte M, Bernabéu C, Quintanilla M. Characterization of murine S-endoglin isoform and its effects on tumor development. *Oncogene* 2005;24:4450-4461.
- Perk LR, Visser GW, Vosjan MJ, Stigter-van Walsum M, Tijink BM, Leemans CR, van Dongen GA.  $^{89}\text{Zr}$  as a PET surrogate radioisotope for scouting biodistribution of the therapeutic radiometals  $^{90}\text{Y}$  and  $^{177}\text{Lu}$  in tumor-bearing nude mice after coupling to the internalizing antibody cetuximab. *J Nucl Med*. 2005;46:1898-1906.
- Perk LR, Vosjan MJWD, Visser GW et al. p-Isothiocyanatobenzyl-desferrioxamine: a new bifunctional chelate for facile radiolabeling of monoclonal antibodies with zirconium-89 for immuno-PET imaging. *Eur. J. Nucl. Med. Mol. Imaging*. 2010;37:250-259.
- Pernodet N, Fang XH, Sun Y, et al. Adverse effects of citrate/gold nanoparticles on human dermal fibroblasts. *Small*. 2006;2:766-773.
- Petit AM, Rak J, Hung MC, Rockwell P, Goldstein N, Fendly B, Kerbel RS. Neutralizing antibodies against epidermal growth factor and ErbB-2/neu receptor tyrosine kinases down-regulate vascular endothelial growth factor production by tumor cells in vitro and in vivo: angiogenic implications for signal transduction therapy of solid tumors. *Am J Pathol*. 1997;151:1523-1530.
- Pietersz GA, Kanellos J, Smyth MJ, Zalberg J, McKenzie IF. The use of monoclonal antibody conjugates for the diagnosis and treatment of cancer. *Immunol Cell Biol*. 1987;65:111-125.
- Pinto Reis C, Neufeld RJ, Ribeiro AJ, Veiga F. Nanoencapsulation I. Methods for preparation of drug-loaded polymeric nanoparticles. *Nanomedicine*. 2006;2:8-21.
- Pirollo KF, Chang EH. Does a targeting ligand influence nanoparticle tumor localization or uptake? *Trends Biotechnol*. 2008;26:552-558.
- Pitsillides CM, Joe EK, Wei X, Anderson RR, Lin CP. Selective cell targeting with light-absorbing microparticles and nanoparticles. *Biophys J*. 2003;84:4023-4032.

- Popovtzer R, Agrawal A, Kotov NA, Popovtzer A, Balter J, Carey TE, Kopelman R. Targeted gold nanoparticles enable molecular CT imaging of cancer. *Nano Lett.* 2008;8:4593-4596.
- Portoghese PS, Larson DL, Yim CB, Sayre LM, Ronsisvalle G, Lipkowski AW, Takemori AE, Rice KC, Tam SW. Stereostructure-activity relationship of opioid agonist and antagonist bivalent ligands. Evidence for bridging between vicinal opioid receptors. *J Med Chem.* 1985;28:1140-1141.
- Powers K, Palazuelos M, Moudgil BM, Roberts S. Characterization of the size, shape, and state of dispersion of nanoparticles for toxicological studies. *Nanotoxicology.* 2007;1:42-51.
- Prencipe G, Tabakman SM, Welsher K, Liu Z, Goodwin AP, Zhang L, Henry J, Dai H. PEG branched polymer for functionalization of nanomaterials with ultralong blood circulation. *J Am Chem Soc.* 2009;131:4783-4787.
- Prewett M, Rockwell P, Rockwell RF, Giorgio NA, Mendelsohn J, Scher HI, Goldstein NI. The biologic effects of C225, a chimeric monoclonal antibody to the EGFR, on human prostate carcinoma. *J Immunother Emphasis Tumor Immunol.* 1996;19:419-427.
- Rahman WN, Bishara N, Ackerly T, He CF, Jackson P, Wong C, Davidson R, Geso M. Enhancement of radiation effects by gold nanoparticles for superficial radiation therapy. *Nanomedicine.* 2009;5:136-142.
- Ram S, Buchsbaum DJ. Radioiodination of monoclonal antibodies D612 and 17-1A with 3-iodophenylisothiocyanate and their biodistribution in tumor-bearing nude mice. *Cancer* 1994;73:808-815.
- Raouf M, Curley SA. Non-invasive radiofrequency-induced targeted hyperthermia for the treatment of hepatocellular carcinoma. *International Journal of Hepatology.* 2011;2011:6 pages. doi:10.4061/2011/676957.
- Raub CB, Orwin EJ, Haskell R. Immunogold labeling to enhance contrast in optical coherence microscopy of tissue engineered corneal constructs. *Conf Proc IEEE Eng Med Biol Soc.* 2004;2:1210-1213.
- Reichert JM. Monoclonal antibodies in the clinic. *Nat Biotechnol.* 2001;19:819-822.
- Reichert JM. Therapeutic monoclonal antibodies: trends in development and approval in the US. *Curr Opin Mol Ther.* 2002;4:110-118.
- Rivera F, Vega-Villegas ME, Lopez-Brea MF, Marquez R. Current situation of Panitumumab, Matuzumab, Nimotuzumab and Zalutumumab. *Acta Oncol.* 2008;47:9-19.
- Romani AA, Borghetti AF, Del Rio P, Sianesi M, Soliani P. The risk of developing metastatic disease in colorectal cancer is related to CD105-positive vessel count. *J Surg Oncol.* 2006;93:446-455.
- Rosen LS, Hurwitz HI, Wong MK, Goldman J, Mendelson DS, Figg WD, Spencer S, Adams BJ, Alvarez D, Seon BK, Theuer CP, Leigh BR, Gordon MS. A phase I first-in-human study of TRC105 (Anti-Endoglin Antibody) in patients with advanced cancer. *Clin. Cancer Res.* 2012;18:4820-4829.

- Ruenraroengsak P, Cook JM, Florence AT. Nanosystem drug targeting: Facing up to complex realities. *J Control Release*. 2010;141:265-276.
- Sajja HK, East MP, Mao H, Wang YA, Nie S, Yang L. Development of multifunctional nanoparticles for targeted drug delivery and noninvasive imaging of therapeutic effect. *Curr Drug Discov Technol*. 2009;6:43-51.
- Sands H, Jones PL. Methods for the study of the metabolism of radiolabeled monoclonal antibodies by liver and tumor. *J Nucl Med*. 1987;28:390-398.
- Sarin H. Physiologic upper limits of pore size of different blood capillary types and another perspective on the dual pore theory of microvascular permeability. *J Angiogenes Res*. 2010;2:14.
- Sato JD, Kawamoto T, Le AD, Mendelsohn J, Polikoff J, Sato GH. Biological effects in vitro of monoclonal antibodies to human epidermal growth factor receptors. *Mol Biol Med*. 1983;1:511-529.
- Schlessinger J. Cell signaling by receptor tyrosine kinases. *Cell*. 2000;103:211-225.
- Schliemann C, Neri D. Antibody-based targeting of the tumor vasculature. *Biochim Biophys Acta*. 2007;1776:175-192.
- Schmolling J, Reinsberg J, Wagner U, Krebs D. Antiidiotypic antibodies in ovarian cancer patients treated with the monoclonal antibody B72.3. *Hybridoma*. 1995;14:183-186.
- Schroeder A, Heller DA, Winslow MM, Dahlman JE, Pratt GW, Langer R, Jacks T, Anderson DG. Treating metastatic cancer with nanotechnology. *Nature Reviews Cancer*. 2012;12:39-50.
- Scott AM, Wolchok JD, Old LJ. Antibody therapy of cancer. *Nat Rev Cancer*. 2012;12:278-287
- Seon BK, Matsuno F, Haruta Y, Kondo M, Barcos M. Long-lasting complete inhibition of human solid tumors in SCID mice by targeting endothelial cells of tumor vasculature with anti-human endoglin immunotoxin. *Clin Cancer Res*. 1997;3:1031-1044.
- Shao X, Agarwal A, Rajaian JR, Kotov NA, Wang X: Synthesis and bioevaluation of <sup>125</sup>I-labeled gold nanoparticles. *Nanotechnology* 2011;13:135102.
- Sharkey RM, Behr TM, Mattes MJ, et al. Advantage of residualizing radiolabels for an internalizing antibody against the B-cell lymphoma antigen, CD22. *Cancer Immunol Immunother* 1997;44:179-188.
- She X, Matsuno F, Harada N, Tsai H, Seon BK. Synergy between anti-endoglin (CD105) monoclonal antibodies and TGF-beta in suppression of growth of human endothelial cells. *Int J Cancer* 2004;108:251-257.

- Shenoy D, Fu W, Li J, Crasto C, Jones G, DiMarzio C, Sridhar S, Amiji M. Surface functionalization of gold nanoparticles using hetero-bifunctional poly(ethylene glycol) spacer for intracellular tracking and delivery. *Int J Nanomedicine*. 2006;1: 51-57.
- Shi X, Sun K, Baker JR. Spontaneous formation of functionalized dendrimer-stabilized gold nanoparticles. *J Phys Chem C Nanomater Interfaces*. 2009;112:8251-8258.
- Shukla R, Bansal V, Chaudhary M, Basu A, Bhonde RR, Sastry M. Biocompatibility of gold nanoparticles and their endocytotic fate inside the cellular compartment: a microscopic overview. *Langmuir*. 2005;21:10644-10654.
- Slater RJ. Labelling of proteins with  $^{125}\text{I}$ . In: Slater RJ, editor. *Radioisotopes in biology: a practical approach*. 2<sup>nd</sup> ed. Oxford University Press, New York;2002. p. 156-158.
- Slater RJ. Radioiodination. In: Slater RJ, editor. *Radioisotopes in biology: a practical approach*. 1<sup>st</sup> ed. Oxford University Press, New York;1990. p. 192-195.
- Sokolov K, Aaron J, Hsu B, Nida D, Gillenwater A, Follen M, MacAulay C, Adler-Storthz K, Korgel B, Descour M, Pasqualini R, Arap W, Lam W, Richards-Kortum R. Optical systems for in vivo molecular imaging of cancer. *Technol Cancer Res Treat*. 2003;2:491-504 [a].
- Sokolov K, Follen M, Aaron J, Pavlova I, Malpica A, Lotan R, Richards-Kortum R. Real-time vital optical imaging of precancer using anti-epidermal growth factor receptor antibodies conjugated to gold nanoparticles. *Cancer Res*. 2003;63:1999-2004 [b].
- Sonavane G, Tomoda K, Makino K. Biodistribution of colloidal gold nanoparticles after intravenous administration: effect of particle size. *Colloids Surf B*. 2008;66:274-280.
- Sorkin A, Krolenko S, Kudrjavitceva N, Lazebnik J, Teslenko L, Soderquist AM, Nikolsky N. Recycling of epidermal growth factor-receptor complexes in A431 cells: identification of dual pathways. *J Cell Biol*. 1991;112:55-63.
- Sperling RA, Rivera Gil P, Zhang F, Zanella M, Parak WJ. Biological applications of gold nanoparticles. *Chem Soc Rev*. 2008;37:1896-1908.
- Stolnik S, Illum L, Davis SS. Long circulating microparticle drug carriers. *Adv. Drug Deliv. Rev*. 1995;16:195-214.
- Storm FK, Harrison WH, Elliott RS, Morton DL. Normal tissue and solid tumor effects of hyperthermia in animal models and clinical trials. *Cancer Res*. 1979;39:2245-2251.

- Sun T, Sun BC, Ni CS, Zhao XL, Wang XH, Qie S, Zhang DF, Gu Q, Qi H, Zhao N. Pilot study on the interaction between B16 melanoma cell-line and bone-marrow derived mesenchymal stem cells. *Cancer Lett.* 2008;263:35-43.
- Sundaresan G, Yazaki PJ, Shively JE, Finn RD, Larson SM, Raubitschek AA, Williams LE, Chatziioannou AF, Gambhir SS, Wu AM. <sup>124</sup>I-labeled engineered anti-CEA minibodies and diabodies allow high-contrast, antigen-specific small-animal PET imaging of xenografts in athymic mice. *J Nucl Med.* 2003;44:1962-1969.
- Tabata M, Kondo M, Haruta Y, Seon BK. Antiangiogenic radioimmunotherapy of human solid tumors in SCID mice using <sup>125</sup>I-labeled anti-endoglin monoclonal antibodies. *Int J Cancer.* 1999;82:737-742.
- Takahashi N, Haba A, Matsuno F, Seon BK. Antiangiogenic therapy of established tumors in human skin/severe combined immunodeficiency mouse chimeras by anti-endoglin (CD105) monoclonal antibodies, and synergy between anti-endoglin antibody and cyclophosphamide. *Cancer Res.* 2001;61:846-854.
- Talapin DV, Mekis I, Götzinger S, Kornowski A, Benson O, Weller H. CdSe/CdS/ZnS and CdSe/ZnSe/ZnS core-shell-shell nanocrystals. *J Phys. Chem. B.* 2004;108:18826-18831.
- Tanaka F, Otake Y, Yanagihara K, Kawano Y, Miyahara R, Li M, Yamada T, Hanaoka N, Inui K, Wada H. Evaluation of angiogenesis in non-small cell lung cancer: comparison between anti-CD34 antibody and anti-CD105 antibody. *Clin Cancer Res.* 2001;7:3410-3415.
- Tanaka R, Yuhi T, Nagatani N, Endo T, Kerman K, Takamura Y, Tamiya E. A novel enhancement assay for immunochromatographic test strips using gold nanoparticles. *Anal Bioanal Chem.* 2006;385:1414-1420.
- Thorek DL, Elias DR, Tsourkas A. Comparative analysis of nanoparticle-antibody conjugations: carbodiimide versus click chemistry. *Mol Imaging.* 2009;8:221-229.
- Thurber GM, Schmidt MM, Wittrup KD. Factors determining antibody distribution in tumors. *Trends Pharmacol Sci.* 2008;29:57-61.
- Tiwari PM, Vig K, Dennis VA, Singh R. Functionalized gold nanoparticles and their biomedical applications. *Nanomaterials.* 2011;1:31-63.
- Torchilin V. Tumor delivery of macromolecular drugs based on the EPR effect. *Adv Drug Deliv Rev.* 2011;6:131-135.
- Torchilin VP, Trubetskoy VS. Which polymers can make nanoparticulate drug carriers long-circulating? *Adv Drug Deliv Rev.* 1995;16:141-155.
- Tseng KH, Liao CY, Huang JC, Tien DC, Tsung TT. Characterization of gold nanoparticles in organic or inorganic medium (ethanol/water) fabricated by spark discharge method. *Mater Lett.* 2008;62:3341-3344.

- Tsujie M, Tsujie T, Toi H, Uneda S, Shiozaki K, Tsai H, Seon BK. Anti-tumor activity of an anti-endoglin monoclonal antibody is enhanced in immunocompetent mice. *Int J Cancer*. 2008;122:2266-2273.
- Tsujie M, Uneda S, Tsai H, Seon BK. Effective anti-angiogenic therapy of established tumors in mice by naked anti-human endoglin (CD105) antibody: differences in growth rate and therapeutic response between tumors growing at different sites. *Int J Oncol*. 2006;29:1087-1094.
- Turkevich J, Stevenson PC, Hillier J. A study of the nucleation and growth processes in the synthesis of colloidal gold. *Discuss. Faraday Soc*. 1951;11:55-75.
- Uneda S, Toi H, Tsujie T, Tsujie M, Harada N, Tsai H, Seon BK. Anti-endoglin monoclonal antibodies are effective for suppressing metastasis and the primary tumors by targeting tumor vasculature. *Int J Cancer*. 2009;125:1446-1453.
- Van Cutsem E, Köhne CH, Hitre E, Zaluski J, Chang Chien CR, Makhson A, D'Haens G, Pintér T, Lim R, Bodoky G, Roh JK, Folprecht G, Ruff P, Stroh C, Tejpar S, Schlichting M, Nippgen J, Rougier P. Cetuximab and chemotherapy as initial treatment for metastatic colorectal cancer. *N Engl J Med*. 2009;360:1408-1417.
- van Dongen GA, Visser GW, Lub-de Hooge MN, de Vries EG, Perk LR. Immuno-PET: a navigator in monoclonal antibody development and applications. *Oncologist*. 2007;12:1379-1389.
- Verel I, Visser GW, Vosjan MJ, et al. High-quality <sup>124</sup>I-labelled monoclonal antibodies for use as PET scouting agents prior to <sup>131</sup>I-radioimmunotherapy. *Eur J Nucl Med Mol Imaging* 2004;31:1645-1652.
- Villiers CL, Freitas H, Couderc R, Villiers MB, Marche PN. Analysis of the toxicity of gold nanoparticles on the immune system: effect on dendritic cell functions. *J Nanopart Res*. 2009;12:55-60.
- Visaria R, Bischof JC, Loren M, Williams B, Ebbini E, Paciotti G, Griffin R. Nanotherapeutics for enhancing thermal therapy of cancer. *Int J Hyperthermia*. 2007;23:501-511.
- Visaria RK, Griffin RJ, Williams BW, Ebbini ES, Paciotti GF, Song CW, Bischof JC. Enhancement of tumor thermal therapy using gold nanoparticle-assisted tumor necrosis factor-alpha delivery. *Mol Cancer Ther*. 2006;5:1014-1020.
- von Maltzahn G, Park JH, Agrawal A, Bandaru NK, Das SK, Sailor MJ, Bhatia SN. Computationally guided photothermal tumor therapy using long-circulating gold nanorod antennas. *Cancer Res*. 2009;69:3892-3900.
- Vosjan MJWD, Perk LR, Visser GW et al. Conjugation and radiolabeling of monoclonal antibodies with zirconium-89 for PET imaging using the bifunctional chelate p-isothiocyanatobenzyl-desferrioxamine. *Nat. Prot*. 2010;5:739-743.

- Vugts DJ, van Dongen GAMS.  $^{89}\text{Zr}$ -labeled compounds for PET imaging guided personalized therapy. *Drug Discov Today Technol*. 2011;8:e53-e61.
- Wang J, Tian S, Petros RA, Napier ME, Desimone JM. The complex role of multivalency in nanoparticles targeting the transferrin receptor for cancer therapies. *J Am Chem Soc*. 2010;132:11306-11313 [b].
- Wang M, Thanou M. Targeting nanoparticles to cancer. *Pharm Res*. 2010;62:90-99 [a].
- Wei-Sheng Lee C, Ho I. Pharmacological Profiles of Oligomerized  $\mu$ -Opioid Receptors. *Cells*. 2013;2:689-714.
- Weissleder R, Kelly K, Sun EY, Shtatland T, Josephson L. Cell-specific targeting of nanoparticles by multivalent attachment of small molecules. *Nat Biotechnol*. 2005;23:1418-1423.
- Wikstrom P, Lissbrant IF, Stattin P, Egevad L, Bergh A. Endoglin (CD105) is expressed on immature blood vessels and is a marker for survival in prostate cancer. *Prostate* 2002;51:268-275.
- Wilbur DS, Hadley SW, Hylarides MD, et al. Development of a stable radioiodinating reagent to label monoclonal antibodies for radiotherapy of cancer. *J Nucl Med* 1989;30:216-226.
- Wilson DS, Nock S. Functional protein microarrays. *Curr Opin Chem Biol*. 2002;6:81-85.
- Wu AM, Senter PD. Arming antibodies: prospects and challenges for immunoconjugates. *Nat Biotechnol* 2005;23:1137-1146.
- Wu AM, Yazaki PJ. Designer genes: recombinant antibody fragments for biological imaging. *Q J Nucl Med*. 2000;44:268-283.
- Xie H, Diagaradjane P, Deorukhkar AA, Goins B, Bao A, Phillips WT, Wang Z, Schwartz J, Krishnan S: Integrin  $\alpha\text{v}\beta\text{3}$ -targeted gold nanoshells augment tumor vasculature-specific imaging and therapy. *Int J Nanomed* 2011;6:259-269.
- Yamamoto T, Naito M, Moriyama H, Umezumi H, Matsuo H, Kiwada H, Arakawa M. Repopulation of murine Kupffer cells after intravenous administration of liposome-encapsulated dichloromethylene diphosphonate. *Am J Pathol*. 1996;149:1271-1286.
- Yarden Y. The EGFR family and its ligands in human cancer: signalling mechanisms and therapeutic opportunities. *Eur J Cancer*. 2001;37:S3-S8.
- Yuan F, Dellian M, Fukumura D, Leunig M, Berk DA, Torchilin VP, Jain RK. Vascular permeability in a human tumor xenograft: molecular size dependence and cutoff size. *Cancer Res*. 1995;55:3752-3756.
- Zalutsky MR, Narula AS. A method for the radiohalogenation of proteins resulting in decreased thyroid uptake of radioiodine. *Int J Rad Appl Instrum A* 1987;38:1051-1055.

Zandi R, Larsen AB, Andersen P, Stockhausen MT, Poulsen HS. Mechanisms for oncogenic activation of the epidermal growth factor receptor. *Cell Signal*. 2007;19:2013-2023.

Zhang G, Yang Z, Lu W, et al. Influence of anchoring ligands and particle size on the colloidal stability and in vivo biodistribution of polyethylene glycol-coated gold nanoparticles in tumor-xenografted mice. *Biomaterials*. 2009;30:1928-1936.

Zhang Y, Hong H, Cai W. PET tracers based on Zirconium-89. *Curr Radiopharm*. 2011;4:131-139.

Zhang Y, Hong H, Orbay H, Valdovinos HF, Nayak TR, Theuer CP, Barnhart TE, Cai W. PET imaging of CD105/endoglin expression with a <sup>61/64</sup>Cu-labeled Fab antibody fragment. *Eur J Nucl Med Mol Imaging*. 2013;40:759-767.

Zhao W, Brook MA, Li Y. Design of gold nanoparticle-based colorimetric biosensing assays. *Chembiochem*. 2008;9:2363-2371.

Zharov VP, Galitovsky V, Viegas M. Photothermal detection of local thermal effects during selective nanophotothermolysis. *Appl. Phys. Lett*. 2003;83, 4897-4899.

Zheng Y, Sanche L. Gold nanoparticles enhance DNA damage induced by anti-cancer drugs and radiation. *Radiat Res*. 2009;172:114-119.



## **APPENDIX**

Appendix 1: Radiolabelled monoclonal antibodies currently FDA approved in oncology and other diseases.

<i>A. Antibody-based imaging agents in the clinic (Olafsen 2010)</i>					
Radioimmunoconjugate (trade name)	Antibody format	Target	FDA-approved cancer indication (approval)		
<sup>111</sup> In-Satumomab pentetide (OncoScint®)*	murine IgG <sub>1</sub>	TAG-72	Colorectal, ovarian carcinoma (1992)		
<sup>99m</sup> Tc-Arcitumomab (CEA-Scan®)	murine IgG <sub>1</sub> Fab'	CEA	Colorectal, breast and small cell lung carcinoma (1996)		
<sup>111</sup> In-Imciromab pentetate (Myoscint®)*	murine IgG <sub>2a</sub> Fab'	Myosin	Myocardial necrosis (1996)		
<sup>99m</sup> Tc-Nofetumomab-merpentan (Verluma®)*	murine IgG <sub>2b</sub> Fab'	EGP-1	Non-small and small cell lung carcinoma (1996)		
<sup>111</sup> In-Capromab pentetide (ProstaScint®)	murine IgG <sub>1</sub>	PSMA	Prostate carcinoma (1996)		
<sup>111</sup> In-ibritumomab tiuxetan (Zevalin®)	murine IgG1	CD20	To confirm the appropriate distribution of Zevalin® and determine if patient is eligible to receive <sup>90</sup> Y-Zevalin® therapy + dosimetry.		
<sup>111</sup> In-Igovomab (Indimacis-125®)*	murine IgG <sub>1</sub> F(ab') <sub>2</sub>	CA-125	Ovarian cancer (not in US)		
<sup>99m</sup> Tc-Sulesomab (LeukoScan®)	murine IgG <sub>1</sub> Fab'	NCA-90	Osteomyelitis, appendicitis, inflammatory bowel disease (not in US)		
<i>B. Radiolabelled antibodies approved for therapeutic use (Boswell 2007)</i>					
				Mechanisms of action	
<sup>90</sup> Y-ibritumomab tiuxetan (Zevalin®)	murine IgG <sub>1</sub>	CD20	Treatment of relapsed or refractory, low-grade or follicular B cell NHL Previously untreated follicular NHL in patients who achieve a partial or complete response to first-line chemotherapy (2002)	Delivery of the radioisotope <sup>90</sup> Y	
<sup>131</sup> I-tositumomab (Bexxar®)	murine IgG <sub>2</sub>	CD20	Treatment of patients with CD20 antigen-expressing relapsed or refractory, low-grade, follicular or transformed NHL (2003)	Delivery of the radioisotope <sup>131</sup> I, ADCC and direct induction of apoptosis	

Appendix 2: Physical data of useful radionuclides for radioimmunoinaging (Boswell 2007).

Radionuclide	Particle emitted (imaging decay)	Half-life	$E_{\beta^+}$ [avg]	Particle energy* (keV) $\gamma$	Mean range* (mm)	Production
Technetium ( $^{99m}\text{Tc}$ )	$\gamma$	6.02 h		140.5	-	$^{99}\text{Mo}/^{99m}\text{Tc}$ generator
Indium ( $^{111}\text{In}$ )	$\gamma$	67.3 h		171.3 245.4	-	$^{111}\text{Cd}(\text{p,n})^{111}\text{In}$
Thallium ( $^{201}\text{Tl}$ )	$\gamma$	73.1 h		167.4 135.3	-	$^{203}\text{Tl}(\text{p,3n})^{201}\text{Pb}/^{201}\text{Tl}$
Copper ( $^{64}\text{Cu}$ )	$\beta^+$ , $\gamma$	12.7 h	278.1	1345.8	0.70	$^{64}\text{Ni}(\text{p,n})^{64}\text{Cu}$
Yttrium ( $^{86}\text{Y}$ )	$\beta^+$ , $\gamma$	14.7 h	672	1076.7 627.8 1153.1	2.46	$^{86}\text{Sr}(\text{p,n})^{86}\text{Y}$
Zirconium ( $^{89}\text{Zr}$ )	$\beta^+$ , $\gamma$	78.4 h	396.9	909.1	1.18	$^{89}\text{Y}(\text{p,n})^{89}\text{Zr}$
Bromine ( $^{76}\text{Br}$ )	$\beta^+$ , $\gamma$	16.0 h	1180	559.1 657.0 1853.7	5.07	$^{76}\text{Se}(\text{p,n})^{76}\text{Br}$
Iodine ( $^{123}\text{I}$ )	$\gamma$	13.13 h	159		-	$^{124}\text{Te}(\text{p,2n})^{123}\text{I}$
Iodine ( $^{124}\text{I}$ )	$\beta^+$ , $\gamma$	100.2 h	830.5	602.7	3.25	$^{124}\text{Te}(\text{p,n})^{124}\text{I}$
Iodine ( $^{125}\text{I}$ )	$\gamma$	60.1 d		35.5	-	$^{124}\text{Xe}(\text{n},\gamma)^{125}\text{Xe}/^{125}\text{I}$
Fluorine ( $^{18}\text{F}$ )	$\beta^+$	1.8 h	250		-	$^{18}\text{O}(\text{p,n})^{18}\text{F}$
Gallium ( $^{68}\text{Ga}$ )	$\beta^+$	1.1 h	1899		-	$^{68}\text{Ge}/^{68}\text{Ga}$ generator

\* As reported by Kocher (1981) and Milenic (2004).

Appendix 3: Physical data of useful radionuclides for radioimmunotherapy (Boswell 2007).

Radionuclide	Particle emitted (RIT decay)	Half-life	Particle energy* (keV) $\alpha$ $E_{\beta^-}$ [avg] Auger e- [max]	Mean range* (mm)	Production
Iodine ( $^{131}\text{I}$ )	$\beta^-$	8 d	181.7	0.36	$^{131}\text{Te}(n,\gamma)^{131}\text{I}$
Yttrium ( $^{90}\text{Y}$ )	$\beta^-$	2.7 d	934.8	3.78	$^{90}\text{Sr}/^{90}\text{Y}$ generator $^{89}\text{Y}(n,\gamma)^{90}\text{Y}$
Rhenium ( $^{186}\text{Re}$ )	$\beta^-$	3.8 d	349.3	0.98	$^{185}\text{Re}(n,\gamma)^{186}\text{Re}$
Rhenium ( $^{188}\text{Re}$ )	$\beta^-$	17 h	764.2	2.91	$^{188}\text{W}/^{188}\text{Re}$ generator $^{187}\text{Re}(n,\gamma)^{188}\text{Re}$
Lutetium ( $^{177}\text{Lu}$ )	$\beta^-$	6.7 d	133	0.22	$^{176}\text{Lu}(n,\gamma)^{177}\text{Lu}$
Copper ( $^{67}\text{Cu}$ )	$\beta^-$	2.6 d	141	0.24	$^{68}\text{Zn}(p,2p)^{67}\text{Cu}$ $^{67}\text{Zn}(n,p)^{67}\text{Cu}$
Astatine ( $^{211}\text{At}$ )	$\alpha$	7.2 h	5867	0.04-0.1	$^{209}\text{Bi}(\alpha,2n)^{211}\text{At}$
Bismuth ( $^{212}\text{Bi}$ )	$\alpha, \beta^-$	45.7 min	6090 717.3	0.04-0.1 2.68	$^{212}\text{Pb}/^{212}\text{Bi}$ generator $^{228}\text{Th}/^{212}\text{Bi}$ generator
Bismuth ( $^{213}\text{Bi}$ )	$\alpha, \beta^-$	0.77 h	5870 430	0.04-0.1 1.32	$^{225}\text{Ac}/^{213}\text{Bi}$ generator
Iodine ( $^{125}\text{I}$ )	Low-energy Auger electrons	60.1 d	350	0.001	$^{124}\text{Xe}(n,\gamma)^{125}\text{Xe}/^{125}\text{I}$
Gallium ( $^{67}\text{Ga}$ )	Low-energy Auger electrons	3.3 d	180	0.001	$^{68}\text{Zn}(p,2n)^{67}\text{Ga}$

\* As reported by Kocher (1981) and Milenic (2004).

Appendix 4: Summary of some preclinical studies using anti-endothelin monoclonal antibodies (anti-CD105 mAbs) (Adapted from Fonsatti 2010).

Anti-CD105 mAbs clone	<i>In vitro</i>		References	<i>In vivo</i>			References
	Activity	Cell type		Activity	Tumour type	Host	
MJ7/18	Targeting agent	murine ECs	Korpany 2005	Cancer imaging Vascular imaging	murine melanoma murine pancreatic adenocarcinoma	C57BL/6 mice	Bredow 2000 Korpany 2007
MAEND3	-	-	-	Cancer imaging	Spontaneous mammary carcinoma	Beagle dog	Fonsatti 2000
E9	-	-	-	Cancer imaging	Human renal carcinoma	Excised human kidneys	Costello 2004
SN6f	-	-	-	Antitumour Antiangiogenic	Human breast cancer	SCID mice	Seon 1997 Tabata 1999 Takahashi 2001
SN6k	-	-	-	Antitumour Antiangiogenic	murine mammary carcinoma murine colon adenocarcinoma human breast cancer	BALB/c mice SCID mice	Matsuno 1999 Takahashi 2001 Uneda 2009
SN6J	Inhibition of proliferation Induction of apoptosis ADCC	HUVEC	She 2004 Tsuje 2008 Uneda 2009	Antitumour Antiangiogenic	murine mammary carcinoma murine colon adenocarcinoma human breast cancer	BALB/c mice SCID mice	Takahashi 2001 Tsuje 2008 Uneda 2009
SN6	Inhibition of proliferation	HUVEC	She 2004	-	-	-	-
SN6a	Inhibition of proliferation	HUVEC	She 2004	Antitumour Antiangiogenic	murine mammary carcinoma murine colon adenocarcinoma	BALB/c mice	Uneda 2009
SN6h	Inhibition of proliferation	HUVEC	She 2004	-	-	-	-
TEC11	Inhibition of proliferation Inhibition of urokinase production	HUVEC HDMC Vascular ECs	Burrows 1995 Maier 1997	-	-	-	-
44G4	Targeting agent	murine fibroblasts	Munoz 2007	-	-	-	-

ECs : endothelial cells; HUVEC: human umbilical vein endothelial cells; ADCC: antibody-dependent cellular cytotoxicity; HDMC : human dermal microvascular endothelial cells.

## Appendix 5: Gold quantification by ICP-MS in mice

The inductively coupled plasma mass spectrometry (ICP-MS) is showing to be a highly sensitive method to quantify elements at trace level, such as gold. Thus, ICP-MS analysis is useful for toxicology and biodistribution studies. This analytical technique combines a high temperature atomizing ion source (ICP) with a mass spectrometer (MS). The biological solid samples, such as tissues are acid digested, dissolved and diluted before running on the ICP-MS instrumentation. The sample is typically introduced by aspirating into a nebulizer in argon atmosphere. Once the sample aerosol is introduced in the ICP torch, it is first gasified and then ionized in argon plasma. The ICP source converts the atomic elements in the sample to ions. The mass spectrometer detects the ions and separated them according to their mass-to-charge ratio ( $m/z$ ) through a quadrupole mass filter, which allows ions with the same  $m/z$  ratio to pass through the detector at a given instant in time. The separated ions are counted by the detector, which translates the number of ions striking the detector into an electrical signal. The signal can be related to the number of atoms of that element in the sample *via* the setting up of a linear calibration curve using calibration standards (Figure 29).

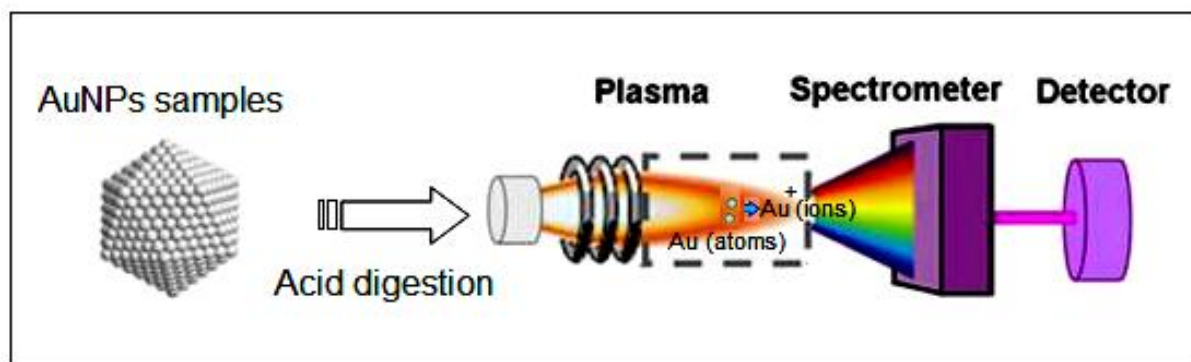


Figure 29: Process scheme of ICP-MS analysis of gold nanoparticles (AuNPs) with prior sample dissolution (Adapted from Allabashi 2009).

